Non-local damage mechanics with evolving interactions for modeling quasi-brittle materials : anisotropic damage and gradient-enhanced Eikonal approach

Breno Ribeiro Nogueira

THESE DE DOCTORAT

NNT : 2024UPAST072

Non-local damage mechanics with evolving interactions for modeling quasi-brittle materials : anisotropic damage and gradient-enhanced Eikonal approach

Mécanique de l'endommagement nonlocal avec interactions évolutives pour la modélisation des matériaux quasi-fragiles : endommagement anisotrope et approche Eikonale à gradient implicite

Thèse de doctorat de l'université Paris-Saclay

École doctorale n° 579, Sciences mécaniques et énergétiques, matériaux et géosciences (SMEMaG)
Spécialité de doctorat : Génie Civil
Graduate School : Sciences de l'ingénierie et des systèmes.
Référent : ENS Paris-Saclay

Thèse préparée dans les unités de recherche **LMPS - Laboratoire de Mécanique Paris-Saclay (Université Paris-Saclay, CentraleSupélec, ENS Paris-Saclay, CNRS)** et **DiBT - Divisione Ingegneria del dipartimento di Bioscienze e Territorio (Università degli Studi del Molise)**, sous la direction de **Fabrice GATUINGT**, Professeur des Universités (ENS), la co-direction de **Carlo CALLARI**, Professeur (Unimol), le co-encadrement de **Cédric Giry**, Professeur (EPF), et le co-encadrement de **Giuseppe RASTIELLO**, Ingénieur chercheur (CEA Saclay)

Thèse soutenue à Paris-Saclay, le 03 juillet 2024, par

Breno RIBEIRO NOGUEIRA

Composition du jury

Membres du jury avec voix délibérative

Djimédo KONDO Professeur des Universités, Sorbonne Université	Président
Gilles PIJAUDIER-CABOT Professeur des Universités, Université de Pau et des Pays de l'Adour	Rapporteur & Examinateur
Nicolas MOËS Professeur des Universités, École Centrale de Nantes	Rapporteur & Examinateur
Bert SLUYS Professeur, TU Delft	Examinateur
Rodrigue DESMORAT Professeur des Universités, ENS Paris-Saclay	Examinateur
Domenico GENTILE Professeur, Università degli Studi del Molise	Examinateur

université PARIS-SACLAY

ÉCOLE DOCTORALE
Sciences mécaniques et énergétiques, matériaux et géosciences (SMEMAG)

Titre : Mécanique de l'endommagement nonlocal avec interactions évolutives pour la modélisation des matériaux quasi-fragiles : endommagement anisotrope et approche Eikonale à gradient implicite

Mots clés : Quasi-fragile, non-local, endommagement anisotrope, gradient implicite, Eikonal

Résumé : La prévision de la nucléation et de la propagation des fissures est essentielle pour décrire la réponse des structures dans des conditions de chargement complexes. On observe l'apparition de microfissures diffuses avant la formation d'une macrofissure. Dans le cas de matériaux quasi-fragiles, on observe un comportement adoucissant lié à une perte progressive de rigidité. D'un point de vue thermodynamique, ce comportement peut être décrit de manière continue par une variable d'état d'endommagement. Cependant, les modèles d'endommagement locaux conduisent inévitablement à un problème aux valeurs limites mal posé. Dans un contexte d'éléments finis, les résultats numériques dépendent donc du maillage. Les modèles d'endommagement non locaux permettent d'obtenir des résultats indépendants du maillage en introduisant des interactions de voisinage par le biais d'une longueur interne. Les approches non locales classiques considèrent des interactions isotropes et constantes, ce qui ne permet pas de reproduire correctement l'ensemble du processus de dégradation. Des approches prenant en compte des interactions évolutives existent et peuvent mieux décrire le comportement de la fissuration. Cette thèse vise à fournir des aspects théoriques et numériques pour le développement de modèles d'endommagement à gradient implicite avec interactions évolutives. Tout d'abord, les modèles non-locaux sont étudiés et comparés en analysant les effets de bord et la diffusion de l'endommagement dans un essai d'écaillage unidimensionnel en dynamique explicite.

L'approche non-locale Eikonale est étudiée, où les interactions évolutives sont considérées par le biais d'une métrique riemannienne dépendante de l'endommagement. La version avec gradient de ce modèle (ENLG) est ensuite dérivée d'un cadre micromorphe basé sur la géométrie différentielle, conduisant à une expression de dissipation respectant au second principe de la thermodynamique. Une formulation variationnelle simplifiée est développée pour évaluer les capacités du modèle dans des simulations numériques quasi-statiques bidimensionnelles avec endommagement isotrope. Enfin, la régularisation ENLG est couplée à un modèle d'endommagement anisotrope prenant en compte un tenseur d'endommagement de second ordre. L'anisotropie induite est naturellement prise en compte dans le comportement et dans les interactions évolutives. Des simulations en deux et trois dimensions sont étudiées et comparées aux résultats expérimentaux existants dans la littérature, tout en soulignant les aspects numériques associés. Une analyse détaillée décrit les avantages de la prise en compte de l'endommagement anisotrope et des interactions anisotropes dépendantes de l'endommagement.

université PARIS-SACLAY

ÉCOLE DOCTORALE
Sciences mécaniques et énergétiques, matériaux et géosciences (SMEMAG)

Title : Non-local damage mechanics with evolving interactions for modeling quasi-brittle materials : anisotropic damage and gradient-enhanced Eikonal approach
Keywords : Quasi-brittle, non-local, anisotropic damage, gradient-enhanced, Eikonal

Abstract : Predicting the cracking nucleation and propagation is essential to describe structural response under complex loading conditions. Diffuse micro-cracks are observed to appear before coalescing into a macro-crack. In the case of quasi-brittle materials, strain-softening behavior is observed and is related to a progressive loss of stiffness. From a thermodynamics viewpoint, this can be described in a continuum way by a damage state variable.

However, local continuum damage mechanics models inevitably lead to an ill-posed rate equilibrium problem. In a finite element context, numerical results are, therefore, mesh-dependent. Non-local damage models can recover mesh-independent results by introducing neighborhood interactions through an internal length. Classic non-local approaches consider isotropic and constant interactions, which cannot reproduce the entire degradation process appropriately. Evolving interaction approaches exist and may better describe the cracking behavior. This thesis aims to provide theoretical and numerical aspects for developing evolving interactions gradient-enhanced damage models. Firstly, non-local models are studied and compared by analyzing boundary effects and damage diffusion in a one-dimensional explicit dynamics spalling test. The Eikonal non-local approach is given attention, where evolving interactions are considered through a damage-dependent Riemannian metric. The gradient-enhanced version of this model (ENLG) is then derived from a differential geometry-based micromorphic framework, leading to a dissipation expression fulfilling thermodynamics second principle. A simplified variational formulation is developed to evaluate the model's capabilities in two-dimensional isotropic damage quasi-static numerical simulations. Finally, the ENLG regularization is coupled to an anisotropic damage model considering a second-order damage tensor. Damage-induced anisotropy is naturally considered in the behavior and the evolving interactions. Simulations in two and three-dimensional contexts are studied and compared to existing experimental results from the literature while highlighting the numerical aspects involved. A detailed analysis describes the advantages of considering anisotropic damage and damage-dependent anisotropic interactions.

Acknowledgements

Après 5 ans (master + doctorat) de mon aventure à l'ENS, il est moment de remercier tous ceux qui ont pu, d'une manière ou d'autre, contribuer à ce beau parcours. Il s'agit pour moi d'une tâche très difficile : m'exprimer en quelques mots sur des sentiments qui mériteraient d'être décrits dans un livre entier. Il est fort probable, et tout à fait normal vu le nombre de gens qui a croisé mon chemin ces dernières années, que j'oublie certains ici. Je m'en excuse d'avance.

Tout d'abord, je voulais remercier les membres de mon jury. Merci à Djimédo Kondo d'avoir présidé mon jury de soutenance. Merci également pour toutes les discussions aussi enrichissantes. Grâce à une question que tu m'avais posée à Giens en 2022, j'ai pris le temps de regarder un peu plus la thermodynamique pour les milieux non-locaux. Le fruit de cette remarque est justement ce qui est discuté au Chapitre 4 de ce manuscrit. J'espère te recroiser les années qui viennent et peut-être collaborer ensemble, comme on en avait discuté juste après la soutenance. Merci à mes rapporteurs, Nicolas Moës et Gilles Pijaudier-Cabot, d'avoir accepté la tâche de lire attentivement ce manuscrit et de m'enrichir avec vos commentaires aussi pertinents. Il a été un plaisir pour moi de donner suite à la discussion pendant la soutenance et de pouvoir échanger avec vous. Enfin, merci à toi Rodrigue Desmorat de m'avoir introduit à la mécanique de l'endommagement quand nous étions encore tous à Cachan il y a 5 ans. Je n'oublierai jamais les pauses midi avec un sandwich pendant qu'on discutait devant un tableau. Merci pour toutes les discussions pendant ces dernières années et pour toutes les remarques indispensables à la réalisation de mes travaux. I switch to english to thank professor Domenico Gentile for accepting evaluating my work and his valuable remarks during the defense. I would like also to thank professor Bert Sluys for the very interesting discussion and his comments.

Finally, it was really a pleasure to me to have all these well known big names of damage mechanics evaluating my work. I have read a lot of your papers and it was very important to have your insights on my work.

Thank you to my supervisors for the opportunity to do this thesis. Thank you Carlo Callari for your availability and the very good times we spent together during my stay in Campobasso. Thank you also for accepting being part of this project and your valuable contributions. Je repasse en Français pour remercier Fabrice Gatuingt. Cela a été un plaisir de travailler avec toi, depuis mon stage de M1 jusqu'à la thèse. Outre tes qualités scientifiques et tes nombreuses remarques pertinentes, je te remercie énormément pour tes qualités humaines. Merci beaucoup pour ton amitié. Et en parlant d'amitié, je ne cesserai pas de dire que je vous considère des amis. Merci à toi Cédric Giry pour tous les conseils, remarques, les livres que tu m'as offert et toutes les discussions, parfois très fondamentales,

mais nécessaires. Enfin, merci beaucoup à toi Giuseppe Rastiello. Tu étais là pendant les moments faciles, difficiles et compliqués, pas seulement en tant qu'encadrant. Merci pour nos discussions sur l'Italie, le Brésil, les couteaux en acier damas, les pantalons japonais, la musique ou beaucoup plus courant, l'endommagement qui courbe l'espace. Merci pour ta rigueur et tout le support durant ces années. Bon courage pour ton HDR mais nous avons encore quelques papiers à sortir ! J'espère vraiment pouvoir continuer à collaborer avec vous trois dans d'autres projets. On se croisera certainement au plateau de Saclay.

J'ai eu également l'honneur de croiser des personnes incroyables au cours de mes années à l'ENS à Cachan-Saclay, au LMT et au LMPS à Saclay. Mes potes de promo de l'ENS qui étaient là pour la soutenance ou le pot après: Nathan, André, Max, Clément et Sofiane. Merci beaucoup à vous pour toutes ces années et bientôt c'est aussi votre tour de soutenir la thèse et je serai là pour fêter tout cela. Merci à Clément pour toutes les discussions souvent très philosophiques. Merci pour ce partage de la passion des maths, de la géométrie différentielle et des nouvelles choses qu'on peut faire avec en méca. En effet, "Les chaussures sont un instrument pour marcher, les maths sont un instrument pour penser. On peut marcher sans chaussures, mais on va moins loin" (Jean-Marie Souriau). Merci Nathan pour ton amitié, tous nos échanges, conseils, blagues et discussions aussi enrichissantes. Enfin, merci Sofiane d'être toujours là depuis longtemps et de partager avec moi des moments essentiels pour ma vie. Tu étais toujours là pour moi et je serai là pour toi également. C'est nous !

Un grand merci aux gens que j'ai croisé au labo durant ces années de thèse. L'ambiance au LMT-LMPS a été un point clé de toute ma réussite. Flavien et Alexandre, merci énormément pour nos discussions au centre de calcul/simulation. Cela paraissait toujours tellement simple de faire des choses compliqués lorsqu'on en parlait entre nous. Cela a été un plaisir de partager ces moments avec vous et nous pourrons continuer et faire pareil pendant notre postdoc au plateau. Merci également à Julien pour des raisons pareils, mais tu as dû nous abandonner un peu plutôt pour tes aventures en Finlande. Vivement ton retour en France pour discuter de la vie en général de vive voix ! Merci Mahmoud pour les discussions les plus folles et les blagues sans aucun sens (on se comprend). Merci à toi Yannick qui est resté jusqu'aux derniers moments du pot à Paris. Nos discussions ont été toujours très enrichissantes pour moi. Merci Donald d'avoir partagé le bureau avec moi et pour toutes nos discussions scientifiques. Merci à Pierre, Marc, Marie, Antoine pour toutes les pauses. Merci Rodolfo, un vrai frère que l'ENS m'a donné lorsqu'il est arrivé pour son postdoc. Merci Héloïse pour tout le support, les pauses, les discussions, les blagues et tous les moments. On a partagé ensemble ces derniers jours de rédaction, pré-soutenance, soutenance et cela a été essentiel pour moi de pouvoir compter sur quelqu'un vivant une situation similaire. Enfin, merci aux gestionnaires qui ont toujours fait un travail incroyable: Lydia, Charlène, Fouleye. Merci à vous pour avoir trouvé la solution pour tous les problèmes possibles. A mes amis de Campobasso, je ne pourrai pas remercier tout le monde, mais un grand merci à Stefano, Tony, Modesto et Rodrigo pour l'aide quand j'étais sur place.

Ceci dit, je ne pourrai jamais finir ces remerciements sans parler de ma famille brésilienne à Paris et ceux qui sont toujours au Brésil. Merci à la team poker stars: Jean et Malou (et le petit Ravi), Martin, Marcelo, Marcos, Philippe, Sarah et Isabela. Paris,

Lyon et Nîmes ne seraient pas les mêmes sans vous. Merci Martin pour avoir partagé les moments de thésard ensemble et toutes les bières au franprix à l'X. Merci spécial à Jean. Cela fait plus de 15 ans qu'on se connaît et on a vécu tout cela ensemble, depuis les cours de français jusqu'à la soutenance de nos thèses et la naissance de Ravi. Grand merci à toi pour tout le support et notre amitié. Merci également à la team BR à Paris: Vini, Louna, Jorge, Olivia, Rena Negreiros, Rena Paulineli, Lucas. Sachez que vous avez été vraiment essentiels et importants dans ma vie. Merci à tous mes amis du Brésil qui, malgré la distance, se sont fait présents pendant cette période. João Artur, mon cousin, frère, je te suis de loin et tes réussites sont mes réussites, merci pour tout.

Finalement, je voulais laisser quelques mots pour remercier toute ma famille au Brésil. Cela m'a chauffé le coeur de savoir que vous étiez tous en ligne en train de regarder. Je vous aime fort. A ma soeur, Marcela, qui n'a pas pu être là, merci pour tes mots. Merci pour ton support, ta gentillesse et pour tout ton effort pour notre famille. Tu es la matérialisation de la définition de soeur/frère. Merci infiniment à mes parents, Fernando Artur et Maria Tereza. Pour être court, vous êtes tout. Tout simplement, tout. J'évite d'écrire en quelques mots ce qui vous représentez pour moi et pour notre famille car cela ne serait jamais suffisant. Merci pour le support inconditionnel, même de si loin.

Enfin, merci à toi Marina. Tu m'as guidé, tu m'as écouté, tu as été juste toi même et c'est ce qui est incroyable. Tu as été un vrai pilier pour moi. Merci infiniment pour ton support et *tua entrega* pour que tout se passe bien. Cela a été difficile, mais certes beaucoup plus simple avec toi à côté.

Breno Ribeiro Nogueira
Paris, le 3 juillet 2024

Contents

List of Tables

List of Figures

List of Symbols

Spaces

$\mathbb{R}$	Real space
$\mathcal{O}(n)$	Orthogonal group of dimension n
$H^n(\cdot)$	n-order Sobolev space

Math

$\bullet'$	Deviatoric part of second-order tensor $\bullet$
$\otimes$	Tensor product
$\overline{\otimes}$	Symmetrized tensor product
:	Double contraction
∇	Gradient operator
∇^s	Symmetrized gradient operator
$\nabla\cdot$	Divergent operator
$[\![\bullet]\!]$	Jump of a quantity $\bullet$
$\mathcal{H}_\Gamma$	Heaviside function at discontinuity Γ
δ_Γ	Dirac-delta at discontinuity Γ
$\mathrm{tr}\,\bullet$	Trace of $\bullet$
$\langle\bullet\rangle$	Positive part of $\bullet$
$\det\bullet$	Determinant of $\bullet$

Constants

$\mathbf{0}$	Null tensor
$\mathbf{I}$	Second-order identity tensor
$\mathbb{I}$	Fourth-order identity tensor
$\mathbb{I}^\flat$	Contravariant 4th-order identity tensor
$\mathbb{I}_\#$	Covariant 4th-order identity tensor

$\mathbb{I}^{\flat}_{\#}$	Mixed contravariant-covariant 4th-order identity tensor
$\mathbb{I}^{\#}_{\flat}$	Conjugated covariant-contravariant 4th-order identity tensor
G	Shear modulus
E	Young's modulus
K	Bulk modulus
λ	First Lamé's parameter
ν	Poisson's ratio
l_c	Characteristic length
c	Gradient parameter
c_e	1D elastic wave speed
κ_0	Damage threshold
B_t	Parameter for isotropic damage evolution
S	Parameter for anisotropic damage evolution
s	Parameter for anisotropic damage evolution
B	Parameter for anisotropic damage evolution
ξ	Residual non-local interactions parameter

Variables

$\boldsymbol{\sigma}$	Stress tensor
$\boldsymbol{\varepsilon}$	Strain tensor
$\mathbf{D}$	Damage tensor
$\mathbf{H}$	Ladevèze's damage tensor
$\mathbf{g}$	Riemannian metric
$\mathbf{P}$	Normalized damage direction tensor
$\boldsymbol{u}$	Displacement field
$\boldsymbol{v}$	Virtual displacement field
$\mathbf{v}$	Velocity field
$\boldsymbol{t}^d$	Imposed stress tractions
$\boldsymbol{n}$	Outward normal vector on the boundary $\partial\Omega$
$\boldsymbol{n}_d$	Normal vector on the discontinuity Γ
$\mathbb{E}$	Elasticity tensor
$\tilde{\mathbb{E}}(\mathbf{D})$	Effective elasticity tensor

$\mathbb{L}$	Tangent operator tensor
ϕ	Weighting function
$\bar{e}$	Non-local equivalent strain
e	Local equivalent strain
κ	Damage history variable
e	Specific internal energy
s	Specific entropy
ρ	Density
D	Scalar damage variable
Ω	Considered domain
$\partial\Omega$	Boundary of Ω
Γ	Discontinuity surface
ψ	Specific Helmholtz free energy
T	Temperature
R_v	Triaxility function
T_X	Triaxility
ε_T	Tangential component of the strain vector
ε_N	Normal component of the strain vector

Acronyms

CDM	Continuum Damage Mechanics
FPZ	Fracture Process Zone
LEFM	Linear Elastic Fracture Mechanics
FM	Fracture Mechanics
FE	Finite Element
GNL	Classic Gradient-enhanced Non-Local model
INL	Classic Integral Non-Local model
NLSB	Integral Non-Local Stress-Sased model
ENL	Eikonal Non-Local approach
ENLI	Integral Eikonal Non-Local model
ENLG	Eikonal Non-Local Gradient-enhanced model

Introduction

1 General context and motivations

Accurately predicting the response of structures subjected to complex loading scenarios is a challenging task in engineering. In practice, standard design codes concentrate on bearing capacity and yield analysis, which implies using safety factors. Therefore, the fine description of failure mechanisms and how energy is dissipated are often simplified or completely neglected. This approach is generally accepted mainly for pragmatic reasons: designed systems can usually resist the incoming loads during their lifespan. However, given that the actual capacities are, in fact, unknown, structural overdesign becomes inevitable.

In the context of climate change, overdesign is directly related to resource consumption and, thus, Greenhouse gas (GHG) emissions. IEA (2019) estimated that, in 2018, 11% of used energy and process-related CO2 emissions came from manufacturing building materials and products (e.g., cement, steel, and glass). We must, therefore, reduce the unnecessary extra material used in construction sites and the industry. Consequently, a better comprehension of material degradation (i.e., the appearance of micro and macro-cracks and their influence on material properties) and durability becomes indispensable. In particular, studying cracking nucleation and propagation is essential to assess realistic structural performances. This is already the case for analyzing sensible structures, where there is little room for errors. For instance, crack opening is an essential input data for the estimation of leakage rate through containment walls of nuclear power plants. In this context, predictions must be more accurate and provide useful information about remaining service life. Therefore, studying material degradation plays a significant role in these estimations.

Research on cracking mechanisms has also gained attention in other engineering problems related to the energetic transition. One can cite the hydrogen embrittlement in metals (transition from ductile to quasi-brittle or brittle behavior), implying severe safety risks in its transportation and storage, or the study of fracture networks in enhanced geothermal systems. Last, but not least, the study of fracture mechanisms plays also a major role in the understanding of ice mechanics. Particularly, accurate models describing degradation become essential in the estimation of mass-loss in ice sheets, which drastically contributes to the sea level rise.

Quasi-brittle materials are present almost everywhere, and some examples are concrete and mortar, some rocks, tough ceramics, masonry, sea ice, wood, and many others. The degradation of the mechanical properties mainly characterizes them due to cracking when subjected to load. Therefore, there is undoubtedly a need to describe their behavior.

2 Scientific approach and objectives

The main aim of this thesis is to provide theoretical and numerical developments concerning modeling degradation mechanisms in quasi-brittle media. The objective is to provide, *in fine*, a reliable and robust numerical framework for predicting cracking in structural simulations. For this sake, we restrict ourselves to only studying material degradation induced by mechanical loading.

Continuum mechanics is used, so the medium is described based on a Representative Elementary Volume, which the size is sufficiently more significant than the material heterogeneity and smaller than the structure considered. Thus, material behavior is defined in a homogenized way following a consistent thermodynamic framework. Energy dissipation and associated irreversible processes are studied following thermodynamics principles, which can guarantee that a constitutive equation is physically admissible. Consequently, the degradation of mechanical properties is modeled through an additional internal variable called damage (Kachanov, 1958; Rabotnov, 1969; Lemaitre, 1971; Mazars, 1984b). Accordingly, micro-cracks are described implicitly within the Representative Elementary Volume, and fracture is considered a consequence of considerable material degradation. Isotropic and anisotropic damage models are considered in this thesis.

Structural simulations are considered within the framework of finite element analysis. Due to their inevitable well-known mesh dependency, regularization techniques should be considered, given that strain localization cannot be described with local damage models (Bažant & Oh, 1983b; Bazant et al., 1984). This dissertation works with non-local damage models of integral and gradient types, which act as localization limiters (Pijaudier-Cabot & Bažant, 1987; Peerlings et al., 1996a). The study of these techniques is the core of the developments described in this work. The non-local continuum concept introduces the idea that the constitutive relation in a given point is a function of what occurs in the entire body. Neighborhood interactions are therefore used to enrich the continuum description by adding higher gradients or spatial averaging based on a material characteristic length (Bažant & Jirásek, 2002). The central assumption is that the damage variable is considered to grow in function of a non-local equivalent strain (Jirásek, 1998).

Although regularizing the response allows recovering mesh objectivity, non-local classical damage models exhibit some physical inconsistencies and can not accurately describe all physical phenomena related to damage (Geers et al., 1998; Simone et al., 2004; Krayani et al., 2009; Giry et al., 2011). Some of these aspects are studied in detail in this work, highlighting the need to consider evolving non-local interactions approaches. We mainly focus on the so-called gradient-enhanced Eikonal approach (Desmorat et al., 2015b). Along with equilibrium, it considers an additional Helmholtz-type differential equation to be solved for the non-local equivalent strain. From a differential geometry-based Micromorphic Media Theory, a new derivation of this model is proposed, which verifies the Clausius-Duhem inequality. The main idea is that damage is supposed to curve the space where non-local interactions occur. Such a space deformation is represented through introducing a damage-dependent Riemmanian metric in the formulation. We propose to formulate this metric based on a qualitative analysis of how micro-cracks development modifies the medium's interactions.

The variational formulation (weak form) of the coupled problem is derived for the generic case of a second-order anisotropic damage tensor. A fixed-point algorithm scheme is applied to the variational formulation at the global level to solve the non-linear coupled problem, whereas an iterative Newton-Raphson procedure is used for behavior integration at the quadrature points. The provided numerical simulations consider both isotropic and anisotropic damage behavior. Based on tensor representation theory concepts (Boehler, 1987), we propose considering the metric as a structural tensor modifying the non-local interactions. The tensors corresponding homogeneous polynomials are used to introduce a visualization tool using ellipses. It highlights how anisotropic damage naturally induces anisotropic evolving non-local interactions. Numerical results are provided and compared to existing experimental data from the literature. The discussion focuses on the model's capabilities to represent realistic cracking mechanisms and its possible application to real-scale structures.

3 Scope and outline

This thesis is organized into two main parts and five chapters. Part I is dedicated to presenting an overall introduction to the main concepts studied in this work. Part II assembles the main contributions of this dissertation to the subject in terms of theoretical derivations, formulations, numerical developments, and results.

The first two chapters are presented in Part I. Chapter 1 first provides an overview of the experimental observations from the literature concerning quasi-brittle materials. The described observations highlight the need to further understand degradation mechanisms in these materials. Secondly, the most common crack modeling strategies are reviewed. Special attention is given to Continuum Damage Mechanics, which is the basis of all developments in this dissertation. Essential concepts of this theory are described, and a few damage models are finally presented.

Chapter 2 provides a literature review of the non-local damage theory. It is highlighted that, from the structure perspective, finite element simulations with local damage models cannot provide meaningful results. The critical elements of strain localization and bifurcation are introduced to highlight the need to regularize the solution. It provides a discussion on non-locality in a broad sense and how the term "non-local" is understood following different communities. Then, the classic integral and gradient-enhanced approaches are described within the damage mechanics framework. The concept of non-local interactions between points in a medium is introduced. It is explained why evolving and eventually anisotropic interactions need to be considered. Attention is given to the so-called Eikonal damage formulation. Finally, other well-known regularization approaches are briefly described.

The last three chapters are presented in Part II. Chapters 3 and 4 are composed of published peer-reviewed journal articles, with some additional developments, illustrations, and modifications to fit this thesis's style and global track. The same holds for Chapter 5, except that, at the moment of the submission of this manuscript, the corresponding article follows the review process.

Chapter 3 concentrates on one-dimensional theoretical and numerical developments concerning non-local damage models (Ribeiro Nogueira et al., 2022a). It starts with a wave dispersion analysis on local and gradient-enhanced damage models. Subsequently, boundary effects and damage diffusion are studied by analyzing a numerical spalling test. A complete explicit dynamics finite element code is developed for this sake. Finally, classic and evolving interactions non-local approaches are compared.

Chapter 4 provides an alternative derivation of the gradient-enhanced Eikonal damage model (Ribeiro Nogueira et al., 2024a). As a departure point, it is proposed to consider the micromorphic approach based on a different geometric description of the problem. Some differential geometry concepts are briefly introduced, and the strong form of the Eikonal problem, along with its boundary condition, is derived. Some additional comments on the bifurcation analysis of gradient-enhanced models are provided, establishing a relation with the results presented in the wave dispersion analysis from Chapter 3. Finally, the numerical implementation of the gradient Eikonal approach is described, and its regularization properties are evaluated through two-dimensional isotropic damage numerical simulations.

Last, Chapter 5 addresses the extension of the gradient Eikonal model to the case of anisotropic damage. The model is coupled to a second-order tensorial damage constitutive behavior. A specific plane-stress behavior is derived for two-dimensional simulations. Visualization of ellipsoid representing damage and metric tensors illustrates how induced anisotropic behavior naturally results in evolving anisotropic interactions. The numerical solution of the coupled problem is detailed, both at the structure and quadrature point levels. A comprehensive discussion on the advantages of such models is provided, presenting well-known structural results in two- and three-dimensional contexts.

Part I

Quasi-brittle materials in the literature: from experimental observations to available crack modeling strategies

1

Experimental findings and Continuum Damage Mechanics for quasi-brittle materials

This chapter has two main objectives. Firstly, it gives an overview of the experimental observations taken from the literature concerning quasi-brittle materials. This introduction will be essential to understand the modeling techniques and the numerical results described in the other chapters. Secondly, it aims to give helpful information about available crack modeling approaches. Particularly, continuum damage mechanics is given attention, and its standard thermodynamic framework is recalled. The main concepts of this theory are described, and a few damage models are finally presented.

Contents

1 Literature review on experimental observations for quasi-brittle materials

In general terms, a material can be defined as quasi-brittle when it shows a strain-softening behavior (*i.e.*, a decrease in stress while the strain increases) after the elastic limit, as shown in Figure 1.1. This behavior is accompanied by a progressive reduction in stiffness, thus introducing the notion of the degradation of material properties. Quasi-brittleness has been documented in various materials, including concrete (*e.g.*, Terrien (1980)), mortar (*e.g.*, Peng et al. (2022)), masonry (*e.g.*, Anthoine et al. (1995)), tough ceramics (*e.g.*, Swain (1991)), wood (*e.g.*, Miyauchi and Murata (2007)) and rocks (*e.g.*, Hudson et al. (1971)).

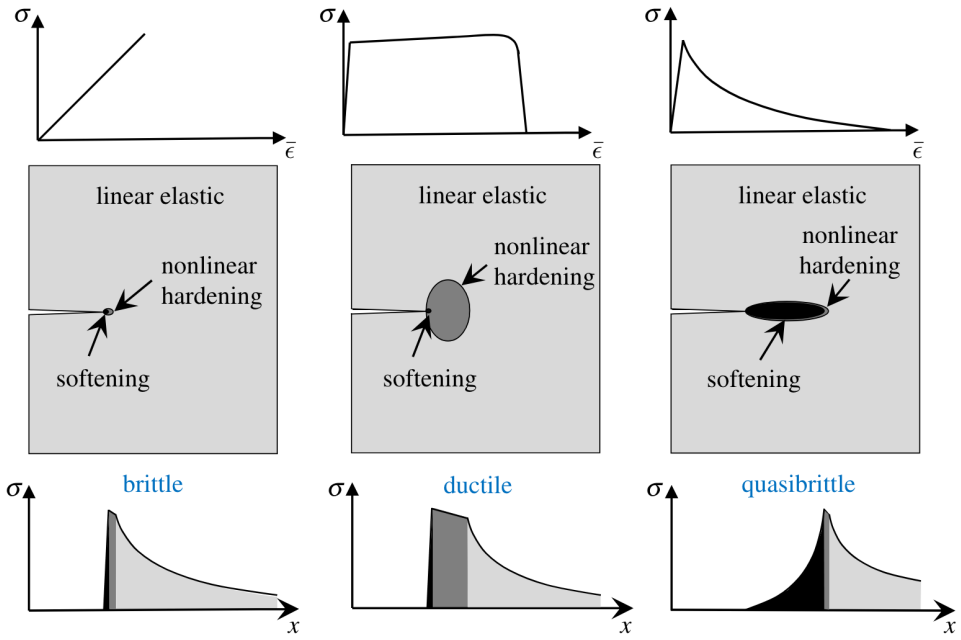

Figure 1.1 • Schematic illustration of different types of material behavior: brittle, ductile and quasi-brittle (Bažant, 2019).

As pointed out by Bažant (2019), it is crucial to notice that the concept of quasi-brittleness depends on the ratio size between the structure and the Fracture Process Zone (FPZ), where micro-cracks develop. These concepts will be further detailed in section Section 1.2.

1.1 Behavior

Quasi-brittle materials exhibit different behavior under quasi-static and fast dynamic loads. In concrete, for instance, Bischoff and Perry (1991) gathered and reviewed experimental observations of the compressive strength for various loading rates. It was observed that the strength obtained in dynamics is considerably higher than that under quasi-static

loading (*i.e.*, strain rate 10^{-6}). Similar results lead to the same conclusions for dynamic tensile tests (Klepaczko & Brara, 2001).

Two different regimes are observed: the first involves a relatively small increase in the strength in function of the strain rate, while the second exhibits a considerable increase in the strength. Either in compression or in tension, the first regime can be attributed to the presence of water in the concrete, while the increase in strength, in tension, can be explained by the Steffan effect (Rossi, 1991; Rossi et al., 1994b). In compression, the strength increase in the second regime is related to structural (inertial) effects of confinement (see, for instance, numerical simulations taking into account inertial effects in (Desmorat et al., 2010)). On the contrary, inertial effects cannot explain the strength increase in tension. A diffusive network of micro-cracks emerges, leading to a delay in failure due to macro-crack localization. In this case, one can refer to the quasi-deterministic fragmentation aspect of rupture under high strain rates (*e.g.*, Denoual and Hild (2002)).

In the following, a concise review of experimental observations concerning quasi-brittle materials is provided, with a focus on quasi-static loading conditions (cyclic or not).

1.1.1 Direct and indirect tension

A typical quasi-brittle response can be experimentally observed for concrete and masonry-unit mortar interface, as shown in Figure 1.2. The end of the elastic regime is characterized by a relatively small tensile strength, followed by a non-linear softening behavior. It will be shown later that this phase is closely related to the growth of micro-cracks within the medium. Under direct tension, cracking mechanisms develop orthogonal to the loading direction. Both curves exhibit unloading and reloading phases, which highlight a degradation of the stiffness (changing in elastic slopes), as well as the appearance of permanent (inelastic) strains. This macroscopic effect is mainly attributed to the roughness of cracked surfaces and aggregate interlock mechanisms, which may create also frictional sliding and manifest as hystereris loops (Bažant & Gambarova, 1984; Andrieux et al., 1986; Ragueneau et al., 2000; Desmorat et al., 2007b; Richard et al., 2010). Similar experimental results were also obtained by Reinhardt and Cornelissen (1984) in uni-axial alternate tensile and compressive loading for concrete. The softening behavior of concrete under direct tensile loading was also demonstrated by Evans and Marathe (1968).

However, experimental set-ups for direct tension tests are particularly complex to handle, due to instabilities and snap-back effects during strain-softening. Alternatively, material behavior under tension can be studied using other tests, such as the Brazilian split test (Carneiro, 1943) and three (*e.g.*, Landis (1999)) or four-point bending tests (*e.g.*, Hordjik (1991) in concrete and Labuz and Biolzi (1998) in rocks), which lead to an indirect tension state.

1.1.2 Compression and dilatancy

In uni-axial compression, cracking mechanisms develop parallel to the loading direction. As for tension, unloading-loading cycles show permanent strains and hysteresis loops, as shown in Figure 1.3a. Another direct observation from experimental results is that the compressive strength is around one order higher than the tensile one for concrete.

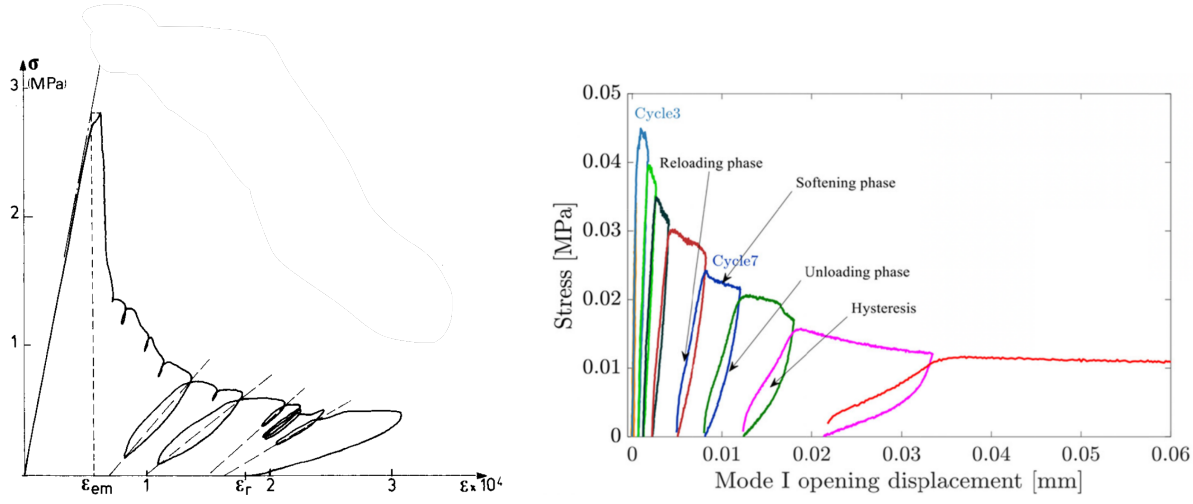

(a) Concrete **(b)** Masonry unity-mortar interface

Figure 1.2 • Experimental behavior observed in direct tension for concrete (Terrien, 1980) and masonry unity-mortar interface (Peng et al., 2022)

Moreover, a quasi-brittle behavior can be observed, but considerably less brittle than the response in tension. These aspects are known as the tension-compression dissymmetry behavior.

As noticed by Mazars (1984b) when developing a material criterion function in terms of an equivalent strain, the cracking mechanisms in quasi-brittle materials, such as concrete, are related to the extensions. In compression, the degradation is mostly a consequence of the transversal (positive) strain generated by Poisson's effect. Given that the cracks are parallel to the load direction, some regions of material still resist to the load, what explain the less brittle behavior. This is the one of the first macroscopic manifestations of the cracking induced anisotropic behavior.

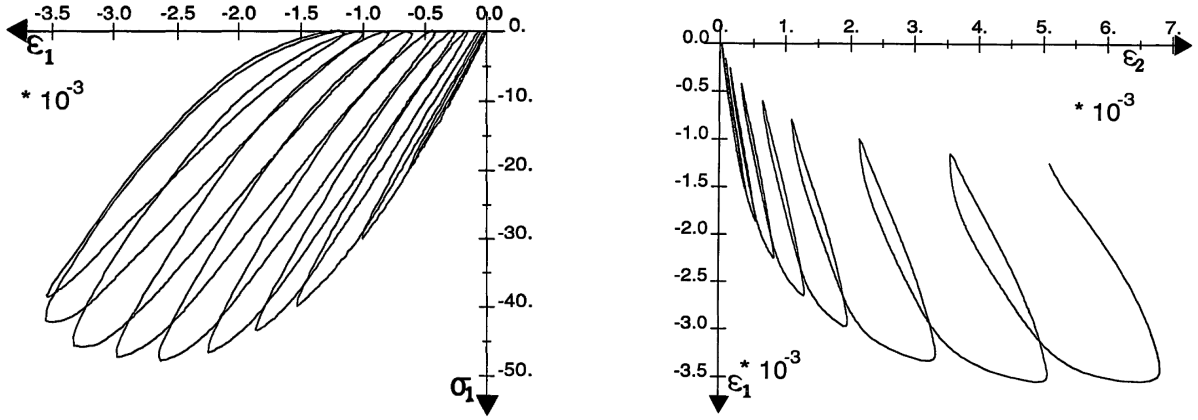

(a) Longitudinal stress-strain response **(b)** Longitudinal strain in function of the transversal one

Figure 1.3 • Experimental behavior observed in uni-axial compression for concrete (Ramtani, 1990).

Another important aspect is the manifestation of dilatancy (*i.e.*, increasing volume). Figure 1.3b shows the evolution of the longitudinal strain (ε_1) in function of the transverse strain (ε_2) during a uni-axial compression test. One can observe that the apparent Poisson's ratio $\nu_{\text{app}} = -\varepsilon_2/\varepsilon_1$, increases, reaching almost $\nu_{\text{app}} = 2$ at the end of the test. Dilatancy can be estimated from the trace of the strain tensor, which in this case equals $\varepsilon_1(1-2\nu_{\text{app}})$. Since $\varepsilon_1 < 0$, one has definitely an increasing volume in the softening regime. This behavior is attributed to the cracking patterns parallel to the loading direction in compression, which reduce the resistance to lateral expansion while maintaining almost the same resistance in the longitudinal direction.

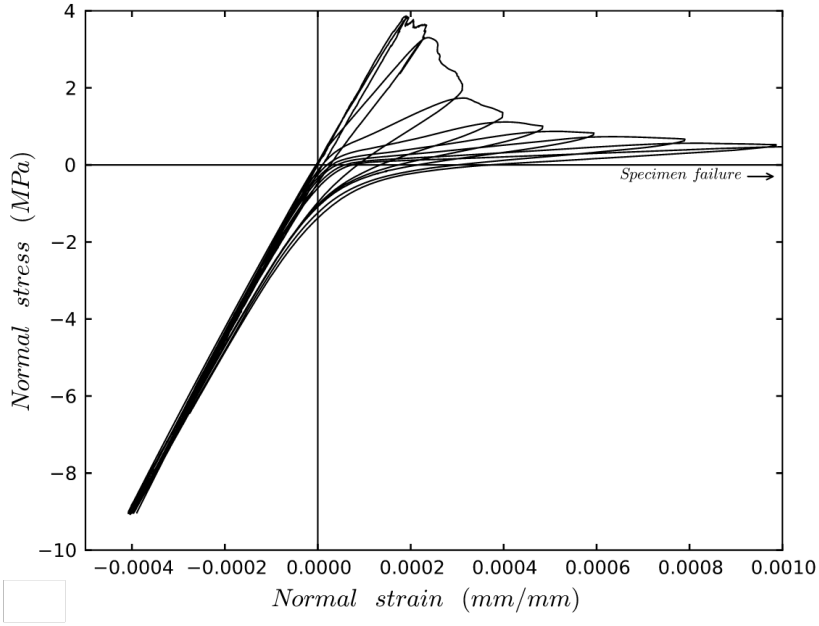

Figure 1.4 • Stress-strain of a cyclic tension-compression test (Nouailletas et al., 2015).

1.1.3 Unilateral effect

The unilateral behavior of concrete was observed in different experimental studies (*e.g.*, Reinhardt and Cornelissen (1984), Mazars et al. (1990), and Nouailletas et al. (2015)). This behavior is characterized by the micro-cracks closure under compression loading, leading to the recovery of the initial stiffness.

Figure 1.4 shows the stress-strain curves obtained from an experimental campaign conducted on notched concrete specimens (Nouailletas et al., 2015). Typical quasi-brittle behavior can be observed during the loading-unloading phases in tension, with a gradual reduction in stiffness. The so-called unilateral effect takes place after tension unloading and reloading in compression (negative stresses and strains). The compressive regime shows an almost elastic response up to approximately twice the tensile strength, indicating that the stiffness was recovered and the micro-cracks were partially or totally closed.

1.1.4 Induced anisotropic character of degradation

Quasi-brittle materials can be considered as initially isotropic, in the sense that the measured elastic properties are the same in all directions. In a homogenized macroscopic framework, the behavior of a given concrete or rock can be initially described by two elastic parameters: Young's modulus and Poisson's ratio.

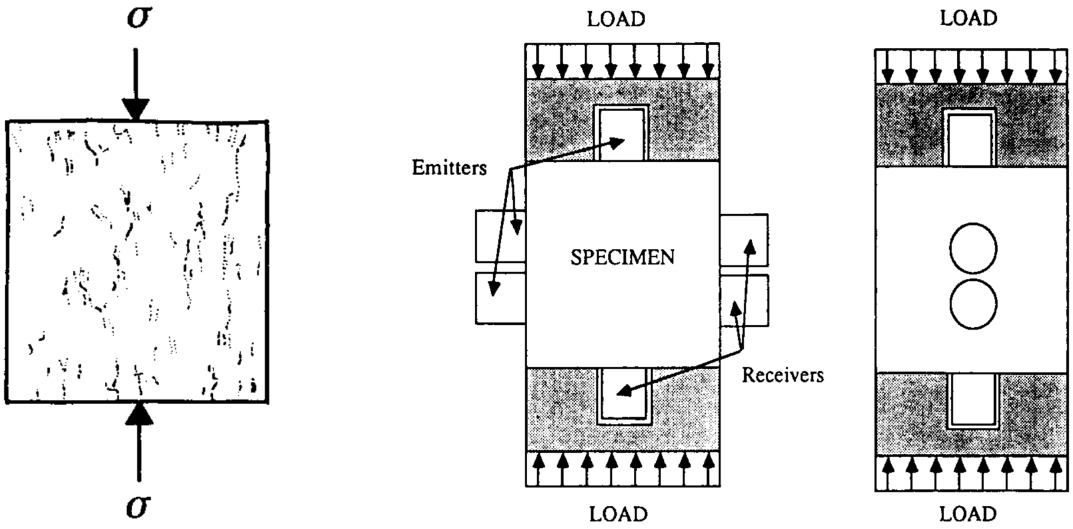

(a) Micro-cracks observed by X-rays

(b) Experimental apparatus for acoustic measurements

Figure 1.5 • Crack patterns observed and experimental set-up used in (Berthaud, 1991).

As previously discussed, elastic properties degrade in the softening phase due to the appearance of micro-cracks. If a sufficiently randomly oriented network of micro-cracks is considered, one expects that the elastic properties will be equally deteriorated in all directions, and the material remains isotropic. However, micro-cracks typically have preferential directions to occur. In tension, they are orthogonal to the loading direction, while in compression they are parallel (Figure 1.5a). The elastic properties are therefore modified according to these preferential directions. For instance, Berthaud (1991) studied the variation on elastic properties along different directions in cubic concrete specimens (Figure 1.5). Wave velocities measurements (Figure 1.5b) confirmed the induced anisotropy in the damaged material, whereas it was initially isotropic. For different damaged states, no considerable impact on the longitudinal waves parallel to the loading direction was observed. Conversely, a decrease of the velocity and amplitude of the waves perpendicular to the loading directions was detected. Similar findings were reported by Bogucka et al. (1998), where it was proposed that the material undergoes a transition from initial isotropic to transverse isotropic during the compression load. It is important to highlight, however, that for general non-proportional loading, the damaged material should not be restricted to the transverse isotropic class of symmetry, as micro-cracks may develop in different directions.

Similar conclusions regarding induced anisotropy can be drawn for rock materials. Passelègue et al. (2018) studied the induced anisotropy behavior, and the associated crack

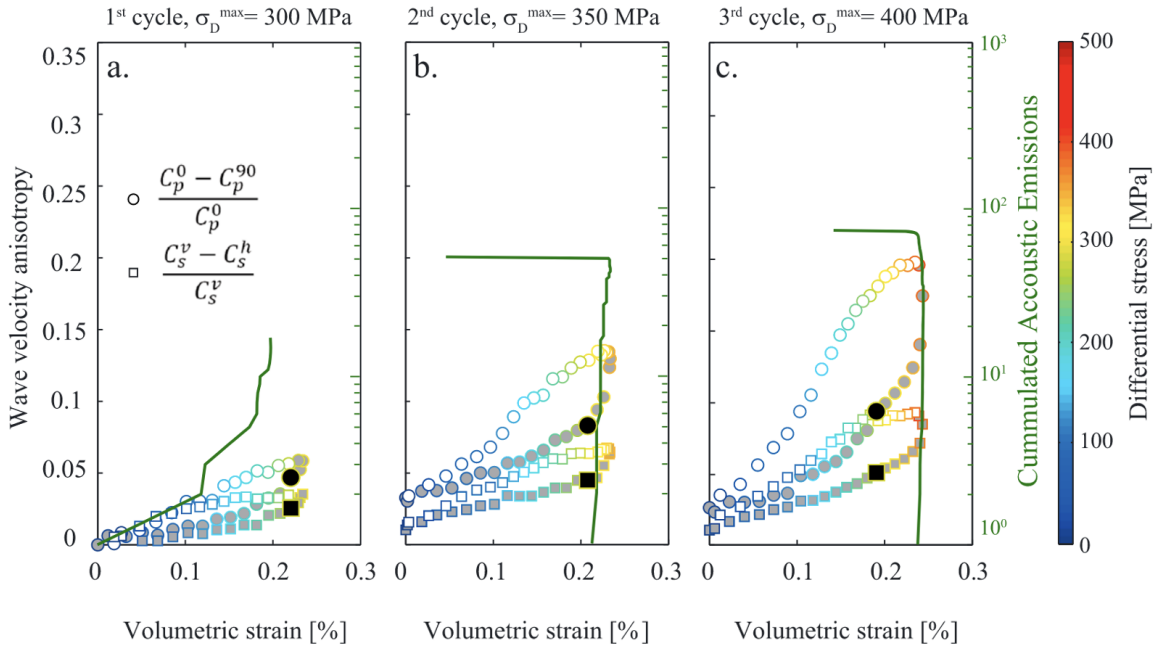

Figure 1.6 • Evolution of the anisotropy degree in function of volumetric strains during loading cycles (Passelègue et al., 2018).

closure effect, applying cyclic loading on Westerly Granite specimens using a triaxial apparatus. During the tests, the confining pressure was maintained constant, and different loading cycles were applied, increasing the value of the axial stress σ_1 to reach a target one $\sigma_{\mathrm{D}} = \sigma_1 - \sigma_3$, with σ_3 denoting the radial stress. The analysis was then enhanced by measuring the acoustic emissions (AE) and the wave velocities with pressure (P) and shear (S) sensors in different directions. Thus, one way of quantifying the anisotropy in the material is to compute anisotropy parameters $(C_p^0 - C_p^{90})/C_p^0$ and $(C_s^v - C_s^h)/C_s^v$, where C_p^0 denotes the P-wave velocity measured at 0° angle with respect to the axial direction. Similarly, C_p^{90} stands for the P-wave velocity measured at a 90° angle. The preferential vertical shear velocity is C_s^v and its horizontal counterpart C_s^h.

Figure 1.6 shows the evolution of the anisotropy parameters as a function of the volumetric strain and the differential stress σ_{D}. For the first loading cycle (grey filled dots) and small values of σ_{D} (dark blue), the wave velocities C_p^0 and C_p^{90} are almost the same. This corroborates the hypothesis of initial isotropy. Then, correlated to a more pronounced increase in the acoustic events, the anisotropy parameters start to increase. Unloading curves (empty dots) highlight a decreasing degree of anisotropy, retrieving almost the initial isotropic state. This is related to the crack closure effect. However, unloading does not follow the same loading path, which indicates hysteresis, particularly noticeable for higher levels of σ_D in the second and third cycles.

1.2 Acoustic emissions, FPZ and size effect

Acoustic emissions and FPZ. Besides the complex experimental behavior observed at the material point level, other aspects have a significant impact in the overall behavior

of quasi-brittle materials: the FPZ and the structure size. Initially, during the early stages of loading, micro-cracks are distributed in a zone of finite size, and may eventually coalesce into a localized macro-crack. This non-linear region of degradation events differs from the surrounding domain, which remains elastic.

Shah (1990) studied the initiation and propagation of the FPZ in notched mortar specimens during cyclic tension loading tests (Figure 1.7a), based on acoustic emissions. The appearance of micro-cracks induces internal micro-seismic events under loading conditions, and can be captured by acoustic sensors fixed on the specimen.

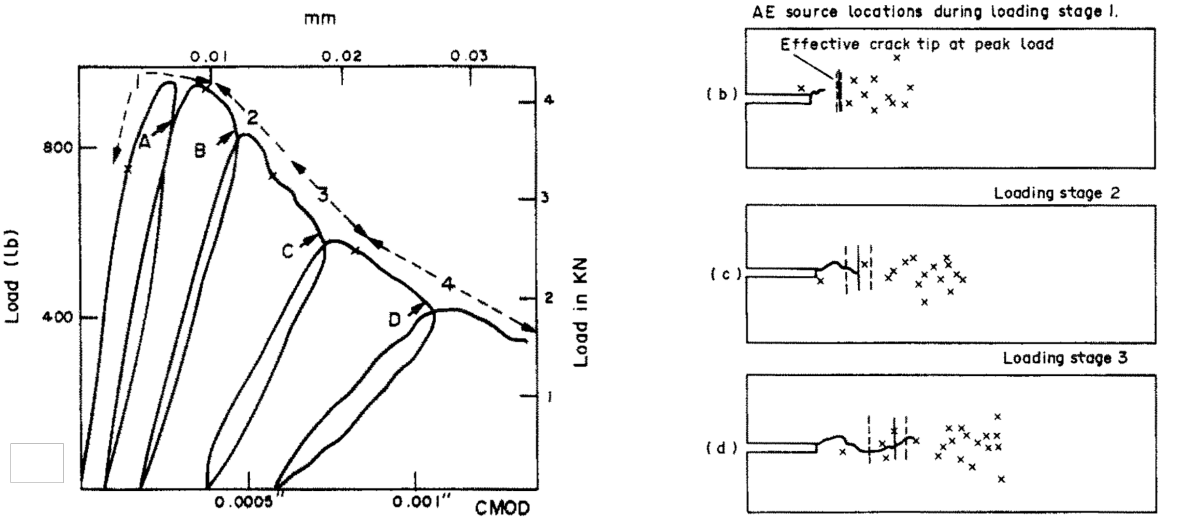

(a) Structural response under cyclic tension loading

(b) Location of acoustic events for different load stages

Figure 1.7 • Experimental observations of the FPZ based on acoustic emissions (Shah, 1990).

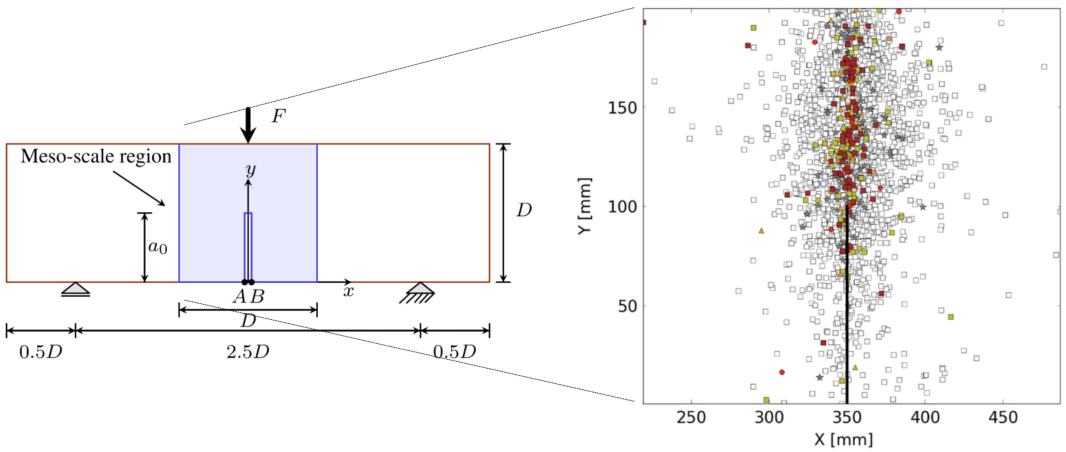

Figure 1.8 • Acoustic emissions in a notched three-point bending test (Grégoire et al., 2015).

Figure 1.7b shows the observed source location of acoustic emissions for different load stages. Initially, distributed acoustic events appear indicating the occurrence of micro-

cracks inside the specimen. Subsequently, as loading progresses, a localized macro-crack takes place in previous damaged zones. A major contribution of this work is the observation that the cluster of micro-cracks moves forward along with crack-tip propagation. These results were confirmed by Labuz and Biolzi (1998) in tests on four-point beams made of Charcoal granite and Berea sandstone. They observed that the size of the intrinsic fracture process zone (*i.e.,* approximately the width where AE events are localized) was much smaller than the structure one. Similar conclusions were obtained by Landis (1999) in a three-point bending test on mortar specimens, where the localization of micro-cracks (see also, for instance, Alam et al. (2014)) into a narrow zone (signaling macro-crack appearance) was correlated to a change in AE events. Grégoire et al. (2015) provided similar results for three-point bending tests in notched and unnotched concrete specimens. In contrast to previous studies, they analyzed acoustic energy for different AE events, as seen in Figure 1.8. Around the notch, it is observed a zone with distributed grey/white points corresponding to a diffuse low acoustic energy at the beginning of the load. This is followed by a concentration of AE events with high energy (in red) from the notch to the top of the beam. In all these results, the width of the FPZ can be estimated based on a window of these acoustic events (*e.g.,* it is considered as the extent of the spatial distribution of energy in (Grégoire et al., 2015)). Other experimental techniques, such as Digital Image Correlation (DIC) (*e.g.*, Roux et al. (2009)), can be used to study the FPZ. A detailed review of experimental techniques used for studying the FPZ in quasi-brittle materials is given in (Zhang & Zhou, 2022).

Size effect. Acoustic data are extremely important to highlight the physical processes behind degradation in quasi-brittle media. Furthermore, the presence of a FPZ, which is confirmed by AE events, has an important consequence for structural scaling: the so-called size effect. The size effect refers to the modification in load capacity (structural strength), represented by a nominal stress σ_N computed in function of the ultimate load, among geometrically similar structures. In quasi-brittle materials, it has been experimentally observed as a decrease in σ_N while the size of the structure increases (*e.g.*, Grégoire et al. (2013) and Hoover et al. (2013) for concrete, Labuz and Biolzi (1998), Pijaudier-Cabot et al. (2022), and Li et al. (2023b) for rocks, Li et al. (2023a) for anisotropic geomaterials).

In the literature, the size effect can be attributed to two main reasons. On one hand, a statistical explanation, concerning the randomness of materials. Larger structures inevitably have a higher probability to fail, and therefore a smaller σ_N (Weibull, 1939; Rossi et al., 1994a). On the other hand, a deterministic one, theoretically introduced by a simplified energy release analysis (Bažant, 1984b). As previously mentioned, its occurrence depends on the size ratio between the FPZ and the structure. We will see later on that these aspects imply an introduction of a characteristic (or internal) length in modeling strategies.

As extensively described in the literature (*e.g.*, Bažant (1984b, 2002) and Bažant and Planas (2019)), in the absence of a material characteristic length in a certain theory, physical scaling functions follow power laws, *i.e.,* $\sigma_N \propto (\text{size})^s$, with s denoting an exponent. This behavior is observed in theories within the framework of classic continuum mechanics, which are based on the principle of local action. Strength of materials and

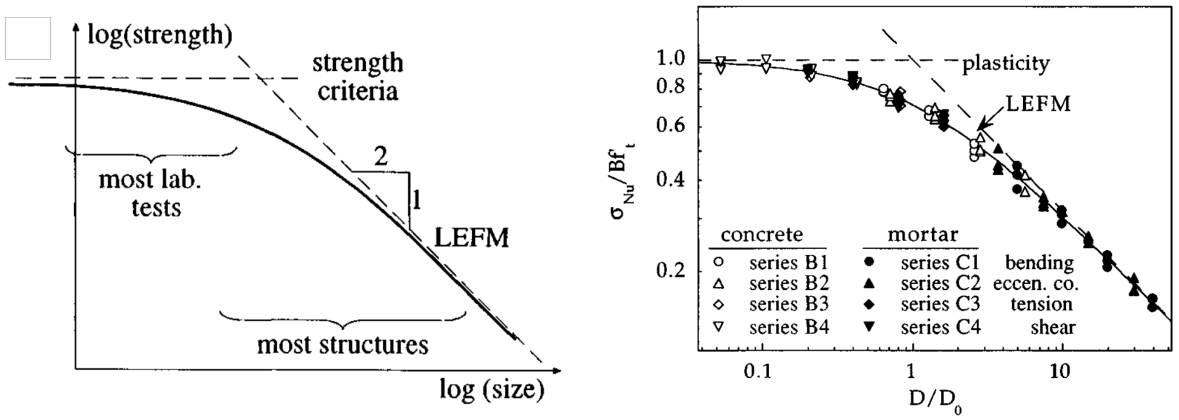

(a) Limit cases of size effect according to

(b) Size effects results (Bažant & Pfeiffer, 1986, 1987) taken from Bažant and Planas (2019)

Figure 1.9 • Asymptotic cases of size-effect and a few experimental results (Bažant & Planas, 2019)

linear elastic fracture mechanics (LEFM) are well known examples (Bažant, 1993). In theories based on strength criteria for elasticity or plasticity (limit analysis), the scaling power law has a null exponent, *i.e.*, σ_N is constant and does not depend on the structure size (Bažant & Planas, 2019). This scenario is intuitive: if the same material is used in geometrically similar structures, they should fail according to the same strength criteria. In a log-log plot, this corresponds to the horizontal dashed line shown in Figure 1.9a, indicating the absence of size effect. This is the case when the size of the FPZ is nearly equal to the structure size. Conversely, in LEFM, the scaling exponent of power laws equals $-1/2$ (see derivations in (Bažant, 1993) based on the J-integral), corresponding to the slope $2:1$ in the log-log plot (Figure 1.9a). This scenario arises when the size of the FPZ is small when compared to the structure size.

The case of quasi-brittle materials corresponds exactly to the transition between both theories. In these materials, the size of the FPZ is not negligible. In practice, it is all about a matter of scale (Bažant, 2002, 2019): structure made of a quasi-brittle material exhibits a brittle response at large scales but a quasi-brittle response at sufficiently small scales. Based on this dual asymptotic behavior, Bažant (1984b) proposed the first deterministic size effect law for quasi-brittle materials. A comparison with experimental results from concrete and mortar is given in Figure 1.9b.

These fundamental aspects of modeling quasi-brittle materials at the structural scale underscore the necessity for models to account for the size effect inherent in these materials. Models are fitted based on experimental results (specimen size in the laboratory), whereas the size of the structural application is of some order of magnitude larger. Therefore, any modeling technique should intrinsically account for this effect to ensure accurate results.

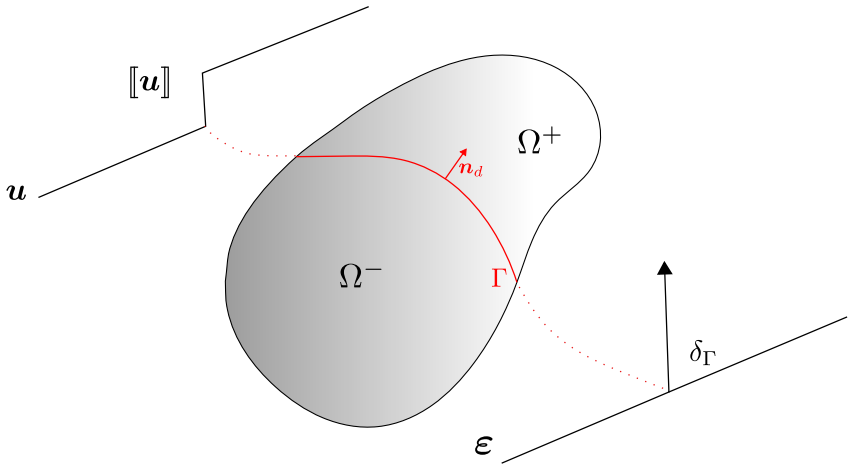

Figure 1.10 • Kinematics of a medium crossed by a discontinuity.

2 Crack description

A crack induces a (strong) discontinuity (denoted by Γ in Figure 1.10) in the structure and is consequently not compatible with the usual notions of continuum mechanics. Let us define a body $\Omega \subset \mathbb{R}^d$, with $d = 1, 2$ or 3 and denote $\boldsymbol{x}$ its local coordinates. In a given time t, the displacement field $\boldsymbol{u}(\boldsymbol{x}, t)$ is no more continuous and can be described by the sum of a smooth contribution $\hat{\boldsymbol{u}}(\boldsymbol{x}, t)$ and a jump $[\![\boldsymbol{u}]\!]$, reading:

$$\boldsymbol{u}(\boldsymbol{x}, t) = \hat{\boldsymbol{u}}(\boldsymbol{x}, t) + \mathcal{H}_\Gamma(\boldsymbol{x})[\![\boldsymbol{u}]\!](\boldsymbol{x}, t) \qquad \forall \boldsymbol{x} \in \Omega \tag{1.1}$$

where $\mathcal{H}_\Gamma(\boldsymbol{x})$ denotes the Heaviside function. The standard gradient definition of the strain tensor $\boldsymbol{\varepsilon}$ becomes deprecated and it can be rewritten as:

$$\boldsymbol{\varepsilon}(\boldsymbol{x}, t) = \nabla^s \hat{\boldsymbol{u}}(\boldsymbol{x}, t) + \mathcal{H}_\Gamma(\boldsymbol{x}) \nabla^s [\![\boldsymbol{u}]\!](\boldsymbol{x}, t) + \delta_\Gamma([\![\boldsymbol{u}]\!] \otimes \boldsymbol{n})^s \qquad \forall \boldsymbol{x} \in \Omega \tag{1.2}$$

with $\nabla^s(\bullet) = \left(\nabla(\bullet) + \nabla^\top(\bullet)\right)/2$ denoting the symmetric part of $\nabla(\bullet)$, $\otimes$ denotes the tensor product, δ_Γ is the Dirac distribution and $\boldsymbol{n}_d$ is the normal vector on the discontinuity surface. Thus, the displacement jump induces a unbounded contribution in the strain tensor field.

Essentially, there are two different ways of describing a crack: explicitly or implicitly. In the explicit approach, the discontinuity is directly taken into account in the formulation, such as its geometry, propagation direction and the kinematics conditions to respect on its surface. Accordingly, dissipation mechanisms (*e.g.,* friction and cohesive crack openings) are described at the crack level. In the implicit approach, the crack is described in a diffusive or smeared manner within the medium. Its effects are thus considered in macroscopic constitutive relations linking strains to stresses. In this case, dissipation mechanisms take place in a finite volume rather than at the crack surface. In the following sections, a brief review of crack modeling techniques is described. Enriched continuum models, such as gradient, micromorphic, non-local and phase-field are given attention in Chapter 2.

2.1 Explicit approaches

Discrete models (DM). Introduced by (Cundall & Strack, 1979) as a discrete model made out of particles (also known as the distinct-element method), the discrete element method (DEM) was initially developed to study granular materials such as sand. In this method, the domain is represented as an assembly of rigid discs in contact with each other, allowing equilibrium states to be obtained by integrating particles movements. The calculation was therefore handled by solving the global dynamic equilibrium with assumed force-displacement laws when contact occurs. Particle deformation was not considered in this approach, as the global behavior was supposed to depend mostly on rigid bodies movements. However, this method cannot effectively represent cohesive cracking in quasi-brittle materials.An alternative approach was proposed by Zubelewicz and Bažant (1987), where the contact laws were replaced by an elastic force-displacement relation with a certain ultimate strength, similar to brittle models. These authors also suggested using irregular polygons in place of perfect discs, which allow a better description of diffuse cracking in these materials.

In the same framework of discrete modeling, lattice models represent the medium as an assembly of ligaments (beam or truss elements). One of the earliest works on this approach appeared even before the distinct-element method. Hrennikoff (1941) proposed to represent the behavior of shells under bending from a network of elastic truss elements. Lattice models have since been extend to the analysis of cracks by introducing failure criteria (random) or softening laws to the ligament elements (*e.g.*, Herrmann et al. (1989), Bažant et al. (1990), and Arslan et al. (2002)).

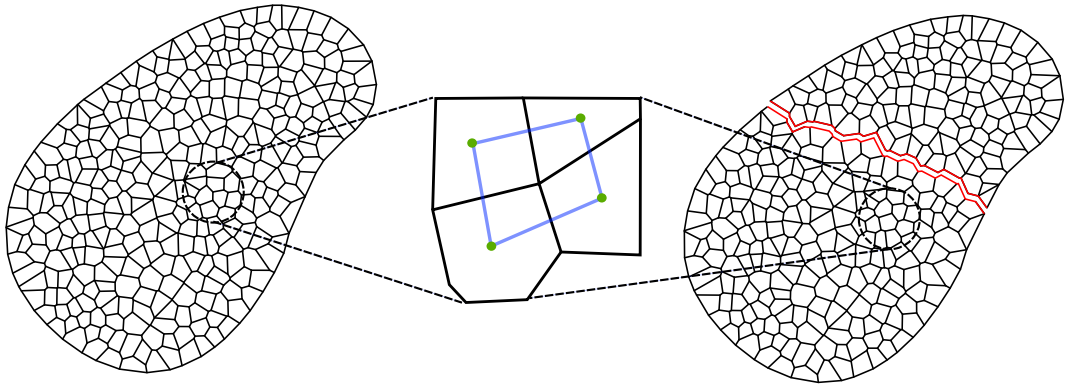

Figure 1.11 • DM – Illustration of a DM mesh and its hybrid elements linked by a network of beams.

Another class of discrete models is the so-called hybrid approach. Basically, this method combines elements of both particle and lattice models, and it is often referred to as beam-particle models (D'Addetta et al., 2002; Cusatis et al., 2011b, 2011a; Vassaux et al., 2016; Pathirage et al., 2023). Typically, the domain of the structure is discretized using irregular polygons, whose centers are connected by beam elements to represent a cohesive behavior (see Figure 1.11). Frictional contact can be modeled on the surface of

particles, whereas cohesive behavior is taken into account by the beam network. Finally, fracture is considered through failure criteria applied to the beam elements, allowing for the explicit observation of global crack paths (Figure 1.11). For instance, Oliver-Leblond (2019) were able to obtain realistic crack paths from the analysis of mixed-mode tests in concrete specimens with a beam-particle model. However, applying these models in industrial application for structural analysis on larger scales can be challenging due to the expensive and time-consuming nature of numerical calculations.

LEFM. An explicit structural approach to model cracks is fracture mechanics (Griffith, 1921; Irwin, 1957; Rice, 1968) and its numerous variations. LEFM studies singular stress fields at crack tips (experimentally confirmed by photo-elasticity, for instance) and crack propagation in materials. As mentioned before, in brittle materials, *i.e.*, when the FPZ is sufficiently small compared to the structure, one expects elastic behavior just before crack propagation. In this situation, the so-called stress intensity factors become important to quantify the stress field in the three main modes of failure. Crack propagation is analyzed in terms of the energy release rate and its comparison with a critical energy required for propagation, which is seen as a material property (Griffith, 1921). This criteria was further extended to the intensity factor in mode I failure by Irwin (1957).

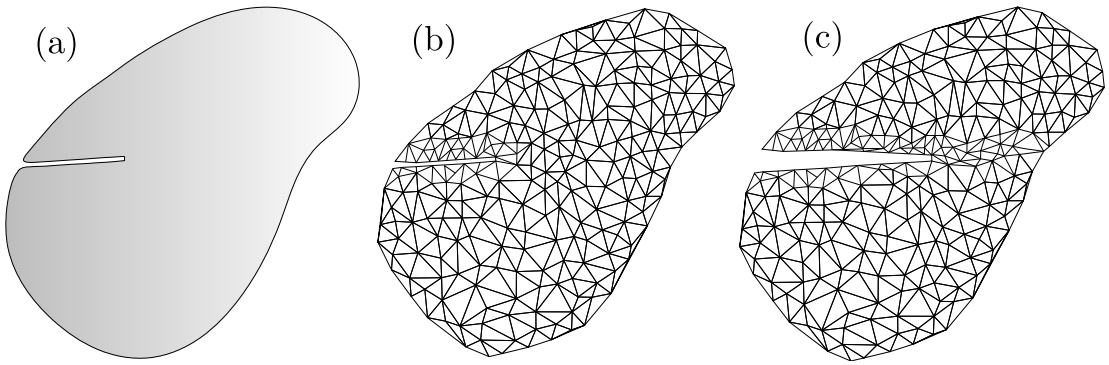

Figure 1.12 • LEFM – (a) Cracked body. (b) Initial finite element mesh. (c) Crack propagation and re-meshed domain.

In the context of finite element analysis, studying crack propagation within LEFM implies using re-meshing techniques (see for instance Bouchard et al. (2000) and the references therein). At the initial phase, the cracked body (Figure 1.12a) is discretized with an initial mesh (Figure 1.12b), taking into account the geometry of the crack at that moment. The propagation direction is then evaluated based on a certain criterion (*e.g.*, maximal normal stress, maximal energy release rate), and the length of propagation is determined. Subsequently, the domain is re-meshed (Figure 1.12c) to account for the new crack geometry.

In these approaches, as cracks are described explicitly, one may have access to information such as crack paths, propagation directions, and crack width. Despite their relevance in describing fracture propagation, these methods are more suitable to study just one (existing) crack and are limited to structural aspects, defining fracture criteria and constitutive relations separately. Crack initiation and the associated non-linearities

in the FPZ cannot be described by LEFM.

Embedded finite element method (EFEM). In the case of a weak discontinuity, where the displacement remains continuous while a jump appears in strains, the finite element problem needs to be modified. Ortiz et al. (1987) proposed to enrich the description of localized shear bands by introducing additional shape functions at the element level. A local bifucartion analysis is used to decide which elements require enrichment. The additional degrees of freedom associated to the incompatible modes are eliminated by static condensation,enabling the representation of discontinuities at the element level. Thus, the global size of the finite element problem remains unchanged, and the implementation can be simplified by incorporating modified material behavior laws at the Gauss points (see for instance Kakarla (2020), Kakarla et al. (2021), and Ribeiro Nogueira et al. (2022b)).

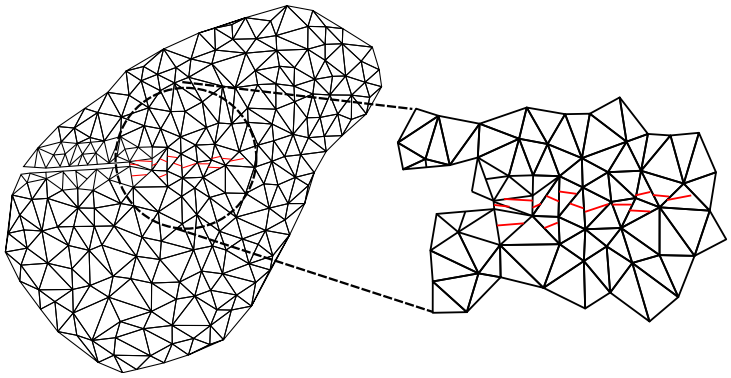

Figure 1.13 • EFEM – Illustration of cracks embedded in finite elements.

It is evident from Equations (1.1) and (1.2) that the kinematics of a crack cannot be described by a standard finite element approach. Usual variational formulations require displacement field and its associate virtual one to belong to the square integrable Sobolev space $H^1(\Omega)$. When unbounded strains occur, as in the presence of strong discontinuities such as cracks, the variational formulation becomes meaningless. Inspired by the discontinuous Galerkin method, Simo et al. (1993) extended the analysis to finite elements crossed by a strong discontinuity, *i.e.*, where there is a jump in the displacement and unbounded strains. Many others contributed to the so-called strong discontinuity approach, and a detailed review of different formulations can be found in (Jirásek, 2000).

Two different major families of models can be distinguished: continuum strong discontinuity approach (CSDA) and discrete strong discontinuity approach (DSDA). In the first case (Oliver, 1996; Oliver et al., 2004), the formulation is based on a transition from weak to strong discontinuity, representing the limit case of the last one by an equivalent regularized continuum approach. In the DSDA case, separation laws are defined on the discontinuity surface, where traction vectors are obtained by the traction continuity condition (*e.g.*, Wells and Sluys (2001), Alfaiate et al. (2002), and Dias-da-Costa et al. (2009)).

Due to its local character, one important drawback of this method is that the continuity of the crack path is not ensured (see Figure 1.13). This can lead to stress locking effects

and tracking algorithms become necessary (*e.g.*, Oliver et al. (2002a) and Riccardi et al. (2017)).

Extended finite element method (XFEM). The extended finite element approach (Moës et al., 1999) was introduced as a technique to avoid remeshing in LEFM numerical analysis. Essentially, the meshed continuum and the discontinuity are treated separately, based on the partition of unity finite element method (PUFEM) introduced by Melenk and Babuška (1996) and Babuška and Melenk (1997). In the literature, one may also find references to the generalized finite element method (GFEM), which is very similar to the XFEM approach (Belytschko et al., 2009).

Unlike the EFEM approach, the XFEM introduces local enrichment functions with associated extra degrees of freedom. Consequently, the approximation of the displacement field is therefore a sum of a regular contribution and an irregular one. The irregular part is treated by these generalized shape functions, which are basically a multiplication of the standard and the enriched ones. A comparison of EFEM and XFEM approaches can be found in (Jirásek & Belytschko, 2002; Oliver et al., 2006).

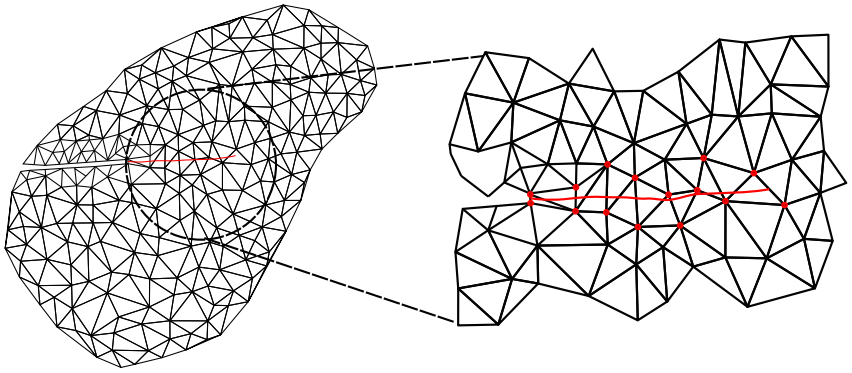

Figure 1.14 • XFEM – Illustration of a continuous crack path and enriched nodes (in red).

The idea of XFEM is to provide jump and near-tip enrichment to specific nodes around a discontinuity (*e.g.*, nodes in red in Figure 1.14). In this sense, the method allows for enriching the problem with extra user defined shape functions based on *a priori* knowledge of the solution. Since the discontinuity is treated independently of the mesh, the continuity of the crack path is guaranteed, and accurate fracture mechanics (FM) results can be obtained even with coarse meshes (Moës et al., 1999). Initially developed to the modeling of stress-free discontinuities, the method was then extended to cohesive cracks by Moës and Belytschko (2002).

However, these methods are limited to study crack propagation and cannot describe the initiation phase based on the coalescence of micro-cracks. The degradation of elastic material properties observed experimentally for quasi-brittle materials is not represented as well.

Cohesive zone models (CZM). The concept of cohesive zone models (CZM) traces back to foundational works by Dugdale (1960) and Barenblatt (1962). Although introduced

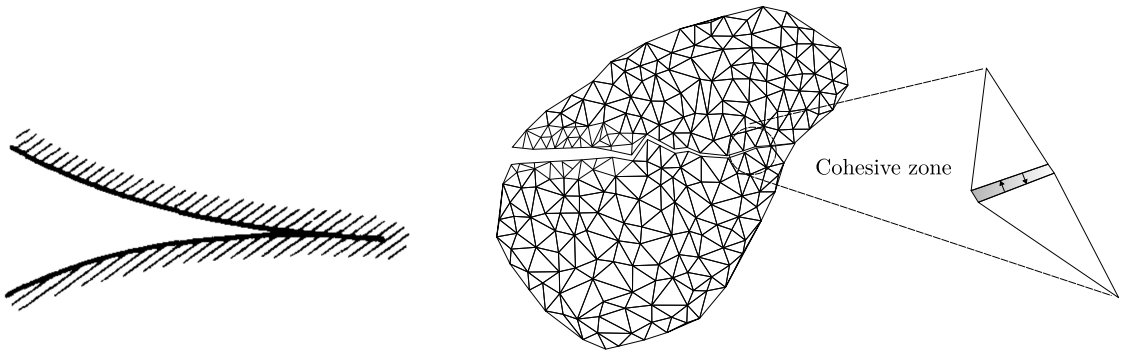

(a) Equilibrium crack contour described by Barenblatt (1962).

(b) Illustration of a crack opening at elements' interface

Figure 1.15 • CZM – Illustrations of theory assumptions and numerical considerations.

for different applications, both authors realized that stresses could still be transmitted between two surfaces located in the material. Barenblatt (1962) studied the analytical solutions for what the author called equilibrium cracks. It was found that some cracks can have a specific contour (Figure 1.15a), with a smooth closing of the opposing faces at the edge. In this situation, the tensile stress at the contour of an equilibrium cracks is finite. Molecular cohesion forces were used to model the crack edges, while the inner region of the crack is considered as stress-free. Dugdale (1960) considered cohesive constant yield stress transmitted through the lips of an internal cut in a steel sheet. In this case, the idea was not used to model fracture itself, but the extension of the plastic zone in function of the applied stress. In terms of application, the work of Hillerborg et al. (1976) is of much importance, as it applies a cohesive model (often referred by fictitious crack model) in finite element analysis. Also, it represents a considerable improvement in crack modeling, because it is capable to describe not only the propagation of existing cracks, but also the initiation. The softening behavior was therefore described in terms of stress and crack opening displacements, which were considered to occur in the fictitious crack zone able to transfer stresses.

Since then, CZM has been widely developed for dynamic (*e.g.*, Xu and Needleman (1994) and Camacho and Ortiz (1996)) and quasi-static (*e.g.*, Bittencourt et al. (1992) and Tijssens et al. (2000)) analyses by various researchers. In finite element simulations, cohesive interface elements are typically employed (see for instance Figure 1.15b) around the boundaries of finite elements to represent the cohesive zones where traction is transmitted and related to separation by softening behaviors. The inner part of finite elements is considered to remain elastic, which is often referred as the bulk material. Thus, energy dissipation is concentrated on the cohesive zones (see Elices et al. (2002) for a detailed review). Consequently, the simulations are strongly mesh-dependent, as pertinently pointed out by Falk et al. (2001) and Tijssens et al. (2000). Indeed, simulations are often mesh-dependent due to the artificial directions imposed by finite element interfaces. This limitation hampers the ability of CZM to predict realistic crack paths in structural analysis applications where the crack initiation location is not known *a priori* (*i.e.*, the majority of cases in structural analysis applications). However, these models can still

accurately provide other results, such as the peak load, for instance (Tijssens et al., 2000).

> **Remark 1.1.** *Probabilistic approaches have been also employed to describe cracking behaviors. For instance, Rossi and Wu (1992) and Rossi et al. (1996) considered a randomly distributed Young's modulus in a finite element mesh to account for material heterogeneity. Also, similar to CZM models, the cracks were modeled by contact elements respecting a Rankine criterion in function of a randomly distributed tensile strength. Continuum damage mechanics formulations of this kind were also developed in (Tailhan et al., 2010; Tailhan et al., 2013; Rastiello et al., 2015), where the tensile strength and fracture energy were considered randomly distributed. The key idea of this family of probabilistic models is to consider that the parameters of the statistical distributions of some material properties depend on the size of the finite element itself, considered as representative of a volume of heterogeneous material. For more details concerning these models, the interested reader is referred to the cited works.*

2.2 Implicit approaches

Smeared crack. The main idea of smeared crack models is the indirect consideration in the stress-strain relationship of distributed cracks inside finite elements. Essentially, this approach partitions strains into elastic and inelastic components (Jirásek, 2011). For instance, Rashid (1968) introduced zero stiffness coefficients in the direction perpendicular to the crack, assuming a transition from isotropic to orthotropic behavior following the axis defined by the crack. In this first approach, however, the crack position is fixed once a strength criterion is reached. A rotating crack model was proposed by Gupta and Akbar (1984), allowing the crack direction change if the principal strains directions change. Yet, Jirásek and Zimmermann (1998a) identified stress transfer inconsistencies (*i.e.*, stress locking) across an open crack in this model. To address this, (Jirásek & Zimmermann, 1998b) proposed transitioning from a rotating crack model to a damage model.

Furthermore, smeared crack models suffer from mesh dependency in terms of structural response and directional mesh bias in crack paths (*e.g.*, Rots (1988)). In this approach, the effects of a crack are smeared within finite element (of finite size) by considering inelastic strains. The main consequence is that energy dissipation therefore depends on the elements' size (*i.e.*, the smeared zone), which implies lack of objectivity in the formulation. Moreover, with mesh refinement, energy dissipation tends to zero, which is nonphysical. This behavior, common in smeared crack models (including damage models), will be further explored in this manuscript. On the contrary, discrete models, such as EFEM, define a traction-separation law on the discontinuity surface. Thus, no size dependence takes place and objectivity is guaranteed.

Crack band. A simple and efficient remedy for mesh-dependency in numerical simulations was proposed by Bažant and Oh (1983b). Inspired by Hillerborg et al. (1976), they introduced the so-called crack band approach. The core concept was to fix the size where the micro-cracks develop (*i.e.*, softening behavior in the FPZ). Here, the softening law

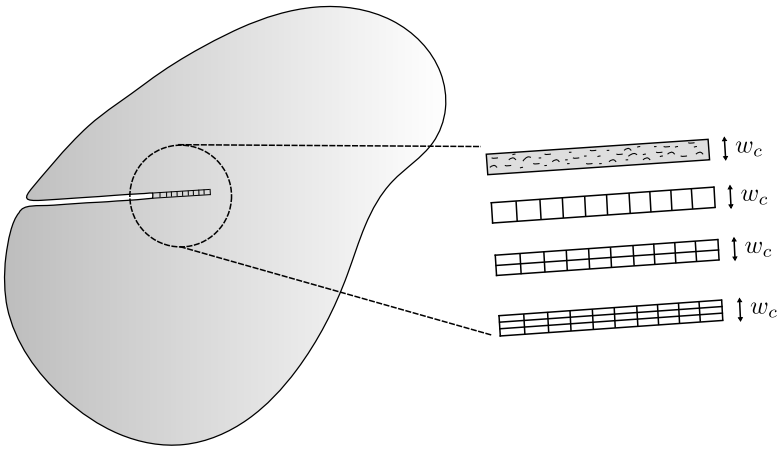

Figure 1.16 • Crack band approach: illustrative scheme of the band containing micro-cracks and three different discretizations.

is adjusted based on the element size to maintain consistent energy dissipation equivalent to the intrinsic dissipation of the material. The equivalent displacement openings in the cracked zone u_f can be computed by $u_f = \varepsilon_f w_c$, where ε_f is the strain due to micro-cracking and w_c is the band width (see Figure 1.16). As described by Bažant and Oh (1983b), the crack band and the fictitious crack (line) model (Hillerborg et al., 1976) are equivalent, provided the latter uses an equivalent stress-opening relation. These methods are often referred as energy regularization methods, a concept that will be further elucidated in Chapter 2.

> Q **Remark 1.2.** *So far, the word* ***damage*** *was intentionally almost not employed in the previous sections. There are two primary reasons for this choice. Firstly, the term holds a specific significance within the context of this manuscript, and it requires a defined framework before its extensive usage. This will be done in the next section. Secondly, by refraining from frequent use, we aim to underline the distinct meaning of the term within our theoretical models and prevent confusion with empirical observations.*

3 Continuum damage mechanics (CDM)

In the present work, CDM will be used to describe the degradation of mechanical properties. Initially developed to study tertiary creep in metals (Kachanov, 1958), this method introduces a new variable (damage) for representing micro cracks, which are in fact discontinuities, at the continuum level. Consequently, cracks are described implicitly (see Figure 1.17) within the REV, and fracture is viewed as the result of material degradation. From a numerical point of view, in finite element analysis, the material is treated as homogeneous at Gauss quadrature points (Figure 1.17), where constitutive relations are defined.

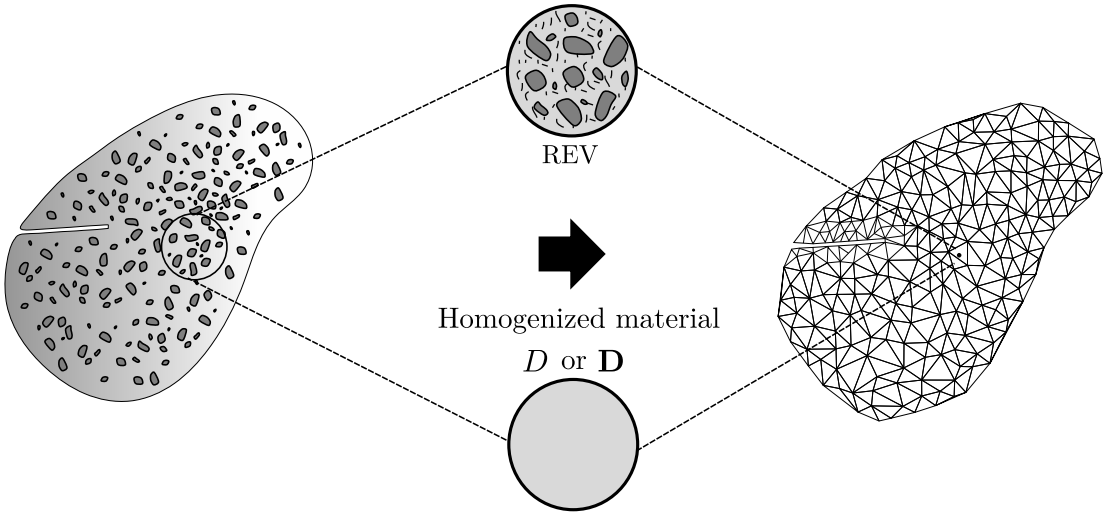

Figure 1.17 • CDM – Notion of Representative Elementary Volume (REV) and micro-cracks described by an equivalent damage variable.

> **Remark 1.3.** *Defined in this context, CDM also falls within the framework of implicit crack approaches, where micro-cracks are treated in a smeared manner. Nevertheless, given its fundamental role in this thesis, CDM deserves a detailed description in a separate section.*

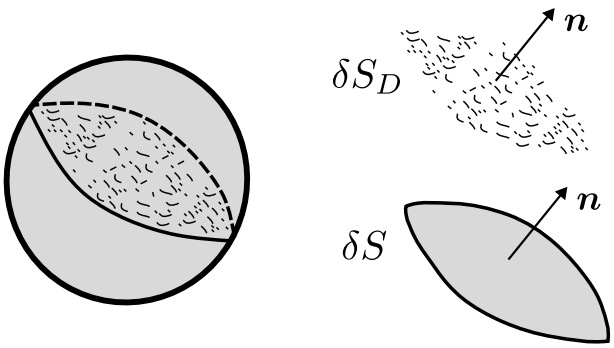

Figure 1.18 • CDM – Illustration of idealized total (δS) and damaged (δS_d) surfaces.

The damage variable can therefore be defined as a surface ratio at the REV scale (see Lemaitre (1996), Lemaitre and Desmorat (2005), and Lemaitre et al. (2009) for further details):

$$D(\boldsymbol{n}) = \frac{\delta S_D}{\delta S} \tag{1.3}$$

where δS and δS_D are the total surface of the section and the surface corresponding to the micro-cracks, respectively (Figure 1.18). In the general case, it can depend on the normal to the surface, considering therefore a preferential direction of micro-cracks. Initially, there are no micro-cracks, and $\delta S_D = 0$ and $D = 0$. When $\delta S_D = \delta S$, all the surface is

covered by micro-cracks (coalescence) and the REV is fully broken. The damage variable is therefore bounded as $0 \leqslant D \leqslant 1$.

Basically, damage can be described by a scalar D, a second-order tensor $\mathbf{D}$ or other variations, and it is supposed to fully represent the degradation state of the material. These aspects are detailed in Section 3.2 and Section 3.3, but before, the thermodynamic framework needs to be introduced.

3.1 Thermodynamic framework

Material laws are commonly defined following a natural phenomenological approach, introducing some material parameters to be identified by experimental data fitting. Increasing the number of constitutive law parameters may help describing material responses but their overuse has a more limited scientific value. A high number of parameters needs a large experimental database to feed the calibration process but could also lead to less physical responses.

In this context, it is important to describe new material laws following a consistent thermodynamic framework. Energy dissipation and associated irreversible processes are therefore studied following thermodynamics principles, which can guarantee if such a constitutive equation is first of all physically admissible.

Let us recall some usual thermodynamic notions, which will be of extreme importance to better understand the formalism introduced in Chapter 4.

First principle. Considering the body Ω introduced in Figure 1.10, at first view without a discontinuity, we can define the following quantities (see Lemaitre et al. (2009) for further details):

- Internal energy E:
$$\mathrm{E} = \int_\Omega \rho \mathrm{e}\, dV \tag{1.4}$$
where ρ is the material density and e is the specific internal energy.

- Kinetic energy K:
$$K = \frac{1}{2}\int_\Omega \rho \mathbf{v}\cdot\mathbf{v}\, dV \tag{1.5}$$
with $\mathbf{v}$ denoting the velocity field.

- Rate of heat Q received by the body Ω:
$$Q = \int_\Omega r\, dV - \int_{\partial\Omega} \boldsymbol{q}\cdot\boldsymbol{n}\, dS \tag{1.6}$$
where r is a heat source, $\boldsymbol{q}$ is the heat flux through the boundary $\partial\Omega$ of normal $\boldsymbol{n}$

- Power of the external forces P_{ext}:
$$P_{\text{ext}} = \int_\Omega \boldsymbol{f}\cdot\mathbf{v}\, dV - \int_{\partial\Omega} \boldsymbol{t}^d\cdot\mathbf{v}\, dS \tag{1.7}$$
where $\boldsymbol{f}$ is the volumetric force and $\boldsymbol{t}^d = \boldsymbol{\sigma}\cdot\boldsymbol{n}$ are the stress vector, with $\boldsymbol{\sigma}$ denoting the Cauchy stress tensor.

- Power of internal forces P_{int}:

$$P_{\text{int}} = -\int_{\Omega} \boldsymbol{\sigma} : \dot{\boldsymbol{\varepsilon}}\, dV \tag{1.8}$$

  where ":" denotes the double contraction between two tensors.

- Power of acceleration forces P_a:

$$P_a = \int_{\Omega} \rho\, \boldsymbol{\gamma} \cdot \mathbf{v}\, dV \tag{1.9}$$

  with the acceleration field $\boldsymbol{\gamma} = d\mathbf{v}/dt$.

The first principles reads (energy conservation):

$$\frac{d}{dt}(\mathrm{E} + K) = P_{\text{ext}} + Q \tag{1.10}$$

or noticing that $P_{\text{ext}} + P_{\text{int}} = P_a$ and $dK/dt = P_a$, combined with the expressions of P_{int} and P_a and divergence theorem, one has:

$$\frac{d}{dt}\int_{\Omega} \rho \mathrm{e}\, dV = \int_{\Omega} \rho \dot{\mathrm{e}}\, dV = \int_{\Omega} \boldsymbol{\sigma} : \dot{\boldsymbol{\varepsilon}}\, dV + \int_{\Omega} (r - \nabla \cdot \boldsymbol{q})\, dV \tag{1.11}$$

which finally reads:

$$\rho \dot{\mathrm{e}} = \boldsymbol{\sigma} : \dot{\boldsymbol{\varepsilon}} + r - \nabla \cdot \boldsymbol{q} \tag{1.12}$$

where "$\nabla\cdot$" denotes the divergent operator.

Second principle. This principle postulates that the rate of entropy production is always greater or equal to the rate of heat divided by the temperature received by the body. Thus:

$$\int_{\Omega} \left[\rho \dot{\mathrm{s}} + \operatorname{div}\left(\frac{\boldsymbol{q}}{T}\right) - \frac{r}{T}\right] dV \geqslant 0 \tag{1.13}$$

Clausius-Duhem inequality. Clausius-Duhem inequality assembles both first and second thermodynamics principles by introducing the specific Helmholtz free energy $\psi = \mathrm{e} - T\mathrm{s}$, where T is the temperature and s is the specific entropy. The inequality locally reads:

$$\boldsymbol{\sigma} : \dot{\boldsymbol{\varepsilon}} - \rho(\dot{\psi} + \mathrm{s}\dot{T}) - \frac{\boldsymbol{q} \cdot \nabla T}{T} \geqslant 0 \tag{1.14}$$

One may notice that ψ is a thermodynamic state potential and is a function of the state variables (internal and observable) that fully define material state. It describes the amount of mechanical energy available. Hence, considering a general material behavior, heat transfer and dissipative mechanisms (represented by general state variables $\mathbb{V}_k$, with $k \geqslant 1$), the Helmholtz free energy reads:

$$\rho\psi = \rho\psi(\boldsymbol{\varepsilon}, T, \mathbb{V}_k) \tag{1.15}$$

The derivative with respect to time is:

$$\rho\dot{\psi} = \rho\frac{\partial \psi}{\partial \boldsymbol{\varepsilon}} : \dot{\boldsymbol{\varepsilon}} + \rho\frac{\partial \psi}{\partial T}\dot{T} + \rho\frac{\partial \psi}{\partial \mathbb{V}_k} \bullet \dot{\mathbb{V}}_k \tag{1.16}$$

where "$\bullet$" denotes a general contraction, depending on the order of the state variable $\mathbb{V}_k$.

State laws. In a Coleman and Noll (1963) fashion, the state laws are obtained by substituting Equation (1.16) in Equation (1.14):

$$\left(\boldsymbol{\sigma} - \rho\frac{\partial\psi}{\partial\boldsymbol{\varepsilon}}\right) : \dot{\boldsymbol{\varepsilon}} + \left(\mathrm{s} + \rho\frac{\partial\psi}{\partial T}\right)\dot{T} - \rho\frac{\partial\psi}{\partial\mathbb{V}_k} \bullet \dot{\mathbb{V}}_k - \frac{\boldsymbol{q}\cdot\nabla T}{T} \geqslant 0 \tag{1.17}$$

Standard arguments allow to separately evaluate each term in the equation. For instance, under isothermal and uniform temperature transformation (*i.e.*, $\dot{T} = 0$ and $\nabla T = \mathbf{0}$), considering no dissipative mechanisms (*i.e.*, $\dot{\mathbb{V}}_k = \mathbf{0}$), one has:

$$\left(\boldsymbol{\sigma} - \rho\frac{\partial\psi}{\partial\boldsymbol{\varepsilon}}\right) : \dot{\boldsymbol{\varepsilon}} = 0 \tag{1.18}$$

which needs to be verified for any $\dot{\boldsymbol{\varepsilon}}$. Thus, the first state law reads:

$$\boldsymbol{\sigma} = \rho\frac{\partial\psi}{\partial\boldsymbol{\varepsilon}} \tag{1.19}$$

We say that $\boldsymbol{\sigma}$ is thermodynamic force associated to the state variable $\boldsymbol{\varepsilon}$. Consequently, under uniform expansion without dissipative mechanisms, one has:

$$\mathrm{s} = -\rho\frac{\partial\psi}{\partial T} \tag{1.20}$$

where the entropy is the thermodynamic force associated to the temperature. In the general case, the state law for dissipative mechanisms is:

$$\mathbb{A}_k = \rho\frac{\partial\psi}{\partial\mathbb{V}_k} \tag{1.21}$$

with $\mathbb{A}_k$ denoting the thermodynamic force associated to the state variable $\mathbb{V}_k$.

Dissipation. The total dissipation verifying the inequality is:

$$\mathcal{D}_{\mathrm{tot}} = -\mathbb{A}_k \bullet \dot{\mathbb{V}}_k - \frac{\boldsymbol{q}\cdot\nabla T}{T} \geqslant 0 \tag{1.22}$$

where the last term is associated to the dissipation by heat conduction and it is always positive following Fourier's law (*i.e.*, $\boldsymbol{q} = -k_{\mathrm{cond}}\nabla T$ and $k_{\mathrm{cond}}\|\nabla T\|^2/T \geqslant 0$). The first term is also called intrinsic dissipation and is related to the (mechanical) energy dissipated as heat, and one has:

$$\mathcal{D} = -\mathbb{A}_k \bullet \dot{\mathbb{V}}_k \geqslant 0 \tag{1.23}$$

Processes are considered thermodynamically acceptable if the Clausius-Duhem inequality is verified at each instant during the evolution mechanisms. Correspondingly, if any irreversible process such as plasticity or damage occurs, energy must be dissipated and remain positive.

Legendre-Fenchel transform and example of elasticity. Some models are better described by the specific Gibbs free enthalpy $\psi^\star$, which can be obtained by the Legendre-Fenchel:

$$\psi^\star = \sup_{\boldsymbol{\varepsilon}} \left[\frac{1}{\rho}\boldsymbol{\sigma} : \boldsymbol{\varepsilon} - \psi(\boldsymbol{\varepsilon}) \right] \tag{1.24}$$

Ignoring the temperature for simplicity, let us consider the case of elasticity with the following Helmholtz free energy:

$$\rho\psi(\boldsymbol{\varepsilon}) = \frac{1}{2}\boldsymbol{\varepsilon} : \mathbb{E} : \boldsymbol{\varepsilon} \tag{1.25}$$

where $\mathbb{E}$ denotes the fourth-order Hooke's tensor. Taking the derivative with respect to $\boldsymbol{\varepsilon}$, one finds $\boldsymbol{\varepsilon} = \mathbb{E}^{-1} : \boldsymbol{\sigma}$, where $\mathbb{E}$ is required to have the major symmetries (*i.e.*, $E_{ijkl} = E_{klij}$), so the existence of an elastic potential is verified. Substitution in Equation (1.24) leads to[1]

$$\rho\psi^\star(\boldsymbol{\sigma}) = \boldsymbol{\sigma} : \mathbb{E}^{-1} : \boldsymbol{\sigma} - \frac{1}{2}\left(\mathbb{E}^{-1} : \boldsymbol{\sigma}\right) : \mathbb{E} : \left(\mathbb{E}^{-1} : \boldsymbol{\sigma}\right) = \frac{1}{2}\boldsymbol{\sigma} : \mathbb{E}^{-1} : \boldsymbol{\sigma} \tag{1.26}$$

with the new state law:

$$\boldsymbol{\varepsilon} = \rho\frac{\partial\psi^\star}{\partial\boldsymbol{\sigma}} \tag{1.27}$$

Remark 1.4. *Given its potential nature, the free energy must preserve the material symmetries. In the case of isotropy, one has:*

$$\rho\psi(\mathbf{Q}^T \cdot \boldsymbol{\varepsilon} \cdot \mathbf{Q}) = \rho\psi(\boldsymbol{\varepsilon}) \quad \forall \mathbf{Q} \mid \mathbf{Q}^T \cdot \mathbf{Q} = \mathbf{I} \tag{1.28}$$

with $\mathbf{I}$ *denoting the second-order identity tensor. It means that the potential should by invariant with respect to any rotation or symmetry. A convenient way to do so is to define it in terms of the invariants of* $\boldsymbol{\varepsilon}$*. In the case of elasticity, the free energy reads:*

$$\rho\psi(\boldsymbol{\varepsilon}) = G\,\boldsymbol{\varepsilon} : \boldsymbol{\varepsilon} + \frac{\lambda}{2}\left(\operatorname{tr}\boldsymbol{\varepsilon}\right)^2 \tag{1.29}$$

where G *is the shear modulus and* λ *is the Lamé's parameter. This expression can be obtained by simply replacing* $\mathbb{E} = 2G\mathbf{I}\overline{\otimes}\mathbf{I} + \lambda\mathbf{I}\otimes\mathbf{I}$ *in Equation* (1.25)*.*
In this way, the derived constitutive relations are invariant under changes of frame reference for a given class of symmetry, respecting the principle of objectivity (see for instance Truesdell and Noll (1965) and Boehler (1987)).

Example of plasticity, normality rule and evolution laws. In the case of a perfect elasto-plastic material (*i.e.*, without hardening), we can introduce the tensor of (irreversible) plastic strains $\mathbb{V}_1 = \boldsymbol{\varepsilon}^p$ as a state variable, and therefore the only dissipative mechanism. Considering the partition of strains $\boldsymbol{\varepsilon} = \boldsymbol{\varepsilon}^e + \boldsymbol{\varepsilon}^p$, with $\boldsymbol{\varepsilon}^e$ the elastic strains

[1] Note that $\left(\mathbb{E}^{-1} : \boldsymbol{\sigma}\right) : \mathbb{E} : \left(\mathbb{E}^{-1} : \boldsymbol{\sigma}\right) = E^{-1}_{ijpq}\sigma_{pq}E_{ijkl}E^{-1}_{klmn}\sigma_{mn} = E^{-1}_{ijpq}\sigma_{pq}I_{ijmn}\sigma_{mn} = \sigma_{ij}E^{-1}_{ijpq}\sigma_{pq}$ where $\mathbb{E} : \mathbb{E}^{-1} = \mathbb{I}$, with $\mathbb{I} = \mathbf{I}\overline{\otimes}\mathbf{I}$ denoting the fourth order symmetrized identity, and $\overline{\otimes}$ is the symmetric tensor product. It is defined as $(\boldsymbol{a}\overline{\otimes}\boldsymbol{b}) : \boldsymbol{c} = \boldsymbol{a}\cdot\boldsymbol{c}\cdot\boldsymbol{b}$ for any second-order tensors $\boldsymbol{a}$, $\boldsymbol{b}$ and $\boldsymbol{c}$.

tensor, and writing the following Helmholtz potential:

$$\rho\psi = \rho\psi(\boldsymbol{\varepsilon}, \boldsymbol{\varepsilon}^p) = \frac{1}{2}(\boldsymbol{\varepsilon} - \boldsymbol{\varepsilon}^p) : \mathbb{E} : (\boldsymbol{\varepsilon} - \boldsymbol{\varepsilon}^p) \tag{1.30}$$

the first state law (constitutive behavior) reads:

$$\boldsymbol{\sigma} = \rho\frac{\partial\psi}{\partial\boldsymbol{\varepsilon}} = \mathbb{E} : (\boldsymbol{\varepsilon} - \boldsymbol{\varepsilon}^p) = \mathbb{E} : \boldsymbol{\varepsilon}^e \tag{1.31}$$

and:

$$\mathbb{A}_1 = \rho\frac{\partial\psi}{\partial\boldsymbol{\varepsilon}^p} = -\mathbb{E} : (\boldsymbol{\varepsilon} - \boldsymbol{\varepsilon}^p) = -\boldsymbol{\sigma} \tag{1.32}$$

where $\mathbb{A}_1$ is the thermodynamic force associated to $\boldsymbol{\varepsilon}^p$. The expression of the dissipation reads therefore:

$$\mathcal{D} = \boldsymbol{\sigma} : \dot{\boldsymbol{\varepsilon}}^p \tag{1.33}$$

Let us introduce a criterion function $f(\boldsymbol{\sigma})$, which defines the conditions for plastic flow. The elastic behavior is characterized by $f < 0$, whereas plasticity takes place when the consistency conditions $f = 0$ and $\dot{f} = 0$ are verified.

According to the Hill principle (Hill, 1948, 1967), among all admissible states, the stress maximizes the plastic dissipation under the constraint $f = 0$. Introducing the plastic multiplier $\dot{\lambda}_f$, and considering that maximizing $\mathcal{D}$ is equivalent to minimize $-\mathcal{D}$, one has:

$$\frac{\partial}{\partial\boldsymbol{\sigma}}\left(-\boldsymbol{\sigma} : \dot{\boldsymbol{\varepsilon}}^p + \dot{\lambda}_f f\right) = 0 \quad \text{and} \quad \frac{\partial}{\partial\dot{\lambda}_f}\left(-\boldsymbol{\sigma} : \dot{\boldsymbol{\varepsilon}}^p + \dot{\lambda}_f f\right) = 0 \tag{1.34}$$

This gives the normality rule:

$$\dot{\boldsymbol{\varepsilon}}^p = \dot{\lambda}_f\frac{\partial f}{\partial\boldsymbol{\sigma}} \quad \text{and} \quad f(\boldsymbol{\sigma}) = 0 \tag{1.35}$$

Therefore, these equations define the evolution of the plastic tensor, following a direction $\partial f/\partial\boldsymbol{\sigma}$, which is normal to the elasticity domain, implying its convexity. From the thermodynamic perspective, the dissipation reads:

$$\mathcal{D} = \dot{\lambda}_f\left(\boldsymbol{\sigma} : \frac{\partial f}{\partial\boldsymbol{\sigma}}\right) \geqslant 0 \tag{1.36}$$

which is naturally verified if f is convex with respect to $\boldsymbol{\sigma}$. This can be generalized to any other behavior by postulating a pseudo-dissipation potential $F(\mathbb{A}_k)$, from which the evolution laws can be obtained:

$$\dot{\mathbb{V}}_k = -\dot{\lambda}_f\frac{\partial F}{\partial\mathbb{A}_k} \quad \text{and} \quad \mathcal{D} = \dot{\lambda}_f\left(\mathbb{A}_k \bullet \frac{\partial F}{\partial\mathbb{A}_k}\right) \geqslant 0 \tag{1.37}$$

verifying the Clausius-Duhem inequality respecting convexity properties of F. At this point, three different situations can exist (Halphen & Nguyen, 1975; Germain et al., 1983):

- Associated evolution (Standard generalized materials). The evolution law is derived from a pseudo-dissipation potential which equals the criterion function (*i.e.* $F = f$). This is the case, for instance, of associated plasticity.

- Non-associated evolution. The evolution law is derived from a pseudo-dissipation potential which is not equal to the criterion function (*i.e.* $F \neq f$). This is the case, for instance, of non-associated plasticity (often employed, *e.g.*, in soils behavior modeling)

- Non-standard evolution. The evolution law does not derive from a pseudo-potential and the positivity of the dissipation needs to be proven. It is generally the case for the majority of damage models avaiable for quasi-brittle materials.

3.2 Isotropic damage

The case of isotropic damage respects $D(\boldsymbol{n}) = D, \ \forall \boldsymbol{n}$, which is reasonable from a physical perspective when micro-cracks have no preferential direction (*i.e.*, they are randomly orientated, as shown in Figure 1.19).

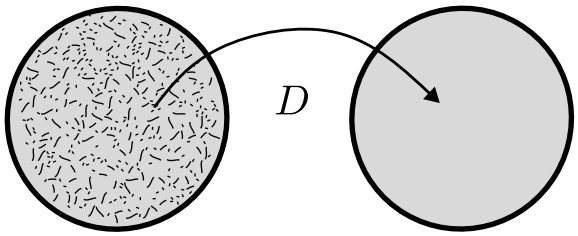

Figure 1.19 • CDM – Illustration of randomly orientated micro-cracks and isotropic (scalar) damage variable

The principle of strain equivalence (Lemaitre, 1971) states that the strain in a damaged material (*i.e.*, $\tilde{\varepsilon}$) equals the strain in a fictitious undamaged material (*i.e.*, ε), where the stress is replaced by its effective counterpart. Mathematically, this is expressed as:

$$\frac{\sigma}{\tilde{E}} = \frac{\tilde{\sigma}}{E} \tag{1.38}$$

with $\tilde{\sigma}$ the effective stress and $\tilde{E}$ the effective Young's modulus.

Following this definition and in conjunction with the concept of effective stress (Rabotnov, 1969), one has:

$$\tilde{\sigma} = \frac{\sigma}{1-D} \qquad \text{and} \qquad \sigma = (1-D)E\epsilon = \tilde{E}\varepsilon \tag{1.39}$$

which basically translates the constitutive relation for one-dimensional problems.

Marigo. One of the first damage models formulated within the framework of standard generalized materials was proposed by Marigo (1981). The Helmholtz free energy potential is expressed as:

$$\rho\psi = \rho\psi(\boldsymbol{\varepsilon}, D) = \frac{1}{2}(1-D)\boldsymbol{\varepsilon} : \mathbb{E} : \boldsymbol{\varepsilon} = \frac{1}{2}\boldsymbol{\varepsilon} : \tilde{\mathbb{E}} : \boldsymbol{\varepsilon} \ \text{ and } \ Y = -\frac{\partial \rho\psi}{\partial D} = \frac{1}{2}\boldsymbol{\varepsilon} : \mathbb{E} : \boldsymbol{\varepsilon} \tag{1.40}$$

with Y denoting the thermodynamic force associated to D, often referred to as the energy release rate, and $\tilde{\mathbb{E}} = (1 - D)\mathbb{E}$ is the effective Hooke's tensor. Therefore, the intrinsic dissipation is $\mathcal{D} = Y\dot{D} \geqslant 0$, naturally verified if $\dot{D}$ is derived from a convex pseudo-potential of dissipation F. Moreover, in the associated evolution case, one has:

$$\dot{D} = \dot{\lambda}_f \frac{\partial F}{\partial Y} = \dot{\lambda}_f \quad \text{with } F = Y - \kappa(D) \tag{1.41}$$

Thus, F also serves as the criterion (yield) function f and D follows a similar normality rule. The function $\kappa(D)$ is often referred to as a consolidation function, reflecting the evolution of the elastic domain with respect to damage. The damage multiplier $\dot{\lambda}_f$ is derived from the consistency condition ($\dot{F} = 0$), yielding:

$$\dot{Y} - \frac{\partial \kappa}{\partial D}\dot{D} = \dot{Y} - \frac{\partial \kappa}{\partial D}\dot{\lambda}_f = 0 \qquad \text{and} \qquad \dot{\lambda}_f = \frac{\dot{Y}}{\frac{\partial \kappa}{\partial D}} \tag{1.42}$$

Finally, modeling choices involve determining the expression of $\kappa(D)$, while verifying the dissipation inequality, guaranteed by $\partial\kappa/\partial D > 0$. It should be noted that this behavior introduces a symmetric yield surface in the stress space, which is not in agreement with experimental observation of tension-compression dissymetry in quasi-brittle materials.

Mazars. A damage model considered more appropriate to quasi-brittle materials, such as concrete, was introduced by Mazars (1984b). The main aspect was related to the experimental observation that extensions (in terms of strains) control the appearance of cracks in concrete, while retaining the same free energy as proposed in (Marigo, 1981). Accordingly, the criterion function was defined in terms of strains:

$$f(e, D) = e - \kappa(D) \quad \text{with} \quad e = \sqrt{\langle \boldsymbol{\varepsilon} \rangle : \langle \boldsymbol{\varepsilon} \rangle} \tag{1.43}$$

Here, e is an equivalent measure of the strains, taken in this case as the Mazars' equivalent strain, written in terms of the principal strains. The operator $\langle \bullet \rangle$ denotes the positive part of $\bullet$, also called Macaulay brackets. The damage threshold κ_0 is defined such that $\kappa(0) = \kappa_0$. One should notice that the equivalent strain is not restricted to isotropic damage behaviors and can be easily adapted for anisotropic damage models, as we will see later.

As described in (Mazars, 1984b; Mazars, 1986), the model is non-standard, and damage evolution is given by $\dot{D} = \tilde{F}(e)\,\langle \dot{e} \rangle$ for $f = 0$ and $\dot{f} = 0$, which does not derive from a pseudo-potential. The only necessary condition to satisfy the Clausius-Duhem inequality is that the function $\tilde{F}(e)$ must be continuous and positive for all e.

This criterion naturally takes into account a slight tension-compression dissimetry in the yield surface. In uni-axial tension $\varepsilon_1 > 0$, one has $e = \varepsilon_1$. On the contrary, in uni-axial compression one has $\varepsilon_1 < 0$ and $\varepsilon_2 = \varepsilon_3 > 0$, with ε_i denoting the principal strains. The equivalent strain is therefore $e = \sqrt{2}\varepsilon_2 = -\sqrt{2}\nu\varepsilon_1 > 0$, where ν is the Poisson's ratio. Given that for concrete-like materials, ν is around 0.2, the criterion is reached earlier in tension than in compression for a given value of ε_1. As a consequence, the associated yield stress is bigger in compression, as damage is a consequence of the Poisson effect.

However, the dissimetry is not only related to the yield stress, but also to damage evolution in compression or in tension. Mazars (1986) proposed to decouple the evolution law by introducing two damage variables:

$$D_{t,c} = 1 - \frac{\kappa_0(1 - A_{t,c})}{\kappa} - A_{t,c}\exp(-B_{t,c}(\kappa - \kappa_0)) \tag{1.44}$$

Here, the indexes indicate which variable and parameters (compression $\cdot_c$ or tension $\cdot_t$) may be employed. The final damage is therefore obtained as a linear combination of these two variables based on the stress state.

Nevertheless, despite the verification of the dissipation inequality, the introduction of two damage variables is questionable. From a thermodynamic point of view, damage is a state variable and should describe the degradation state of a given material independently of the load sign. This can be achieved, for instance, with damage variables of tensorial nature, as we will see later on.

De Vree. Another definition of an equivalent strain measure was proposed by De Vree et al. (1995), based on a modified Von Mises equivalent stress. The expression is then extended to strains and reads:

$$e = \frac{k-1}{2k(1-2\nu)} I_1 + \frac{1}{2k}\sqrt{\frac{(k-1)^2}{(1-2\nu)^2} I_1^2 - \frac{12k}{(1+\nu)^2} J_2} \tag{1.45}$$

where $I_1 = \operatorname{tr}\boldsymbol{\varepsilon}$ is the first invariant of strain tensor and $J_2 = \frac{1}{6}\left(3\operatorname{tr}\left(\boldsymbol{\varepsilon}\cdot\boldsymbol{\varepsilon}\right) - I_1^2\right)$ is the second one. The parameter k is obtained as a ratio between compression and tension strength (usually $k = 10$), which enforces the dissimetry tension-compression in the criterion. Due to the introduction of J_2 in the formulation, this criterion can be more useful for problems dealing with mixed mode failure or when shear is predominant. Moreover, it is more adapted to be used with only one damage variable and its associated evolution law, as the one proposed by Peerlings et al. (1998):

$$D = 1 - \frac{\kappa_0}{\kappa}\left(1 - \alpha_t + \alpha_t \exp\left[-B_t\left(\kappa - \kappa_0\right)\right]\right) \tag{1.46}$$

which is very similar to the one proposed by Mazars, with an additional term α_t accounting for residual stresses. As highlighted by the authors, softening starts exactly at $\kappa = \kappa_0$, so the initial increase in the stress under compression, experimentally observed, is neglected.

Other propositions of equivalent measures of the strain. For instance, Jirásek and Patzák (2002) introduced an equivalent strain based on a energy norm and a Rankine criterion. A modified smooth Rankine equivalent strain was proposed in (Jirásek & Bauer, 2012), where a scaling factor was used to guarantee that the equivalent strain equals the axial one in uni-axial tension. Nguyen et al. (2018) compared the response of different equivalent strain formulations with a gradient-enhanced regularized damage model at the structural scale. The authors proposed a new bi-energy norm equivalent strain, capable of dealing with both compression and tension separately. Shedbale et al. (2021) studied different equivalent strains with the so-called localizing gradient damage model. They

showed that the common equivalent strains, coupled with this specific regularization approach, were not capable of reproducing realistic crack paths in mixed-mode failure problems. The authors therefore proposed a modified Ottosen equivalent strain, which proved to be more adequate for treating these problems.

Isotropic model taking into account for unilateral effect and hysteresis. Once the thermodynamic framework is defined, damage models can increase in complexity to describe additional effects observed experimentally, such as the unilateral effect and hysteresis, which are experimentally observed for quasi-brittle materials. For instance, this can be achieved by adding state variables and splitting deviatoric and hydrostatic contributions in the potential.

Richard et al. (2010) proposed the following free energy potential:

$$\rho\psi = \frac{1}{2}[\frac{K}{3}\left((1-D)\left\langle \operatorname{tr}\boldsymbol{\varepsilon}\right\rangle^2 - \left\langle -\operatorname{tr}\boldsymbol{\varepsilon}\right\rangle^2\right) + 2(1-D)G\boldsymbol{\varepsilon}' : \boldsymbol{\varepsilon}' + 2DG\left(\boldsymbol{\varepsilon}' - \boldsymbol{\varepsilon}^\pi\right) : \left(\boldsymbol{\varepsilon}' - \boldsymbol{\varepsilon}^\pi\right) + \gamma\boldsymbol{\alpha} : \boldsymbol{\alpha}] + H(z) \quad (1.47)$$

where K is the bulk modulus, $\bullet'$ is the deviatoric part of $\bullet$, $\boldsymbol{\varepsilon}^\pi$ is a second order tensor accounting for sliding, $\boldsymbol{\alpha}$ is the second order tensor associated to the kinematic hardening, z is the internal variable related to the isotropic hardening and $H(z)$ its associated consolidation function. Notice that a similar approach was proposed by Desmorat et al. (2007b).

The term $(1-D)$ acts directly on positive hydrostatic strains, but does not affect the bulk modulus under compression. This simple split allows to consider a partial recovery of the stiffness due to the unilateral effect. Dissipation from sliding between the lips of a crack is accounted for through the state plasticity-type variable $\boldsymbol{\varepsilon}^\pi$, affecting only the deviatoric part of the free energy. Additionally, friction is considered by introducing common kinematic and isotropic hardening mechanisms. Richard et al. (2010) showed that the final model can accurately reproduce well known experimental findings, such as permanent strains, unilateral effect, and hysteric loops. However, the induced anisotropic character of degradation cannot be represented by this model. For further insights into CDM models considering cyclic loading effects, the reader may also refer to Richard and Ragueneau (2013) and Sellier et al. (2013a, 2013b).

Isotropic damage models accounting for strain rate effects. To accurately describe the experimentally observed increase in strength under high strain rates (see Section 1.1), the evolution of the damage variable needs to be adapted. For instance, Dubé et al. (1996) proposed to modify the expression of the damage multiplier issued form the normality rule to directly consider strain rate. The main idea is that, for high strain rates, damage evolution should become slower. From the observation that the damage rate cannot decrease without any constraints, Allix and Deü (1997b) and Allix (2001) introduced a bounded rate-dependent damage evolution for laminated composites. They showed that these so-called delay damage models were also capable of regularizing the response in terms of mesh-objectivity, by indirectly introducing a characteristic length in the formulation. Gatuingt and Pijaudier-Cabot (2002) developed a viscoplastic rate-dependent isotropic

damage model for the analysis of structures subjected to explosion and impacts. The model is based on a intersection between Mazars' and Gurson's yield surfaces, activating viscoplastic mechanisms based on the stress state.

3.3 Anisotropic damage

The use of isotropic damage models, such as those proposed by Mazars (1984b), has proven successful in modeling one-dimensional (1D) problems and providing reasonable approximations for three-dimensional (3D) damage under proportional loading conditions (Lemaitre & Desmorat, 2005). However, in quasi-brittle materials, such as concrete, damage is inherently anisotropic due to various well-established behaviors, including the dissimilarity between tension and compression, unilateral effects, and induced anisotropy.

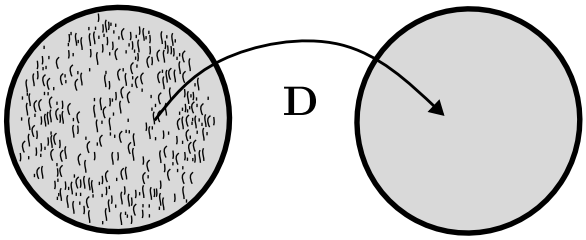

Figure 1.20 • CDM – Illustration of micro-cracks orientated following a preferential direction and anisotropic (tensorial) damage variable

In general, micro-cracks have a notable preferential direction (see for instance Figure 1.20). Thus, describing damage with tensors, instead of a single scalar variable, becomes crucial, taking into account the preferential directions of material degradation (Fichant et al., 1999).

Various anisotropic damage models have been developed, where damage was represented through vectors (Krajcinovic & Fonseka, 1981), second-order tensors, fourth-order tensors (Krajcinovic & Mastilovic, 1995; Maire & Chaboche, 1997) and even eighth-order tensors (Chaboche, 1982). However, fourth-order and eighth-order tensors prove to be too complex due to the large number of components, making them challenging to identify fully. As a result, many authors have opted to work with second-order tensors (Cordebois & Sidoroff, 1982a; Ladevèze, 1983; Murakami, 1988; Halm & Dragon, 1998; Desmorat, 2004; Desmorat, 2015), restricting the damage description to orthotropic behaviors. This assumption allows representing well with the observed crack patterns in quasi-brittle materials, where cracks typically propagate either perpendicular or parallel to the loading direction. In the following, the principles of mechanical equivalence are briefly recalled and a few anisotropic damage models are described.

On the principle of strain equivalence in anisotropic damage. The direct generalization of the effective stress concept in the case of a second order anisotropic damage $\mathbf{D}$ reads (see Sidoroff (1981), Cordebois and Sidoroff (1982a), Lemaitre (1996), and Murakami (2012) for further details):

$$\tilde{\boldsymbol{\sigma}} = (\mathbf{I} - \mathbf{D})^{-1} \cdot \boldsymbol{\sigma} \tag{1.48}$$

where $\tilde{\boldsymbol{\sigma}}$ is essentially an asymmetric tensor (*i.e.*, $\tilde{\sigma}_{ij} \neq \tilde{\sigma}_{ji}$). If one applies the principle of strain equivalence in this case, it turns out that the inverse of the effective elasticity tensor, or more precisely, the effective compliance, is not symmetric. Consequently, the existence of a (damaged) elastic potential becomes impossible.

More generally speaking, one has (Sidoroff, 1981; Cordebois & Sidoroff, 1982a):

$$\tilde{\boldsymbol{\sigma}} = \mathbb{M}(\mathbf{D}) : \boldsymbol{\sigma} \tag{1.49}$$

with $\mathbb{M}(\mathbf{D})$ a fourth-order damage effect tensor, mapping the stress tensor to its effective counterpart. Notice that, in practice, it can be dependent on damage variables of any order, but a second-order tensor $\mathbf{D}$ is considered here for illustration. The principle of strain equivalence reads:

$$\tilde{\mathbb{E}}^{-1} : \boldsymbol{\sigma} = \mathbb{E}^{-1} : \tilde{\boldsymbol{\sigma}} = \mathbb{E}^{-1} : (\mathbb{M}(\mathbf{D}) : \boldsymbol{\sigma}) \tag{1.50}$$

which leads to:[2]

$$\tilde{\mathbb{E}}^{-1} = \mathbb{E}^{-1} : \mathbb{M}(\mathbf{D}) \tag{1.51}$$

This is required to have the major symmetries to allow the existence of an elastic potential. As pointed out by Sidoroff (1981), this strongly restricts the construction of tensor $\mathbb{M}(\mathbf{D})$. For instance, a symmetric tensor $\tilde{\mathbb{E}}^{-1}$ can be obtained in the case of isotropic damage, which definitely makes no sense within an anisotropic damage framework. In other situations, expressions of $\mathbb{M}(\mathbf{D})$ will generally not lead to a symmetric effective compliance tensor.

Principle of energy equivalence. To address the issues presented above, Sidoroff (1981) and Cordebois and Sidoroff (1982a) proposed a principle of complementary energy (Gibbs) equivalence, which reads:

$$\rho\psi^\star(\boldsymbol{\sigma}, \mathbf{D}) = \frac{1}{2}\boldsymbol{\sigma} : \tilde{\mathbb{E}}^{-1} : \boldsymbol{\sigma} = \rho\psi^\star(\tilde{\boldsymbol{\sigma}}) = \frac{1}{2}\tilde{\boldsymbol{\sigma}} : \mathbb{E}^{-1} : \tilde{\boldsymbol{\sigma}} \tag{1.52}$$

Combined with Equation (1.49) this leads to:

$$\tilde{\mathbb{E}}^{-1} = \mathbb{M}^T(\mathbf{D}) : \mathbb{E}^{-1} : \mathbb{M}(\mathbf{D}) \tag{1.53}$$

where $\tilde{\mathbb{E}}^{-1}$ is symmetric for any appropriate choice of $\mathbb{M}(\mathbf{D})$ (*e.g.*, Chow and Wang (1987a, 1987b)), such as a symmetric fourth-order tensor. For instance, one can define the equivalent stress as the symmetric tensor (Cordebois & Sidoroff, 1982a):

$$\tilde{\boldsymbol{\sigma}} = (\mathbf{I} - \mathbf{D})^{-\frac{1}{2}} \cdot \boldsymbol{\sigma} \cdot (\mathbf{I} - \mathbf{D})^{-\frac{1}{2}} = \left[(\mathbf{I} - \mathbf{D})^{-\frac{1}{2}} \,\overline{\otimes}\, (\mathbf{I} - \mathbf{D})^{-\frac{1}{2}}\right] : \boldsymbol{\sigma} \tag{1.54}$$

which allows to define a symmetric effective Hooke's tensor based on the concept of complementary energy equivalence. Saanouni et al. (1994) extended this concept to the principle of total energy equivalence. Notice that a general thermodynamic framework was proposed by Ladevèze (1983) where the Ladevèze tensor $\mathbf{H} = (\mathbf{I} - \mathbf{D})^{-\frac{1}{2}}$ was used as a state variable.

[2] $\mathbb{E}^{-1} : (\mathbb{M}(\mathbf{D}) : \boldsymbol{\sigma}) = E^{-1}_{ijkl} M_{klpq} \sigma_{pq} = \left(\mathbb{E}^{-1} : \mathbb{M}(\mathbf{D})\right) : \boldsymbol{\sigma}$

Q **Remark 1.5.** *Here,* $\mathbf{H}$ *is a tensor-valued function of* $\mathbf{D}$*, so the power* $-1/2$ *is applied in terms of the principal values.*

Maire and Chaboche. Maire and Chaboche (1997) introduced a thermodynamic framework to describe anisotropic damage with a few options to be considered separately in behavior formulations. In the case of an initial isotropic material, the Helmholtz potential is defined as:

$$\rho\psi = \frac{1}{2}\boldsymbol{\varepsilon} : \tilde{\mathbb{E}} : \boldsymbol{\varepsilon} \quad \text{and} \quad \tilde{\mathbb{E}} = \mathbb{E} - \mathbb{D} : \mathbb{E} \tag{1.55}$$

where the variable $\mathbb{D}$ depends on the modeling state variable chosen. Considering a second order damage tensor, the fourth-order variable $\mathbb{D}$ reads:

$$\mathbb{D} = \frac{(\alpha - \beta)}{2}\left(\mathbf{I} \otimes \mathbf{D} + \mathbf{D} \otimes \mathbf{I}\right) + \beta\left(\mathbf{I} \underline{\otimes} \mathbf{D}\right) \tag{1.56}$$

where α and β are weighting coefficients. Other modeling choices (fourth-order damage tensor, scalar decomposition, etc.) can be found in (Maire & Chaboche, 1997). In spite of being defined following an usual thermodynamics framework, Cormery and Welemane (2002) showed that this approach would lead to different Helmholtz potentials in function of the basis vectors used to represent $\mathbf{D}$. As a consequence, the damage model formulated as so induces the existence of a potential that is not unique.

Halm and Dragon. This model proposes a second order damage tensor written in terms of eigenvalues D_i and respective eigenvectors $\boldsymbol{v}_i$ (Halm & Dragon, 1998):

$$\mathbf{D} = \sum_{i=1}^{3} D_i \boldsymbol{v}_i \otimes \boldsymbol{v}_i \tag{1.57}$$

The damage variable $\mathbf{D}$ is a symmetric second order tensor and admits 3 non negative eigenvalues. Basically, any damage state can be described by a family of three orthogonal systems of microcracks. The Helmholtz potential is therefore written in terms of the invariants family of $\boldsymbol{\varepsilon}$ and $\mathbf{D}$, namely:

$$\operatorname{tr}\boldsymbol{\varepsilon}, \quad \operatorname{tr}\left(\boldsymbol{\varepsilon} \cdot \boldsymbol{\varepsilon}\right), \quad \operatorname{tr}\left(\boldsymbol{\varepsilon} \cdot \mathbf{D}\right), \quad \operatorname{tr}\left(\boldsymbol{\varepsilon} \cdot \boldsymbol{\varepsilon} \cdot \mathbf{D}\right) \tag{1.58}$$

The final model is capable to represent some complex aspects such as the unilateral effect, induced anisotropy, and frictional blockage and sliding that occurs while exhibiting hysteric effects.

Lemaitre, Desmorat and Sauzay. Based on the work of Ladevèze (1983), Lemaitre et al. (2000) proposed a different form of the Gibbs potential decoupling deviatoric and hydrostatic contributions, while the principle of strain equivalence remained valid:

$$\rho\psi^{\star} = \frac{1+\nu}{2E}\operatorname{tr}\left(\mathbf{H} \cdot \boldsymbol{\sigma}' \cdot \mathbf{H} \cdot \boldsymbol{\sigma}'\right) + \frac{3(1-2\nu)}{2E}\frac{\sigma_H^2}{1 - \eta_D D_H} \tag{1.59}$$

where $\sigma_H = 1/3\,\mathrm{tr}\,\boldsymbol{\sigma}$, $D_H = 1/3\,\mathrm{tr}\,\mathbf{D}$, and η_D is parameter generally taken as $\eta_D \approx 3$. This expression naturally induces the elasticity law:

$$\boldsymbol{\varepsilon} = \rho\frac{\partial\psi^\star}{\partial\boldsymbol{\sigma}} = \frac{1+\nu}{E}\tilde{\boldsymbol{\sigma}} - \frac{\nu}{E}\mathrm{tr}\,\tilde{\boldsymbol{\sigma}}\mathbf{I} \quad \text{with} \quad \tilde{\boldsymbol{\sigma}} = (\mathbf{H}\cdot\boldsymbol{\sigma}'\cdot\mathbf{H})' + \frac{\sigma_H}{1-\eta_D D_H}\mathbf{I} \tag{1.60}$$

where the expression of the effective stress derives directly from the potential, which was not the case for Cordebois and Sidoroff (1982a), for instance. Further discussions take place in (Lemaitre & Desmorat, 2005), where a detailed expression of the damage effect tensor $\mathbb{M}(\mathbf{D})$ is derived.

Desmorat. Desmorat (2015) proposed a specific model for quasi-brittle materials. According to this formulation, damage is represented using the second-order Ladevèze tensor $\mathbf{H} = (\mathbf{I}-\mathbf{D})^{-\frac{1}{2}}$. Denoting once again with $\boldsymbol{v}_i$ the eigenvectors of $\mathbf{D}$ and with D_i the corresponding eigenvalues, the Ladevèze tensor reads $\mathbf{H} = H_i\boldsymbol{v}_i\otimes\boldsymbol{v}_i = (1-D_i)^{-\frac{1}{2}}\boldsymbol{v}_i\otimes\boldsymbol{v}_i$. As a consequence, $H_i = 1$ when $D_i = 0$ (undamaged state), and $H_i \to \infty$ when $D_i \to 1$ (fully damaged state). The unbounded nature of H_i enhances the formulation's ability to model the extreme scenario of fully damaged material at infinite strain (Desmorat, 2015). Moreover, from a numerical perspective, the unboundedness simplifies the handling of upper bounds (see for instance Desmorat et al. (2007a)) for damage tensors when implementing the constitutive law at the integration point level.

In this model, the Ladevèze tensor $\mathbf{H}$ is a state variable, instead of $\mathbf{D}$. Accordingly, the Gibbs free enthalpy reads:

$$\rho\psi_0^* = \rho\psi_0^*(\boldsymbol{\sigma},\mathbf{H}) = \frac{\mathrm{tr}\,(\mathbf{H}\cdot\boldsymbol{\sigma}'\cdot\mathbf{H}\cdot\boldsymbol{\sigma}')}{4G} + \frac{1}{18K}\left[\frac{1}{3}\mathrm{tr}\,\mathbf{H}^2\,\langle\mathrm{tr}\,\boldsymbol{\sigma}\rangle^2 + -\langle\mathrm{tr}\,\boldsymbol{\sigma}\rangle^2\right] \tag{1.61}$$

and the strain tensor is obtained as:

$$\boldsymbol{\varepsilon} = \rho\frac{\partial\psi_0^*}{\partial\boldsymbol{\sigma}} = \frac{1}{2G}(\mathbf{H}\cdot\boldsymbol{\sigma}'\cdot\mathbf{H})' + \frac{1}{9K}\left[\frac{1}{3}\mathrm{tr}\,\mathbf{H}^2\,\langle\mathrm{tr}\,\boldsymbol{\sigma}\rangle + \langle-\mathrm{tr}\,\boldsymbol{\sigma}\rangle\right]\mathbf{I} \tag{1.62}$$

The stress-strain constitutive relation is given by:

$$\boldsymbol{\sigma} = \tilde{\mathbb{E}} : \boldsymbol{\varepsilon} \tag{1.63}$$

where $\tilde{\mathbb{E}}$ represents the effective (damaged) Hooke's tensor, defined as:

$$\tilde{\mathbb{E}} = 2G\left[\mathbf{H}^{-1}\underline{\otimes}\,\mathbf{H}^{-1} - \frac{\mathbf{H}^{-2}\otimes\mathbf{H}^{-2}}{\mathrm{tr}\,\mathbf{H}^{-2}}\right] + m(\mathbf{H})\mathbf{I}\otimes\mathbf{I} \qquad m(\mathbf{H}) = \begin{cases}\frac{3K}{\mathrm{tr}\,\mathbf{H}^2} & \text{if } \mathrm{tr}\,\boldsymbol{\varepsilon} > 0\\ K & \text{otherwise}\end{cases} \tag{1.64}$$

> **Remark 1.6.** *For an undamaged medium,* $\mathbf{H} = \mathbf{I}$ *and the undamaged Hooke's tensor is retrieved. With* $\lambda = K - 2G/3$ *being the Lamé's parameter, one has:*
>
> $$\tilde{\mathbb{E}} = \mathbb{E} = 2G\left[\mathbf{I}\underline{\otimes}\,\mathbf{I} - \frac{\mathbf{I}\otimes\mathbf{I}}{\mathrm{tr}\,\mathbf{I}}\right] + \frac{3K}{\mathrm{tr}\,\mathbf{I}}\mathbf{I}\otimes\mathbf{I} = 2G\,\mathbf{I}\underline{\otimes}\,\mathbf{I} + \lambda\,\mathbf{I}\otimes\mathbf{I} \tag{1.65}$$

In this thesis, this constitutive behavior will serve as the anisotropic model used in regularized damage simulations at the structural scale. Compared to the original formulation, a few modifications are introduced and a plane-stress version of such a model is derived. A detailed explanation of its numerical implementation is provided in Chapter 5.

Microplane. An alternative approach to modeling anisotropic damage is presented in (Bažant & Oh, 1983a; Bažant, 1984a; Bažant & Gambarova, 1984; Bažant & Prat, 1988; Bažant et al., 1996). Inspired by the work of Taylor (1938) and the "Slip theory of plasticity" by Batdorf and Budianski (1949), the microplane theory was first developed by Bažant and Oh (1983a) regarding quasi-brittle materials such as concrete.

The main idea employed by Taylor in polycrystalline metals plasticity was that the constitutive relations could be described on planes of various orientations within the material, instead of laws written in tensorial form. Later, Batdorf and Budianski (1949) assumed that the stress on these "slip planes" must be obtained by projection of the macroscopic stress tensor (static constraint). The strain tensor is therefore calculated by superposing all contributions of the slip planes.

In fact, the slip theory was found to be more suitable to describe plastic behaviours. The strain softening typical behaviour of quasi-brittle materials needed a description adapted to its own micro structure. Bažant and Oh (1983a) and Bažant (1984a) introduced the microplane theory with major changes in comparison with the slip theory.

As the main mechanisms controlling softening behavior in concrete are the extensions, the static constraint was replaced by a kinematic constraint, projecting the strain tensor on each microplane. Furthermore, contributions on each plane are no more superposed and the corresponding macroscopic stress tensor is obtained by the means of the principle of virtual work. Despite the fact that the model actually describes the behavior in a lower scale, microplane behaviors are defined as a homogenized material, with material parameters obtained in function of REV parameters.

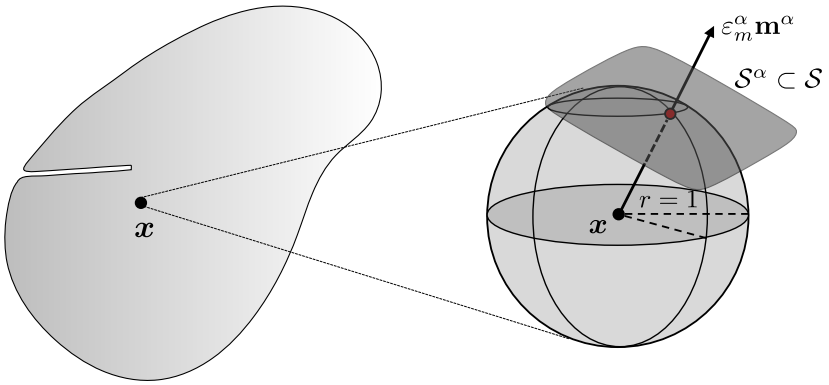

Figure 1.21 • microplane

In terms of continuum mechanics, each point of the body $\boldsymbol{x} \in \Omega$ can be seen as a group of microplanes (denoted here by α) of all possible orientations in space. The basic assumption is that, in a kinematic constraint condition, the behavior can be described independently on each plane and a variational principle is used to construct the equivalent macroscopic stress tensor $\boldsymbol{\sigma}$. The unit sphere $\mathcal{S}$ is considered to represent all microplanes possible directions of normal $\mathbf{m}^\alpha$, as seen Figure 1.21.

In spite of well experimental data fitting, a few microplane models proposed could not verify some thermodynamic criteria, as shown in (Carol et al., 2001). Basically, previous microplane models used to define stress and strain in a more intuitive way, which lead to

formulations where the micro stresses were not taken as the associated variables of the strains. Carol et al. (2001) and Kuhl et al. (2001) presented a few examples of microplane formulations leading to spurious energy dissipation or even energy generation regarding some loading cycles.

In the aim of creating a consistent approach for microplane new developments, Carol et al. (2001) proposed a thermodynamic framework based on the main assumption that the macroscopic free Helmholtz potential is obtained in function of potentials defined at each microplane. This is obtained by:

$$\psi = \frac{3}{2\pi} \int_{\frac{S}{2}} \psi^{\alpha}(\varepsilon_m^{\alpha}, \boldsymbol{\varepsilon}_t^{\alpha}, \varepsilon_V^{\alpha}, \varepsilon_D^{\alpha})\, dV \tag{1.66}$$

where the specific free energy at each microplane ψ^{α} is a function of the microstrains $\varepsilon_m^{\alpha}, \boldsymbol{\varepsilon}_T^{\alpha}, \varepsilon_V^{\alpha}, \varepsilon_D^{\alpha}$, obtained by projection, and all state variable controlling the behavior at the microscopic level. The satisfaction of the second principle implies that (Kuhl et al., 2001):

$$\mathcal{D}^{\alpha} = -\frac{\partial \psi^{\alpha}}{\partial \mathbb{V}_k^{\alpha}} \cdot \dot{\mathbb{V}}_k^{\alpha} \geq 0 \tag{1.67}$$

where $\mathbb{V}_k^{\alpha}$ is used for all internal variables defined at the microplane level. This simple assumption guarantees that dissipating a positive energy at each microplane leads to a positive dissipation in the macroscopic level. The microplane consistent stresses are therefore defined as:

$$\sigma_V^{\alpha} = \frac{\partial \rho\psi^{\alpha}}{\partial \varepsilon_V}, \quad \sigma_D^{\alpha} = \frac{\partial \rho\psi^{\alpha}}{\partial \varepsilon_D}, \quad \boldsymbol{\sigma}_T^{\alpha} = \frac{\partial \rho\psi^{\alpha}}{\partial \boldsymbol{\varepsilon}_T} \tag{1.68}$$

Micro-mechanics damage. Notice that for the previous approaches, the characteristics of micro-cracks, such as orientation, spatial distribution and geometry, were never considered. Micro-mechanics based damage models can account for this information by up-scaling homogenization techniques. Essential information, such as friction and sliding mechanisms can be studied in detail. These aspects are not covered in this thesis. For further information, the reader may refer to Pensée et al. (2002), Zhu et al. (2008), Kachanov (1992), Kachanov et al. (1994), and Kachanov (1993).

Summary of Chapter 1

Experimental observations:

- **Softening behavior** due to the degradation of elastic properties.
- **Asymmetric** behavior between tension and compression.
- **FPZ** diffuse micro-cracks occur before coalescence into a macro-crack (confirmed by acoustic emissions).
- **Induced anisotropic** behavior due to preferential directions of degradation.
- **Unilateral** effect under cyclic loading, stiffness recovery, hysteresis and permanent strains.
- **Size effect** related to the ratio size between the structure and size of the FPZ.

Crack description:

- **Explicit approaches:** cracks are explicitly considered in the formulations. Examples: DM, CZM, EFEM, XFEM, GFEM, LEFM.
- **Implicit approaches:** the effects of a crack are smeared over a volume and indirectly considered in the macroscopic behavior law. Examples: smeared cracks (fixed and rotating), crack band, **CDM**.
- **CDM**: derived within thermodynamic principles. Micro-cracking is described in a continuum framework using **isotropic** (scalar) or **anisotropic** (*e.g.*, tensorial) damage variables.

2

Generalities for non-local damage mechanics

Essential concepts of damage mechanics, from a structural point of view, are described in this chapter. The critical elements of strain localization and bifurcation are introduced to highlight the need to regularize the solution. An overview of the so-called non-local damage theory in integral and gradient versions is provided. The reasons for incorporating evolving and potentially anisotropic interactions are detailed. Finally, other well-known regularization approaches are briefly described.

Contents

1 Localization, bifurcation and mesh sensitivity

Physical point of view. The term "localization" refers to the physical observation wherein mechanical fields become concentrated in a narrow but finite zone. For instance, shear bands were experimentally observed in some soils or granular materials, such as sand (see Figure 2.1a)). In this scenario Figure 2.1a, the non-linear behavior is concentrated in this zone, while the rest of the domain remains elastic. The corresponding kinematics are given in Figure 2.1b, where the displacement field remains continuous and a jump may appear in the strain field. In contrast to a strong discontinuity observed in crack kinematics, as introduced in Chapter 1, this situation is often referred to as a weak discontinuity.

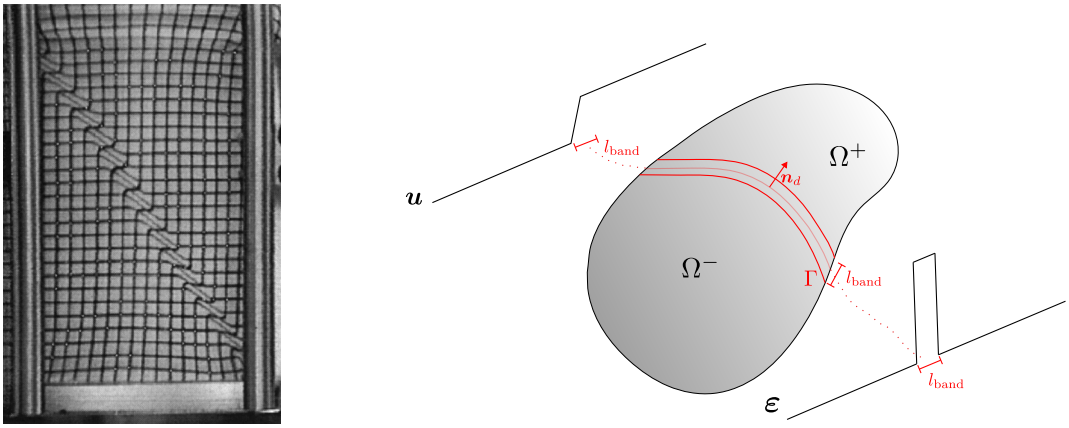

(a) Shear band experimentally observed in a sand specimen (Alshibli & Sture, 2000)

(b) Kinematics of a weak discontinuity

Figure 2.1 • Localized shear band and weak discontinuity

In the context of describing the cracking behavior of quasi-brittle materials, nonlinear behavior occurs within a significant FPZ, where micro-cracks develop (resulting in nonlinearity) and eventually merge to form a macro-crack. In this scenario, the localized band can be perceived as a region where these micro-cracks accumulate, while other areas of the domain exhibit elastic behavior. The strong discontinuity kinematics is therefore retrieved when a **fully localized** macro-crack appears (see for instance Figure 1.8).

> **Remark 2.1.** *Models like crack-band and smeared crack address the scenario of weak discontinuity case, where dissipation occurs in a finite zone (band).In contrast, models like CZM or some strong discontinuity approaches, assume that dissipation happens at the interface of the discontinuity through traction-separation laws.*

Mathematical point of view. The main scientific question is to determine under which conditions localization takes place. Specifically, the question pertains to how a continuum transitions from a uniform state to a bifurcated one, characterized by the concentration of inelastic strains within a localized band.

Hadamard (1903) was one of the first to study the discontinuities in this sense and proposed a relation to express jumps of continuum quantities across surfaces. Further work was carried out in some classic papers, such as Hill (1958) for the uniqueness and stability in solutions, Thomas (1961), Hill (1962), and Rudnicki and Rice (1975) for elasto-plastic behaviors and Rizzi et al. (1995) for damage. A comprehensive mathematical analysis of localization for damage models can be found in (Jirásek, 2007; Masseron et al., 2022). In the aim of introducing the basic concepts of localization analysis and its consequences, the main equations of bifurcation theory are briefly recalled in the following. For simplicity, interactions with boundaries are disregarded. For further details on these aspects, interested readers may refer to the work of Benallal and co-authors (Benallal & Billardon, 1991; Benallal et al., 1993; Lemaitre et al., 2009).

The departure point is the continuum depicted in Figure 2.1b, so the study of localization seeks to establish the necessary conditions for the occurrence of a weak discontinuity. Let $\bullet^-$ and $\bullet^+$ denote any quantity associated to Ω^- and Ω^+, respectively. As previously introduced, by definition, the associated jump can be computed by $[\![\bullet]\!] = \bullet^+ - \bullet^-$. At the onset of localization (*i.e.*, just before the emergence of the localized band), the general framework assumes the following hypotheses:

(*i*) Initial uniform and homogeneous state.

(*ii*) The strain is still continuous but a jump takes place in the strains rate.

(*iii*) Continuity of stresses rate vector on the discontinuity surfaces, *i.e.*, $\dot{\boldsymbol{\sigma}}^- \cdot \boldsymbol{n}_d = \dot{\boldsymbol{\sigma}}^+ \cdot \boldsymbol{n}_d$

(*iv*) Discontinuity of velocity gradients can only take place in the out-of-plane direction.

Following Hadamard (1903), the jump in components of the gradient of a vector field $\boldsymbol{a}$ is written in index notation as $[\![a_{i,j}]\!] = m_i n_{dj}$, where m_i denotes a proportionality coefficient and n_{dj} represents the components of the normal vector to the surface $\boldsymbol{n}_d$. In the case of the strain rates, the expression needs to be symmetrized, resulting in:

$$[\![\dot{\boldsymbol{\varepsilon}}]\!] = \left[\!\left[\frac{\partial \dot{\boldsymbol{u}}}{\partial \boldsymbol{x}}\right]\!\right] = \frac{1}{2}\left(\boldsymbol{m} \otimes \boldsymbol{n}_d + \boldsymbol{n}_d \otimes \boldsymbol{m}\right) \tag{2.1}$$

Vector $\boldsymbol{m}$ has a specific physical meaning defining the bifurcation mode. For instance, if $\boldsymbol{m}$ is co-linear to $\boldsymbol{n}_d$, one has a mode I failure, whereas mode II shear failure is characterized by the orthogonality between $\boldsymbol{m}$ and $\boldsymbol{n}_d$ (see the case depicted in Figure 2.1a).

The constitutive behavior can be written in a incremental form as $\dot{\boldsymbol{\sigma}} = \mathbb{L} : \dot{\boldsymbol{\varepsilon}}$, with $\mathbb{L}$ denoting the fourth-order tangent stiffness tensor, depending only on the state variables at the current state for a rate-independent material behavior. Consider the case where the inelastic behavior evolves outside and inside the band, leading to $[\![\dot{\boldsymbol{\sigma}}]\!] = \mathbb{L} : [\![\dot{\boldsymbol{\varepsilon}}]\!]$ (continuous bifurcation). Substituting this expression and Equation (2.1) into the traction continuity condition yields:

$$\left(\mathbb{L} : \frac{1}{2}\left(\boldsymbol{m} \otimes \boldsymbol{n}_d + \boldsymbol{n}_d \otimes \boldsymbol{m}\right)\right) \cdot \boldsymbol{n}_d = \left(\boldsymbol{n}_d \cdot \mathbb{L} \cdot \boldsymbol{n}_d\right) \cdot \boldsymbol{m} = \boldsymbol{0} \tag{2.2}$$

Remark 2.2. *In index notation and using Einstein summation convention, the left side of above equation reads:*

$$\begin{aligned}\frac{1}{2}L_{ijkl}(m_k n_l + n_k m_l)n_j &= \frac{1}{2}\left(n_j L_{jikl} m_k n_l + n_j L_{jilk} n_k m_l\right)\\ &= n_i L_{ijkl} n_l m_k\\ &= (\boldsymbol{n}_d \cdot \mathbb{L} \cdot \boldsymbol{n}_d) \cdot \boldsymbol{m}\end{aligned} \tag{2.3}$$

where the minor symmetries of the tangent stiffness were used (i.e., $L_{ijkl} = L_{jikl} = L_{ijlk}$) and the subscript "d" of the normal $\boldsymbol{n}_d$ was omitted for readability.

Therefore, Equation (2.3) is an eigenvalue problem with null eigenvalues, where the bifurcation modes $\boldsymbol{m}$ are the eigenvectors associated with the null eigenvalues of the so-called second-order acoustic tensor $\boldsymbol{n}_d \cdot \mathbb{L} \cdot \boldsymbol{n}_d$. For a non-trivial solution, the following necessary condition for bifurcation must be satisfied:

$$\det\left[\boldsymbol{n}_d \cdot \mathbb{L} \cdot \boldsymbol{n}_d\right] = 0 \tag{2.4}$$

Thus, bifurcation can occur if and only if there exist a direction $\boldsymbol{n}_d$ such that the acoustic tensor becomes singular. The case where the region outside the band is under elastic unloading (discontinuous bifurcation, where $\det\left[\boldsymbol{n}_d \cdot \mathbb{L} \cdot \boldsymbol{n}_d\right] < 0$) can be also easily derived (Lemaitre et al., 2009). However, it is pertinent to highlight, as noted by the same authors, the continuous bifurcation is reached first, and the discontinuous case may follow. Therefore, the majority of localization studies limit the analysis to the singularity of the acoustic tensor (*e.g.*, Jirásek (2007), Jirásek and Suárez (2016), and Masseron et al. (2022)).

Remark 2.3. *The acoustic tensor has this name for a specific reason. In the case of an isotropic elastic material, the acoustic tensor takes on a specific form. Let's consider its expression:*

$$\begin{aligned}\boldsymbol{n}_d \cdot \mathbb{E} \cdot \boldsymbol{n}_d &= \boldsymbol{n}_d \cdot \left(2G\mathbf{I} \underline{\otimes} \mathbf{I} + \lambda \mathbf{I} \otimes \mathbf{I}\right) \cdot \boldsymbol{n}_d\\ &= G\left(n_i \delta_{ik} \delta_{jl} n_l + n_i \delta_{il} n_l \delta_{jk}\right) + \lambda\, n_i \delta_{ij} \delta_{kl} n_l\\ &= G\left(n_k n_j + n_i n_i \delta_{jk}\right) + \lambda\, n_j n_k\\ &= G\,\mathbf{I} + (G + \lambda)\left(\boldsymbol{n}_d \otimes \boldsymbol{n}_d\right)\end{aligned} \tag{2.5}$$

where, once again, the lower script "d" of the normal was again omitted for readability. In a orthonormal basis containing $\boldsymbol{n}_d$, we can represent this in matrix format:

$$\boldsymbol{n}_d \cdot \mathbb{E} \cdot \boldsymbol{n}_d = \begin{bmatrix} 2\,G + \lambda & & \\ & G & \\ & & G \end{bmatrix}_{(\bullet,\bullet,\boldsymbol{n}_d)} = \begin{bmatrix} \rho c_L^2 & & \\ & \rho c_T^2 & \\ & & \rho c_T^2 \end{bmatrix}_{(\bullet,\bullet,\boldsymbol{n}_d)} \tag{2.6}$$

where $c_L = \sqrt{(2\,G + \lambda)/\rho}$ and $c_T = \sqrt{G/\rho}$ are the longitudinal and the transversal wave speeds, respectively.

> *Therefore, the acoustic tensor contains essential information about the wave velocities related to the material properties. As seen in Chapter 1, acoustic measurements can provide useful information about damage and degraded elastic properties.*

Important mathematical and numerical consequences. In quasi-static analysis, the singularity of the acoustic tensor implies the **loss of ellipticity** (see for instance Benallal and Billardon (1991)) of the boundary value problem. This loss of ellipticity leads to an ill-posed linearized rate equilibrium problem, where an infinite number of linearly independent solutions can be obtained at the bifurcation point. As a consequence, the size of the localization zone cannot be uniquely determined. In dynamics, the hyperbolic equilibrium equations become elliptic, defining the **loss of hyperbolicity** and the ill-posedness of the problem. In a one-dimensional context, Sluys (1992) analytically demonstrated that a local medium will inevitably lead to imaginary wave speeds. This implies that the structure is divided into two different zones: one where elastic waves can propagate and another one where the wave speed becomes imaginary. These last aspects will be further studied in Chapter 3.

A significant numerical consequence of this behavior is that finite element simulations do not converge upon mesh refinement. To illustrate this, let us consider the simulation of the well known L-shape test (Winkler et al., 2001, 2004) with a local anisotropic damage model (Desmorat, 2015). Figure 2.2 shows the global response obtained for different meshes in terms of the force and displacement computed at the point of loading application. The corresponding maps of the first damage eigenvalue D_1 show that damage tends to localize in a zone of vanishing volume as the mesh is refined. As expected, convergence with respect to the mesh is not observed in either the global response or the damage maps.

Therefore, finite element numerical simulations with local damage models are not meaningful, exhibiting a significant sensitivity to spatial discretization. This sensitivity can lead to spurious energy dissipation at the structural level, which is physically unacceptable. Moreover, damage patterns depend on the mesh orientation. To obtain meaningful results with these approaches, the numerical solution needs to be regularized.

Energetic regularization. One may employ regularization techniques to guarantee a mesh-independent solution when dealing with strain softening. As explained in Section 2, one option is to utilize a simple energetic regularization approach (Hillerborg et al., 1976; Bažant & Oh, 1983b). This approach involves defining model parameters in each element (depending on the characteristic size of the element) to dissipate the same amount of energy that is needed to create a crack surface for such a material (see for instance derivations in (Kakarla et al., 2021) for a microplane model).

Nevertheless, several authors (Mosler & Meschke, 2004; Jirásek & Grassl, 2008; Jirásek & Bauer, 2012) have shown that these regularization methods lead to different crack paths for different mesh orientations. For instance, Figure 2.3 shows considerably different damage maps obtained for different meshes in the simulation of the Shi-test (Shi et al., 2000) with a energy-regularized microplane damage model (Ribeiro Nogueira et al., 2022b).

Consequently, while energy-based methods can help regularize the overall structural

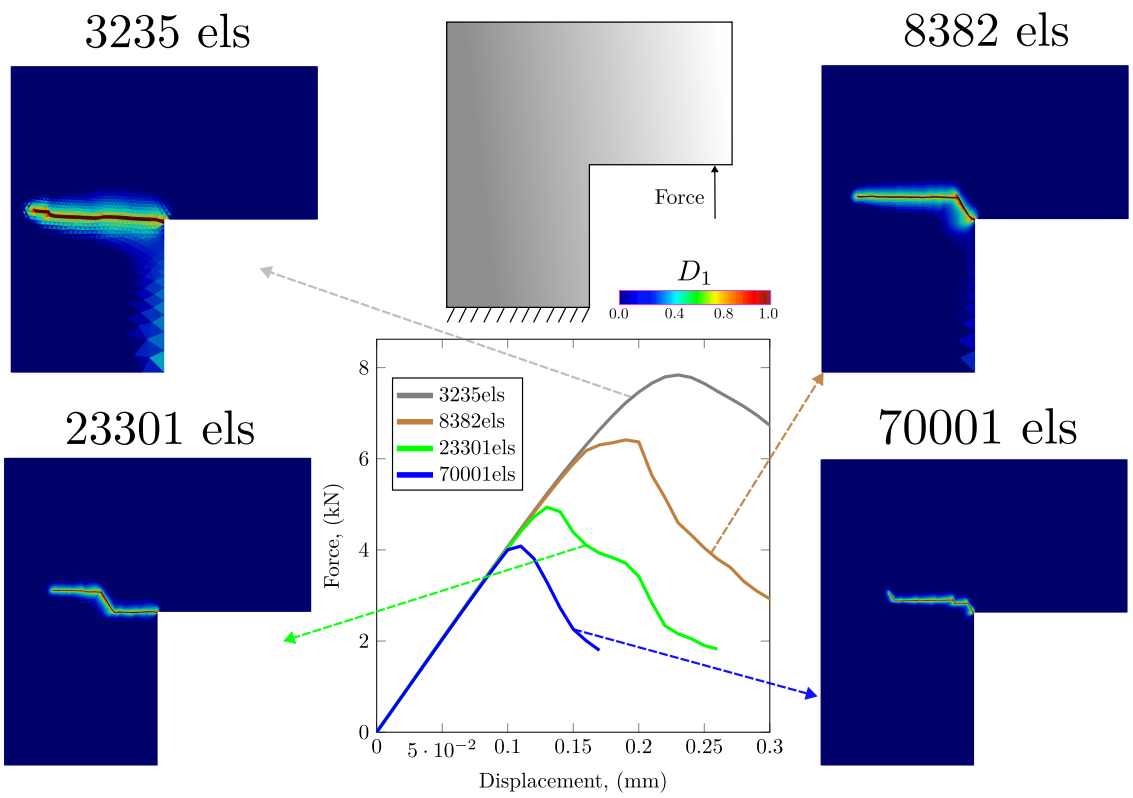

Figure 2.2 • Mesh dependency of local damage simulations

response, they might not suffice for sophisticated analyses aiming to capture detailed crack paths and failure patterns. In such cases, more advanced regularization approaches become necessary. These approaches typically involve introducing additional parameters that account for the localization process within a continuous medium.

2 General non locality and enriched continua

As micro-cracking that is responsible of strain-softening is distributed over a region of finite size within the media, it is reasonable to apply a continuum framework to describe the behavior of the REV under consideration (Bazant et al., 1984). However, the lack of a formulation capable to provide a meaningful solution to the differential equilibrium equations led to some distrust among certain researchers (Bažant & Jirásek, 2002). In fact, from a mathematical viewpoint, it is shown that the local damage problem provides a solution when treated with certain initial and boundary conditions (Bažant & Belytschko, 1985). The main challenge to overcome is that the basic assumption of a classical local continuum does not provide a representative solution of quasi-brittle media (Bažant (1976), Bazant et al. (1984)). Non-local continuum approaches can be applied, to provide consistent solutions and in particular numerical finite implementations that converge towards a physical response.

In the following section a brief description of a variety of non-local damage models acting as localization limiters is presented. The fundamental concepts of non-local

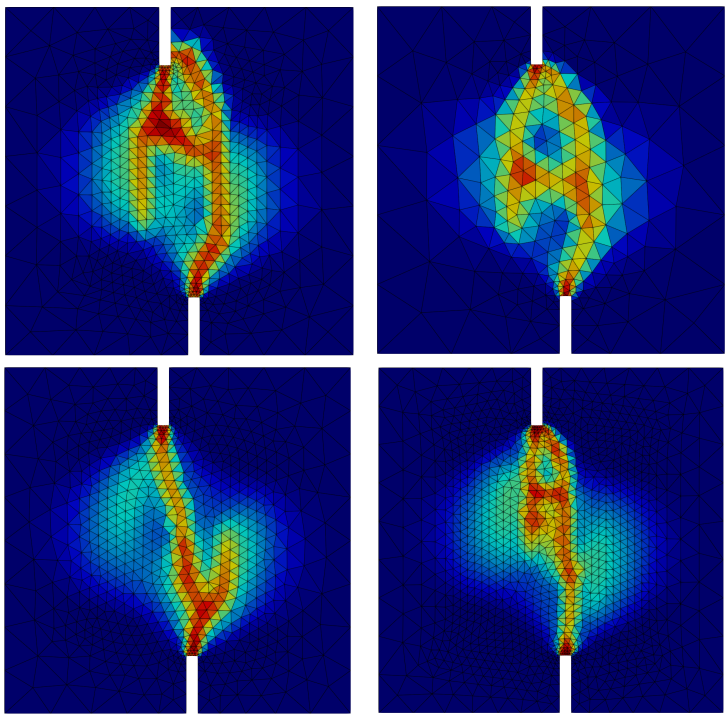

Figure 2.3 • Mesh-dependent damage profiles obtained with a energy-based regularized microplane model (Ribeiro Nogueira et al., 2022b)

approaches will be introduced, as well as the physical justifications of their use for the simulation of quasi-brittle media. The main feature of these models is the introduction of a characteristic length into the constitutive relations, which is treated as a material parameter. The size of the FPZ is related to this length.

Essentially, non-locality is introduced in quantum mechanics where a particle can know the state of another one instantaneously, even when they are far away from each other. Numerous academic discussions may take place regarding a possible violation of the principle of locality and therefore of the special relativity postulates (see for instance Popescu (2014) and the references therein). Indeed, locality implies that different points in space can only influence each other by the existence of fields, so the information (or effects) can propagate (Haag, 1992). Therefore, the speed at which effects are propagating is limited to the speed of light by Einstein's postulates (see EPR papers by Einstein et al. (1935)). In this context, the discussion between general local and non-local theories in physics is actually a vast subject.

Let us introduce the non-local concept from the viewpoint of other domains, which is less general than the notion of non-locality brought by quantum mechanics, but still similar in some ways.

Non-local means algorithms are used for instance in image denoising (Buades et al. (2005a), Buades et al. (2008)). The idea is basically an extension of neighborhood image filters, using pixels similarity to reduce noise. For a discretized image, the non-local quantity for a given noisy pixel i is the result of a weighted average of all the other pixels j of the entire image. This is achieved by introducing a weight function (Gaussian in this case), which computes the similarity between two given pixels by the Euclidean L^2

Figure 2.4 • Example of image denoising with a non-local algorithm (Buades et al., 2005b)

distance. This procedure is responsible for smoothing a given image (Figure 2.4). In fact, this filtering technique can be seen as a convolution integral between a correlation Gaussian function and a given field.

Similarly, a convolution product is used in the field of topology optimization, where mesh dependent designs and non-convergent sequences of the minimization problem are also an issue. As shown for image analysis, the main idea is to regularize a sort of density field of the material, which equals 0 for a void and 1 for the material itself. Applying a similar non-local integral average, one substitutes a possible non-regular density field (as done for image noise) by a smooth differentiable one (Bourdin, 2001). An equivalent approach for regularizing the topology optimization problem is to apply a Helmholtz-type partial differential equation. In this case, the aim is to replace the classical non-local integral density filtering approach by a more numerical friendly one, which is also more efficient and suitable for parallel computing (Lazarov & Sigmund, 2011).

A huge variety of physical problems have been addressed using non-local approaches (Eringen, 2002): dispersion of high frequency waves in electromagnetic field theories, fracture in non-regular solids, viscosity in micro-channel flows in fluid dynamics and many others. In regards specifically to solid mechanics, the concept of a non-local continuum is introduced to overcome the incapability of local theories to describe some behaviors. For better comprehension, it is necessary to enhance the concept of a local continuum theory.

One of the basic assumptions of continuum mechanics is the principle of local action (Truesdell & Toupin, 1960; Truesdell & Noll, 1965). For instance, for a given continuum body $\Omega \subset \mathbb{R}^3$, this principle dictates that the state of a material is defined for each point $\boldsymbol{x} \in \Omega$ and it is a functional of the state variables computed at that point. Moreover, this state depends also on what occurs at infinitesimal distance from the point $\boldsymbol{x}$, but neglects for example long-range effects (Eringen & Kafadar, 1976).

But how is it possible to speak about a continuum in the case of heterogeneous materials like concrete?

Essentially, a continuum body can be conceptually subdivided into infinitesimal elements. The decision to treat a material as a continuum is intricately linked to the scale

chosen for analysis. This is where the notion of a Representative Elementary Volume (REV) comes into play. The size of the REV must be sufficiently large to encompass the material's heterogeneity yet small enough to remain within the scope of the structure under consideration. In this context, fields (e.g., displacement field) are considered as continuous and regular enough for differentiation, enabling the solution of partial differential equations within the body.

While classical (local) field approaches suitably describe various material behaviors, they fail when confronted with certain experimental findings. It is the case for instance of local elasticity, which wrongly predicts the material wave speed when dealing with short wavelengths excitation (Eringen and Kafadar (1976), Eringen (1978)). As shown in Section 1, local damage models fail to predict the fracture process in strain-softening materials, providing physically meaningless results in finite element simulations. As showcased in Section 1, the strain field becomes close to a Dirac delta distribution upon localization, which means that high strain gradients take place in small (but finite) zones (obviously, this remark depends on the structural scale considered). Consequently, the equivalent homogenized volume for continuum damage mechanics analysis is not representative of what happens in lower scales. Indeed, the stress field is not smooth in this region, indicating the necessity of accounting for micro-structural aspects in the macroscopic model (Bažant and Oh (1983b), Bazant et al. (1984)). In fact, the assumption of distributed micro-cracks within the REV is no longer valid as the damage field is no more smooth (Peerlings, 1999). The size of a localization zone can vary from millimeters in metals to up to 3 times maximum aggregate size in concrete (Bažant & Pijaudier-Cabot, 1988). Hence, material degradation is concentrated in a finite zone, which implies finite energy dissipation.

Visibly, classical continuum approaches lack some information in the scale of the micro-structure, which becomes necessary for treating some specific problems such as strain localization. Introducing a characteristic length (intrinsically linked to a characteristic time in dynamics) facilitates the description of interactions at a lower scale and delineates the range of validity of the theory under consideration. In continuum mechanics, a characteristic length l_c (or internal length) may be introduced into the constitutive relations, which is related to the size of the REV and the FPZ (Bažant & Jirásek, 2002). Thus, if the wavelength of the excitation (or the strain/stress fields) is approximately equal to l_c, local theories ay inadequately describe the material behavior (Eringen (1976), Eringen (1978), Bažant and Jirásek (2002), Jirásek (2004)).

One may argue that an explicit description of the micro-structure (e.g., aggregates and cement paste for concrete) would be capable to overcome this issues, which is true. However, the implementation of lattice, discrete or hybrid models at a structural level is still impractical due to expensive calculations. Alternatively, local continuum models can be enriched to take into account the missing micro-structural information. Various enriched continuum approaches exist, such as Cosserat-type models (Cosserat & Cosserat, 1909), micropolar and micromorphic theories (Eringen & Suhubi, 1964; Mindlin, 1964; Suhubl & Eringen, 1964; Eringen & Kafadar, 1976; Eringen, 1999), and gradient theories (Aifantis, 1984; Frémond & Nedjar, 1996; Lorentz & Andrieux, 1999). Other approaches are more numerically oriented, primarily aiming to introduce a characteristic length

scale into the formulation to mitigate the ill-posedness of the problem without directly addressing micro-structural phenomena. In this latter case, non-locality primarily serves as a mathematical tool (a localization limiter) to regularize the response provided by the model. Among them, it is worth citing integral non-local formulations (Pijaudier-Cabot & Bažant, 1987), implicit gradient formulations (Peerlings et al., 1996a; Peerlings et al., 2004), the thick level-set model (Moës et al., 2011), phase-field formulations (Francfort & Marigo, 1998; Bourdin et al., 2000; Miehe et al., 2010; Pham et al., 2011), and more recently the Lipschitz regularization (Moës & Chevaugeon, 2021; Chevaugeon & Moës, 2022) and the graded damage approach (Valoroso & Stolz, 2022).

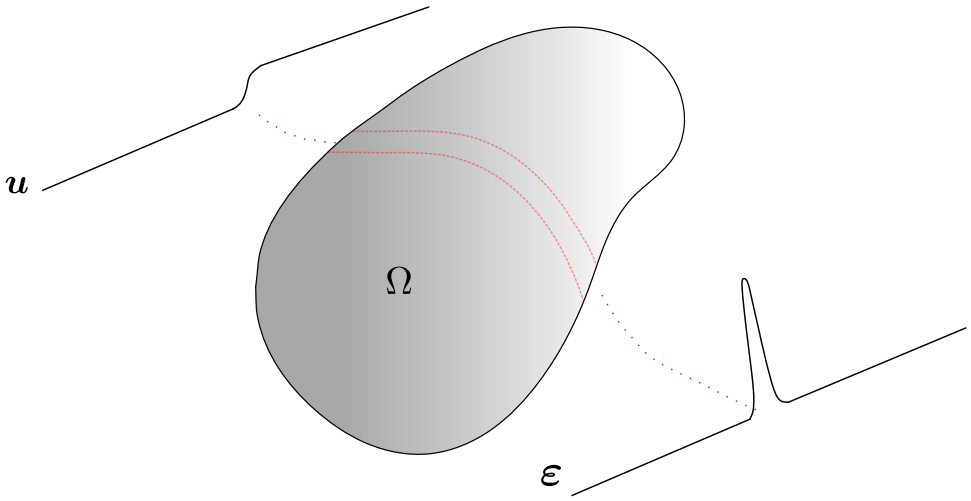

Figure 2.5 • Illustrative scheme of the kinematics in a regularized continuum

In these regularized continuum models, the strain and the displacement fields remain, *a priori*, continuous, as shown in Figure 2.5. Damage and strains concentrate in a finite zone and can take higher values in its center. Notice that this last tends to a Dirac distribution for a vanishing internal length, which corresponds, in the limit case, to a jump in the displacement field.

The concept of non-local continuum introduces the notion that the constitutive relation in a given point is a function of what occurs in the entire body. Neighborhood interactions are therefore used to enrich the continuum description by incorporatinghigher gradients or spatial averaging, based on a material characteristic length. From a thermodynamic viewpoint, the balance equations such as energy exchange, are no longer locally defined. The material state in a specific point is therefore a functional of the internal variables of all the points in its vicinity (Eringen, 2002).

Non-locality is a complex subject and more aspects may be covered. Some theories introduce only a weak or limited form of non-locality (Eringen (2002), Bažant and Jirásek (2002)), such as the gradient (explicit) ones, where interactions are limited to infinitesimal distances (Peerlings et al., 2004). In the following, non-local damage models will be presented in integral and implicit gradient forms, which are considered as strong non-local approaches, allowing long-range interactions. A visco-damage law could be also used, which is similar to apply a characteristic length by means of a rate effect (Bažant & Jirásek,

2002) and can be treated as a temporal regularization (Sluys & de Borst, 1994). From now on, the terms non-local and local will be used to referrer to continuum mechanics applications, but relations may exist between these theories and the general non-locality in physics (Eringen, 2002). Indeed, both approaches study long-range interactions and information exchange between material points.

> **Remark 2.4.** *Some notions of interactions between points in a continuum date back to the work of French researchers in molecular models for elasticity. Names, such as Poisson, Cauchy and Navier, formulated and discussed different aspects regarding models of matter. A detailed review on these theories is provided in (Capecchi et al., 2010). For instance, as described in the last cited work, Poisson had already postulated the existence of an internal length for molecular actions (the radius of molecular activity).*

3 Classic integral and gradient-enhanced non-local approaches

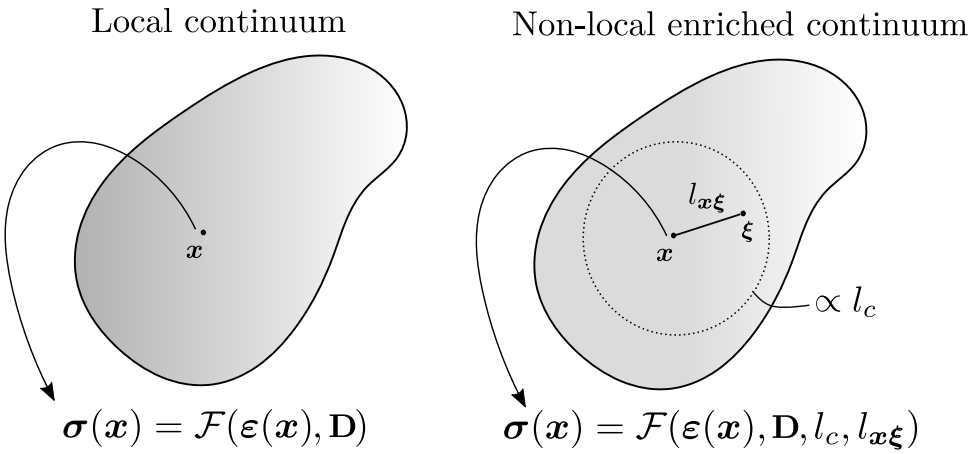

Figure 2.6 • Illustrative scheme on the difference between a local and a non-local damaged continuum

In local damage models, the constitutive relations are defined for every point $\boldsymbol{x} \in \Omega$, and $\boldsymbol{\sigma}(\boldsymbol{x}) = \mathcal{F}(\boldsymbol{\varepsilon}(\boldsymbol{x}), \mathbf{D}(\boldsymbol{x}))$ with $\mathcal{F}$ representing a functional (see Figure 2.6 left). In non-local damage models, the constitutive relation is enriched by considering what happens in the neighborhood, so one has $\boldsymbol{\sigma}(\boldsymbol{x}) = \mathcal{F}(\boldsymbol{\varepsilon}(\boldsymbol{x}), \mathbf{D}(\boldsymbol{x}), l_c, l_{\boldsymbol{x}\boldsymbol{\xi}})$, with $l_{\boldsymbol{x}\boldsymbol{\xi}} = ||\boldsymbol{x} - \boldsymbol{\xi}||$ denoting an euclidean distance between points $\boldsymbol{x}$ and $\boldsymbol{\xi}$. This last is often referred as an **interaction distance**.

3.1 Classic integral non-local approach (INL)

Pijaudier-Cabot and Bažant (1987) proposed a non-local integral damage theory, which replaces a local field $X(\boldsymbol{x})$ driving the damage evolution by a weighted average over the

whole domain Ω:

$$\bar{X}(\boldsymbol{x}) = \frac{1}{V_r(\boldsymbol{x})} \int_\Omega \phi(\boldsymbol{x}, \boldsymbol{\xi}, l_c) X(\boldsymbol{\xi}) dV_{\boldsymbol{\xi}} \quad \text{and} \quad V_r(\boldsymbol{x}) = \int_\Omega \phi(\boldsymbol{x}, \boldsymbol{\xi}, l_c) dV_{\boldsymbol{\xi}} \tag{2.7}$$

with $\bar{X}(\boldsymbol{x})$ denoting the corresponding non-local field and $\phi(\boldsymbol{x}, \boldsymbol{\xi}, l_c)$ is a weight function generally taken as the Gaussian distribution:

$$\phi(\boldsymbol{x}, \boldsymbol{\xi}, l_c) = \frac{1}{2\pi^{\frac{2}{3}} l_c^3} \exp\left(-\frac{||\boldsymbol{x} - \boldsymbol{\xi}||^2}{2l_c^2}\right) \tag{2.8}$$

for which $V_r(\boldsymbol{x}) = 1$ when $\Omega = \mathbb{R}^3$. A visualization of the Gaussian distribution on $\mathbb{R}^2$ is shown in figure Figure 2.7.

> **Remark 2.5.** *Another possibility is to use a bell-shaped function, which has a bounded support, instead of an unbounded one for the Gaussian function.*

The Gaussian weight function $\phi(\boldsymbol{x}, \boldsymbol{\xi}, l_c)$ is non negative and decreases with the distance $l_{\boldsymbol{x}\boldsymbol{\xi}}$. It is usual to use different weight functions for the averaging integral, most of them are modified versions of the common Gaussian one. For instance, a weight function used in (Krayani et al., 2009; Giry, 2011; Pijaudier-Cabot & Grégoire, 2014) is the Gaussian $\phi(\boldsymbol{x}, \boldsymbol{\xi}, l_c) = \exp\left(-4||\boldsymbol{x} - \boldsymbol{\xi}||^2 / l_c^2\right)$.

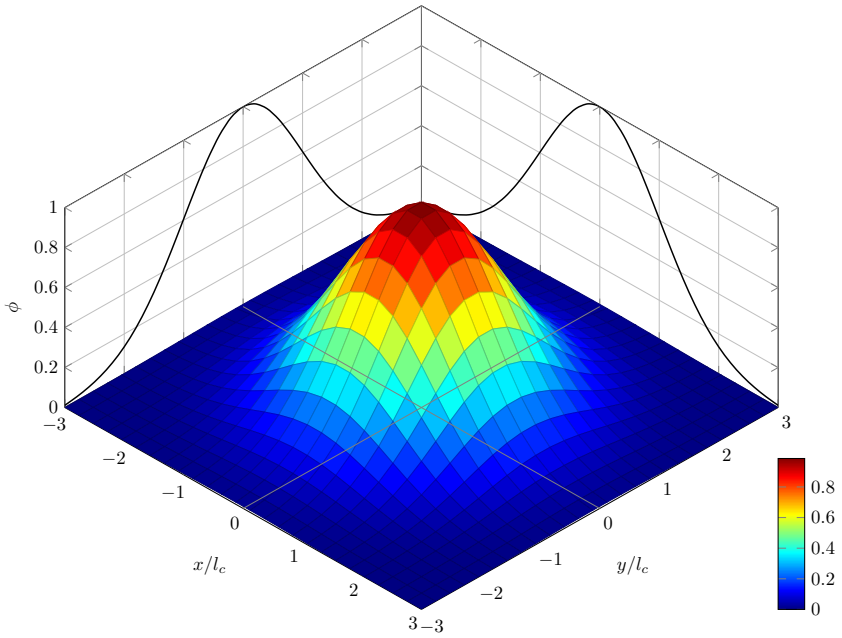

Figure 2.7 • Typical Gaussian weight function

One may notice that l_c defines also the significant part of the domain which will contribute to the resulting non-local field. In the (1D) case, statistical analyses show that $99,9\%$ of non-zero values of ϕ are obtained for the interval $[-3l_c, 3l_c]$.

Originally, Pijaudier-Cabot and Bažant (1987) introduced the non-local damage theory for averaging the thermodynamic force Y, so the scalar damage variable D is computed in function of $\bar{Y}$. Bažant and Pijaudier-Cabot (1988) proposed to average D itself so

the constitutive equations were computed with the non-local damage variable $\bar{D}$. Jirásek (1998) tested different ways of introducing non-locality in damage formulations, considering also the average of other variables. Particularly, it is shown that averaging D would lead to stress locking behaviors, what could not describe the crack initiation. In a 1D context, the author shows that formulations which average either Y or the strain ε are more capable to describe the degradation process.

In this thesis, the local equivalent strain field e is averaged and the evolution respects the modified damage criterion $f = \bar{e} - \kappa$, where e is substituted by its non-local counterpart $\bar{e}$. Direct substitution in Equation (2.7) gives the non-local equivalent strain field:

$$\bar{e}(\boldsymbol{x}) = \frac{1}{V_r(\boldsymbol{x})} \int_\Omega \phi(\boldsymbol{x}, \boldsymbol{\xi}, l_c) e(\boldsymbol{\xi}) dV_{\boldsymbol{\xi}} \tag{2.9}$$

where the definition of $V_r(\boldsymbol{x})$ from Equation (2.7) implies that the non-local integral does not change an uniform equivalent strain field.

In a 1D framework, the Gaussian weight function reads:

$$\phi(l_{x\xi}, l_c) = \frac{1}{\sqrt{2\pi} l_c} \exp\left(-\frac{l_{x\xi}^2}{2 l_c^2}\right) \tag{2.10}$$

where $l_{x\xi} = |x - \xi|$ is the Euclidean distance between points x and ξ. For a given characteristic length, Figure 2.8a shows two different Gaussian functions. The choice of the multiplying factor (4 or 0.5) can drastically change the size of the FPZ and give different results for the same material (*i.e.*, same characteristic length). The form of the damage profile is basically a combination between l_c and this multiplying factor. Moreover, Figure 2.8b shows the influence of the characteristic length on the form of the Gaussian weight function.

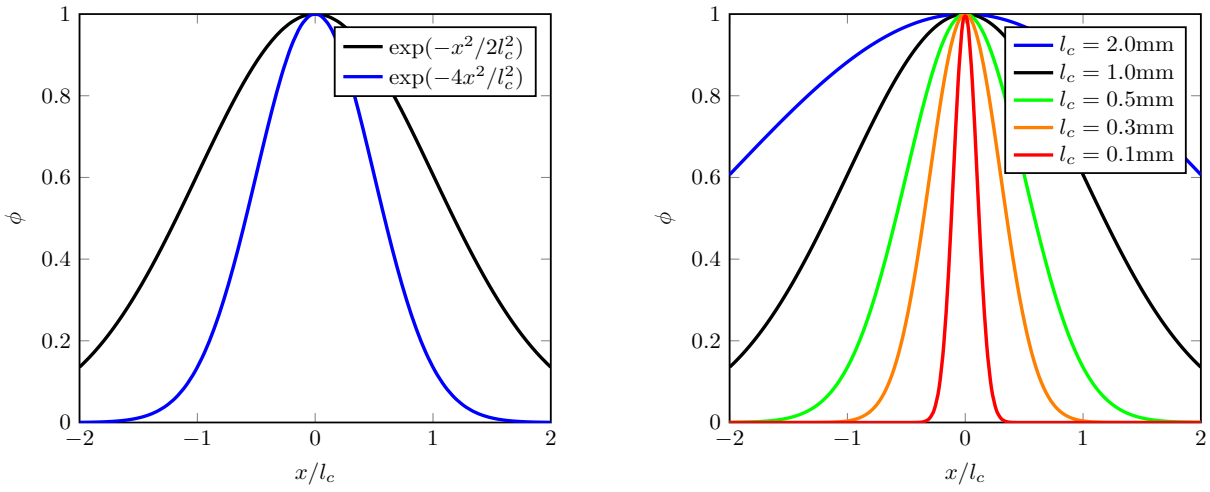

(a) Comparison between two different Gaussian weight functions

(b) Influence of the characteristic length on the shape of the function

Figure 2.8 • Different Gaussian functions and the role of the characteristic length.

3.2 Gradient-enhanced non-local damage (GNL)

Gradient-enhanced models were firstly introduced in plasticity theories with the contribution of several authors (e.g., see Aifantis (1984), Lasry and Belytschko (1988), Aifantis (1987), and Mühlhaus and Aifantis (1991)), where the main idea was to introduce high-order gradients of the equivalent plastic strain into the constitutive relations. These models were developed to overcome usual drawbacks in materials simulations, particularly in scenarios where localization phenomena induce mesh dependency, such as in shear band problems.

Inspired by these concepts, gradient-enhanced descriptions were also introduced in damage mechanics (e.g., Nedjar (1995), Peerlings et al. (1996a)), where high-order gradients (strain, internal variables, etc.) are also used in the constitutive relations. The objective was to capture the influence on the macroscopic behavior of important microscopic phenomena not well described in the usual local damage continuum mechanics. In fact, as mentioned before, the main hypothesis of continuum mechanics is to work with a REV of the material studied, which entails considering a finite volume size much bigger than the inhomogeneities of the micro structure. Within this framework, the constitutive relation may be defined locally for each point of the continuum. However, under high strain gradients, it is more appropriate to describe the behavior in a global manner, in which all the structure volume contributes to the stress-strain relation computed for a given point $\boldsymbol{x}$ (Bazant et al., 1984).

Gradient-enhanced damage approaches enable taking into account the spatial interaction between points (such as the influence of microstructure on the damage process) by introducing non-locality in the form of high-order gradients (Peerlings, 1999). Basically, gradient regularization can be achieved by using the conventional integral non-local theory, substituting the local equivalent strain in Equation (2.9) by its Taylor expansion:

$$e(\boldsymbol{\xi}) = e(\boldsymbol{x}) + \nabla e(\boldsymbol{x}) \cdot (\boldsymbol{\xi} - \boldsymbol{x}) + \frac{1}{2}\nabla^{(2)} e(\boldsymbol{x}) : (\boldsymbol{\xi} - \boldsymbol{x}) \otimes (\boldsymbol{\xi} - \boldsymbol{x}) + ... \tag{2.11}$$

where $\nabla^{(2)}$ is the second-order gradient, ":" is the double contraction product and $\otimes$ is the tensor product between two second-order tensors. Substituting Equation (2.11) in Equation (2.9) and neglecting high order terms, one has the approximation:

$$\bar{e}(\boldsymbol{\xi}) \approx e(\boldsymbol{x}) + \frac{\nabla e(\boldsymbol{x})}{V_r(\boldsymbol{x})} \cdot \int_\Omega \phi(\boldsymbol{x}, \boldsymbol{\xi}, l_c)(\boldsymbol{\xi} - \boldsymbol{x}) dV_{\boldsymbol{\xi}} + \frac{\nabla^{(2)} e(\boldsymbol{x})}{2V_r(\boldsymbol{x})} : \int_\Omega \phi(\boldsymbol{x}, \boldsymbol{\xi}, l_c)(\boldsymbol{\xi} - \boldsymbol{x}) \otimes (\boldsymbol{\xi} - \boldsymbol{x}) dV_{\boldsymbol{\xi}} \tag{2.12}$$

As previously discussed, the Gaussian distribution is commonly taken as the weight function $\phi(\boldsymbol{x}, \boldsymbol{\xi}, l_c)$. By computing the integrals in Equation (2.12) over $\mathbb{R}^3$, one obtains the following explicit gradient equation:

$$\bar{e}(\boldsymbol{x}) = e(\boldsymbol{x}) + c\nabla^2 e(\boldsymbol{x}) \tag{2.13}$$

where the first integral of Equation (2.12) vanishes due to the isotropy of the Gaussian function averaging an odd function. The term ∇^2 is the Laplacian operator and the

gradient coefficient c is given by (Peerlings, 1999):

$$c_i = c = \frac{1}{2V_r(\boldsymbol{x})} \int_\Omega \phi(\boldsymbol{x}, \boldsymbol{\xi}, l_c)(\xi_i - x_i)^2 dV_{\boldsymbol{\xi}}. \tag{2.14}$$

In fact, considering the isotropy of the Gaussian function when integrating over $\mathbb{R}^3$, the second integral of Equation (2.12) equals $c\mathbf{I}$, where $\mathbf{I}$ is the second-order identity tensor. In this case, $\nabla^{(2)}e(\boldsymbol{x}) : c\mathbf{I} = c\nabla^2 e(\boldsymbol{x})$ and $c = l_c^2/2$ for the Gauss function introduced in Equation (2.8).

One may notice that normally $\Omega \subset \mathbb{R}^3$, as the structure is finite and has its own boundaries. In this case, the first integral does not vanish while the coefficient c is also different. Nevertheless, it is more important to verify that the gradient-enhanced non-local models are useful as an approximation of the conventional integral one (Peerlings et al., 2001).

Solving Equation (2.13) by applying a variational formulation followed by a Galerkin approach leads to $\mathcal{C}^1$ continuity requirements for the displacement shape functions (as e is a function of the displacement field). From a numerical viewpoint, the explicit gradient damage model is not suitable to be used with usual linear shape functions. A more numerical friendly approach is obtained by differentiating two times the Equation (2.13) and neglecting high order terms, which results in the implicit gradient-enhanced damage equation (Peerlings et al., 1996a):

$$\bar{e}(\boldsymbol{x}) - c\nabla^2 \bar{e}(\boldsymbol{x}) = e(\boldsymbol{x}) \tag{2.15}$$

which only requires $\mathcal{C}^0$ displacement shape functions in a finite element context. The global problem consists therefore in finding a couple $(\boldsymbol{u},\bar{e})$ solution of the equilibrium equation and the Helmholtz-type differential equation. This will be solved in the following sections by a finite element coupled problem, as introduced in (de Borst et al., 1995) and Peerlings et al. (1996a).

> **Remark 2.6.** *An exact equivalence between the implicit gradient formulation and the integral non-local one is derived by Peerlings et al. (2001), by means of a Green function $G(\boldsymbol{x};\boldsymbol{y})$ solution of a similar Helmholtz problem, replacing $e(\boldsymbol{x})$ by the Dirac distribution:*
>
> $$G(\boldsymbol{x};\boldsymbol{y}) - c\nabla^2 G(\boldsymbol{x};\boldsymbol{y}) = \delta(\boldsymbol{x};\boldsymbol{y}) \tag{2.16}$$
>
> *so the non-local equivalent strain field is obtained by:*
>
> $$\bar{e}(\boldsymbol{x}) = \int_\Omega G(\boldsymbol{x};\boldsymbol{y}) e(\boldsymbol{y}) dV_{\boldsymbol{y}} \tag{2.17}$$
>
> *Thus, the implicit gradient approach can be seen as the non-local integral approach with a Green weighting function.*

A comparison of integral non-local models and explicit/implicit gradient ones can be found in (Peerlings et al., 2001). It demonstrates that the explicit gradient formulation allows only interaction between points at infinitesimal distances. Consequently, this

formulation and other high-order gradient ones are classified as weakly non-local models (Bažant & Jirásek, 2002). From a mathematical perspective, they can even be regarded as local (Peerlings et al., 2001). Conversely, the implicit gradient-enhanced damage model developed in (Peerlings et al., 1996a) is considered as a strongly non-local model (Bažant & Jirásek, 2002). This classification arises from its equivalence to the integral type ones. Indeed, spatial interactions are not restricted to an infinitesimal domain, but can occur within the entire structure. Additionally, while the explicit gradient approach presents an unbounded wave velocity, both the implicit and the integral non-local models show a limit which is the elastic wave velocity (Peerlings et al., 2001).

> **Remark 2.7.** *The solution of Equation* (2.15) *requires the introduction of a boundary condition. In the variational framework of finite element analysis, the literature (e.g., Peerlings et al. (1996a), Peerlings et al. (1998), and Geers et al. (1998)) often refers to a* ***natural*** *zero flux condition, i.e.,* $\nabla \bar{e} \cdot \boldsymbol{n} = 0$ *on* $\partial\Omega$*, with* $\boldsymbol{n}$ *denoting the outward normal to the boundary* $\partial\Omega$*. Peerlings et al. (1998) showed that this leads to equal averages of* $\bar{e}$ *and* e *over the domain. However, the physical interpretation of the homogeneous Neumann boundary condition remains an open question(Peerlings et al., 1996b, 2004; Simone, 2007).*

3.3 Comments on bifurcation and regularization in non-local continuum

Convergence with respect to the mesh can be obtained in finite element simulations when a characteristic length is introduced in the formulation (see for instance Pijaudier-Cabot and Bažant (1987) and Peerlings et al. (1996a)). However, providing a mathematical proof of regularization for such models is a challenging task and requires a detailed localization analysis. Bifurcation analysis in non-local or enriched continuum were conducted by many authors.

Pijaudier-Cabot and Benallal (1993) studied strain localization and bifurcation in quasi-statics and dynamics for a non-local continuum of integral-type. They derived the expression of a pseudo-acoustic tensor, containing the wavelength of the bifurcation mode by the means of the Fourier transform of the weighting function. Based on a geometric solution, they showed that the bifurcation condition in a local continuum is a lower bound of the non-local one. Contrarily to the local continuum, only one wavelength, proportional to the characteristic length, is allowed at bifurcation in a non-local one. Moreover, wave propagation is dispersive in a such medium.

Sluys and de Borst (1994) studied bifurcation in gradient-dependent mediums through wave propagation and dispersion analysis in one-dimensional bars. They analyzed the characteristics of the resulting wave equation, highlighting that the problem is well-posed in a gradient-dependent medium. While the wave speed is always imaginary in local classic models, it becomes real for most of the wavelengths in the case with gradient enhancement. Other authors developed similar studies for different gradient and integral non-local models, leading to similar conclusions (Peerlings et al., 1996b, 2001; Askes &

Sluys, 2002; Pijaudier-Cabot et al., 2004; Di Luzio & Bažant, 2005; Comi et al., 2007).

Nonetheless, it is important to notice that, in general, these analyses consider the classical (but strong) hypothesis of a linear comparison solid (Hill, 1958). In other words, the linearized rate equilibrium problem is considered, so all the regions of the continuum have the same tangent stiffness at the onset of softening. These aspects will be further studied in Chapter 3 and Chapter 4.

4 Non-local models with evolving interactions

In spite of the agreement that continuum damage should be non-local, the classical regularized models are not capable to reproduce the entire degradation process occurring in quasi-brittle materials. For instance, damage attraction on the boundary has been reported (Krayani et al., 2009) and leads to non physical spalling failures. Simone et al. (2004) showed that classical integral or implicit gradient theories fail to describe crack initiation, specially near strong variations on the strain field, which was not related to boundary effects, for example. Additionally, when strain localization occurs, the coalescence of micro-cracks into a macro-crack should induce a discontinuity in the displacement field. Classic models do not enable describing such a transition, as damage is diffused in a large zone. Thus, despite regularizing the response to recover objectivity, non-local classical damage models exhibit physical inconsistencies and therefore can not accurately describe all physical phenomena related to damage.

Bažant (1991) investigated the interaction between micro cracks and showed that for the case where damage is not sufficiently small, the weight function should depend on the stress state in the vicinity of a given point. This implies that non-local interactions must evolve as damage grows, rather than remaining isotropic and constant throughout the fracture process. Geers et al. (1998) showed that the classical constant gradient damage model, fails when treating highly damaged zones. To address this, they proposed a strain-based transient-gradient damage model, considering that the gradient parameter c ($\propto l_c$) evolves in function of the local strain state. This simple assumption yields a damage profile that does not spread over a zone upon localization, thus being consistent with the mechanical material response. Giry et al. (2011) proposed a stress-based non-local damage model which allows the internal (or characteristic) length to evolve in function of the stress state. The internal length is computed by applying an influence factor depending on the principal stresses of a neighborhood point. The evolution of non-local interactions was also proposed in many other damage models, based on the stress, strain, damage or the micro structure (*e.g.*, Bažant (1994), Pijaudier-Cabot et al. (2004), Desmorat and Gatuingt (2007b), Pijaudier-Cabot and Dufour (2010), Nguyen (2011), Rojas-Solano et al. (2013), Desmorat et al. (2015b), Poh and Sun (2017), Vandoren and Simone (2018), Nguyen et al. (2018), Jirásek and Desmorat (2019), and Negi et al. (2020)).

Although not yet clearly clarified, the influence of the fracture process in non-local interactions needs to be taken into account. The goal is to fully simulate the physical behavior from diffused micro cracks to a fully localized macro crack. In this context, the non-local damage models should overcome the following drawbacks: damage initiation,

damage diffusion and boundary effects (these points are further explained in the remainder of this manuscript). In the following sections, a few of the previously mentioned approaches are described, giving attention to the so-called eikonal approach (Desmorat et al., 2015b).

4.1 Strain-based gradient-enhanced

From the observation that the GNL approach leads to the growth of a damage band that is not physical, Geers et al. (1998) proposed one of the earliest evolving (isotropic) interaction models, where the gradient parameter varied with strain. The resulting modified differential equation is as follows:

$$\bar{e} - \zeta(e)\nabla^2\bar{e} = e \tag{2.18}$$

where $\zeta(e)$ is a transient gradient parameter (the gradient activity), defined as:

$$\zeta(e) = \begin{cases} c\left(\frac{e}{e_\zeta}\right)^{n_\zeta} & \text{if } e \leqslant e_\zeta \\ c & \text{if } e > e_\zeta \end{cases} \tag{2.19}$$

Here, e_ζ and n_ζ denote material parameters. A simplified version of this model, which is more numerical friendly, was proposed by Saroukhani et al. (2013). This approach enables better modeling of the transition behavior between CDM and FM, as the damage band does not spread upon localization and the gradient activity converges to a discontinuity.

4.2 Non-local stress-based (NLSB)

The main idea of the NLSB model is to take into account the influence of the stress field when computing the weight function. This is done by introducing an influence factor, denoted as ρ, into the non-local regularization, leading to the following modified weight function (Giry et al., 2011):

$$\phi(\boldsymbol{x}, \boldsymbol{\xi}, l_c, \rho_{\text{fac}}) = \exp\left(-4\left(\frac{||\boldsymbol{x} - \boldsymbol{\xi}||}{\rho_{\text{fac}} l_c}\right)^2\right) \tag{2.20}$$

where ρ_{fac} is a function of the stress field and is defined as $\rho_{\text{fac}} = \rho_{\text{fac}}(\boldsymbol{x}, \sigma_i(\boldsymbol{\xi}))$ with σ_i denoting the principal stresses. In the general case, $\rho_{\text{fac}}(\boldsymbol{x}, \sigma_i(\boldsymbol{\xi}))$ is the radial coordinate of an ellipsoid associated with the stress state of a nearby point $\boldsymbol{\xi}$. Thus, this model naturally addresses boundary effects issues, given that the stress state is considered to modify non-local interactions in the presence of a free boundary.

In the 1D case, the influence factor is defined as:

$$\rho_{\text{fac}}(\xi) = \frac{|\sigma(\xi)|}{f_t} \tag{2.21}$$

where $\sigma(\xi)$ is the stress computed for the point ξ and f_t is the tensile strength of the material. According to this definition, the influence factor $\rho_{\text{fac}}(\xi)$ is equal to zero when ξ belongs to a free boundary, corresponding to the zero normal stress condition. Consequently, the weight computed between a given point inside the domain and another one on the free edge is null (*i.e.*, no interactions are modeled). Moreover, if $\rho_{\text{fac}}(\xi) = 1$, the classical INL formulation is recovered.

4.3 Stress-based gradient-enhanced damage

Vandoren and Simone (2018) proposed a stress-based anisotropic gradient-enhanced model that builds upon the integral version introduced by Giry et al. (2011) to account for evolving internal interactions based on the stress state in the medium. The following Helmholtz differential equation was proposed:

$$\bar{e} - \nabla \cdot (\mathbf{c} \cdot \nabla \bar{e}) = e \tag{2.22}$$

where $\mathbf{c}$ is a second-order tensor accounting for the influence of the anisotropic stress state on the interactions. Once again, Equation (2.22) needs to be supplemented by a modified Neumann boundary condition, which reads $(\mathbf{c} \cdot \nabla \bar{e}) \cdot \boldsymbol{n} = 0$. Two different models can be derived, depending on the definition of tensor $\mathbf{c}$ which can be based on either the principal stress components or the equivalent stress. In the first case, one has:

$$\mathbf{c} = \mathbf{R} \left(\frac{\sigma_i}{f_t} \boldsymbol{s}_i \otimes \boldsymbol{s}_i \right) \mathbf{R}^\top \tag{2.23}$$

where $\boldsymbol{s}_i$ is the stress eigenvector, f_t is the material strength, and $\mathbf{R}$ is the rotation tensor from the basis of principal stress directions to the external basis in which $\nabla \bar{e}$ is written. Additional details can be found in the cited work.

4.4 Localizing gradient damage model

A localizing gradient damage model was proposed by Poh and Sun (2017). Developed within the framework of the micromorphic theory, this model modifies the extended thermodynamic potential proposed by Peerlings et al. (2004) and Forest (2009) to account for damage-dependent non-local interactions. The resulting modified Helmholtz-type differential equation reads:

$$\bar{e} - \nabla \cdot (gc \nabla \bar{e}) = e \tag{2.24}$$

where $g(D)$ is an exponentially decreasing function of the scalar damage variable D, given by:

$$g(D) = \frac{(1 - R) \exp(-\eta_0 D) + R - \exp(-\eta_0)}{1 - \exp(-\eta_0)} \tag{2.25}$$

with η_0 denoting a material parameter and $R > 0$ being a small parameter accounting for residual non-local interactions. It is chosen such that $g(0) = 0$ and $g(D \to 1) = R$. A similar formulation that couples the effects of damage and stress on non-local interactions was introduced by Negi et al. (2020).

4.5 Internal time non-local approach

In the INL model introduced in Section 3.1, points interact through an Euclidean distance $l_{\boldsymbol{x}\boldsymbol{\xi}}$ normalized by the characteristic length l_c. The basic idea of considering an internal time (Desmorat & Gatuingt, 2007b) instead of a distance is to naturally take into account the influence of damage in the evolution of non-local interactions. The key modification is to consider a Gaussian weight function $\phi = \phi(\tau_{\boldsymbol{x}\boldsymbol{\xi}}, \tau_c)$, where $\tau_{\boldsymbol{x}\boldsymbol{\xi}}$ is the information time

propagation and τ_c the characteristic (or internal) time. Thus, the classical Euclidean distance between points $\boldsymbol{x}$ and $\boldsymbol{\xi}$ is replaced by the propagation time of an elastic wave in the continuum, which varies based on damage.

The material elastic wave speed c_0 is proportional to the square root of the Young's modulus (E), which is reduced to the effective modulus $\tilde{E} = (1 - D)E$ when damage occurs. Therefore, for a homogeneously damaged material ($D = D_0$), the information propagation time is defined as:

$$\tau_{\boldsymbol{x}\boldsymbol{\xi}} = \frac{||\boldsymbol{x} - \boldsymbol{\xi}||}{\tilde{c}} = \frac{l_{\boldsymbol{x}\boldsymbol{\xi}}}{c_0\sqrt{1 - D_0}} \quad \text{and} \quad \frac{\tau_{\boldsymbol{x}\boldsymbol{\xi}}}{\tau_c} = \frac{l_{\boldsymbol{x}\boldsymbol{\xi}}}{l_c\sqrt{1 - D_0}} = \frac{\tilde{l}_{\boldsymbol{x}\boldsymbol{\xi}}}{l_c} \tag{2.26}$$

where $\tilde{c}$ is the effective wave speed affected by damage.

According to Equation (2.26), if damage occurs, the time required to propagate information (interaction) between points increases, and tends to infinity when damages tends to the unity. Furthermore, one has:

$$\frac{\tau_{\boldsymbol{x}\boldsymbol{\xi}}}{\tau_c} = \frac{l_{\boldsymbol{x}\boldsymbol{\xi}}}{l_c\sqrt{1 - D_0}} = \frac{\tilde{l}_{\boldsymbol{x}\boldsymbol{\xi}}}{l_c} \tag{2.27}$$

where $l_c = \tau_c c_0$ and $\tilde{l}_{\boldsymbol{x}\boldsymbol{\xi}}$ is an effective distance which increases with damage (Desmorat et al., 2015b). For an undamaged material, the internal time is thus equivalent to the classical non-local integral model. Similarly, the internal time approach can be seen as a non-local damage model with evolving internal length $\tilde{l}_c = l_c\sqrt{1 - D_0}$ (Desmorat & Gatuingt, 2007b; Desmorat et al., 2015b). Pijaudier-Cabot and Dufour (2010) proposed a similar non-local model, using an attenuation function to describe the influence of damage on interactions.

4.6 Eikonal non-local approach (ENL)

The ENL damage model is a geometric extension of the non-local internal time model introduced by Desmorat and Gatuingt (2007b). Desmorat et al. (2015b) proposed to search a solution to the wave propagation equation based in the Wentzel–Kramers–Brillouin (WKB) approximation. The WKB method is used mostly in quantum mechanics to give an approximated solution of the Schrödinger equation. Here, it is applied to high-frequency (*i.e.*, high wave number and small wave length) waves propagating in a damaged medium, which corresponds to the onset of localization introduced before and the limitations of local models.

As derived in (Desmorat et al., 2015b) and further detailed in (Marconi, 2022) following the principal of virtual work, the expression of the displacement field can be written as:

$$\boldsymbol{u}(\boldsymbol{x}, t) = \boldsymbol{u}_0(\boldsymbol{x}) \exp\left[i\left(k_0 S(\boldsymbol{x}) - \omega t\right)\right] \tag{2.28}$$

where $\boldsymbol{u}_0(\boldsymbol{x})$ is the wave amplitude, $\kappa_0 = \omega/c_0$ is the wave number, ω the angular frequency, and $S(\boldsymbol{x})$ is the eikonal function. In the case of isotropic damage, substituting this expression in the wave equation leads to the following so-called eikonal equation (see Desmorat et al. (2015b) for a detailed development):

$$\|\nabla S\| = \frac{1}{\sqrt{1 - D}} \tag{2.29}$$

As highlighted by Desmorat et al. (2015b), S is equivalent to a signed distance $\tilde{l}$, if one considers the initial wave front as the zero level set of function S. For instance, in a 1D framework, Equation (2.29) reduces to:

$$d\tilde{l} = \frac{dx}{\sqrt{1-D}} \tag{2.30}$$

which defines a field of damage-dependent effective distances. The Euclidean distance $l_{\boldsymbol{x}\boldsymbol{\xi}}$ between points $\boldsymbol{x}$ and $\boldsymbol{\xi}$ is therefore scaled by the factor $1/\sqrt{1-D}$, as already observed in the internal approach in Equation (2.26). Therefore, the effective distances increase with damage and can eventually tend to infinity in the limit case where $D \to 1$.

In the generic case of anisotropic damage modeled by a second-order tensor, the eikonal equation reads:

$$\nabla\tilde{l} \cdot \mathbf{g}^{-1} \cdot \nabla\tilde{l} = 1 \tag{2.31}$$

where $\mathbf{g} = (\mathbf{I} - \mathbf{D})^{-1}$ is a damage-dependent Riemannian metric. Therefore, the effective distances $\tilde{l}$ are geodesics in a space curved by damage. Notice that the above equations remains valid for the case of isotropic damage, so one retrieves Equation (2.29) with $\mathbf{g} = \mathbf{I}/(1-D)$. For an undamaged medium, the Riemannian metric reduces to a Euclidean one, *i.e.*, $\mathbf{g} = \mathbf{I}$ and one has $\tilde{l}_{\boldsymbol{x}\boldsymbol{\xi}} = l_{\boldsymbol{x}\boldsymbol{\xi}}$.

Further details on this approach are provided in Chapter 4, where an independent derivation of the method following the micromorphic approach is presented.

Eikonal non-local integral (ENLI). In its integral form, the isotropic damage ENLI formulation proposes the following weighting function when computing the non-local equivalent strain:

$$\phi(\boldsymbol{x}, \boldsymbol{\xi}, l_c, D) = \exp\left(-4\frac{\tilde{l}^2_{\boldsymbol{x}\boldsymbol{\xi}}}{l_c^2}\right) \tag{2.32}$$

where the damage-dependent effective distances field replaces the Euclidean one. Thus, the general theoretical framework of integral non-local theories is preserved.

As the distances increase with damage, points separated by a highly damaged zone become considerably far apart from each other and the non-local interactions are reduced through Equation (2.32). A tendency toward the transition between CDM and FM is naturally considered in such an approach, as the non-local interactions vanish upon localization (*i.e.*, a new traction-free boundary is created).

The computation of the geodesic interaction distances requires specific algorithms, such as the Fast Marching Method (Sethian, 1996). The first numerical implementation of this method in a finite element context was proposed by Rastiello et al. (2018b). Additionally, Thierry et al. (2020a) and Jirásek and Desmorat (2019) conducted studies on the regularization properties of the ENLI approach in 1D settings. Further studies regarding its regularization properties and behavior near free boundaries are provided in (Ribeiro Nogueira et al., 2022a). These aspects are also detailed in Chapter 3.

Figure 2.9 depicts an example of effective (geodesic) interactions distances (Rastiello et al., 2018b) field compared to the wave propagation obtained by the internal time approach in a notched specimen (Desmorat & Gatuingt, 2007b). For the ENL case,

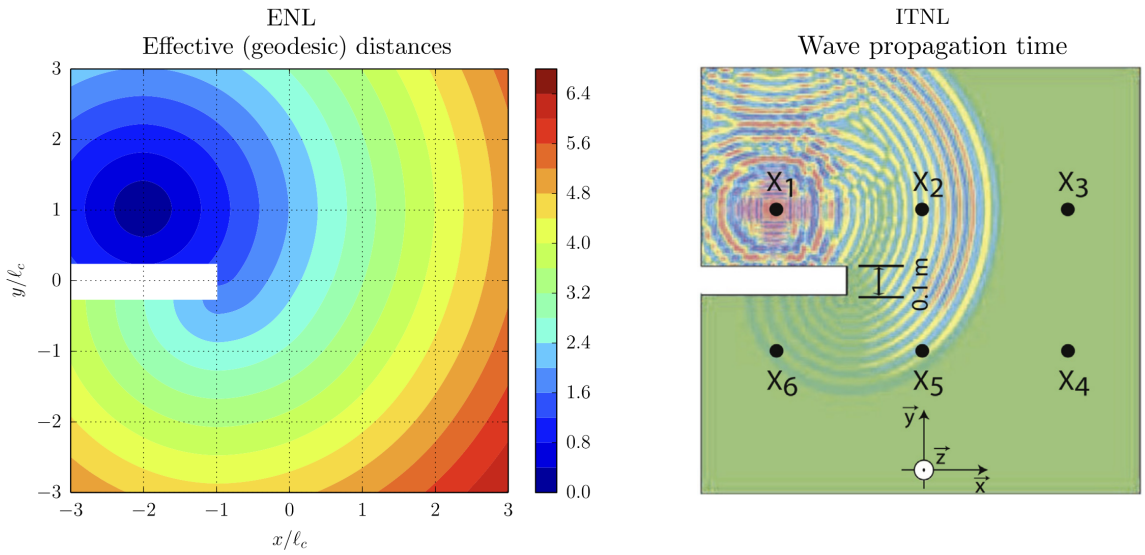

Figure 2.9 • Illustration of geodesic distances (left) obtained by the Eikonal approach and the corresponding wave propagation (right) obtained by the internal time approach (taken from Rastiello et al. (2018b)).

the notch is represented by a completely damaged zone. This illustration shows a good agreement between the effective distances and the wave propagation, highlighting that the Eikonal solution represents a geometric approximation of the wave propagation.

One of the disadvantages of the use of such an approach in finite element computations is the fact that the interaction distances field needs to be computed for every iteration at every Gauss point by using very fine Fast-Marching grids for achieving accurate results and a robust implementation (Rastiello et al., 2018b). The extension of this method to anisotropic damage and its applications at large-scale analysis, eventually in 3D, can become rapidly prohibitive. This is also true for the internal time approach.

Eikonal gradient-enhanced (ENLG). Following the derivation introduced by Peerlings et al. (1996a), a gradient-enhanced version of the ENL approach was proposed in (Desmorat et al., 2015b). The differential problem for calculating the non-local variable $\bar{e}$ that controls damage evolution is:

$$\bar{e} - \frac{c}{\sqrt{\det \mathbf{g}}} \nabla \cdot \left(\sqrt{\det \mathbf{g}}\, \mathbf{g}^{-1} \cdot \nabla \bar{e} \right) = e \qquad \Omega \qquad (2.33)$$

$$\mathbf{g}^{-1} \cdot \nabla \bar{e} \cdot \boldsymbol{n} = 0 \qquad \partial\Omega \qquad (2.34)$$

where $\det \mathbf{g}$ must stay positive, according to Equation (5.1). Notice that the GNL model by Peerlings et al. (1996a) is retrieved by considering an Euclidean metric $\mathbf{g} = \mathbf{I}$.

The key concept is that anisotropic behavior in quasi-brittle materials is induced by damage, while the medium is initially considered isotropic. The induced anisotropy is incorporated through the ENLG model, where non-local interactions naturally evolve from isotropic to anisotropic based on the damage-dependent Riemannian metric.

An analysis on its regularizing properties and boundary effects in a 1D framework is provided in (Ribeiro Nogueira et al., 2022a) and further detailed in Chapter 3. Marconi

(2022) conducted two-dimensional computations utilizing an ENLG regularized isotropic damage model and investigated the coupling between damage and plasticity within a one-dimensional framework. Recently, Ribeiro Nogueira et al. (2024a) proposed a robust thermodynamics framework based on the Micromorphic Media Theory (Forest, 2009) to derive the eikonal formulation. Using concepts from differential geometry, the authors independently derived (5.1), obtained the boundary condition (5.2) (a detail not covered by Desmorat et al. (2015b)), characterized energy dissipation, and verified the Clausius-Duhem inequality.

> **Remark 2.8.** *Given its numerical friendly aspect, as well as its capability to describe anisotropic evolving interactions coupled with anisotropic damage, this is the approach that is further studied and developed in this thesis.*

5 Other regularization approaches

Other regularization approaches exist, and some of them merit a few comments here due to the similarities with the main approach exploited in this thesis. The micromorphic framework, in particular, will be given special attention in Chapter 4.

Apart from the recent developments in (Masseron et al., 2023), its is worth mentioning that all the regularization approaches mentioned in the following are typically restricted to applications in the case of isotropic damage.

5.1 Phase-field

The phase-field approach can find its origins in the variational approach to brittle fracture (Francfort & Marigo, 1998), which was numerically implemented and further discussed in (Bourdin et al., 2000). The main idea is to regularize a sharp crack by introducing a diffuse and smooth scalar phase-field variable φ, which equals 1 in the crack surface and decays to zero in its surroundings. In a 1D setting, the diffusive variable can be written as a decaying exponential $\varphi = \exp\left(-|x|/l_0\right)$, which is solution of the differential equation (Miehe et al., 2010):

$$\varphi - l_0^2 \frac{d^2\varphi}{dx^2} = 0 \tag{2.35}$$

with l_0 denoting a length-scale parameter. The generalization of this equation to a multi-dimensional framework gives:

$$\varphi - l_0^2 \nabla^2 \varphi = 0 \quad \text{in } \Omega \qquad \Gamma_{l_0} = \int_\Omega \gamma(\varphi, \nabla\varphi)\, dV = \int_\Omega \frac{1}{2l_0} \left(\varphi^2 + l_0^2 \nabla\varphi \cdot \nabla\varphi\right) dV \tag{2.36}$$

where γ is the so-called crack surface density function and Γ_{l_0} is the regularized crack functional, which can be seen as the crack surface (Miehe et al., 2010). The gradient equation on φ can be obtained by a variational principle from the crack functional.

A particular form of the total energy functional can be written as:

$$\mathcal{E}(\boldsymbol{u}, \varphi) = \frac{1}{2}\int_\Omega (1-\varphi)^2 \boldsymbol{\varepsilon} : \mathbb{E} : \boldsymbol{\varepsilon}\, dV + \frac{1}{2}\int_\Omega \frac{G_c}{l_0} \left(\varphi^2 + l_0^2 \nabla\varphi \cdot \nabla\varphi\right) dV \tag{2.37}$$

where the second term stands for the volumetric regularized version of the energy dissipated upon the creation of crack surface, with G_c denoting the critical fracture energy. The left-hand side of Equation (2.37) stands for the elastic energy degraded by the term $(1-\varphi)^2$. The phase-field problem consists in finding a solution couple $(\boldsymbol{u},\varphi)$ that minimizes the total energy functional under the work of external forces, following the so-called alternating minimization approach. Therefore, from a purely pragmatic point of view, the final problem is very similar to gradient-enhanced non-local damage models described earlier. A comparison between these approaches is presented in (de Borst & Verhoosel, 2016) and an extensive review on phase-field methods can be found in (Wu et al., 2019).

It is important to notice that the phase-field variable is, in principle, not related to the damage variable in the sense of CDM. The classic degradation term $(1-\varphi)^2$, for instance, induces a stress-strain relationship different from the one derived for CDM. Moreover, as highlighted by Bažant et al. (2022b), l_0 is not linked to a characteristic length intrinsic to a material, but mainly serves as a regularization parameter. Thus, the overall approach needs to be modified and enriched with CZM techniques to address realistic quasi-brittle fracture and size effect (see for instance Feng and Wu (2018)). The application of phase-field models to induced anisotropy in quasi-brittle materials is still an open question, specially if one seeks to model its influence in the degradation of elasticity properties.

> **Remark 2.9.** *Given that gradients of the phase-field variable are considered in the regularized form of the fracture energy, the phase-field approach is essentially non-local.*

5.2 Thick level set (TLS)

Introduced by Moës et al. (2011) and further developed in (Bernard et al., 2012; Parrilla Gómez et al., 2015; Salzman et al., 2016; Moreau et al., 2017), the idea of the TLS approach is that the evolution of the damage variable D follows the motion of a level set ϕ_l, which represents a distance between the boundary of an undamaged zone and a damaged one, while respecting:

$$\begin{cases} D(\phi_l) = 0 & \text{if } \phi_l \leqslant 0 \\ D'(\phi_l) \geqslant 0 & \text{if } 0 \leqslant \phi_l \leqslant l_c \\ D(\phi_l) = 1 & \text{if } \phi_l \geqslant l_c \end{cases} \tag{2.38}$$

where l_c is a characteristic length defining the damaged zone.

The free-energy Helmholtz potential of this approach is the same as the one of local isotropic damage models (see Equation (1.40)), which need to be regularize to obtain meaningful responses. The regularizing non-local character of TLS model entirely relies on the evolution of damage in function of the level set under the condition $\|\nabla\phi_l\| = 1$ (see Cazes and Moës (2015) for further details).

A total energy functional can also be written for such an approach (Cazes & Moës,

2015):

$$\mathcal{E}(\boldsymbol{u}, \phi_l) = \frac{1}{2}\int_\Omega (1 - D(\phi_l))\boldsymbol{\varepsilon} : \mathbb{E} : \boldsymbol{\varepsilon}\, dV + \int_\Omega Y_c D(\phi_l) dV \tag{2.39}$$

where Y_c is a material parameter. The stationarity with respect to ϕ_l gives the evolution criteria of the damage front. For instance, a criterion proposed by Bernard et al. (2012) postulates that the front moves when $\bar{Y}$ reaches $\bar{Y}_c$, which are the non-local counterparts (weighted average) of Y and Y_c.

In this approach, the damage definition in the sense of CDM is not lost. However, applications to anisotropic damage behavior may become arduous, as one should define the evolution of a damage tensor, and not a single scalar variable, in function of the level set.

5.3 Lip-field approach

Moës and Chevaugeon (2021) introduced the Lipschitz regularization for softening in a 1D setting. Recently, Chevaugeon and Moës (2022) presented 2D numerical implementations of this method applied to quasi-brittle fracture. The main idea of this method is to impose a Lipschitz regularity on the damage field, defined by the Lipschitz constant $\text{lip}(D)$ as the minimum value M, so that:

$$|D(\boldsymbol{x}) - D(\boldsymbol{\xi})| \leqslant M \text{dist}(\boldsymbol{x}, \boldsymbol{\xi}) \quad \forall\, \boldsymbol{x}, \boldsymbol{\xi} \in \Omega \tag{2.40}$$

where $\text{dist}(\boldsymbol{x}, \boldsymbol{\xi})$ is the minimal length path between $\boldsymbol{x}$ and $\boldsymbol{\xi}$. This enforces the non-local character of the method, as the damage variable depends on its neighbors. The regularization space is defined as:

$$\mathcal{L} = \{D \in L^\infty \;\mid\; \text{lip}(D) \leqslant 1/l'\} \tag{2.41}$$

with l' denoting the regularizing length, equivalent to an internal length. The solution of the coupled problem follows an alternating minimization procedure under constraints. Numerically, an additional lip-mesh is needed to link the integration points of the finite elements where the damage field is defined. As shown in (Moës & Chevaugeon, 2021; Chevaugeon & Moës, 2022), this approach is suitable to model the transition between CDM and FM, since the damage band does not spread upon localization. This is a characteristic similar to non-local damage models with evolving internal length.

Finally, given that the Lipschitz constraint is imposed for the damage field, there is no need to penalize the damage behavior by adding its gradients to the energy functional. The potential is purely local, while the non-locality is brought into play by the regularity constraint. First results concerning the extension of this regularization approach to anisotropic damage behaviors are provided by Masseron et al. (2023).

5.4 Peridynamics

Introduced in the pioneering work of Silling (2000) and further enhanced in (Silling & Askari, 2005; Silling et al., 2007), the peridynamics formulation is an alternative point of view of continuum mechanics. Differential equations are replaced by integral ones, which

is an essential characteristic to model discontinuities inside a continuum (*i.e.*, there is no need to impose derivative requirements). The equations of motion, in its original version, can be written as:

$$\rho(\boldsymbol{x})\ddot{\boldsymbol{u}}(\boldsymbol{x},t) = \int_{\mathcal{R}_x} \boldsymbol{f}\left(\boldsymbol{u}' - \boldsymbol{u}, \boldsymbol{x}' - \boldsymbol{x}\right) dV_{\boldsymbol{x}'} + \boldsymbol{b}_d(\boldsymbol{x},t) \tag{2.42}$$

where $\ddot{\boldsymbol{u}}$ denotes the acceleration field, $\boldsymbol{f}$ is a sort of interaction force vector, $\boldsymbol{b}_d$ stands for a prescribed body force vector and $\mathcal{R}_x$ is a neighbor region of $\boldsymbol{x}$. It is easy to see that, this approach is, by nature, non-local since interactions between material particles are not only allowed but used to construct the entire theory. Recently, Hobbs et al. (2022) studied the capability of a bond-based model to reproduce size effect experiments.

Due to some inconsistencies with the original approach (*e.g.*, permanent strains not linked to shear in metals), Silling et al. (2007) proposed to generalize the theory with the notion of force and deformation state vectors. For instance, one may refer to Tupek et al. (2013) for the incorporation of damaging behaviors in this kind of method.

Based on a wave dispersion analysis, Bažant et al. (2016) showed that peridynamics models suffer from some inconsistencies. Particularly, it is shown that the dispersive behavior in elasticity is coupled to the one acting as a localization limiter. In other words, all the behavior is non-local, both in the elastic and damaging phases. Bažant et al. (2022b) extended the critics to phase-field models while comparing it to peridynamics and the microplane-based crack-brand approach (see also Bažant and Nguyen (2023)).

Motivated by these criticisms, Bazilevs et al. (2022) recently proposed to incorporate the M7 microplane model into peridynamics to simulate concrete failure. As analyzed in (Bažant & Nguyen, 2023), this could improve the performance of the peridynamics approach to model realistic quasi-brittle fracture.

Summary of Chapter 2

Localization:

- **Strain localization** is a physical phenomenon which cannot be described with local models.
- In quasi-static, the rate equilibrium problem is ill-posed (**loss of ellipticity**) and an infinite number of linearly independent solutions can be obtained.
- In dynamics, the problem is ill-posed as hyperbolic equilibrium equations become elliptic (**loss of hyperbolicity**). The obtained wave speed is imaginary and waves cannot propagate.
- As a consequence, finite element simulation **do not converge** upon mesh refinement and can lead to spurious dissipation upon failure.
- The response needs to be **regularized**.

Non-local damage mechanics:

- **Localization limiters** for smoothing the field controlling damage evolution.
- Concept of **neighborhood interactions** between points introduced by weighted average integral or spatial gradients.
- Classic approaches consider **isotropic and constant interactions**, leading to an incorrect description of material degradation.
- Approaches with **evolving non-local interactions** were proposed to address the issues of classic non-local models.
- Other regularization approaches exist, but most of them are **limited to the case of isotropic damage.**

Part II

Non-local damage mechanics with evolving interactions

The following chapters present the main contributions of this thesis to the subject.

3

Analytical and numerical one-dimensional study of non-local damage models

This chapter provides one-dimensional analytical and numerical developments concerning non-local damage models. The analysis is extended to approaches with evolving non-local interactions, particularly the eikonal formulation. Except from the wave dispersion analysis in Section 1, a few modifications in the text, and the figures adjusted to fit the global style of the thesis, this chapter was extracted from Ribeiro Nogueira et al. (2022a), Comptes Rendus. Mécanique, 350 (G3).

Contents

1 Wave dispersion analysis

The developments in this section are entirely based on the works of Sluys (1992), Sluys et al. (1993), Sluys and de Borst (1994), Peerlings et al. (1996b, 2001), Di Luzio and Bažant (2005), and Comi et al. (2007) (see also the references therein). Here, it is proposed to extend the discussion to the ENLG model in a 1D isotropic damage setting.

Let us consider a one-dimensional bar of infinite length, so we can neglect boundary effects in the following wave dispersion analysis. In the case of uni-axial tension on the x direction (with corresponding basis vector $\boldsymbol{e}_x$), the rate equilibrium equation reads:

$$\frac{\partial \dot{\sigma}}{\partial x} = \rho \frac{\partial^2 \dot{u}}{\partial t^2} \tag{3.1}$$

where σ is the stress in the bar and $\dot{u}$ stands for the velocity. The following (classical) hypothesis are made:

(i) The bar departs from a homogeneous uniform state (ε_0, D_0) at $t = t_0$, where ε_0 and D_0 denote the initial strain and damage in the bar, respectively. At $t = t_0 + \Delta t$, one has $\varepsilon = \varepsilon_0 + \varepsilon_a$, $\dot{\varepsilon} = \dot{\varepsilon}_a$, $D = D_0 + D_a$ and $\dot{D} = \dot{D}_a$, with $\bullet_a$ denoting a small perturbation of quantity $\bullet$. The problem is therefore linearized by neglecting high order terms.

(ii) It is supposed that $\dot{f} = 0$ (consistency condition), *i.e.*, damage grows everywhere in the bar.

(iii) Only positive strains are considered (tension case), so the local equivalent strain is the strain ε itself.

Under these conditions, the local constitutive behavior is written in terms of stress and strain rates:

$$\dot{\sigma} = E(1 - D_0)\dot{\varepsilon} - \dot{D}E\varepsilon_0 \tag{3.2}$$

1.1 Local damage model

In the local model, damage evolves in function of the equivalent strain, or here, directly ε. Here, one has:

$$\dot{D} = g' \frac{\partial \kappa}{\partial \varepsilon} \dot{\varepsilon} = g' \dot{\varepsilon} \tag{3.3}$$

where $g' = \partial D / \partial \kappa$ and $\partial \kappa / \partial \varepsilon = 1$ under the consistency condition. Substituting Equation (3.3) into Equation (3.2) leads to:

$$\dot{\sigma} = \left[E(1 - D_0) - g' E \varepsilon_0\right] \dot{\varepsilon} = L\dot{\varepsilon} \tag{3.4}$$

where L denotes the tangent modulus. Substituting into Equation (3.1) and taking into account that $\dot{\varepsilon} = \partial \dot{u} / \partial x$, one obtains the following wave equation (see for instance Peerlings et al. (2001)):

$$c_p^2 \frac{\partial^2 \dot{u}}{\partial x^2} - \frac{\partial^2 \dot{u}}{\partial t^2} = 0 \tag{3.5}$$

where:

$$c_p = \sqrt{\frac{L}{\rho}} = c_e\sqrt{1 - D_0 - g'\varepsilon_0} \tag{3.6}$$

is the phase velocity and $c_e = \sqrt{E/\rho}$ denotes the elastic wave speed.

One can easily see from Equation (3.6) that the medium is not dispersive, *i.e.*, the phase velocity does not depend on the wave number k. Moreover, the phase velocity becomes imaginary during strain-softening ($L < 0$), and waves cannot propagate in a local softening medium. This corresponds to the loss of hyperbolicity of the dynamic equilibrium problem (see for instance Sluys (1992)) and, therefore, it is ill-posed (see for instance (Benallal et al., 1993)). One should also notice that the condition $L = 0$, at the onset of softening in a 1D setting, corresponds to the singularity of the acoustic tensor previously mentioned.

1.2 GNL model

Linearized GNL model. When considering non-locality, the linearized equilibrium can be rewritten as:

$$(1 - D_0)E\frac{\partial^2 \dot{u}}{\partial x^2} - g'E\varepsilon_0\frac{\partial \dot{\bar{e}}}{\partial x} = \rho\frac{\partial^2 \dot{u}}{\partial t^2} \tag{3.7}$$

In the proposed 1D framework, differentiating the Helmholtz-type differential equation of the GNL model (Peerlings et al., 1996a) with respect to time gives:

$$\dot{\bar{e}} - c\frac{\partial^2 \dot{\bar{e}}}{\partial x^2} = \frac{\partial \dot{u}}{\partial x} \tag{3.8}$$

which is coupled to the equilibrium Equation (3.7) through the term $\partial\dot{u}/\partial x$.

Wave propagation. The dispersion relation can be found by introducing solutions into Equation (3.7) and Equation (3.8) in the form of harmonic waves:

$$\dot{u} = \hat{v}\exp\left(ik(x - c_p t)\right) \tag{3.9}$$

$$\dot{\bar{e}} = \hat{\bar{e}}\exp\left(ik(x - c_p t)\right) \tag{3.10}$$

Substituting Equation (3.10) into Equation (3.8) gives:

$$\hat{v} = \frac{\hat{\bar{e}}(1 + ck^2)}{ik} \tag{3.11}$$

and in Equation (3.7):

$$-E(1 - D_0)k^2\hat{v} - g'E\varepsilon_0 ik\hat{\bar{e}} = -\rho(c_p k)^2\hat{v} \tag{3.12}$$

which is finally simplified by introducing the expression of $\hat{v}$ from Equation (3.8), yielding:

$$k^2\left[\left(\rho c_p^2 - E(1 - D_0)\right)(1 + ck^2) + g'E\varepsilon_0\right] = 0 \tag{3.13}$$

A non-trivial solution of the above equation is obtained for $k \neq 0$, which, after some algebra, gives:

$$c_p = c_e\sqrt{1 - D_0 - \frac{g'\varepsilon_0}{1 + ck^2}} \tag{3.14}$$

which differs from the phase velocity obtained for the local model because of the term $(1+ck^2)$. When $c = 0$, *i.e.*, when the material has no internal length, the retrieved behavior is purely local with $\bar{e} = e$ with an imaginary wave velocity. Moreover, Equation (3.14) shows that the gradient-enhanced non-local medium is dispersive. The overall envelope group is a superposition of several harmonic waves propagating at different speeds (the phase velocity), such that the shape of the global pulse can be deformed during propagation.

The phase velocity from Equation (3.14) is real for any $k > k_c$, with:

$$k_c = \sqrt{\frac{1}{c}\left(\frac{\varepsilon_0 g'}{1-D_0} - 1\right)} \tag{3.15}$$

denoting the critical wave number, and $\lambda_c = 2\pi/k_c$ the corresponding critical wave length.

As highlighted in previous studies (see, for instance, *inter alia* Sluys (1992),Sluys et al. (1993), Sluys and de Borst (1994), Peerlings et al. (2001)), harmonic waves with wavelengths bigger than λ_c (associated to $k < k_c$) cannot exist in a realistic softening medium, so the phase velocity remains real. Indeed, strain-softening regions are small but finite, defined by some internal length scale $\propto 1/k_c$. Consequently, large wavelengths do not fit in these zones, so such waves do not exist.

Given the dispersive character of the propagation, the loading wave can be transformed into an unique stationary (*i.e.*, with $c_p = 0$) harmonic localization wave (Sluys & de Borst, 1994; Comi et al., 2007). This situation happens exactly when $k = k_c$ (associated to λ_c), which highlights the existence of an internal length associated to the critical wavelength. This is further detailed in Section 1.4.

1.3 ENLG model

Linearized ENLG model. In the case of uni-axial tension on the x direction and written in the basis $(\boldsymbol{e}_x, \boldsymbol{e}_y, \boldsymbol{e}_z)$, the anisotropic damage tensor and the Riemannian metric reduce to:

$$\mathbf{D} = \begin{bmatrix} D & & \\ & 0 & \\ & & 0 \end{bmatrix} \qquad \mathbf{g} = \begin{bmatrix} \frac{1}{1-D} & & \\ & 1 & \\ & & 1 \end{bmatrix} \tag{3.16}$$

Given that $\nabla\bar{e} \cdot \boldsymbol{e}_y = 0$ and $\nabla\bar{e} \cdot \boldsymbol{e}_z = 0$, substituting into Equation (5.1) yields:

$$\bar{e} - c\sqrt{1-D}\frac{\partial}{\partial x}\left(\sqrt{1-D}\frac{\partial \bar{e}}{\partial x}\right) = e \tag{3.17}$$

which is essentially the same equation as the GNL model, with the additional term $\sqrt{1-D}$. Now, computing the derivative with respect to x, one has:

$$\bar{e} + \frac{c}{2}\frac{\partial D}{\partial x}\frac{\partial \bar{e}}{\partial x} - c(1-D)\frac{\partial^2 \bar{e}}{\partial x^2} = e \tag{3.18}$$

Then, differianting with respect to time, gives:

$$\dot{\bar{e}} + \frac{c}{2}\left[\frac{\partial \dot{D}}{\partial x}\frac{\partial \bar{e}}{\partial x} + \frac{\partial D}{\partial x}\frac{\partial \dot{\bar{e}}}{\partial x}\right] - c(1-D)\frac{\partial^2 \dot{\bar{e}}}{\partial x^2} + c\dot{D}\frac{\partial \bar{e}}{\partial x} = \dot{e} \tag{3.19}$$

Now, considering $D = D_0 + D_a$, $\bar{e} = \bar{e}_0 + \bar{e}_a$ and $e = e_0 + e_a$, with $\bullet_a$ denoting a small perturbation of quantity $\bullet$ (*i.e.*, $|\bullet_a| \ll |\bullet_0|$), Equation (3.19) can be rewritten as:

$$\begin{aligned}\dot{\bar{e}}_a + \frac{c}{2}\left[\frac{\partial \dot{D}_a}{\partial x}\left(\frac{\partial \bar{e}_0}{\partial x} + \frac{\partial \bar{e}_a}{\partial x}\right) + \left(\frac{\partial D_0}{\partial x} + \frac{\partial D_a}{\partial x}\right)\frac{\partial \dot{\bar{e}}_a}{\partial x}\right] \\ - c(1-(D_0+D_a))\frac{\partial^2 \dot{\bar{e}}_a}{\partial x^2} + c\dot{D}_a\left(\frac{\partial \bar{e}_0}{\partial x} + \frac{\partial \bar{e}_a}{\partial x}\right) \\ = \dot{e}_a\end{aligned} \tag{3.20}$$

After linearization this becomes:

$$\dot{\bar{e}}_a + \frac{c}{2}\left[\frac{\partial \dot{D}_a}{\partial x}\frac{\partial \bar{e}_0}{\partial x} + \frac{\partial D_0}{\partial x}\frac{\partial \dot{\bar{e}}_a}{\partial x}\right] - c(1-D_0)\frac{\partial^2 \dot{\bar{e}}_a}{\partial x^2} + c\dot{D}_a\frac{\partial \bar{e}_0}{\partial x} = \dot{e}_a \tag{3.21}$$

Noting that all the derivatives of the initial quantities with respect to the spatial coordinate vanish in the homogeneous initial state, and that $\dot{\bullet} = \dot{\bullet}_a$ for all quantities, one obtains the linearized rate form of the ENLG model:

$$\dot{\bar{e}} - c(1-D_0)\frac{\partial^2 \dot{\bar{e}}}{\partial x^2} = \frac{\partial \dot{u}}{\partial x} \tag{3.22}$$

Wave propagation. Substituting Equation (3.9) and Equation (3.10) into Equation (3.22) gives:

$$\hat{v} = \frac{\hat{\dot{\bar{e}}}(1 + c(1-D_0)k^2)}{ik} \tag{3.23}$$

which is exactly the same equation obtained for the GNL model with the term $c(1-D_0)$ in the place of c. In the case of the ENLG model, this represents the evolving character of the non-local interactions. As done for the GNL model, a similar reasoning allows to define the phase velocity for the ENLG model:

$$c_p = c_e\sqrt{1 - D_0 - \frac{g'\varepsilon_0}{1 + c(1-D_0)k^2}} \tag{3.24}$$

and the corresponding critical wave number:

$$k_c = \sqrt{\frac{1}{c(1-D_0)}\left(\frac{\varepsilon_0 g'}{1-D_0} - 1\right)} \tag{3.25}$$

It's noteworthy that at the onset of softening in an undamaged medium, the ENLG and GNL models essentially give the same response. The same conclusions as before hold for the ENLG model, with some small differences, as detailed in Section 1.4.

1.4 Results, discussion and comparison of models

Exponential softening law. To illustrate the wave dispersion behavior of the models described above, let us consider the following damage evolution law:

$$D = 1 - \frac{\kappa_0}{\kappa}\exp\left[-B_t\left(\kappa - \kappa_0\right)\right] \tag{3.26}$$

with:

$$g' = \frac{\partial D}{\partial \kappa} = (B_t \kappa_0/\kappa + \kappa_0/(\kappa^2)) \exp(-B_t(\kappa - \kappa_0)) \tag{3.27}$$

Here, the damage threshold κ_0 is a fixed parameter and should not be confused with a quantity referring to the initial homogeneous state of the medium. Damage evolves based on the criterion function $f = \bar{e} - \kappa$, respecting Karush-Kuhn-Tucker (KKT) conditions:

$$f\dot{\kappa} = 0, \quad f \leqslant 0, \quad \dot{\kappa} \geqslant 0 \tag{3.28}$$

The parameters used for this study were taken from Peerlings et al. (2001), with the additional parameter $B_t = 1000$. The other ones are $E = 20\,000\,\text{MPa}$, $\kappa_0 = 0.0001$, $c_e = 1\,000\,\text{m/s}$ and $c = 1\,\text{mm}^2$.

Figure 3.1 shows the obtained dispersive behavior by plotting the phase velocities, for both the GNL and ENLG models, considering three different initial homogeneous states (ε_0, D_0).

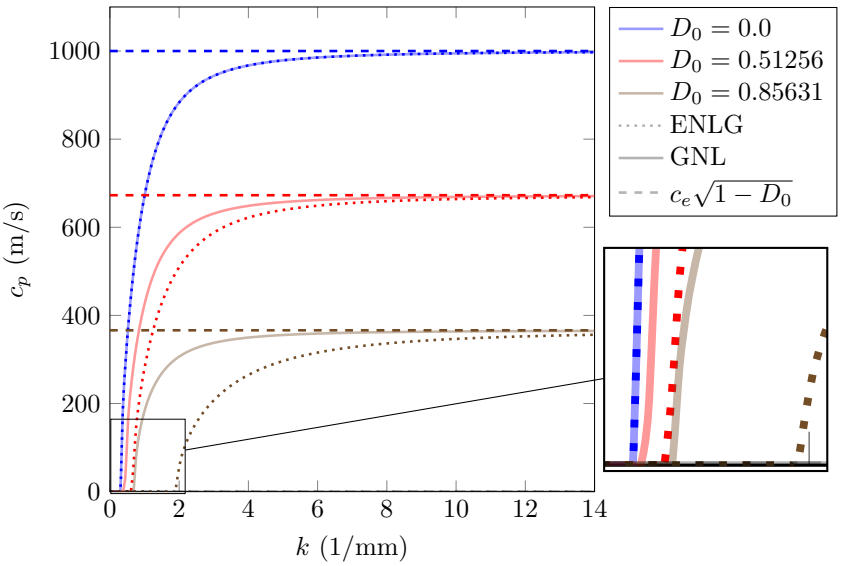

Figure 3.1 • Exponential softening law – phase velocity curves as functions of the wave number for the GNL and ENLG models. Blue lines correspond to $D_0 = 0.0$, red lines to $D_0 = 0.51256$ and brown lines to $D_0 = 0.85631$.

At damage initiation, *i.e.*, when $\varepsilon_0 = \kappa_0$ and $D_0 = 0$, one can easily see that the GNL and ENLG models give exactly the same response (solid and dashed blue lines in Figure 3.1). For higher initial strain states, and consequently higher initial damage levels, the phase velocity is reduced, so the propagation is slower for a damaged medium. In all the situations, the damaged elastic wave velocity $c_e\sqrt{1 - D_0}$ in the medium (dashed lines in Figure 3.1) is an upper bound, representing a physical limit to the propagation.

Furthermore, the critical wave number k_c (*i.e.*, the intersection point of the curve with the horizontal axis) increases with the damage level (see the zoom in Figure 3.1). This is the case for both models, with a faster increase for the ENLG approach. This is in agreement with the WKB approximation used to derive the ENLG model, which works for high frequency waves (small wavelengths and therefore high wave numbers).

These differences, more pronounced for higher damage levels, appear also in the overall evolution of the phase velocity. For the same relatively small wave number, the propagation is slower for the ENLG model compared to the GNL one, which is due to the additional term $(1 - D_0)$ in Equation (3.24).

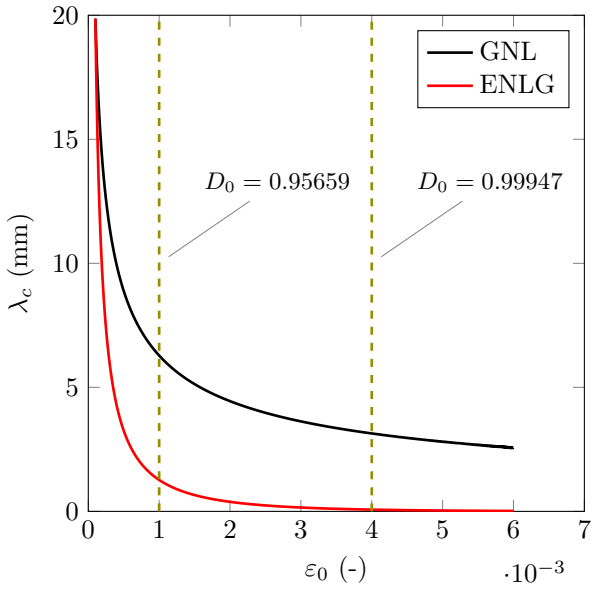

Figure 3.2 • Exponential softening law – evolution of the critical wavelength as a function of the initial homogeneous strain state.

Moreover, the associated critical wavelength λ_c is expected to decrease as a function of the initial strain state (or the initial damage level). Figure 3.2 shows its evolution as a function of ε_0 for the GNL and ENLG models. This is a typical result already observed in analyses concerning other non-local models (*e.g*, Pijaudier-Cabot and Benallal (1993), Peerlings et al. (1996b, 2001), Di Luzio and Bažant (2005), and Comi et al. (2007)). As λ_c is well defined for both models, localization is expected to take place in a band of finite width. Given its decreasing nature, the critical wave length describes a narrowing localization band when $D \to 1$, which is retrieved before by the ENLG model, as indicated in Figure 3.2.

> **Remark 3.1.** *Besides its utility in studying the regularization properties of non-local models, this wave dispersion analysis can be extremely useful in the context of damage-fracture transition modeling. Comi et al. (2007) provide useful insights into how the critical wavelength can be related to the number of finite elements needed to describe the localization band. For instance, the authors show that a critical damage value can be derived, from which a discontinuity should be introduced in the formulation. Moreover, they argue that non-local models with very fine meshes could be sufficient to describe the narrowing localization band but find their limits in applications concerning large-scale structures.*

In the case of the exponential law used here, $D \to 1$ at infinity strain, and therefore λ_c slowly decreases for the GNL model, since the evolution of k_c (Equation (3.15)) is

affected by the damage evolution law through the only term $(1 - D_0)$. On the contrary, the ENLG model provides a more realistic description of this phenomenon, since the term $(1 - D_0)$ appears two times in Equation (3.25) due to the damage-dependent evolving interactions. In this case, $\lambda_c \to 0$ is reached before for the ENLG model with a realistic value of $D_0 = 0.99947$, as shown in Figure 3.2. This behavior highlights the capability of the ENLG model to describe the transition from damage to fracture.

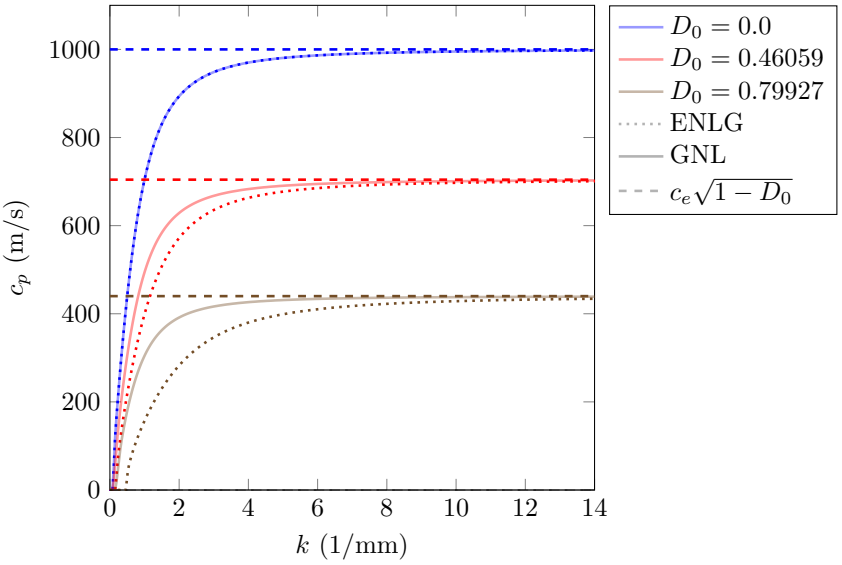

Figure 3.3 • Linear softening law – phase velocity curves as functions of the wave number for the GNL and ENLG models. Blue lines correspond to $D_0 = 0.0$, red lines to $D_0 = 0.46059$, and brown lines to $D_0 = 0.79927$.

Linear softening law. To illustrate the influence of the damage evolution law in the observations previously described, let us consider the linear softening law, as done in (Peerlings et al., 2001):

$$D = \begin{cases} \frac{\kappa_c}{\kappa} \frac{\kappa - \kappa_0}{\kappa_c - \kappa_0} & \text{if } \kappa < \kappa_c \\ 1 & \text{if } \kappa \geqslant \kappa_c \end{cases} \tag{3.29}$$

where κ_c is a material parameter, so $\sigma = 0$ for a finite value of the strain. The derivative with respect to history variable is:

$$g' = \frac{\partial D}{\partial \kappa} = \frac{\kappa_c \kappa_0}{\kappa^2 (\kappa_c - \kappa_0)} \tag{3.30}$$

Figure 3.3 shows the corresponding phase velocities obtained for the linear softening law, as done in Figure 3.1 for the exponential one. The material parameters remain the same as before, with $\kappa_c = 0.0125$, as used in (Peerlings et al., 2001). In general, the same conclusions as before hold, except for the fact that k_c seems to slowly increase with damage for the GNL model.

This is confirmed by the evolution of λ_c in function of the initial strain state. In this case, as depicted in Figure 3.4, a considerable difference is observed when compared to Figure 3.2. Given that for the linear law one has $D = 1$ for a finite strain, one can easily

see that the critical wavelength vanishes when $\varepsilon_0 = \kappa_c$ for the GNL model. Therefore, both GNL and ENLG models should describe a narrowing localization band upon failure with a linear softening law. Nonetheless, this is achieved more rapidly for the ENLG model, which has smaller critical wavelengths for a same initial strain state.

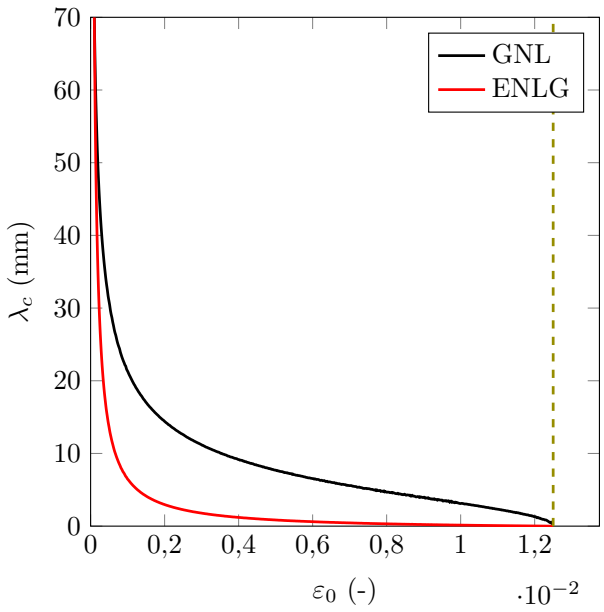

Figure 3.4 • Linear softening law – evolution of the critical wavelength as a function of the initial homogeneous strain state.

2 Boundary effects and damage diffusion in explicit dynamics

This section analyzes and compares numerically several non-local damage formulations, particularly regarding the obtained damage evolution close to the domain's boundaries and/or in highly damaged zones. Following previous works in literature, numerical studies are performed by simulating the so-called spalling phenomenon, *i.e.*, the tensile failure under an impact compression load. Experimentally, this loading condition is obtained thanks to Hopkinson-bar spall experiments (Klepaczko & Brara, 2001; Schuler et al., 2006; Erzar & Forquin, 2010). It is well-known that local damage models cannot reproduce the experimental spalling, as strain localization will inevitably lead to an ill-posed boundary value problem and, therefore, mesh-dependent results. Classical non-local models (*i.e.*, with a constant characteristic length) should naturally recover objectivity but fail to determine the spalling thickness (Krayani et al., 2009), leading to non-physical spalling failures.

Attention is given to five non-local approaches for regularizing the damage problem. Localization is numerically studied in a 1D dynamic problem similar to the one presented in Section 1. The latter is not intended to reproduce the dynamic material behavior but is used here as a localization tool. An explicit dynamic 1D finite element (FE) analysis

code is therefore developed to illustrate the advantages and drawbacks of each approach. In the following, all the formulations are written for the 1D case for conciseness.

2.1 Local model

In the isotropic case, one may consider a scalar damage variable D. Following a thermodynamic framework, the Helmholtz free energy potential and the intrinsic dissipation read $\rho\psi = \rho\psi(\varepsilon, D) = \frac{1}{2}(1-D)E\varepsilon^2$ and $\mathcal{D} = Y\dot{D}$, respectively. Here, E is the Young modulus, ε is the small strain, and $Y = -\rho\partial\psi/\partial D$ is the energy release rate. The Cauchy stress is thus written as:

$$\sigma = \rho\frac{\partial\psi}{\partial\varepsilon} = (1-D)E\varepsilon \tag{3.31}$$

Damage is considered to evolve according to the exponential (Feenstra, 1993) law from Equation (3.26) and the equivalent strain is defined as the positive part of the strain (*i.e.*, if $\varepsilon > 0$, $e = \varepsilon$; else $e = 0$).

2.2 Non-local models

Two main families of non-local models are considered in this section in a 1D settting:

(i) **Integral formulations (INL)**. The non-local equivalent strain is computed by:

$$\bar{e}(x) = \frac{1}{V_r(x)}\int_\Omega \phi(l_{xy}, l_c)e(y)dy \qquad V_r(x) = \int_\Omega \phi(l_{xy}, l_c)dy \tag{3.32}$$

where $l_{xy} = |x-y|$ is the Euclidean distance between points x and y in Ω, and $\phi(l_{xy}, l_c)$ is the weight function taken as a Gaussian distribution:

$$\phi(l_{xy}, l_c) = \exp\left(-4\left(\frac{l_{xy}}{l_c}\right)^2\right) \tag{3.33}$$

(ii) **Gradient formulations (GNL)**. The non-local equivalent strain is now the solution of the following Helmholtz-like differential equation:

$$\bar{e}(x) - c\frac{d^2\bar{e}(x)}{dx^2} = e(x) \;\text{ in }\; \Omega \quad\text{with}\quad \frac{d\bar{e}(x)}{dx} = 0 \;\text{ on }\; \partial\Omega \tag{3.34}$$

with c being a model parameter (homogeneous to the square of a length) and $\partial\Omega$ denoting the boundary of Ω. To provide the variational formulation corresponding to Equation (3.34), let us introduce the non-local virtual strains admissibility set:

$$\mathcal{E} = \{\eta \;\mid\; \eta(x) \in H^1(\Omega)\} \tag{3.35}$$

The problem to be solved for computing the non-local equivalent strain field thus reads:

$$\int_0^L c\frac{d\bar{e}}{dx}\frac{d\eta}{dx}dx + \int_0^L \bar{e}\eta dx = \int_0^L e\eta dx \qquad \forall\eta \in \mathcal{E} \tag{3.36}$$

where the zero flux boundary condition has been used (Lasry & Belytschko, 1988; Mühlhaus & Aifantis, 1991; Peerlings et al., 1996a). In the previous equation the dependency of $(e, \bar{e}, \eta)$ on the space variable x was omitted for the sake of conciseness.

2.3 Non-local models with evolving internal length

Several authors proposed to take into account the influence of the damaging process on non-local interactions. In general, one aims to completely simulate the strain localization process from diffused damage (*i.e.*, micro-cracking phase) to damage localization (*i.e.*, fully localized macro-crack phase). To achieve this goal, several drawbacks of standard INL and GNL formulations should be overcome:

(i) *Damage initiation near a crack tip.* This is the shift of the maximum non-local equivalent strain far from the crack tip, leading to damage initiation problems (Simone et al., 2004). This drawback will not be treated in this section.

(ii) *Damage attraction to the boundaries.* This is the gradual shift of the maximum damage value to the boundary of the domain. This is related to the truncated interaction domain for INL models or the symmetry imposed by the zero flux condition on the boundary for GNL models. However, one expects that the response should become local in this case (vanishing non-local interactions) (Krayani et al., 2009; Pijaudier-Cabot & Dufour, 2010).

(iii) *Damage diffusion.* Upon strain localization, the micro-cracks coalescence into a macro-crack should induce a discontinuity in the displacement field. Classic models do not enable describing such a transition, as damage is diffused in a large zone. Thus, the internal length should account for this effect and be modified throughout the damage process (Geers et al., 1998). In the 1D numerical context of the analysis presented in the following, damage diffusion will be considered to occur when $D \approx 1$ in more than one FE. Conversely, a perfectly localized damage profile is considered when $D \approx 1$ in just one FE.

In particular, attention is focused on a Stress-Based integral Non-Local (NLSB) formulation (Giry et al., 2011), and on the Eikonal Non-Local (ENL) formulation (Desmorat et al., 2015b; Rastiello et al., 2018b) (in both integral and gradient forms). Already introduced in Chapter 2, these approaches are briefly recalled here in the 1D setting of the present analysis.

2.3.1 Stress-based non-local damage model

The NLSB model (Giry et al., 2011) takes into account the influence of the stress field at point y in the computation of the weight function at point x. This is done by replacing the characteristic length in Equation (3.33) by:

$$l_{c,xy} = \rho_{\text{fac}}(y) l_c \qquad \rho_{\text{fac}}(y) = \frac{|\sigma(y)|}{f_t} \tag{3.37}$$

2.3.2 Eikonal non-local damage model

Integral-type formulation (ENLI). It is supposed that non-local interactions between a point x and any other point y belonging to Ω depend on an effective distances field

$\tilde{l}_{xy}(y)$ which is the solution of an eikonal equation with a damage dependent metric field. In a 1D context, the eikonal equation to be solved $\forall\, x \in \Omega$ can be written as:

$$\sqrt{1-D(y)}\left|\frac{d\tilde{l}_{xy}(y)}{dy}\right| = 1 \quad \text{with} \quad \tilde{l}_{xy}(y=x) = 0 \tag{3.38}$$

Equation (3.38) can be integrated analytically, and the effective distance between points x and y reads (Desmorat et al., 2015b; Thierry et al., 2020a):

$$\tilde{l}_{xy} = \int_{\min(x,y)}^{\max(x,y)} \frac{dy}{\sqrt{1-D(y)}} > l_{xy} \tag{3.39}$$

According to such an approach, the main modification with respect to the INL formulation is the use of the $\tilde{l}_{xy}$ instead of l_{xy} in Equation (3.33).

Gradient-type formulation (ENLG). In 1D tension, the modified version of the Helmholtz's Equation (3.34) to be solved to compute the non-local strain field is:

$$\bar{e}(x) - c\sqrt{1-D(x)}\frac{d}{dx}\left(\sqrt{1-D(x)}\frac{d\bar{e}(x)}{dx}\right) = e(x) \text{ in } \Omega \quad \text{with} \quad \frac{d\bar{e}(x)}{dx} = 0 \text{ on } \partial\Omega \tag{3.40}$$

Similarly to Equation (3.36), the variational formulation of the ENLG problem reads:

$$\int_0^L c\sqrt{1-D}\frac{d\bar{e}}{dx}\frac{d\eta}{dx}dx + \int_0^L \frac{\bar{e}\eta}{\sqrt{1-D}}dx = \int_0^L \frac{e\eta}{\sqrt{1-D}}dx \qquad \forall \eta \in \mathcal{E} \tag{3.41}$$

The latter is basically the same equation obtained for the classical GNL model, with the additional term $\sqrt{1-D}$. In the ENLI formulation, this term appears in Equation (3.38) and is related to the determinant of the Riemannian metric.

2.4 Unidimensional dynamic problem

The spalling test (Figure 3.5) will be used to underline some typical drawbacks and advantages of different regularization models. As already done in (Krayani et al., 2009; Giry et al., 2011), this test is simulated to study boundary effects and localization properties of modified non-local formulations. A precise review of this problem was also presented in (Pijaudier-Cabot & Grégoire, 2014), where the advantages of considering a modified interaction-based non-local approach (Rojas-Solano et al., 2013) were presented.

Description of the spalling test. Experimentally, spalling can be obtained with a modified Hopkinson test (Figure 3.5). The experimental setup consists of an input striker, an incident bar, and the specimen. After being transmitted to the specimen, the compression wave starts to reflect as a tensile wave at the free boundary. For a strain-softening material, when the sum of the compression and tensile contributions to the elastic wave is greater than the material tensile strength, a fully localized cracking occurs. Thus, the spalling test is an excellent tool for simulating strain localization and evaluating the properties of damage models.

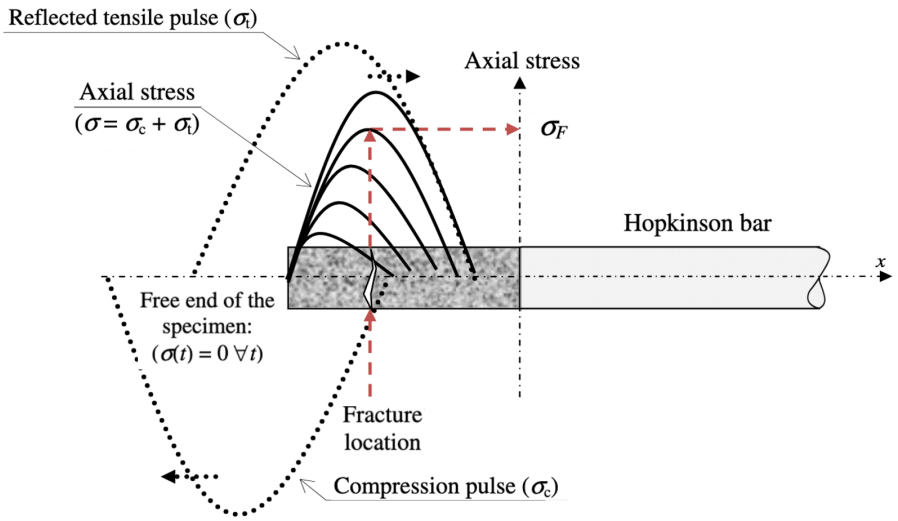

Figure 3.5 • Illustrative scheme of the spalling test with a Hopkinson bar (Erzar & Forquin, 2010)

2.4.1 Weak form of the dynamic equilibrium problem

Let us consider a 1D domain $\Omega = [0, L]$, with an imposed Neumann condition (external impulsive force) on $\partial\Omega_F = \{x = L\}$. The other boundary is stress-free.

Variational problem. Let us introduce the following admissibility spaces:

$$\mathcal{U} = \{u \ \mid \ u(x,t) \in H^1(\Omega), \quad u(x,t) \in H^2(I) \ , \quad u(x, t=0) = 0 \ \ \forall x \in \Omega\} \tag{3.42}$$

$$\mathcal{V} = \{v \ \mid \ v(x) \in H^1(\Omega), \quad v(x,t) = 0 \ \ \text{on} \ \ \partial_u\Omega\} \tag{3.43}$$

where $H^n(\cdot)$ denotes the n-order Sobolev space over a domain and $I = [0, T]$ is the time interval.

Neglecting body forces, the variational dynamic equilibrium problem to be solved consists in finding $u = u(x,t) \in \mathcal{U}$ such that:

$$\int_0^L \sigma(u)\epsilon(v)dx + \int_0^L \rho\ddot{u}vdx = T_d(t)v(L) \quad \forall\, v \in \mathcal{V} \tag{3.44}$$

where $\ddot{u} = \partial^2 u/\partial t^2$ is the acceleration field, and $T_d(t)$ is the applied traction (force per unit area) on $\partial_F\Omega$.

Time discretization. The equation (3.44) is solved for each time instant $t \in I$ after time discretization (*e.g.*, using the Newmark scheme). Here, the explicit central difference scheme is employed. Accordingly, the time interval is discretized as $t \to t_n \in [0, T = n_t\Delta t]$ with $n \in [\![1, n_t]\!]$ and Δt the time step. At time t_{n+1}, one thus solves for $\ddot{u}_{n+1}$ the time discretized variational equation:

$$\int_0^L \rho\ddot{u}_{n+1}vdx = T_{d,n+1}v(L) - \int_0^L \sigma(u_{n+1})\epsilon(v)dx \quad \forall\, v \in \mathcal{V} \tag{3.45}$$

where:

$$\begin{cases} u_{n+1} = u_n + \Delta t \dot{u}_n + \dfrac{1}{2}\Delta t^2 \ddot{u}_n \\ \dot{u}_{n+1} = \dot{u}_n + \dfrac{\Delta t}{2}\left(\ddot{u}_{n+1} + \ddot{u}_n\right). \end{cases} \tag{3.46}$$

In Equations (3.44) and (3.46), down-scripts n and $n+1$ are used to denote quantities computed at time instants t_n and t_{n+1}. The same nomenclature will be adopted in the remainder of the text.

Space discretized problem. To solve the variational Equation (3.44), the computational domain Ω is discretized into a FE mesh Ω^h containing n_{el} linear bar elements of constant length h. Accordingly, the displacement field is approximated as a function of the nodal displacements through the elementary shape functions. Stress and strains are computed at the quadrature points of the FEs. A single integration point located at the center of the FE is considered for linear elements. We denote by $\mathcal{G}$ the set of the $n_{gp} = n_{el}$ integration points of Ω^h.

Constitutive model. The stress is evaluated according to the constitutive relation from Equation (3.31). For the numerical simulations of this paper, the history function driving damage evolution is defined as the historical maximum of the non-local strain. For the integration point x_i, it is computed as $\kappa_i = \kappa(x_i) = \max_t(\kappa_0, \bar{e}_i)$ with $\bar{e}_i = \bar{e}(x_i)$. Damage grows according to Equation (3.26).

2.5 Non-local fields computation

The non-local field ($\bar{e}$) is computed following one of the methods introduced before: INL, GNL, ENLI, ENLG or NLSB. In a FE context, one computes the non-local strain field to evaluate damage, and thus the stress, for each Gauss integration point of Ω^h.

2.5.1 Integral non-local methods

For a given Gauss point $x_i \in \mathcal{G}$, the non-local equivalent strain $\bar{e}_i = \bar{e}(x_i)$ is obtained as:

$$\bar{e}_i = \frac{\sum_{j=1}^{n_{gp}} e_j \phi(l^*_{ij}, l^*_{c,ij})}{\sum_{j=1}^{n_{gp}} \phi(l^*_{ij}, l^*_{c,ij})} \tag{3.47}$$

where $e_j = e(x_j)$ and we exploited the fact that all FEs have the same size.

The main difference between the different integral-type non-local formulations discussed before is in the way how l^*_{ij} and $l^*_{c,ij}$ are computed.

INL. In the standard INL formulation, $l^*_{ij} = l_{ij} = |x_i - x_j|$ and $l^*_{c,ij} = l_c$.

NLSB. In the NLSB damage model (Giry et al., 2011), the weighting function depends on the stress field. In the explicit 1D implementation of this work, the modified internal length $l^*_{c,ij}$ is directly computed from the stress ($\sigma_{j,n} = \sigma_n(x_j)$) at the previous time step, whereas $l^*_{ij} = l_{ij} = |x_i - x_j|$.

The following steps are needed to perform the computation. The coefficient $\rho_{\text{fac},j} = \rho_{\text{fac}}(\sigma_{j,n})$ is first computed for $x_j \in \mathcal{G}$ as:

$$\rho_{\text{fac},j} = \begin{cases} |\sigma_{j,n}|/f_t & \text{if} \quad |\sigma_{j,n}|/f_t \leqslant 1 \\ 1 & \text{otherwise} \end{cases} \tag{3.48}$$

The modified characteristic length is then computed as:

$$l^*_{c,ij} = \begin{cases} \rho_{\text{fac},j} l_c & \text{if} \quad \rho_{\text{fac},j} l_c \geqslant h \\ h & \text{otherwise} \end{cases} \tag{3.49}$$

Finally, the non-local weight $\phi(l_{ij}, l^*_{c,ij})$ is computed and used in Equation (3.47).

ENLI. For the ENLI formulation, the damage dependent interaction distances need to be computed. In Equation (3.47), $l^*_{c,ij}$ is taken equal to l_c whereas l^*_{ij} is the effective distance $\tilde{l}_{i,j}$ between the two integration points x_i and x_j (Jirásek & Desmorat, 2019; Thierry et al., 2020a). Numerically, the integral (3.39) is replaced by a finite sum over all the points in the interval $[x_i, x_j]$.

Jirásek and Desmorat (2019) proposed two schemes to perform the integral calculations: a simple trapezoidal rule such that $\sqrt{1-D}$ is element-wise constant and a modified approach assuming that damage is linear between two adjacent integration points. As shown in (Thierry et al., 2020a), the first approach has better localization properties, especially when combined with appropriate path-following algorithms (Rastiello et al., 2022).

According to the latter approximation, $l^*_{ij} = \tilde{l}_{i,j}$ is computed as:

$$\tilde{l}_{i,j} = \tilde{l}_{i,j-1} + \frac{h}{2}\left(\frac{1}{\sqrt{1-D_{j-1,n}}} + \frac{1}{\sqrt{1-D_{j,n}}}\right), \qquad x_j > x_i \tag{3.50}$$

where $D_{j-1,n} = D_n(x_{j-1})$ and $D_{j,n} = D_n(x_j)$.

2.5.2 Gradient-enhanced non-local methods

GNL. Equations (3.36) and (3.44) need to be solved as a coupled problem (Simone et al., 2003a).

> **Remark 3.2.** *This is similar to implement thermo-elasticity equations with an equivalence between nodal temperatures and nodal non-local strains (Pijaudier-Cabot & Grégoire, 2014). This simple analogy allows to easily incorporate non-local gradient formulations (or even phase-field models) in commercial FE analysis software (see, e.g., Azinpour et al., 2018; Marconi, 2022).*

Accordingly, the non-local strain field and the corresponding trial field (η) are discretized by appropriated shape functions. Many authors argued that it was necessary (or at least advisable) to employ displacement shape functions one order higher than those used for the non-local field (Peerlings et al., 1996a; de Borst et al., 1996). Indeed, using

the same interpolation functions for the displacement and the non-local strain may lead to stress oscillations. However, Simone et al. (2003a) showed that the gradient-enhanced damage problem should not be considered as a mixed problem (*i.e.*, the Babuska-Brezzi condition does not apply) but rather a coupled one. Consequently, the interpolation functions chosen for the two unknown fields are not related and can be taken simply as linear-linear.

ENLG. Similarly to the standard GNL formulation, the governing Equations (3.41) and (3.44) are solved as a coupled problem. To preserve the explicit feature of the present FE implementation, the Helmholtz Equation (3.41) is computed with $D_n = D(\kappa_n)$. This is consistent with the choice made for the ENLI formulation.

2.5.3 More numerical details

Computation of evolving non-local interactions. For all the non-local models with evolving distance models, damage and stress are always one step delayed with respect to the displacement, given the choice to explicitly compute the non-local evolving interactions. This is in agreement with the quasi-static implementations developed by Rastiello et al. (2018b) for the ENLI model, and by Giry et al. (2011) for the NLSB model.

Equivalent strain interpolation for the GNL and ENL models. For both gradient models, once the nodal non-local equivalent strain field is obtained at time $t_{\mathrm{n+1}}$, the shape interpolation functions are applied to obtain the corresponding values at the Gauss points.

Dealing with the case of D tending to the unity. Generally, FE solvers for CDM problems limit damage growth to a certain fixed quantity $D^\star$ at the Gauss quadrature point while integrating the material behavior law (updating internal variables, computing the stress, and evaluating the elemental stiffness matrix). In nonlinear quasi-static analyses, where the stiffness matrix need to be inverted to compute the solution displacement field, $D^\star$ is chosen in a way that the stiffness matrix does not become singular.

In the case of the explicit time integration scheme of this work, there is no need to inverse the stiffness matrix for the computations. Thus, $D^\star$ is taken as close as possible to unity, to avoid problems when computing the effective distances field for ENLI. This is automatically handled by the library `numpy` in Python. Machine precision is taken into account by setting $1/\sqrt{1-D^\star}$ equal to `numpy.inf`, which is equivalent to the largest number that can exist with the available memory in the machine. Then, when evaluating the Gauss weighting function with $\tilde{l}_{i,j} =$ `numpy.inf`, the Python code will return 0. This is in agreement with the fact that non-local interactions should vanish upon damage localization as stated by the ENLI model. So in this case, $D^\star$ can be taken as high as the machine supports.

2.6 Results and discussion

The spalling experiment will be treated hereafter. To limit numerical noise at the introduction of the loading, a linear ascending and descending compression stress is

applied during a finite time t_{ste} (Figure 3.6). The total loading time is t_{loa} and the final stress applied is $-\sigma_0$. A signal length l_0 can be related to the loading time by $l_0 = t_{\text{loa}} c_e$, where $c_e = \sqrt{E/\rho}$ denotes the longitudinal wave velocity. Choosing $\sigma_0 \geqslant f_t$ leads to strain localization and therefore damage develops. The main advantage of comparing non-local models studying this problem is the easiness to control where localization occurs; the fracture will be located exactly at a distance $l_{\text{spal}} = l_0/2$ from the free-edge.

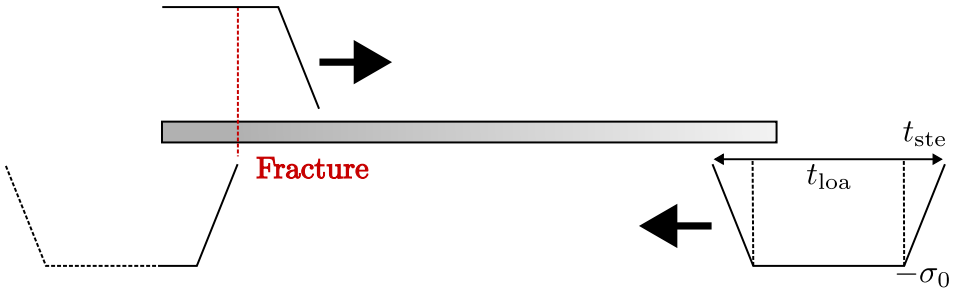

Figure 3.6 • One dimensional bar model of the spalling problem. A compression signal comes from the right and is reflected in tension when it reaches the free left boundary.

The material parameters used for the simulations are the same as those in Krayani et al., 2009; Giry et al., 2011, *i.e.*, $E = 1\text{MPa}$, $\kappa_0 = 1$, $B_t = 2$, $L = 25\text{cm}$, $f_t = 1\text{MPa}$, $\sigma_0 = \alpha f_t, l_c = 3\text{cm}$ and $\rho = 1\text{kg/m}^3$. Here, $\alpha \geqslant 1$ is a constant parameter chosen arbitrarily to make damage appears. The simulation time is set to $T = 1.5L/c_e = 0.3750\text{ms}$. Time step is chosen as $\Delta t = \Delta t^{\text{crit}}/2$, where Δt^{crit} is the critical time step related to the explicit scheme and depends on the mesh size. A study of the influence of Δt on the obtained responses for the considered non-local formulations is presented in (Ribeiro Nogueira et al., 2022a).

2.7 Boundary effects and damage diffusion with fixed interactions models

Let us first consider the standard INL model. Different mesh discretizations (with n_{el} ranging from 100 to 400) are used in computations to study mesh sensitivity of the obtained responses. A sufficiently large loading time is considered. In particular, $t_{\text{loa}} = L/c_e$ and $t_{\text{ste}} = 0.05 t_{\text{loa}}$. This means that $l_0 = L$; therefore, one should expect a damaged band centered in the middle of the bar.

2.7.1 Damage regularization and diffusion

Figure 3.7 (left) shows the damage distribution along the bar obtained for $\alpha = 1.1$. As expected, damage reaches its maximum close to the middle of the bar ($x = L/2$) but it diffuses on a bigger zone than one FE. Moreover, the INL model regularizes the response as the damage profiles converge upon mesh refinement.

The choice of α may modify the obtained response. Figure 3.7 (right) shows the damage profiles computed for different values of α. For a fixed loading duration, changing

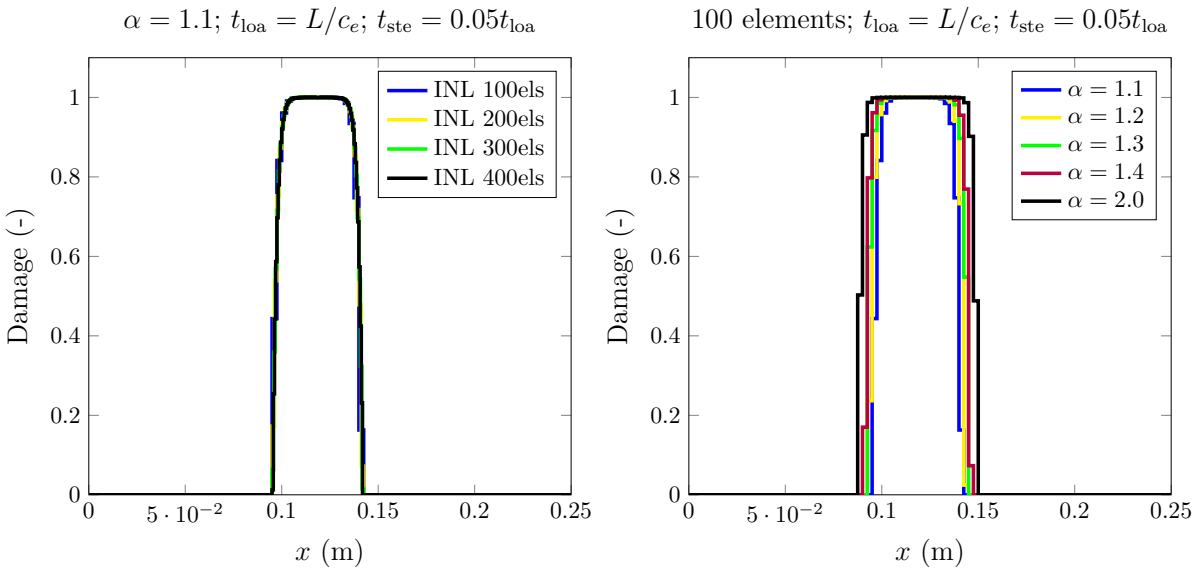

Figure 3.7 • INL damage model – Convergence of the damage profile upon mesh refinement (left) and influence of the loading parameter α on damage diffusion upon damage localization (right).

α changes the strain rate, which would affect the non-local averaging. This is also the case for the other non-local models studied in this work. However, the presented results can provide information on the main features of the responses provided by the different formulations studied (when compared for a given α).

The time evolution of the damage field on the bar is shown in Figure 3.8 for $\alpha = 2$. Damage first takes its maximum value in only one FE, then starts to diffuse in the surrounding FEs. At the end of the simulation, damage equals unity in a quite large zone. As already pointed out in (Geers et al., 1998), the non-local field still evolves outside the localization zone due to strain intensification. Non-local interactions are even allowed to take place between points separated by highly damaged zones, as the material state is not taken into account in the averaging process.

2.7.2 Boundary effects

Damage attraction to the free boundary is observed when $l_{\text{spal}} < l_c$. To highlight this problem, a few values of l_0 are used with a FE mesh of 100 elements. Here, α is set equal to 2 to observe a damaging process up to failure (*i.e.*, $D \approx 1$ in at least one FE).

INL formulation. For values of $l_{\text{spal}} < l_c$, damage is gradually attracted by the boundary and takes its maximum at the free-edge (Figure 3.9). This effect is related to the fact that the interactions introduced through the non-local weight function ϕ only depend on the euclidean distance between points. Near a free boundary, the interaction domain is truncated; therefore the non-local weights computed for these points are bigger. In this case, this results in an infinitely small spalling thickness: the distance from the free-edge to the point of maximum damage is nil ($D \approx 1$ shifts to the free boundary). As shown in Figure 3.9 (right) damage diffusion is also present in the last steps of the computation. As

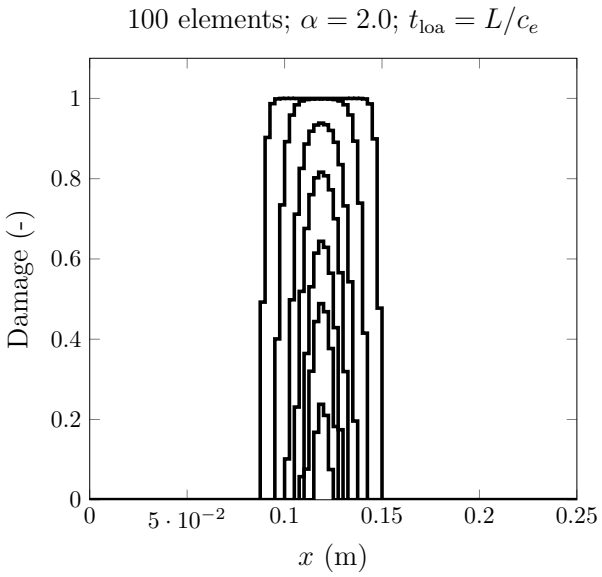

Figure 3.8 • INL damage model – Damage evolution throughout time for $l_0 = 25$ cm.

expected, this indicates that the transition from diffuse damage to fully localized damage cannot be conveniently described with this model.

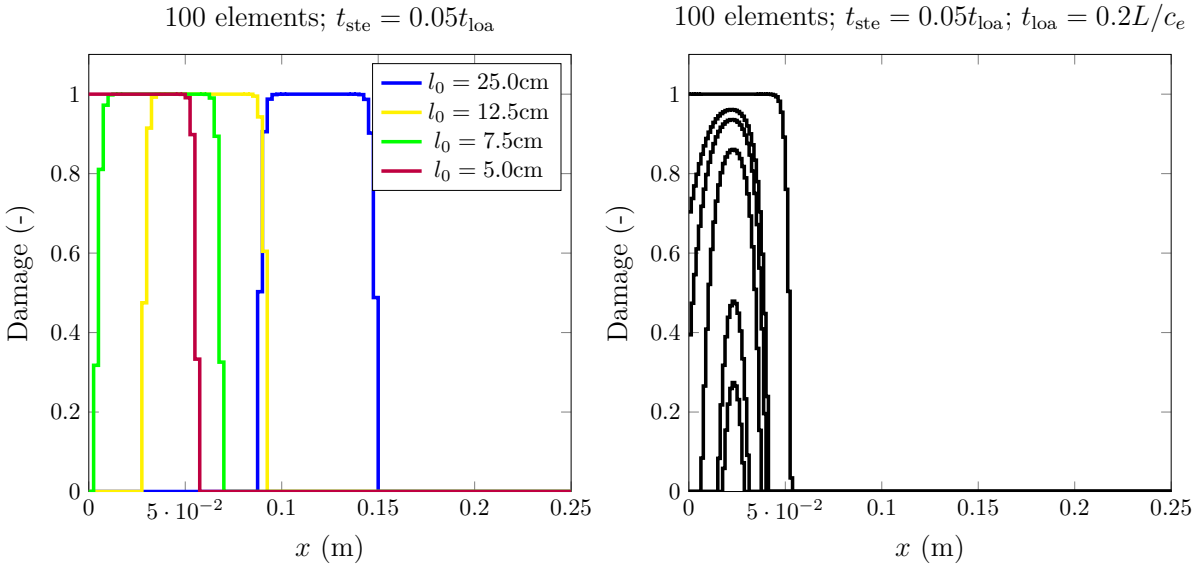

Figure 3.9 • INL damage model – Influence of l_0 on damage attraction (left) and its evolution throughout time (right).

INL vs GNL formulations. This result may also be extended to the classical gradient-enhanced damage model (GNL), as a zero flux condition is applied to solve the non-local strain diffusion equation. Figure 3.10 illustrates the equivalence between GNL and INL formulations. The two models provide very similar results. The small differences between them are certainly related to the fact that they are equivalent *stricto sensu* only when an infinite domain is considered for a Green's weight function (Peerlings et al., 2001). Mesh refinement may slightly reduce the differences between these models (see Figure 3.10).

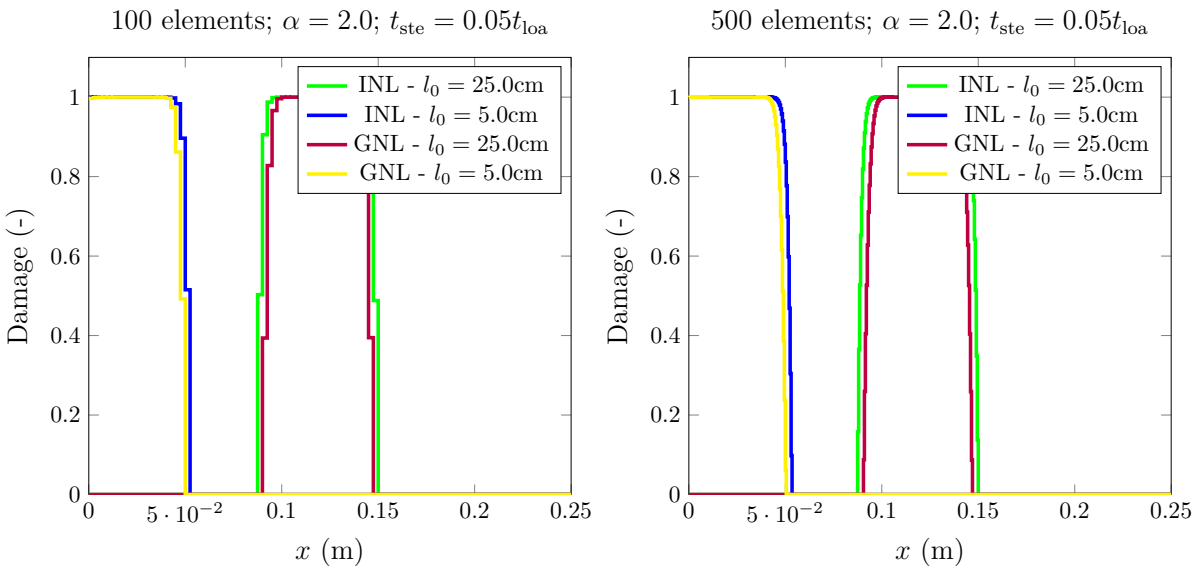

Figure 3.10 • INL and GNL damage models – Equivalence between the two formulations for 100 and 500 FEs.

2.8 Boundary effects and damage diffusion with evolving interactions models

In this section, a comparison of the non-local models with evolving interactions is performed. Two different loading cases are considered:

(i) **Loading case A** – Damage localization far from the free boundary ($l_{\text{spal}} = 6.250\text{cm} > l_c$): $t_{\text{loa}} = 0.5L/c_e$.

(ii) **Loading case B** – Damage localization near the free boundary ($l_{\text{spal}} = 2.500\text{cm} < l_c$): $t_{\text{loa}} = 0.2L/c_e$.

In all the cases studied, t_{ste} is assumed equal to $0.1t_{\text{loa}}$. The effect of the strain rate on the localization process is studied by modifying the loading parameter α. Since changing t_{ste} has almost the same effect, this parameter is taken constant for the sake of simplicity and conciseness of presentation.

2.8.1 Damage diffusion (loading case A)

Integral formulations. The loading case A is simulated for two meshes containing 100 and 500 linear FEs and $\alpha = 1.5$. Figure 3.11 (left) compares the damage profiles computed using the INL, NLSB, ENLI, ENLG, and GNL damage models at time $t = T$. Damage diffusion is observed for the INL model, but is much smaller for the NLSB and ENLI formulations. As expected, the ENLI model allows for a better description of the damage localization process, since damage concentrates on only one FE as non-local interactions vanish when damage localizes. Conversely, damage is spread over three FEs for the NLSB model. Figure 3.11 (right) gives the same results for a mesh with 500 FEs. Here, the ENLI formulation spreads damage over three FEs, whereas the NLSB model spreads it over on nine FEs.

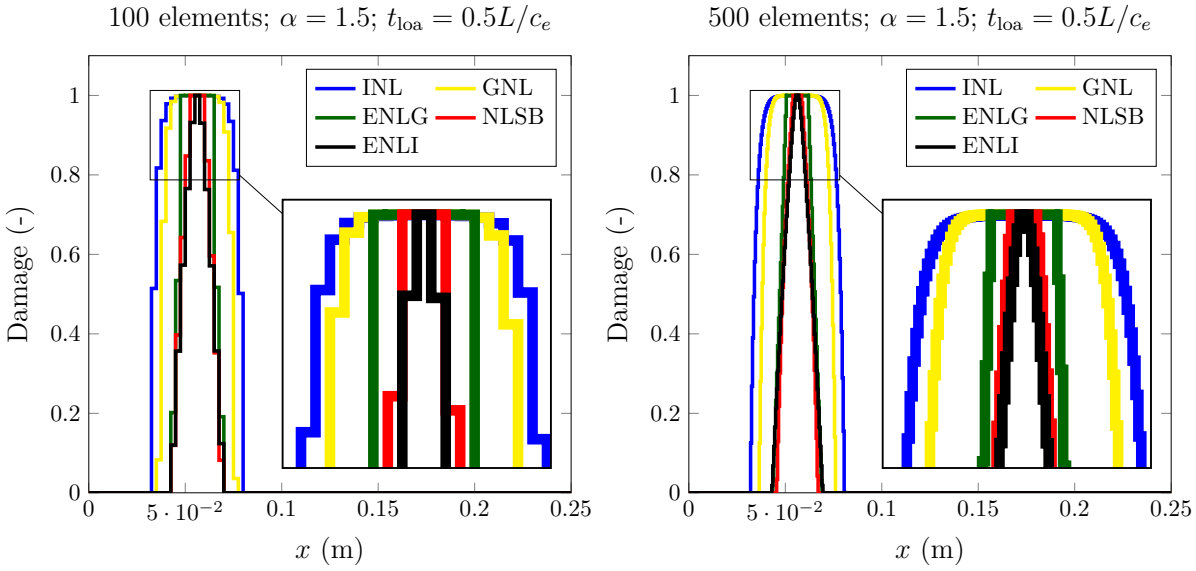

Figure 3.11 • INL, GNL, NLSB, ENLI, and ENLG damage models – Comparison between all the models studied for two meshes with 100 and 500 FEs.

Integral vs. gradient formulations. The damage profile computed with the GNL model is thinner than the one obtained using the INL formulation. The ENLG model provides almost the same damage profile as the ENLI formulation, except for highly damaged zones (Figure 3.11 right). Indeed, the damage is spread over a large region (its width is still smaller than the one computed by the classical non-local models). This is an unexpected behavior, given that the ENLG formulation is an approximation of the ENLI model and therefore should give similar results. However, the damage diffusion is clearly reduced upon mesh refinement for the ENLG formulation (Figure 3.11).

Table 3.1 • INL, GNL, NLSB, ENLI, and ENLG damage models – Width of the damaged zones for each non-local model for a mesh with 500 FEs.

Non-local model	INL	GNL	ENLI	ENLG	NLSB
Width (% l_c) of the damaged area when $D_{\max} = 0.99$	157	120	90	87	73
Width (% l_c) of the damaged area when $D_{\max} \to 1$	170	133	90	87	73

From Figure 3.11, one can also see that the widths of the damaged zones for the models with evolving interactions are smaller than those given by the classic formulations. Moreover, the models with fixed distances propagate the damage front while time passes even after damage attains unity, as we will see later on. Thus, widths of the damaged area (*i.e.*, total of elements where $D > 0$) are not constant for these models and tend to increase (see Table 3.1). Differently, models with evolving distances do not show an evolution of the damage zone when comparing profiles for $D_{\max} = 0.99$ and $D_{\max} \to 1$. In this situation, the ENLG and ENLI formulations give very similar widths, and the NLSB model shows the smaller one. Smaller damaged zones are indeed expected for the evolving

interaction approaches. In the case of the ENLI and ENLG models, the interactions begin to evolve since damage appears and vanish upon damage localization. For the NLSB model, the stress field is reduced when damage occurs, leading to an evolution of the internal length. Even in the case where there is no damage, $\sigma < f_t$ induces an evolution of the interactions for the NLSB model. Furthermore, one may expect these widths to not evolve after damage localization on one FE, as interactions between points through highly damaged zones should not occur.

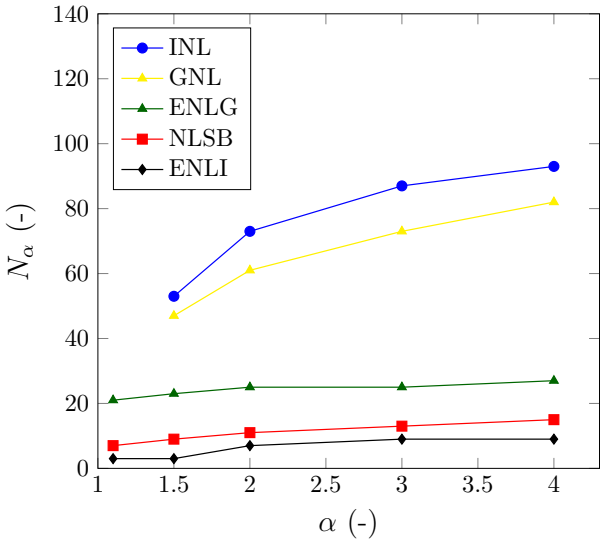

Figure 3.12 • INL, GNL, NLSB, ENLI, and ENLG damage models – Influence of α on the size of the localization zone for a mesh with 500 FEs.

Influence of the strain rate. Parameter α influences the damage diffusion process for all the considered models. In any case, evolving interaction models give more representative results of the degradation process. The damage profiles obtained by these approaches are almost insensitive to mesh refinement. The main difference between the formulations is their capability to describe damage localization, which ENLI better simulates. Figure 3.12 allows quantifying better the influence of α on the damage diffusion mentioned above for a mesh with 500 FEs. The number (N_α) of FEs where diffusion occurs is dependent on the value of α for all the models, but the influence of such a parameter is more pronounced for the INL and GNL models.

2.8.2 Boundary effects (loading case B)

Another usual situation for which one may compare non-local models is when the damaged band is located near a free boundary.

Integral vs. gradient formulations. Figure 3.13 shows the results for the INL, ENLG, ENLI and NLSB models for $\alpha = 2$. No damage attraction from the boundary is observed for the ENLG and NLSB formulations. In those cases, the boundary effect does not occur, so it is possible to determine the spall location numerically. Contrarily, the

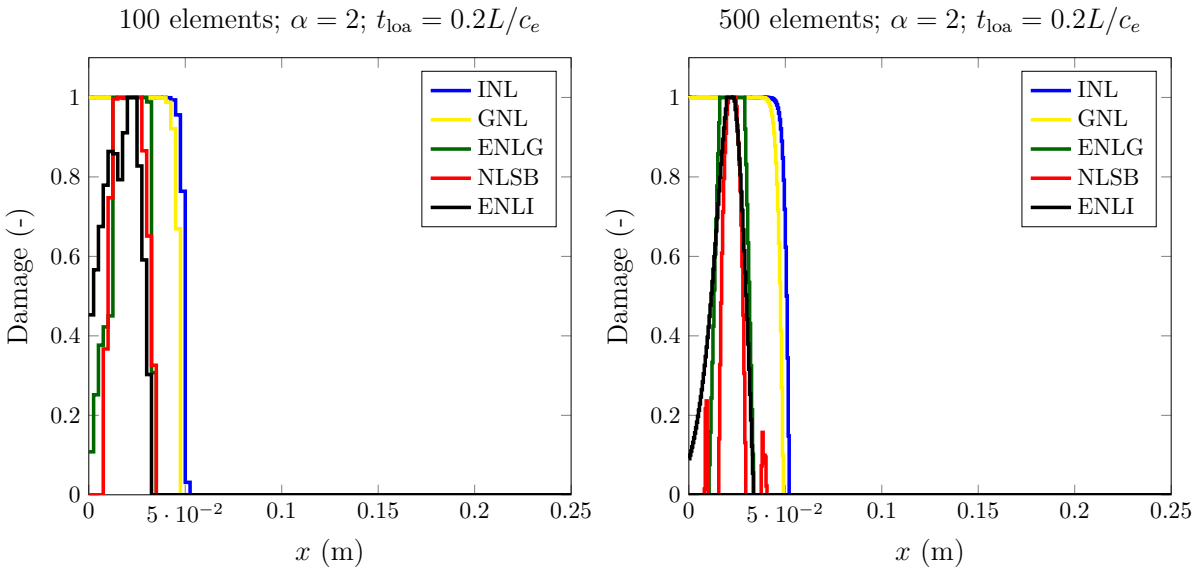

Figure 3.13 • INL, GNL, NLSB, ENLI, and ENLG damage models – Comparison of damage profiles near the boundary for $\alpha = 2$.

ENLI formulation shows a minor boundary effect compared to the INL model, but some influence on its response is still observed. Despite such a damage attraction, it is still possible to define the spall location for the ENLI formulation, as the fully damaged area does not reach the free-edge.

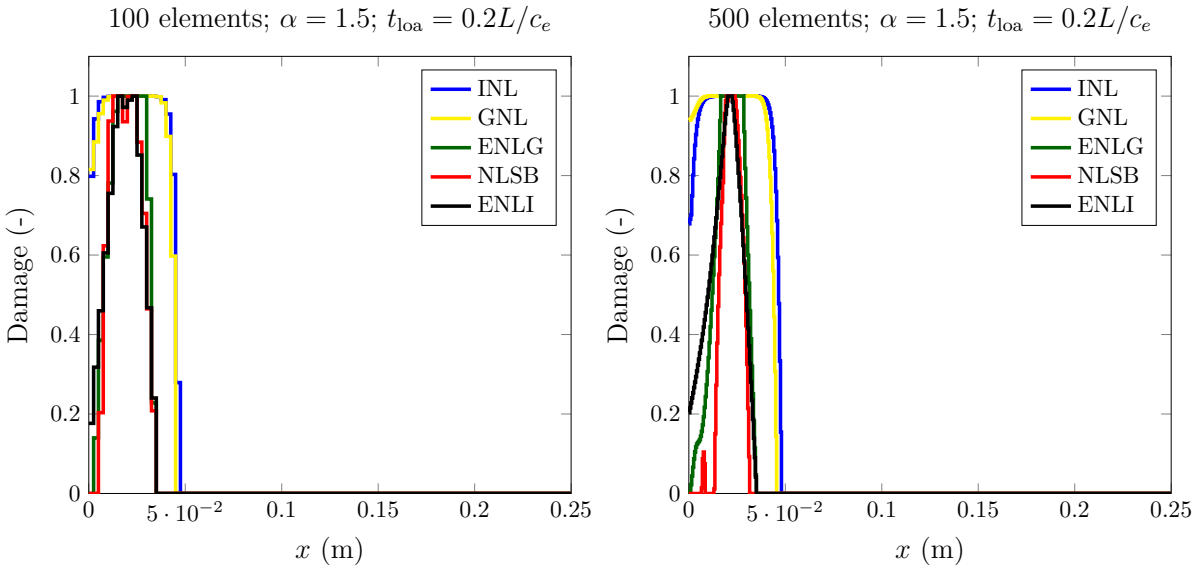

Figure 3.14 • INL, GNL, NLSB, ENLI, and ENLG damage models – Comparison of damage profiles near the boundary for $\alpha = 1.5$.

Influence of the strain rate. Figure 3.14 shows the same results, but for $\alpha = 1.5$. Decreasing α reduces the damage diffusion for all the models. The boundary effect is also reduced for the INL and GNL models (for the given problem). However, the damage value at the free-edge increases when reducing α from 2 to 1.5 for the ENLI formulation. In this

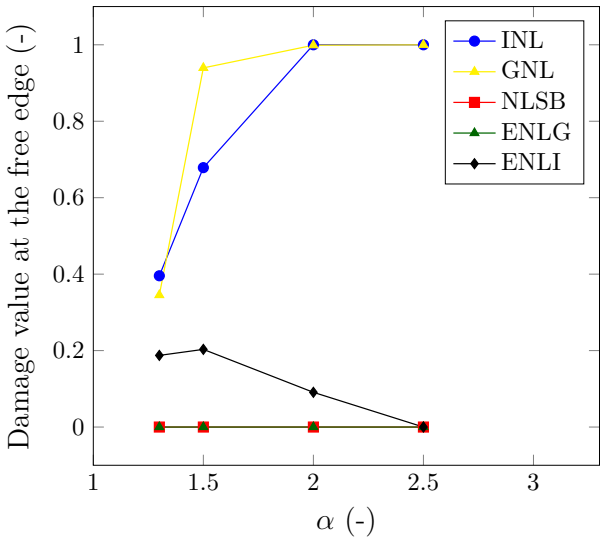

Figure 3.15 • INL, GNL, NLSB, ENLI, and ENLG damage models – Comparison regarding the effect of α on the damage value on the boundary for a mesh with 500 elements.

situation, a minor parasite effect can also be observed for the ENLG model. The NLSB model does not show any boundary effect. Still, it exhibits a small region of minor damage (also for $\alpha = 2$) in the vicinity of the main damaged zone (see Ribeiro Nogueira et al. (2022a) for a better explanation of this effect). Figure 3.15 shows the comparison between all the non-local models regarding the influence of α on the boundary effect considering only the cases where damage reaches the unity. Finally, although the ENLG formulation shows damage diffusion, the model gives more reliable results regarding the maximum damage location when the bar is submitted to higher strain rates than the ENLI model.

The spall location can be numerically estimated without any problem despite minor damage diffusion or attraction for the models with evolving interactions. One should consider, for example, the middle of the region where damage attains its maximum and compute its distance to the free-edge. This is not possible with the classic non-local formulations, as maximum damage inevitably shifts to the free-edge during the simulation, which is shown in detail in the following.

2.9 Further analyses: differences observed between models with evolving interactions

Given the results presented in the previous section, a more specific analysis may be performed to highlight better and justify the differences between the different formulations with evolving interaction distances. In particular, it is essential to understand the differences observed between the ENLG and ENLI models regarding damage diffusion, as they should give similar results. Moreover, an overall comparison between the ENLG, ENLI, and NLSB formulations is also necessary. For this purpose, one may compare the dissipated energy and the evolution of the free-surface/face velocity (*i.e.*, the velocity registered on the free-edge of the ejected part of the specimen, which corresponds to the

spalling phenomenon). The standard INL and GNL formulations are also analyzed for completeness.

A semi-analytical study is also developed in (Ribeiro Nogueira et al., 2022a) to illustrate the differences between the integral models in the computation of the non-local strain field. The observed behaviors are in agreement with the numerical results given in the following and may highlight how these models deal with existing or newly created boundaries.

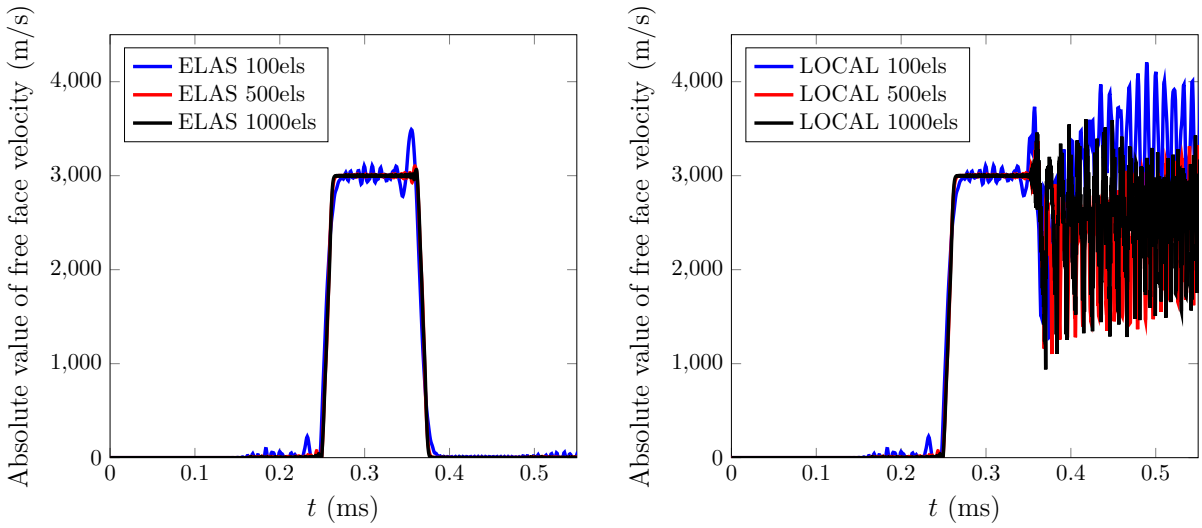

Figure 3.16 • Linear elastic (left) and local damage (right) models – Free-surface velocity profiles.

2.9.1 Free-surface velocity

As already explained, when damage attains unity in the bar, the left part of the bar is ejected. The free-face velocity (at $x = 0$ cm), *i.e.*, the so-called ejection velocity, is a good indicator of regularization and can be used to highlight the differences observed between the models studied. To this end, let us consider once again the loading case A of Section 2.8.1. The same material parameters as in the previous examples are used, and $\alpha = 1.5$ for all the models. It should be noticed that, for the numerical examples of this work, the input signal comes from the right to the left, so the free-surface velocity has a negative sign. For better comprehension, the absolute value of this velocity will be taken for the analyses presented hereafter. Comments are given using only the term "velocity", but one may consider that this refers to its absolute value.

Elastic and local damage response. The free-surface velocity obtained for a linear elastic material model is shown in Figure 3.16 (left). As expected, convergence is obtained upon mesh refinement. Moreover, one may only see the input signal which is reflected on the free-edge, given that no damage occurs. If a local damage model is considered (see, *e.g.*, Section 2.1), damage will take place at a certain distance from the free boundary (*i.e.*, the spalling distance). Figure 3.16 (right) shows the free-surface velocity profile obtained for a local damage model. In this case, mesh dependency is clearly observed after the maximum velocity value is reached.

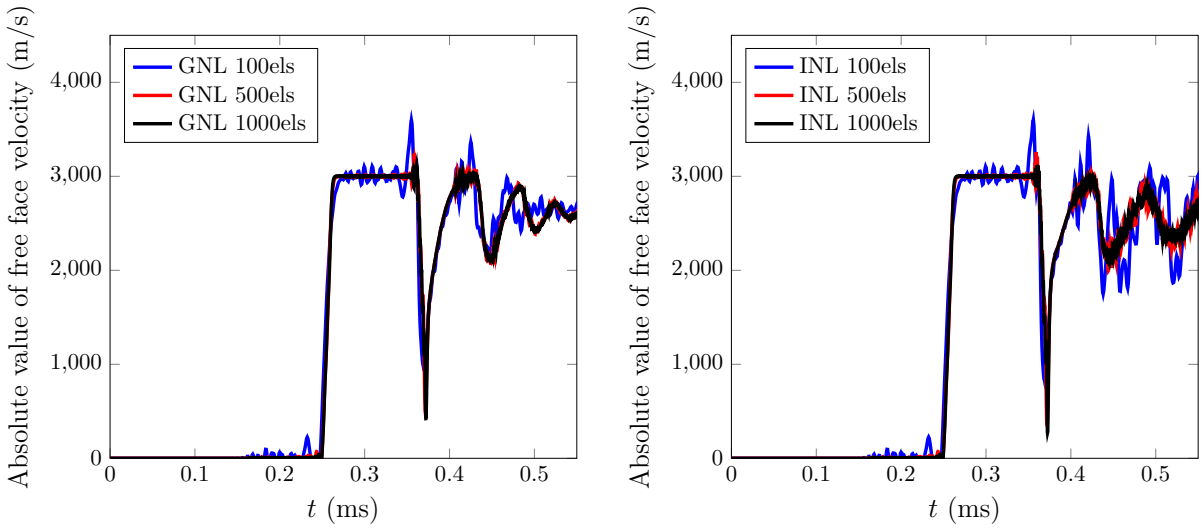

Figure 3.17 • GNL (left) and INL (right) damage models – Mesh convergence of the free-surface velocity response.

Models with fixed interaction distances. In the case of the INL and GNL models, the free-surface velocities computed for different meshes are shown in Figure 3.17. As expected, both models give similar results, but some differences exist after the first reflection on the damaged zone occurs. In both cases, one may see the subsequent periodic signals arriving at the free-edge. However, the signal periods reduce after each round trip between the free-surface and the damaged zone. This indicates that the damage profile is still evolving after damage reached unity in the middle of the damaged band. Due to damage diffusion, the velocity also attains a limit point when time passes, but this condition arrives sooner for the GNL model than for the INL one.

Models with evolving interaction distances. The limit point of the velocity is not observed for the models with evolving interactions (Figure 3.18). For the three considered formulations (ENLI, ENLG, and NLSB), the reflections due to spalling can be seen in the velocity profile. Here, the signal periods are not reduced, which indicates that there is no propagation of the damage front after damage localization. The convergence is only attained for more than 500 FEs, and the velocities given by the three considered models are similar to the ones found in (Dandekar & Bartkowski, 2001; Dandekar, 2001; Mariani & Gobat, 2019). Significantly, the ENLG model shows the same type of velocity when compared to the simulations obtained for cohesive elements in (Camacho & Ortiz, 1996). Further details concerning these aspects are provided in (Ribeiro Nogueira et al., 2022a). In any case, these results show that the ENLG regularizes the response and corroborate the analytic results obtained in Section 1.

2.9.2 Dissipated energy

To study how energy is dissipated for all the non-local models discussed in this work, loading case A is again considered assuming $\alpha = 1.5$. This choice ensures that damage attains unity for all models. However, as shown in Sections 2.8.1 and 2.8.2, models with

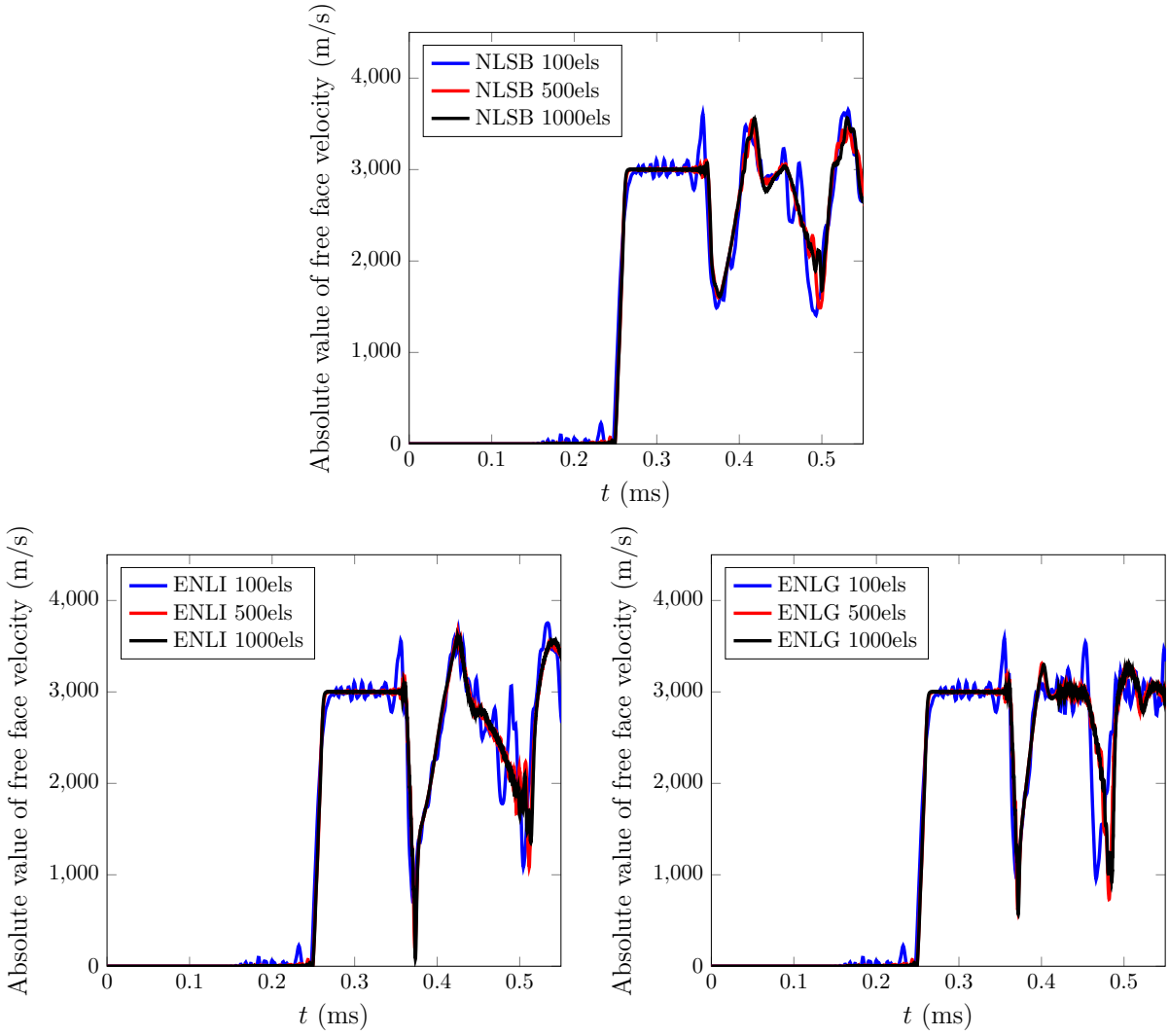

Figure 3.18 • NLSB (top), ENLI (left), and ENLG (right) damage models – Mesh convergence of the free-surface velocity response.

evolving internal length tend to spread damage over more FEs. In this work, the simple local expression of the intrinsic energy dissipation ($Y\dot{D}$) is employed. This latter quantity is computed for all time instants using a conventional numerical integration scheme and is accumulated over time. The profiles of dissipated energy along the bar are depicted in Figure 3.19 (left) for time $t = T$.

> **Remark 3.3.** *Peerlings et al. (2004) presented a thermodynamic formulation of the classic GNL approach, showing that the thermodynamic force Y remains unchanged compared to the local description. Same comments on this subject are given by Desmorat et al. (2010), following also the framework proposed by Forest (2009), regarding the micromorphic approach for damage. However, to our knowledge, there is no similar development for models considering evolving non-local interactions. It is still unclear if these formulations imply different expressions of Y. This subject is addressed in Chapter 4.*

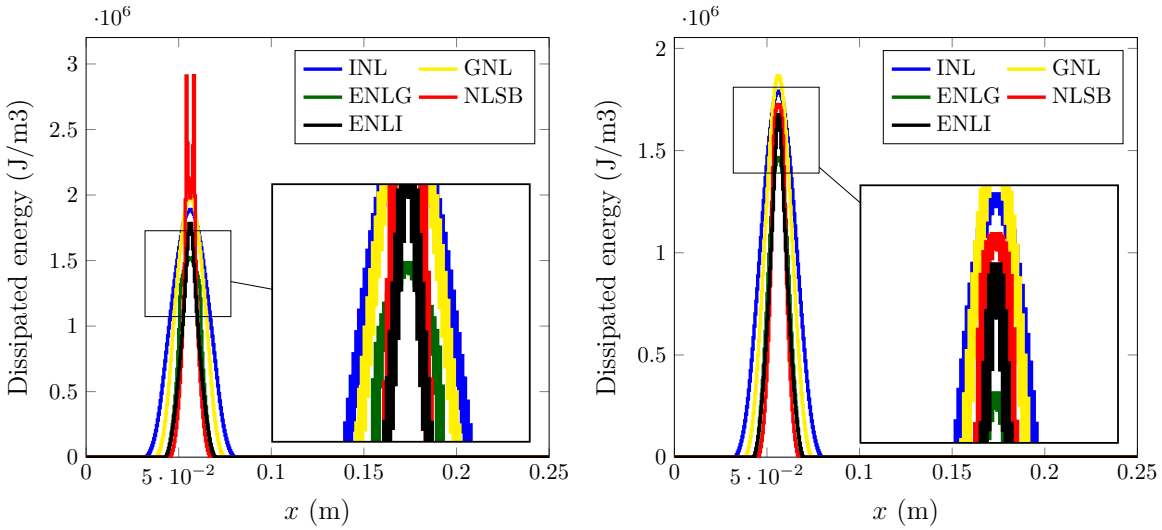

Figure 3.19 • INL, GNL, NLSB, ENLI, and ENLG damage models – Dissipated energy for $t = T$ (left) and when the maximum damage value reaches 0.99 (right).

Models with fixed distances. As expected, the widths of the zones where dissipation occurs are higher for the classical formulations than for the models with evolving interactions. The GNL model dissipates energy on a thinner region compared to the INL formulation.

Models with evolving distances. Despite the similarity observed in Figure 3.11 in terms of damage profiles obtained with all the formulations with evolving distances, one observes a huge difference in the dissipated energy between the NLSB model and the other formulations. The stress-based model continues to dissipate energy in the vicinity of the damage localization zone. Similarly, the ENLG formulation spreads the energy over a considerable zone compared to the ENLI model, thus reflecting the damage diffusion observed for this model.

Slightly different considerations can be done if one observes what happens at the time instant such that the first FE reaches a damage value of about 0.99 (Figure 3.19 (right)). In that case, models with evolving interactions give energy profiles that are similar between them but are different from those obtained through the classical approaches. Figure 3.21 shows the corresponding total dissipated energies (*i.e.*, previous results integrated over the bar). The total dissipated energy is very similar between the approaches with evolving interactions and is almost the same for the ENLG and ENLI models when $D = 0.99$. For $t = T$ (end of the analysis), the ENLG and NLSB models show an increased dissipation, whereas the dissipation no more evolves for the ENLI model. The models with evolving non-local interactions dissipate much less energy than the classic formulations with fixed distances, which is expected as the widths of the damaged zones are smaller for the evolving distances approaches.

These conclusions can also be extended to the damage profiles (Figure 3.20). The evolving non-local models give almost the same damage profiles, except for some slight differences near the highly damaged zone. Damage diffusion is observed neither for the

NLSB nor the ENLG formulations, as damage localizes in only one FE as for the ENLI model. These considerations signal that some unexpected behavior occurs when damage tends to unity, especially for the ENLG formulation, which should not diffuse damage upon localization.

It should be noticed that, from a theoretical viewpoint, eikonal formulations (ENLI or ENLG) should not continue to compute a damage evolution after localization (Desmorat et al., 2015b; Rastiello et al., 2018b; Thierry et al., 2020a). For the ENLI model, the computed effective interaction distances tend to infinity when damage tends to one. Consequently, non-local interactions vanish. The equivalent conclusion for the ENLG model is that the contributions of a highly damaged element in Equation (3.41) also tend to infinity. Thus, one should expect that after damage localization, the non-local strain field computed by the ENLG model should not evolve in the vicinity of the localized element.

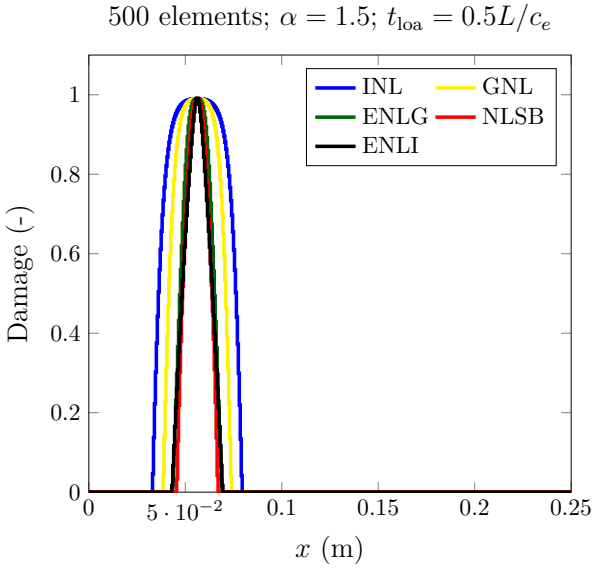

Figure 3.20 • INL, GNL, NLSB, ENLI, and ENLG damage models – Damage profiles when the first element reaches $D = 0.99$ for the different non-local model studied.

Remark 3.4. *Geers et al. (1998) encountered the same problem when implementing a similar evolving interactions gradient model based on the strain state. The strain-based gradient damage model converged to a discontinuity for high levels of damage ($D = 0.999$). Still, they argued that any further increase in damage at this moment was completely local and of numerical sources. They proposed to stop any evolution of the non-local equivalent strain inside the localized zone when a critical value of the equivalent strain was attained. Moreover, without this modification, they saw oscillations of $\bar{e}$ in the surroundings of the highly damaged regions, which was responsible for damage evolution in these zones.*

In other words, the non-local averaging and the equilibrium equations become decoupled

upon localization, which is the theoretical case for ENLG (from a physical viewpoint, micro-cracks should not interact through the new boundary created by a highly damaged zone). However, damage diffusion is much more present in the ENLG formulation, as interactions are directly computed from the FE solving of the Helmhotz-like problem. A similar behavior was described in (Geers et al., 1998) for a strain-based GNL model without the introduction of artificial modifications to decouple the equilibrium and Helmthotz equations. For ENLI, the computed distances are introduced into the weight function; therefore, the use of an integral approach is more suitable to reduce the interactions numerically.

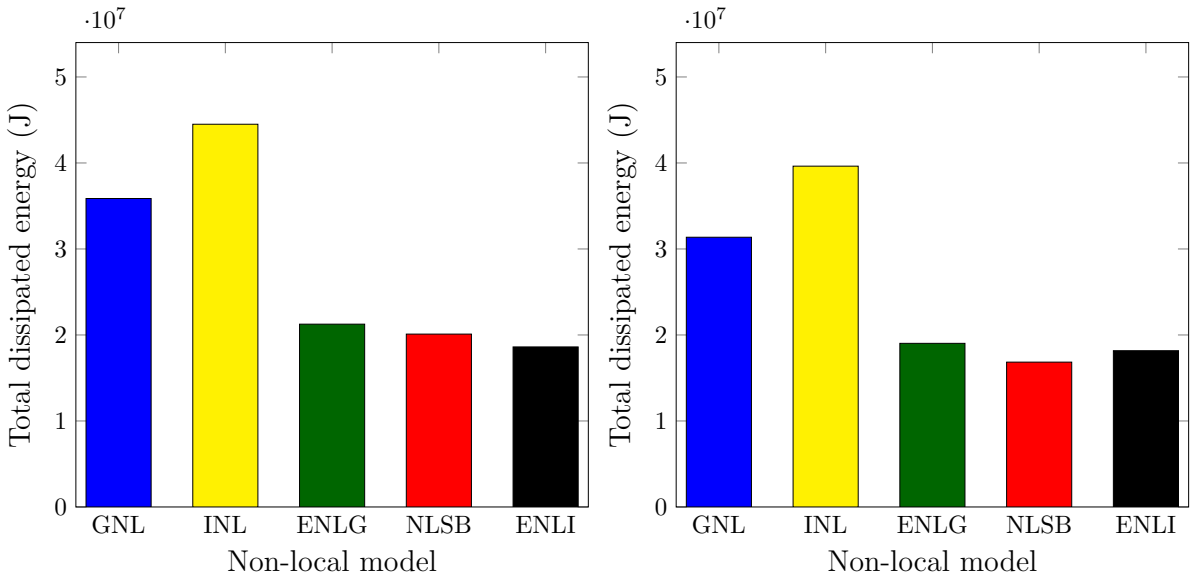

Figure 3.21 • INL, GNL, NLSB, ENLI, and ENLG damage models – Total dissipated energy for $t = T$ (left) and when damage value reaches 0.99 (right).

2.9.3 Numerically modified ENLG

To obtain a numerical approximation of the ENLG model corresponding to its theoretical assumptions, the gradient problem is restated in a modified way. Following the same arguments of Geers et al. (1998), one can decouple the non-local averaging Helmholtz-type equation from the equilibrium equation when damage tends to unity on a FE. In other words, the non-local equivalent strain is frozen in the localized FE, and interactions between FEs crossed by the damaged band vanish. One should notice that another option is to limit the evolution of the internal length (or the gradient parameter) considering the size of elements in a mesh (*e.g.*, Giry et al. (2011) and Vandoren and Simone (2018)).

From a numerical viewpoint, when damage reaches a limit value $D_c = D^\star$ at a given integration point, the second term of the left-hand-side and the right-hand-side in Equation (3.41) are multiplied by a very large value,[1] and the first term of the left-hand-side is multiplied by a null one. This corresponds to the case where damage tends to unity. Such a modification is done at the FE matrix contribution of the localized element and not in the entire domain.

[1] `numpy.inf` in the Python code used in this chapter.

As detailed in (Ribeiro Nogueira et al., 2022a), this solution allows palliating the parasite damage diffusion of the ENLG model. It is shown in the following chapters that this effect is in some ways less, but still present, in 2D and 3D quasi-static simulations with the ENLG model.

Summary of Chapter 3

Wave dispersion analysis:

- Wave propagation is **dispersive** in non-local models, which is also true for the ENLG evolving interactions approach.
- Contrarily to a local damage model, the phase velocity remains **real** and **waves do propagate** in a gradient-enhanced medium.
- GNL and ENLG models give essentially the same response at damage initiation, but **differ for higher initial strain states**.
- Loading waves can be transformed into an unique stationary harmonic localization wave, associated to a **critical wavelength** λ_c.
- For both GNL and ENLG models, λ_c decreases with the initial strain state, and the **narrowing localizing band is better described by the ENLG approach**.
- In all situations, the velocities are **limited** to the physical damaged elastic wave velocity $c_e\sqrt{1-D_0}$.

Boundary effects and damage diffusion:

- Classical non-local approaches with fixed non-local interactions are prone to drawbacks such as damage **diffusion** across damage bands and damage **attraction** from the free boundaries.
- The formulations with evolving interactions proved to be **more efficient** in dealing with boundary effects and damage diffusion, while retaining their **regularization** properties.
- The eikonal approach has shown to be more efficient in simulating the bridge between **Continuum Damage Mechanics and Fracture Mechanics** since the damage field naturally tends to localize in only one FE.
- The NLSB model has shown a **good response** when boundary effects occur, especially when the damaged band is located close to the free-edge.
- The eikonal formulations are **more sensitive** to boundary effects, but the ENLG model is **less affected** by the free boundary problem when compared to the ENLI formulation.
- The ENLG model showed, however, an **unexpected damage diffusion** upon localization. This latter spurious response can be treated by a numerical procedure limiting damage to a critical value and **freezing the interactions**.
- The ENLG model **regularizes** the response, which is in agreement with the wave dispersion analysis.

4

Differential geometry-based derivation of ENLG models using a micromorphic media framework

This chapter presents a derivation of ENLG damage models within a micromorphic media framework using differential geometry. Firstly, the boundary value problem is defined in its weak (variational) form. Then, a geometric description of the thermodynamics of the isotropic and anisotropic ENLG models is introduced. After recalling a few essential elements of differential geometry, the equations of the ENLG model are obtained, and the expressions of the stress tensor and energy dissipation are derived. The importance of adopting a differential geometry framework is emphasized by highlighting certain thermodynamic inconsistencies that arise when the ENLG model is derived using a standard micromorphic media framework. Additionally, a brief comparison with other formulations is presented, along with comments on the regularization properties of the ENLG are provided through a bifurcation analysis. Finally, numerical simulations are illustrated to compare the GNL and ENLG models regarding structural responses, damage profiles, and "pseudo-crack" paths. Apart from some text modifications, additional developments, comments and figures, this chapter was extracted from Ribeiro Nogueira et al. (2024a), Engineering Fracture Mechanics, 295, 109670.

Contents

1 Introduction

One of the main criticisms of non-local regularization techniques is that they lack a well-defined thermodynamic background. In these models, the variable controlling damage growth is usually taken as the non-local equivalent strain, whereas the damage variable remains purely local. Thus, the intrinsic energy dissipation is evaluated following the standard thermodynamics theory (i.e., no effects of non-locality are taken into account in the free-energy potential).

To overcome this issue, Peerlings et al. (2004) proposed a thermodynamics framework for deriving the GNL model. The non-local equivalent strain and its gradient were considered state variables in the free-energy potential, together with damage and the displacement field. To account for non-local interactions and the exchange of energy in the entire body, the Clausius-Duhem inequality was globally verified (i.e., the positivity of the total dissipation on the whole body was exploited). Constitutive relations were derived following usual arguments, leading to a modification of the elasticity law. The Helmholtz differential equation was derived with no need to define some generalized stresses. A very similar free-energy potential was proposed in (Forest, 2009), where the micromorphic approach was used to derive the same equations of the model, with the explicit contribution of generalized terms in the local energy balance. Other equivalent techniques introduce a residual term, respecting an insulation condition, in the point-wise Clausius-Duhem inequality, taking into account the energy exchange between neighbor points (Polizzotto et al., 1998; Borino et al., 1999; Polizzotto, 2003).

In this chapter, a differential geometry-based derivation of the ENLG formulation is presented based on a micromorphic media framework (Forest, 2009). A form of the free

energy potential is then proposed. In this formulation, the non-local strain is considered a morphological description of the abstract differentiable manifold where the Riemannian metric is defined (i.e., it is defined on a Riemannian space deformed by damage). Figure 4.1 depicts a qualitative representation of the curved space. An exponential isotropic damage profile was considered in one direction to compute the metric field. From top left to bottom right, snapshots are given at increasing damage levels in the middle of the damaged band. The red line represents the geodesic path between two points separated by the damaged zone. Computations were carried out with the SageManifolds project, within the open-source SageMath software (The Sage Developers, 2022). Similar results where obtained by (Rastiello et al., 2018b) using a Fast-Marching method to solve the Hamilton-Jacobi equation controlling damage dependent non-local interaction distances.

Employing differential geometry concepts, all the equations of the ENLG non-local model are derived. It is also shown that the expression of the energy dissipation for the ENLG model differs from the usual ones considered in the classic non-local models.

2 ENLG model

This section presents the ENLG model considering a second-order damage tensor ($\mathbf{D}$) for describing material degradation (its principal components take values between zero (sound material) to unity (totally damaged material) in the corresponding directions). First, the variational boundary value problem to be solved is introduced in its general anisotropic framework. The formulation concerning the isotropic damage case is then introduced as a special case.

2.1 ENLG boundary value problem (BVP)

The ENLG regularization (Desmorat et al., 2015b) naturally considers non-local interactions which are function of the damage state (represented through the second-order damage tensor $\mathbf{D}$). This agrees with the desired characteristics described by (Bažant et al., 2022a) for non-local models to represent the crack-parallel stresses well. The resulting differential problem to be solved was already introduced in Equations (5.1) and (5.2).

Let us consider a n-dimensional solid body $\Omega \subset \mathbb{R}^n$, with $n \in [\![1, 3]\!]$ (Figure 4.2). The boundary $\partial\Omega \subset \mathbb{R}^n$ of the body is split into two subdomains $\partial\Omega_F \subset \mathbb{R}^n$ and $\partial\Omega_u \subset \mathbb{R}^n$ such that $\partial\Omega = \overline{\partial\Omega_F \cup \partial\Omega_u}$ and $\partial\Omega_F \cap \partial\Omega_u = \emptyset$. Neumann conditions are applied on $\partial\Omega_F$ and Dirichlet conditions on $\partial\Omega_u$. Quasi-static conditions are considered. Given this choice, the time dependence of all quantities is omitted in the following, and all the variables introduced should be referred to the present time $t \in [0, T]$ with T being the total time.

Admissibility spaces. Let us introduce the following functional spaces:

$$\mathcal{U} = \{\boldsymbol{w} \ \mid \ \boldsymbol{w} \in H^1(\Omega) \ \ , \ \ \boldsymbol{w} = \boldsymbol{u}^d \ \text{ on } \partial\Omega_u\} \tag{4.1}$$

$$\mathcal{U}(\mathbf{0}) = \{\boldsymbol{w} \ \mid \ \boldsymbol{w} \in H^1(\Omega) \ \ , \ \ \boldsymbol{w} = \mathbf{0} \ \text{ on } \partial\Omega_u\} \tag{4.2}$$

$$\mathcal{V} = \{w \ \mid \ w \in H^1(\Omega)\} \tag{4.3}$$

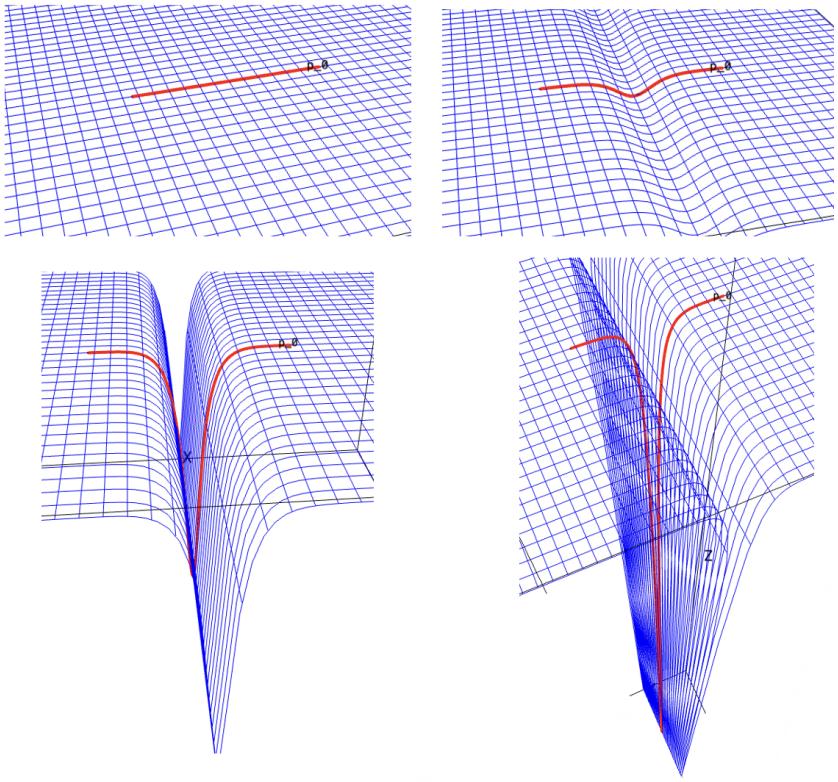

Figure 4.1 • Qualitative representation of damage curving the space where non-local interactions take place.

where $\boldsymbol{u}^d = \boldsymbol{u}^d(\boldsymbol{x}) : \partial\Omega_u \to \mathbb{R}^n$ is the imposed displacement on $\partial\Omega_u$ and H^1 denotes a square integrable Sobolev space.

Equilibrium problem. Neglecting body forces, and under quasi-static conditions, the variational equilibrium problem to be solved consists in finding at each time t, the admissible displacement field $\boldsymbol{u} \in \mathcal{U}$ satisfying:

$$\int_\Omega \boldsymbol{\sigma}(\boldsymbol{\varepsilon}(\boldsymbol{u}), \mathbf{D}) : \boldsymbol{\varepsilon}(\boldsymbol{v})\, dV = \int_{\partial\Omega} \boldsymbol{t}^d \cdot \boldsymbol{v}\, dS \quad \forall\, \boldsymbol{v} \in \mathcal{U}(\mathbf{0}). \tag{4.4}$$

where $\boldsymbol{u} = \boldsymbol{u}(\boldsymbol{x}) : \Omega \to \mathbb{R}^n$ is the displacement vector field, $\boldsymbol{v} = \boldsymbol{v}(\boldsymbol{x}) : \Omega \to \mathbb{R}^n$ is a virtual displacement field, $\boldsymbol{\sigma}(\boldsymbol{\varepsilon}(\boldsymbol{u}), \mathbf{D})$ is the Cauchy stress tensor, $\boldsymbol{\varepsilon}(\boldsymbol{u})$ (respectively, $\boldsymbol{\varepsilon}(\boldsymbol{v})$) is the small strain tensor applied to $\boldsymbol{u}$ (respectively, $\boldsymbol{v}$), ":" denotes the double contraction between tensors, and $\boldsymbol{t}^d = \boldsymbol{t}^d(\boldsymbol{x}) : \partial\Omega_F \to \mathbb{R}^n$ is the imposed traction vector on $\partial\Omega_F$.

Damage problem. The variational form of the Helmholtz Equation (5.1) reads:

$$\int_\Omega \sqrt{\det \mathbf{g}}\, \bar{e}\, \eta\, dV - \int_\Omega c\nabla \cdot (\sqrt{\det \mathbf{g}}\, \mathbf{g}^{-1} \cdot \nabla \bar{e})\, \eta\, dV = \int_\Omega \sqrt{\det \mathbf{g}}\, e\, \eta\, dV \quad \forall\, \eta \in \mathcal{V} \tag{4.5}$$

where $\eta = \eta(\boldsymbol{x}) : \Omega \to \mathbb{R}$ is a virtual non-local equivalent strain field. Using the identity:

$$c\nabla \cdot (\sqrt{\det \mathbf{g}}\, \mathbf{g}^{-1} \cdot \nabla \bar{e}\, \eta) = c\nabla \cdot (\sqrt{\det \mathbf{g}}\, \mathbf{g}^{-1} \cdot \nabla \bar{e})\eta + c(\sqrt{\det \mathbf{g}}\, \mathbf{g}^{-1} \cdot \nabla \bar{e}) \cdot \nabla \eta \tag{4.6}$$

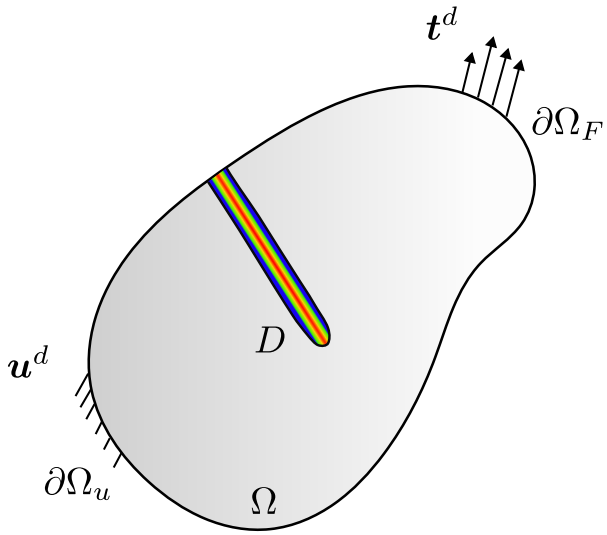

Figure 4.2 • Domain and boundary conditions.

equation (4.5) can be rewritten as:

$$\int_\Omega \sqrt{\det \mathbf{g}}\,\bar{e}\,\eta\,dV - \int_{\partial\Omega} c\sqrt{\det \mathbf{g}}\,\eta\,(\mathbf{g}^{-1}\cdot\nabla\bar{e})\cdot\boldsymbol{n}\,dS + \int_\Omega c(\sqrt{\det \mathbf{g}}\,\mathbf{g}^{-1}\cdot\nabla\bar{e})\cdot\nabla\eta\,dV = \int_\Omega \sqrt{\det \mathbf{g}}\,e\,\eta\,dV \quad \forall\eta\in\mathcal{V} \tag{4.7}$$

Taking into account for the Neumann zero flux condition (5.2), one obtains the final problem to be solved. It consists in finding at each time t the field $\bar{e}\in\mathcal{V}$ satisfying:

$$\int_\Omega \sqrt{\det \mathbf{g}}\,\bar{e}\,\eta\,dV + \int_\Omega (c\sqrt{\det \mathbf{g}}\,\mathbf{g}^{-1}\cdot\nabla\bar{e})\cdot\nabla\eta\,dV = \int_\Omega \sqrt{\det \mathbf{g}}\,e\,\eta\,dV \quad \forall\eta\in\mathcal{V} \tag{4.8}$$

The variational formulation of the GNL model by (Peerlings et al., 1996a) is retrieved by considering $\mathbf{g}=\mathbf{g}^{-1}=\mathbf{I}$ (*i.e.*, the Euclidean metric).

2.2 Isotropic ENLG model as a special case

Simplified two- (2D) and three-dimensional (3D) isotropic damage mechanics formulations can be obtained by considering specific metrics. In the following, the 3D, full 2D, plane-stress, and plane-strain problems are treated separately for completeness.

3D problem. The isotropic 3D Helmholtz problem to be solved can be derived considering $\mathbf{D}=D\mathbf{I}$, such that the metric tensor reads:

$$\mathbf{g}=\frac{\mathbf{I}}{1-D} \tag{4.9}$$

Observing that:

$$\det\mathbf{g}=\frac{1}{(1-D)^3}\,;\quad \mathbf{g}^{-1}=(1-D)\mathbf{I}\,;\quad \sqrt{\det\mathbf{g}}\,\mathbf{g}^{-1}=\frac{1}{\sqrt{1-D}}\mathbf{I} \tag{4.10}$$

equations (5.1) and (5.2) can be simplified as:

$$\bar{e} - c\sqrt{(1-D)^3}\nabla\cdot\left(\frac{1}{\sqrt{1-D}}\nabla\bar{e}\right) = e \qquad \text{on } \Omega \tag{4.11}$$

$$\nabla\bar{e}\cdot\boldsymbol{n} = 0 \qquad \text{on } \partial\Omega \tag{4.12}$$

where we exploited the condition $1-D>0$ to simplify the Neumann boundary condition. The variational equation (4.8) can thus be rewritten as:

$$\int_\Omega \frac{1}{\sqrt{(1-D)^3}}\,\bar{e}\,\eta\,dV + \int_\Omega \frac{c}{\sqrt{1-D}}\nabla\bar{e}\cdot\nabla\eta\,dV = \int_\Omega \frac{1}{\sqrt{(1-D)^3}}\,e\,\eta\,dV \quad \forall\eta\in\mathcal{V} \tag{4.13}$$

2D Plane-stress and plane-strain conditions. The equations introduced above can be used to address the situations of plane-stress and plane-strain, as well as full 2D conditions:

(*i*) *Plane-strain conditions.* The complete 3D equations (4.11)-(4.12) are still applicable since the out-of-plane component of $\nabla\bar{e}$ can be assumed null whereas the out-of-plane component of the damage tensor can be assumed to be the same as in the other directions.

(*ii*) *Plane-stress conditions.* In this case one can assume the size of the domain in the out-of-plane direction to be negligible with respect to other dimensions. As a consequence, $\nabla\bar{e}$ has in-plane components only and the Riemannian metric can be written as:

$$\mathbf{g} = \frac{\mathbf{I_2}}{1-D} \tag{4.14}$$

where $\mathbf{I_2}$ denotes the in-plane identity tensor. According to this choice:

$$\det\mathbf{g} = \frac{1}{(1-D)^2}\,; \quad \mathbf{g}^{-1} = (1-D)\mathbf{I_2}\,; \quad \sqrt{\det\mathbf{g}}\,\mathbf{g}^{-1} = \mathbf{I_2} \tag{4.15}$$

Equations (5.1) and (5.2) can be finally simplified as:

$$\bar{e} - c(1-D)\nabla\cdot\nabla\bar{e} = e \qquad \text{on } \Omega \tag{4.16}$$

$$\nabla\bar{e}\cdot\boldsymbol{n} = 0 \qquad \text{on } \partial\Omega \tag{4.17}$$

The variational equation to be solved finally reads:

$$\int_\Omega \frac{1}{1-D}\,\bar{e}\,\eta\,dV + \int_\Omega c\nabla\bar{e}\cdot\nabla\eta dV = \int_\Omega \frac{1}{1-D}\,e\,\eta\,dV \quad \forall\eta\in\mathcal{V} \tag{4.18}$$

(*iii*) *Full 2D conditions.* Equations (4.16), (4.17) and (4.18) also hold in full 2D conditions.

3 Differential geometry viewpoint to the thermodynamics of ENLG models

Starting from a free-energy potential inspired by the one proposed by (Peerlings et al., 2004) for deriving the GNL model, this section gives the first insights into a possible

thermodynamics framework to derive the ENLG model. The method is based on the formalism presented by (Forest, 2009) for micromorphic media. It is shown that non-locality comes into the picture in the expression of the stress tensor (even in elastic conditions) and affects the intrinsic dissipation. This latter can no more be computed using the standard expression valid for local models, as for the GNL model.

3.1 Geometric description

Two different spaces are used in the eikonal problem:

(*i*) A Euclidean space, where the body Ω is placed in a given configuration;

(*ii*) A Riemannian space, where non-local interactions are computed. In the latter case, a tangent space is defined at each point of an abstract differentiable manifold $\mathcal{M}$ (i.e., a topological manifold with a globally defined differential structure), where the metric $\mathbf{g}$ defines a scalar product.

To derive the formulation, the non-local equivalent strain is seen as a morphological descriptor and is an element of $\mathcal{M}$ (see (Mariano & Stazi, 2005) for further discussions). This idea directly stems from the theoretical assumption that damage curves the space where the non-local interactions are computed (Desmorat et al., 2015b). Similar ideas were presented in (Ganghoffer & de Borst, 2000; Ganghoffer, 2003), where a metric was coupled with an internal variable distribution. In their work, the strength of interactions is incorporated into the space's geometry, and their effect on the curvature is discussed.

Other contributions where geometric concepts are used to describe damage behaviors exist. For instance, (Steinmann & Carol, 1998) proposed a geometric framework for second-order tensorial damage coupled to hyperelasticity. They introduced the concept of energy metric and its degradation to a damage metric, whose evolution is described by a dissipation surface. The free-energy was defined then as a function of the degraded metric. Similarly, (Das et al., 2021) introduced damage-dependent Riemannian metrics in undeformed and deformed damage configurations for modeling compressible elastomers. They supposed that these metrics could be obtained by scaling the Euclidean one with a function in terms of an isotropic damage variable. The introduction of damage gradients in the free-energy was a consequence of considering the influence of the Ricci scalar curvature. They highlighted that "...the curvature might be negative and that it tends to infinity as D approaches 1, which is indicative of a singularity consistent with the physical understanding of damage.". General geometric analysis was used in (Mariano, 2010). This author discussed introducing the so-called curvature varifolds terms in the energy functional to describe crack patterns through measures in a fiber bundle. The minimization problem searches, therefore, for admissible solutions over a class of possible cracked bodies. He also provides a few more insights on considering a morphological descriptor (and its gradient) in the expression of the energy for studying crack nucleation.

3.2 A few useful elements of differential geometry

In curved spaces, contravariant and covariant coordinates differ. The basic rules are: (*i*) if $\boldsymbol{a}$ is a vector living in a vectorial space E, then its coordinates are represented by a^i (with upper index); (*ii*) if $\boldsymbol{a}$ is a covector living in the dual space E^*, then its coordinates are represented by a_i (with lower index); (*iii*) metric tensors are totally symmetric (and positive definite) second-order tensors of covariant nature. The metric tensor $\mathbf{g} \in \mathrm{E}^* \times \mathrm{E}^*$ is represented by its covariant components g_{ij}, and the metric inverse $\mathbf{g}^{-1} \in \mathrm{E} \times \mathrm{E}$ is represented by its contravariant components g^{ij}; (*iv*) only upper and lower indexes can be contracted; (*v*) the covector $\boldsymbol{a}_\#$ (of components $(a_\#)_i$) associated with vector $\boldsymbol{a}$ is given by:

$$\boldsymbol{a}_\# = \mathbf{g} \cdot \boldsymbol{a} \tag{4.19}$$

whereas the vector $\boldsymbol{b}^\flat$ (of components $(b^\flat)^i$) associated with covector $\boldsymbol{b}$ is given by:

$$\boldsymbol{b}^\flat = \mathbf{g}^{-1} \cdot \boldsymbol{b} \tag{4.20}$$

Scalar product. The scalar product between two covectors $\boldsymbol{b}$ and $\boldsymbol{c}$ is defined as:

$$\langle \boldsymbol{b}, \boldsymbol{c} \rangle_{\mathbf{g}} := \boldsymbol{b} \cdot \boldsymbol{c}^\flat = \boldsymbol{b} \cdot \mathbf{g}^{-1} \cdot \boldsymbol{c} \tag{4.21}$$

Gradient of a function. In local coordinates (x^i), $(\partial_i = \partial/\partial x^i)$ denotes the basis of the tangent space $\mathrm{T}_{\boldsymbol{x}}\mathcal{M}$ and dx^i is the dual basis of the cotangent space $\mathrm{T}^\star_{\boldsymbol{x}}\mathcal{M}$ for $\boldsymbol{x} \in \mathcal{M}$ (it is such that $dx^i(\partial_j) = \delta^i_j$).

The derivative df of a function $f : \mathcal{M} \to \mathbb{R}$ is the 1-form of covariant components $df_i = \partial_i f$. The gradient of f is therefore the vector of contravariant components $(\nabla f)^i = \partial^i f$:

$$\nabla f = df^\flat = \mathbf{g}^{-1} \cdot df \tag{4.22}$$

In the case of Euclidean spaces, one can easily show that the gradient ∇f and the 1-form df do not differ, i.e., $\nabla f = df$.

The Riemannian norm of the gradient $\|\nabla f\|_{\mathbf{g}}$ is defined as:

$$\|\nabla f\|^2_{\mathbf{g}} = \langle \nabla f, \nabla f \rangle_{\mathbf{g}} = \nabla f \cdot \mathbf{g} \cdot \nabla f = df \cdot \mathbf{g}^{-1} \cdot df = \langle df, df \rangle_{\mathbf{g}} = \|df\|^2_{\mathbf{g}} \tag{4.23}$$

Laplacian of a function. The divergence of the gradient on a manifold is the so-called "connection Laplacian" or "Laplace-Beltrami operator". It is defined as:

$$\Delta f := \nabla \cdot \nabla f = \frac{1}{\sqrt{\det \mathbf{g}}} d\left(\sqrt{\det \mathbf{g}}\, \mathbf{g}^{-1} \cdot df \right). \tag{4.24}$$

In Euclidean spaces, the Laplace-Beltrami operator generalizes the usual Laplacian definition, i.e., $\Delta f = d \cdot (df) = \nabla \cdot (\nabla f)$.

Following the so-called "micromorphic media theory" (Forest, 2009), $\bar{e}$ is taken as the micromorphic variable, while e is its equivalent macro quantity. As a result, $\boldsymbol{u}$ and $\bar{e}$ are the unknowns of the problem.

3.3 Damage-deformed Riemannian space

Let us assume that damage is represented through an Euclidean second order tensor $\mathbf{D} \in \mathrm{E}^* \times \mathrm{E}^*$ of covariant components D_{ij}. According to the Eikonal damage approach, in the Riemannian space curved by damage, the metric and its inverse read:

$$\mathbf{g} = (\mathbf{q}^{-1} - \mathbb{I}^\flat : \mathbf{D})^{-1} \tag{4.25}$$

$$\mathbf{g}^{-1} = \mathbf{q}^{-1} - \mathbb{I}^\flat : \mathbf{D} \tag{4.26}$$

where $\mathbf{q} = \mathbf{I} = \delta_{ij}$ and $\mathbb{I}^\flat \in \mathrm{E} \times \mathrm{E} \times \mathrm{E} \times \mathrm{E}$ is the Euclidean contravariant 4th-order identity tensor such that:

$$\mathbb{I}^\flat = \mathbf{q}^{-1} \,\underline{\overline{\otimes}}\, \mathbf{q}^{-1} \tag{4.27}$$

where $\underline{\overline{\otimes}}$ denotes the standard symmetrized tensor product. Similarly, tensor the covariant identity tensor $\mathbb{I}_\# \in \mathrm{E}^* \times \mathrm{E}^* \times \mathrm{E}^* \times \mathrm{E}^*$, the mixed contravariant-covariant fourth-order identity tensor ${\mathbb{I}^\flat}_\# \in \mathrm{E} \times \mathrm{E} \times \mathrm{E}^* \times \mathrm{E}^*$ and the conjugated mixed covariant-contravariant fourth-order identity tensor $\mathbb{I}_\#{}^\flat \in \mathrm{E}^* \times \mathrm{E}^* \times \mathrm{E} \times \mathrm{E}$ are defined as:

$$\mathbb{I}_\# = \mathbf{q} \,\underline{\overline{\otimes}}\, \mathbf{q} \tag{4.28}$$

$${\mathbb{I}^\flat}_\# = \mathbb{I}^\flat : \mathbb{I}_\# = \mathbf{q}^{-1} \,\underline{\overline{\otimes}}\, \mathbf{q} \tag{4.29}$$

$$\mathbb{I}_\#{}^\flat = \mathbb{I}_\# : \mathbb{I}^\flat = \mathbf{q} \,\underline{\overline{\otimes}}\, \mathbf{q}^{-1} \tag{4.30}$$

> **Remark 4.1.** *Given three tensors* $\mathbf{S} \in \mathrm{E} \times \mathrm{E}$, $\mathbf{U} \in \mathrm{E} \times \mathrm{E}$ *and* $\mathbf{T} \in \mathrm{E}^* \times \mathrm{E}^*$ *one has:* $(\mathbf{S} \,\underline{\overline{\otimes}}\, \mathbf{U}) : \mathbf{T} = \mathbf{S} \cdot \mathbf{T} \cdot \mathbf{U}$. *Given a covariant tensor* $\mathbf{T} \in \mathrm{E}^* \times \mathrm{E}^*$ *and a contravariant second order tensor* $\mathbf{S} \in \mathrm{E} \times \mathrm{E}$, *one has:* $\mathbf{T}^\flat = \mathbb{I}^\flat : \mathbf{T}$, $\mathbf{S}_\# = \mathbb{I}_\# : \mathbf{S}$, $\mathbf{T} = \mathbb{I}_\#{}^\flat : \mathbf{T}$, *and* $\mathbf{S} = {\mathbb{I}^\flat}_\# : \mathbf{S}$.

In the undamaged medium (i.e., in the Euclidean space), one has:

$$\mathbf{g} = \mathbf{q} = \mathbf{I} = \delta_{ij} \qquad \mathbf{g}^{-1} = \mathbf{q}^{-1} = \mathbf{I}^{-1} = \delta^{ij} \tag{4.31}$$

so that (4.21) defines the standard scalar product. Based on this description, the isotropic elasticity law can be easily rewritten as:

$$\boldsymbol{\sigma} = 2G\mathbb{I}^\flat : \boldsymbol{\varepsilon} + \lambda \mathrm{Tr}(\mathbf{q}^{-1} \cdot \boldsymbol{\varepsilon})\mathbf{q}^{-1} \tag{4.32}$$

with G and λ denoting the two Lamé parameters. Notice that according to previous equation $\boldsymbol{\varepsilon}$ is a covariant tensor (components ε_{ij}) whereas $\boldsymbol{\sigma}$ is a contravariant tensor (components σ^{ij}).

> **Remark 4.2.** *If one considers* $\mathbf{g}$ *as a tensor-valued function of* $\mathbf{D}$, *as it is the case of Ladevèze's damage variable (see Chapter 1), the standard definition* $\mathbf{g} = (\mathbf{I} - \mathbf{D})^{-1}$ *still holds. The inverse is taken in function of the principal values of* $\mathbf{D}$, *while retaining its covariant nature.*

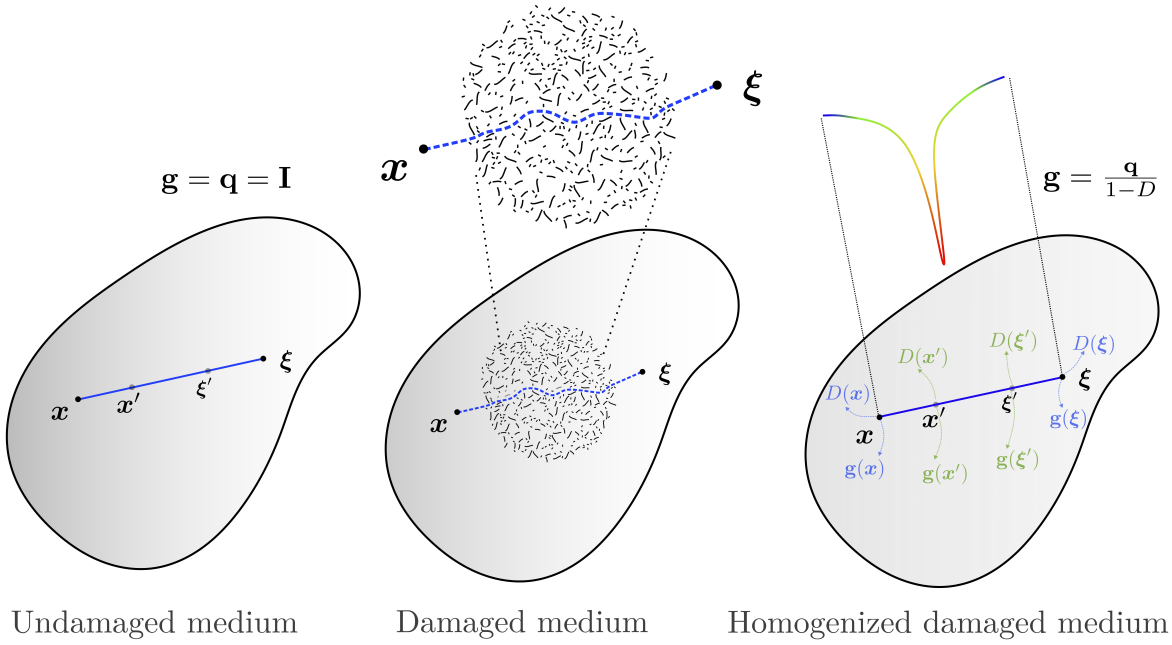

Figure 4.3 • Illustrative scheme of the Riemannian metric in an isotropic damaged medium.

Qualitative representation of the damage-dependent Riemannian metric. To illustrate the idea behind using a modified metric for computing the non-local interactions, let us consider first the case of isotropic damage. As explained in Chapter 2, the non-local fields are computed based on the notion of interaction distances. In the Eikonal approach, one has interaction Euclidean distances (see Equation (4.31)) for an undamaged medium (Figure 4.3 left). In other words, the distance between two material points $\boldsymbol{x}$ and $\boldsymbol{\xi}$ is a straight line.

For a damaged medium, the "communication path" between points $\boldsymbol{x}$ and $\boldsymbol{\xi}$ is rather tortuous than straight (see Figure 4.3 middle) due to the micro-cracks, and the distance increases with damage. If the micro-cracks are randomly orientated, one retrieves the case of isotropic damage. On average, the path is the same for all the possible directions from point $\boldsymbol{x}$ in this case. For highly damaged mediums, the elevated density of micro-cracks can make it impossible to find a path through which the points may interact (vanishing non-local interactions).

Within the framework of CDM, the damaged state is described by an equivalent homogenized medium. In the case of isotropic damage, the micro-cracks are represented by the scalar D, and the Riemannian metric is obtained by scaling the Euclidean one with the factor $1/(1-D)$. Therefore, points $\boldsymbol{x}$ and $\boldsymbol{\xi}$ are connected by a sort of **slower** path, depending on the damage state of all the points $\boldsymbol{x}'$ and $\boldsymbol{\xi}'$ belonging to it. As, shown in Figure 4.3 right, this is equivalent to consider a curved path defined by the Riemannian metric $\mathbf{g}$.

When the micro-cracks have a notable preferential direction (denoted by the number 1 in Figure 4.4), the damage state can be described by a single tensor variable $\mathbf{D}$. For instance, this situation can occur in the case of tension loading following the principal

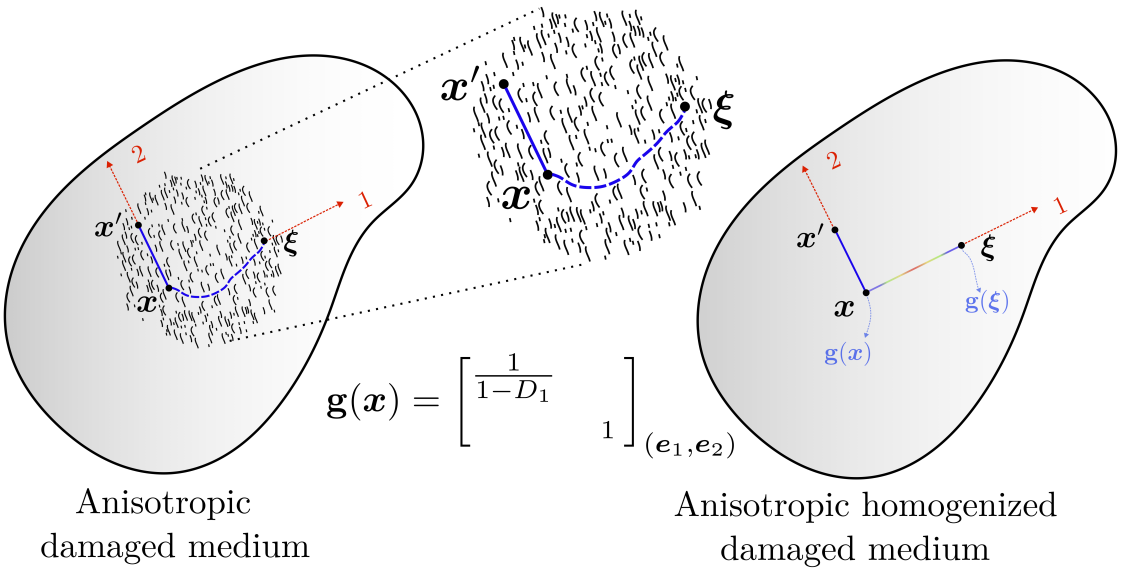

Figure 4.4 • Illustrative scheme of the Riemannian metric in an anisotropic damaged medium.

direction 1. As shown in Figure 4.4 left, points $\boldsymbol{x}$ and $\boldsymbol{x}'$ hardly see the effect of the micro-cracks in the damaged medium, and a straight path can still connect them. On the contrary, the communication path between $\boldsymbol{x}$ and $\boldsymbol{\xi}$ is no more straight, given that the micro-cracks are perpendicular to the principal direction.

In the equivalent homogenized medium (Figure 4.4 right), this can be represented by the anisotropic metric. Considering the 2D case for simplicity with the only non-zero damage principal component D_1, and writing the metric in its eigenbasis, one can easily see that this last is only affected in the principal direction 1. Thus, interactions decrease in the direction of major damage, representing the induced anisotropic character of the ENLG model.

3.4 Micromorphic media framework

Extended virtual power principle. Neglecting contact and volume forces, the virtual power principle reads:

$$\mathcal{P}^*_{\text{int}}(\boldsymbol{v}^*, \dot{\eta}^*) + \mathcal{P}^*_{\text{ext}}(\boldsymbol{v}^*, \dot{\eta}^*) = 0 \quad \forall\, \boldsymbol{v}^*, \dot{\eta}^* \tag{4.33}$$

where $\boldsymbol{v}^*$ and $\dot{\eta}^*$ are the virtual velocity and the virtual variation rate of $\bar{e}$, respectively. The generalized virtual powers of the internal ($\mathcal{P}^*_{\text{int}}$) and external ($\mathcal{P}^*_{\text{ext}}$) forces read (Forest, 2009):

$$\mathcal{P}^*_{\text{int}}(\boldsymbol{v}^*, \dot{\eta}^*) = -\int_\Omega \underbrace{\left(\boldsymbol{\sigma} : \boldsymbol{\varepsilon}(\boldsymbol{v}^*) + a\,\dot{\eta}^* + \boldsymbol{b} \cdot \nabla \dot{\eta}^*\right)}_{:= p^{(i)}(\boldsymbol{v}^*, \dot{\eta}^*)} dV \tag{4.34}$$

$$\mathcal{P}^*_{\text{ext}}(\boldsymbol{v}^*, \dot{\eta}^*) = \int_\Omega \left(a^e \dot{\eta}^* + \boldsymbol{b}^e \cdot \nabla \dot{\eta}^*\right) dV + \int_{\partial\Omega} \left(\boldsymbol{t}^d \cdot \boldsymbol{v}^* + a^c \dot{\eta}^*\right) dS \tag{4.35}$$

where a and $\boldsymbol{b}$ are generalized stresses related to the micromorphic variable and its first gradient, a^e and $\boldsymbol{b}^e$ are the generalized body forces, and a^c are the generalized tractions applied on the boundary $\partial\Omega$.

Exploiting the arbitrary nature of the virtual velocity fields $(\boldsymbol{v}^*, \dot{\eta}^*)$, one obtains the following momentum balance equations and the corresponding boundary conditions:

$$\nabla \cdot \boldsymbol{\sigma} = \mathbf{0} \qquad \text{on } \Omega \tag{4.36}$$

$$\nabla \cdot (\boldsymbol{b} - \boldsymbol{b}^e) - a + a^e = 0 \qquad \text{on } \Omega \tag{4.37}$$

$$\boldsymbol{t}^d = \boldsymbol{\sigma} \cdot \boldsymbol{n} \qquad \text{on } \partial\Omega \tag{4.38}$$

$$a^c = (\boldsymbol{b} - \boldsymbol{b}^e) \cdot \boldsymbol{n} \qquad \text{on } \partial\Omega \tag{4.39}$$

Entropy principle. Under isothermal conditions, the entropy principle reads:

$$p^{(i)} - \rho\dot{\psi} = \boldsymbol{\sigma} : \dot{\boldsymbol{\varepsilon}} + a\dot{\bar{e}} + \boldsymbol{b} \cdot \nabla\dot{\bar{e}} - \rho\dot{\psi} \geqslant 0. \tag{4.40}$$

where the free energy potential ψ is considered to be a function of the micromorphic quantities and their gradients. For a anisotropic damage model with a second order tensorial damage variable one has:

$$\rho\psi = \rho\psi(\boldsymbol{\varepsilon}, \mathbf{D}, \bar{e}, \nabla\bar{e}) \tag{4.41}$$

Computing the time derivative of $\rho\psi$ and replacing the obtained expression into (4.40), one obtains:

$$\left(\boldsymbol{\sigma} - \rho\frac{\partial\psi}{\partial\boldsymbol{\varepsilon}}\right) : \dot{\boldsymbol{\varepsilon}} + \left(a - \rho\frac{\partial\psi}{\partial\bar{e}}\right)\dot{\bar{e}} + \left(\boldsymbol{b} - \rho\frac{\partial\psi}{\partial\nabla\bar{e}}\right) \cdot \nabla\dot{\bar{e}} - \rho\frac{\partial\psi}{\partial\mathbf{D}} : \dot{\mathbf{D}} \geqslant 0 \tag{4.42}$$

The following state laws can therefore be written:

$$\boldsymbol{\sigma} = \rho\frac{\partial\psi}{\partial\boldsymbol{\varepsilon}} \quad \mathbf{Y} = -\rho\frac{\partial\psi}{\partial\mathbf{D}} \quad a = \rho\frac{\partial\psi}{\partial\bar{e}} \quad \boldsymbol{b} = \rho\frac{\partial\psi}{\partial\nabla\bar{e}} \tag{4.43}$$

3.5 Derivation of the anisotropic ENLG model

Let us suppose that the non-local equivalent strain is a map, i.e., a linear application from the manifold to the real space, $\bar{e} : \mathcal{M} \to \mathbb{R}$.

Drawing from the free-energy potential postulated by (Peerlings et al., 2004) for deriving the standard isotropic GNL model, a free-energy potential for the anisotropic ENLG model can directly be written on the manifold as:

$$\rho\psi = \rho\psi(\boldsymbol{\varepsilon}, \mathbf{D}, \bar{e}, \tilde{\nabla}\bar{e}) = \rho\psi_0 + \frac{1}{2}h(e - \bar{e})^2 + \frac{1}{2}hc\|\tilde{\nabla}\bar{e}\|^2_{\mathbf{g}} \tag{4.44}$$

where, to avoid confusion, the symbol $\tilde{\nabla}$ is used to denote that the gradient (and also the divergence in the remainder of this section) is computed in the deformed space by damage (i.e., on the manifold $\mathcal{M}$). The symbol ∇ is used to denote the Euclidean gradient. Here, $\rho\psi_0 = \rho\psi_0(\boldsymbol{\varepsilon}, \mathbf{D})$ is the free-energy potential postulated by the anisotropic damage model (see e.g., (Desmorat et al., 2007a; Desmorat, 2015; Masseron et al., 2022)) and $h > 0$ is a model parameter (homogeneous to a stiffness). Moreover, notice that in such a differential geometry description, the damage tensor $\mathbf{D}$ is of covariant nature as $\boldsymbol{\varepsilon}$.

State laws. The expression of the stress tensor, the generalized stresses and the thermodynamic force associated with damage can be obtained by applying these state law, as follows:

(*i*) The stress tensor $\boldsymbol{\sigma}$ reads as the sum of a standard contribution ($\boldsymbol{\sigma}_0$) and a damage-dependent term related to non-locality:

$$\boldsymbol{\sigma} = \boldsymbol{\sigma}_0 + h(e - \bar{e})\frac{\partial e}{\partial \boldsymbol{\varepsilon}} \tag{4.45}$$

with:

$$\boldsymbol{\sigma}_0 = \rho\frac{\partial \psi_0(\boldsymbol{\varepsilon}, \mathbf{D})}{\partial \boldsymbol{\varepsilon}} \tag{4.46}$$

> **Remark 4.3.** *Since $\boldsymbol{\varepsilon}$ is a covariant second-order tensor, $\partial e/\partial \boldsymbol{\varepsilon}$ and $\partial \psi_0/\partial \boldsymbol{\varepsilon}$ are both contravariant second-order tensors. This can be easily inferred by:*
>
> $$\delta e = \frac{\partial e}{\partial \boldsymbol{\varepsilon}} : \delta\boldsymbol{\varepsilon} \qquad \delta e = \left(\frac{\partial e}{\partial \boldsymbol{\varepsilon}}\right)^{ij} \delta\boldsymbol{\varepsilon}_{ij} \tag{4.47}$$
>
> $$\delta\psi_0 = \frac{\partial \psi_0}{\partial \boldsymbol{\varepsilon}} : \delta\boldsymbol{\varepsilon} + \frac{\partial \psi_0}{\partial \mathbf{D}} : \delta\mathbf{D} \qquad \delta\psi_0 = \left(\frac{\partial \psi_0}{\partial \boldsymbol{\varepsilon}}\right)^{ij} \delta\boldsymbol{\varepsilon}_{ij} + \left(\frac{\partial \psi_0}{\partial \mathbf{D}}\right)^{ij} \delta\mathbf{D}_{ij} \tag{4.48}$$
>
> *As a consequence, $\boldsymbol{\sigma}$ is a contravariant second-order tensor.*

(*ii*) The generalized stresses a and $\boldsymbol{b}$ (covariant vector of components b_i) read:

$$a = -h(e - \bar{e}) \tag{4.49}$$

$$\boldsymbol{b} = \rho\frac{\partial \psi}{\partial \tilde{\nabla}\bar{e}} = hc\mathbf{g} \cdot \tilde{\nabla}\bar{e} \tag{4.50}$$

(*iii*) The thermodynamic force associated with damage $\mathbf{Y}$ is once again contravariant (components Y^{ij}) and reads:

$$\mathbf{Y} = \mathbf{Y}_0 + \mathbf{Z} \tag{4.51}$$

with:

$$\mathbf{Y}_0 = -\rho\frac{\partial \psi_0(\boldsymbol{\varepsilon}, \mathbf{D})}{\partial \mathbf{D}} \tag{4.52}$$

$$\mathbf{Z} = -\frac{hc}{2}\frac{\partial \|d\bar{e}\|^2_{\mathbf{g}}}{\partial \mathbf{g}^{-1}} : \frac{\partial \mathbf{g}^{-1}}{\partial \mathbf{D}} \tag{4.53}$$

The tensorial function $\mathbf{Z}$ can be understood as a non-local rate of energy restitution of the model. Such an additional non-local term does not appear in the case of the GNL model (Peerlings et al., 2004). As already mentioned, in this last case the dissipation does not differ from the one corresponding to the local model.

> **Remark 4.4.** *Since $\mathbf{D}$ and $\mathbf{g}^{-1}$ are covariant and contravariant second-order tensors, respectively, $\partial \psi_0/\partial \mathbf{D}$ is a contravariant second-order tensor,*

> *$\partial \mathbf{g}^{-1}/\partial \boldsymbol{D}$ is a contravariant fourth-order tensor and $\partial \|d\bar{e}\|^2_{\mathbf{g}}/\partial \mathbf{g}^{-1}$ is a covariant second-order tensor. The double contraction between these two latter tensors is thus possible and gives a contravariant second-order tensor $\mathbf{Z}$.*

Helmholtz problem. Introducing the usual assumption (Forest, 2009) of no generalized volume forces ($a^e = 0, \boldsymbol{b}^e = \mathbf{0}$), from the balance equation (4.37), one has:

$$\tilde{\nabla} \cdot \boldsymbol{b}^\flat - a = 0 \tag{4.54}$$

where $\boldsymbol{b}^\flat$ is the vector associated with the covector $\boldsymbol{b}$:

$$\boldsymbol{b}^\flat = hc\mathbf{g}^{-1} \cdot \boldsymbol{b} = hc\tilde{\nabla}\bar{e} \tag{4.55}$$

Substituting (4.55) into (4.54) one obtains:

$$\tilde{\nabla} \cdot (hc\tilde{\nabla}\bar{e}) - h\bar{e} + he = 0 \tag{4.56}$$

and then, exploiting the fact that h and c are both constant and non-null:[1]

$$\bar{e} - c\tilde{\nabla} \cdot \left(\tilde{\nabla}\bar{e}\right) = e \tag{4.57}$$

To derive the boundary condition on $\partial\Omega$ for the Helmholtz problem, one can rewrite (4.39) as:

$$\langle \boldsymbol{b}, \boldsymbol{n} \rangle_{\mathbf{g}} = \boldsymbol{b}^\flat \cdot \boldsymbol{n} = 0 \tag{4.58}$$

which implies:

$$\tilde{\nabla}\bar{e} \cdot \boldsymbol{n} = 0 \tag{4.59}$$

or equivalently:

$$\mathbf{g}^{-1} \cdot d\bar{e} \cdot \boldsymbol{n} = 0 \tag{4.60}$$

> **Remark 4.5.** *The normal vector $\boldsymbol{n}$ is a covector of components n_i to be consistent with (4.38).*

Exploiting, as in (Desmorat et al., 2015b), that in an Euclidean space $d\bar{e} = \nabla\bar{e}$, equation (4.57) can also be written as:

$$\bar{e} - \frac{c}{\sqrt{\det \mathbf{g}}} \nabla \cdot (\sqrt{\det \mathbf{g}}\ \mathbf{g}^{-1} \cdot \nabla\bar{e}) = e \tag{4.61}$$

Similarly, the boundary condition on $\partial\Omega$ reads:

$$\mathbf{g}^{-1} \cdot \nabla\bar{e} \cdot \boldsymbol{n} = 0 \tag{4.62}$$

The problem (5.1)-(5.2) is thus retrieved.

[1] The same expression was obtained by (Desmorat et al., 2015b).

Remark 4.6. *Different from the derivation proposed in (Ribeiro Nogueira et al., 2024a), another appropriate choice is to use the free energy $\rho\psi(\boldsymbol{\varepsilon}, \boldsymbol{D}, \bar{e}, d\bar{e})$, which leads to the same equations. In this case, one has directly the vector (b^i):*

$$\boldsymbol{b} = \rho\frac{\partial\psi}{\partial d\bar{e}} = hc\mathbf{g}^{-1}\cdot d\bar{e} = hc\tilde{\nabla}\bar{e} \tag{4.63}$$

with the boundary condition on $\partial\Omega$:

$$\langle \boldsymbol{b}, \boldsymbol{n}\rangle_{\mathbf{g}} = \mathbf{g}^{-1}\cdot d\bar{e}\cdot\boldsymbol{n} = 0 \tag{4.64}$$

Variational formulation. A variational formulation for the ENLG model can be obtained directly starting from equation (4.57).[2] One has:

$$\int_{\mathcal{M}}\bar{e}\,\eta\,\mathrm{vol}_g - \int_{\mathcal{M}} c\tilde{\nabla}\cdot\left(\tilde{\nabla}\bar{e}\right)\eta\,\mathrm{vol}_g = \int_{\mathcal{M}} e\,\eta\,\mathrm{vol}_g. \tag{4.65}$$

where:

$$c\tilde{\nabla}\cdot\left(\tilde{\nabla}\bar{e}\eta\right) = c\tilde{\Delta}\bar{e}\eta + c\langle\tilde{\nabla}\bar{e},\tilde{\nabla}\eta\rangle_{\mathbf{g}} \tag{4.66}$$

and vol_g is the n-form (the volume form):

$$\mathrm{vol}_g = \sqrt{\det(\mathbf{g})}dx^1\wedge dx^2 ... \wedge dx^n \tag{4.67}$$

with $\wedge$ denoting the so-called wedge product. The above integral thus becomes:

$$\int_{\mathcal{M}}\bar{e}\,\eta\,\mathrm{vol}_g - \int_{\mathcal{M}} c\tilde{\nabla}\cdot\left(\tilde{\nabla}\bar{e}\,\eta\right)\mathrm{vol}_g + \int_{\mathcal{M}} c\langle\tilde{\nabla}\bar{e},\tilde{\nabla}\eta\rangle_{\mathbf{g}}\mathrm{vol}_g = \int_{\mathcal{M}} e\,\eta\,\mathrm{vol}_g \tag{4.68}$$

Applying the divergence theorem:

$$\int_{\mathcal{M}} c\tilde{\nabla}\cdot\left(\tilde{\nabla}\bar{e}\,\eta\right)\mathrm{vol}_g = \int_{\partial\mathcal{M}} c\,\eta\tilde{\nabla}\bar{e}\cdot\boldsymbol{n}\,dS \tag{4.69}$$

enforcing the boundary condition (4.59) and remembering that $\langle\tilde{\nabla}\bar{e},\tilde{\nabla}\eta\rangle_{\mathbf{g}} = \langle d\bar{e}, d\eta\rangle_{\mathbf{g}}$ (see equation (4.23)), one ends up with:

$$\int_{\mathcal{M}}\bar{e}\,\eta\,\mathrm{vol}_g + \int_{\mathcal{M}} c\,\langle d\bar{e}, d\eta\rangle_{\mathbf{g}}\mathrm{vol}_g = \int_{\mathcal{M}} e\,\eta\,\mathrm{vol}_g. \tag{4.70}$$

A straightforward rewriting of last variational equation is:

$$\int_{\Omega}\sqrt{\det\mathbf{g}}\,\bar{e}\,\eta\,dV + \int_{\Omega} c\sqrt{\det\mathbf{g}}(\mathbf{g}^{-1}\cdot\nabla\bar{e})\cdot\nabla\eta\,dV = \int_{\Omega}\sqrt{\det\mathbf{g}}\,e\,\eta\,dV \tag{4.71}$$

On the expression of Y (and of Z). The terms figuring in the expression of the thermodynamic force $\mathbf{Z}$ in (4.53) read:

$$\frac{\partial\|d\bar{e}\|^2_{\mathbf{g}}}{\partial\mathbf{g}^{-1}} = \frac{\partial\mathbf{g}^{-1}}{\partial\mathbf{g}^{-1}} : (d\bar{e}\otimes d\bar{e}) = \mathbb{I}^{\flat}{}_{\#} : (d\bar{e}\otimes d\bar{e}) = \mathbb{I}_{\#}{}^{\flat} : (d\bar{e}\otimes d\bar{e}) = d\bar{e}\otimes d\bar{e} \tag{4.72}$$

$$\frac{\partial\mathbf{g}^{-1}}{\partial\mathbf{D}} = -\mathbb{I}^{\flat} \tag{4.73}$$

[2] Alternatively, one could use the micromorphic approach by writing the principle of virtual work in the curved space.

The tensor $\mathbf{Z}$ can thus be written as:[3]

$$\mathbf{Z} = \frac{hc}{2}\mathbb{I}^\flat : (d\bar{e} \otimes d\bar{e}) \tag{4.74}$$

Finally, the expression of the dissipation rate taking into account the modified energy release rate for the 3D anisotropic ENLG model is (substituting into equation (4.53)):

$$\mathcal{D} = \mathbf{Y} : \dot{\mathbf{D}} = \left(\mathbf{Y}_0 + \frac{hc}{2}\mathbb{I}^\flat : (d\bar{e} \otimes d\bar{e})\right) : \dot{\mathbf{D}} \geqslant 0 \tag{4.75}$$

where $\mathbf{Y}_0 : \dot{\mathbf{D}}$ is supposed to be positive or null by local model construction (see, e.g., (Desmorat, 2015)).

To rewrite previous equation in the Euclidean space, one can exploit the fact that $d\bar{e} = \nabla\bar{e}$. As a consequence, $\mathbb{I}^\flat : (d\bar{e} \otimes d\bar{e}) = \nabla\bar{e} \otimes \nabla\bar{e}$, and the above expression can be simplified as:

$$\mathcal{D} = \left(\mathbf{Y}_0 + \frac{hc}{2}(\nabla\bar{e} \otimes \nabla\bar{e})\right) : \dot{\mathbf{D}} \geqslant 0 \tag{4.76}$$

Damage-induced curvature of the space. For the case of the ENLG model, the Christoffel symbols are damage-dependent (Desmorat et al., 2015b), which also induces a damage-dependent Ricci curvature tensor $\mathbf{R}$ (of components R_{ij}) by definition. One can obtain a scalar measure of the curvature in the space created by damage via the contraction $\mathbf{g}^{-1} : \mathbf{R}$. The metric becomes the identity for an undamaged medium, and Christoffel symbols vanish, so the curvature is null. As pointed out by (Ganghoffer, 2003), further investigation is necessary to better understand the meaning of this curvature in terms of topological aspects, bridging micro-structural to macroscopic approaches.

3.6 Isotropic ENLG model derivation

Let us now consider the isotropic ENLG damage formulation. The metric $\mathbf{g}$ is now given in local coordinates by $\mathbf{g} = \mathbf{q}/(1-D)$ and its inverse reads $\mathbf{g}^{-1} = (1-D)\mathbf{q}^{-1}$.

The expression of the stress tensor $\boldsymbol{\sigma}$, and of a and $\boldsymbol{b}$, are exactly the same as in Equation (4.45), Equation (4.49) and Equation (4.50). The thermodynamic force Z figuring in Equation (4.86) can be derived from the one obtained for the anisotropic model considering:

$$\mathbf{Y}_0 = -\rho\frac{\partial\psi_0}{\partial D}\mathbf{q}^{-1} \qquad \mathbf{D} = D\mathbf{q} \tag{4.77}$$

Substituting (4.77) into (4.75), one has:

$$\begin{aligned}\mathcal{D} &= \mathbf{Y} : \dot{\mathbf{D}} \\ &= \left(-\rho\frac{\partial\psi_0}{\partial D}\mathbf{q}^{-1} + \frac{hc}{2}\nabla\bar{e} \otimes \nabla\bar{e}\right) : \dot{D}\mathbf{q} \\ &= \left(-3\rho\frac{\partial\psi_0}{\partial D} + \frac{hc}{2}\nabla\bar{e} \cdot \nabla\bar{e}\right)\dot{D} = Y\dot{D} \geqslant 0\end{aligned} \tag{4.78}$$

[3]Notice that $\mathbb{I}^\flat : (d\bar{e} \otimes d\bar{e}) \neq d\bar{e}^\flat \otimes d\bar{e}^\flat$ since the Euclidean metric is used in $\mathbb{I}^\flat$.

where we exploited the following property:

$$(\nabla\bar{e}\otimes\nabla\bar{e}):\mathbf{q}=\mathrm{tr}(\nabla\bar{e}\otimes\nabla\bar{e})=\nabla\bar{e}\cdot\nabla\bar{e} \tag{4.79}$$

Remark 4.7. *Alternatively one could follow an independent derivation. In that case, one obtains:*

$$\begin{aligned} Z &= -\frac{hc}{2}\frac{\partial\|\tilde{\nabla}\bar{e}\|^2_{\mathbf{g}}}{\partial D} \\ &= -\frac{hc}{2}\frac{\partial}{\partial D}(\mathbf{g}^{-1}\cdot d\bar{e}\cdot\mathbf{g}\cdot\mathbf{g}^{-1}\cdot d\bar{e}) \\ &= -\frac{hc}{2}\frac{\partial}{\partial D}\left[(1-D)\mathbf{q}^{-1}\cdot d\bar{e}\cdot\mathbf{q}\cdot\mathbf{q}^{-1}\cdot d\bar{e}\right] \\ &= \frac{hc}{2}d\bar{e}\cdot\mathbf{q}^{-1}\cdot d\bar{e} \end{aligned} \tag{4.80}$$

Now, one can easily notice that $d\bar{e}\cdot\mathbf{q}^{-1}\cdot d\bar{e}$ *in* (4.80) *is a scalar product in the Euclidean space, i.e.:*

$$d\bar{e}\cdot\mathbf{q}^{-1}\cdot d\bar{e}=\|d\bar{e}\|^2=\langle d\bar{e},d\bar{e}\rangle_{\mathbf{q}}=d\bar{e}\cdot d\bar{e}=\nabla\bar{e}\cdot\nabla\bar{e} \tag{4.81}$$

As a consequence, the expression of the dissipation rate taking into account the modified energy release rate for the full 3D isotropic ENLG model is:

$$\mathcal{D}=Y\dot{D}=\left(-3\rho\frac{\partial\psi_0}{\partial D}+\frac{hc}{2}\nabla\bar{e}\cdot\nabla\bar{e}\right)\dot{D}\geqslant 0 \tag{4.82}$$

3.7 On the importance of using a differential geometry framework

To underline the importance of a proper geometrical description, let us now try deriving the ENLG model using a standard approach, i.e., by assuming that all the quantities belong to the same Euclidean space.

Drawing from the free-energy potential postulated by (Peerlings et al., 2004), a free-energy potential for the anisotropic ENLG model in a fully Euclidean context can be written as:

$$\rho\psi=\rho\psi(\boldsymbol{\varepsilon},\mathbf{D},\bar{e})=\rho\psi_0+\frac{1}{2}h\sqrt{\det\mathbf{g}}\,(e-\bar{e})^2+\frac{1}{2}hc\sqrt{\det\mathbf{g}}\;\mathbf{g}^{-1}:(\nabla\bar{e}\otimes\nabla\bar{e}) \tag{4.83}$$

To study the implications of such a choice, let us consider the 3D isotropic formulation. Using (4.10), the free-energy potential (4.83) can be rewritten as:

$$\rho\psi=\rho\psi(\boldsymbol{\varepsilon},D,\bar{e})=\rho\psi_0(\boldsymbol{\varepsilon},D\mathbf{I})+\frac{1}{2}h\frac{1}{\sqrt{(1-D)^3}}\,(e-\bar{e})^2+\frac{1}{2}hc\frac{1}{\sqrt{1-D}}\nabla\bar{e}\cdot\nabla\bar{e} \tag{4.84}$$

From the state laws, one obtains:

$$\boldsymbol{\sigma} = \boldsymbol{\sigma}_0 + h\frac{1}{\sqrt{(1-D)^3}}(e-\bar{e})\frac{\partial e}{\partial \boldsymbol{\varepsilon}} \tag{4.85}$$

$$Y = Y_0 + Z \tag{4.86}$$

$$a = -\frac{h}{\sqrt{(1-D)^3}}(e-\bar{e}) \tag{4.87}$$

$$\boldsymbol{b} = \frac{hc}{\sqrt{1-D}}\nabla\bar{e} \tag{4.88}$$

where:

$$Y_0 = -\rho\frac{\partial \psi_0}{\partial(D\mathbf{I})} : \mathbf{I} = -3\rho\frac{\partial \psi_0}{\partial D} \geqslant 0 \tag{4.89}$$

$$\begin{aligned} Z &= -\frac{h}{2}\frac{\partial}{\partial D}\left[\frac{1}{\sqrt{(1-D)^3}}(e-\bar{e})^2 + \frac{c}{\sqrt{1-D}}\nabla\bar{e}\cdot\nabla\bar{e}\right] \\ &= -\frac{h}{2}\left[\frac{3}{2}\frac{1}{\sqrt{(1-D)^5}}(e-\bar{e})^2 + \frac{c}{(1-D)^2}\nabla\bar{e}\cdot\nabla\bar{e}\right] \leqslant 0 \end{aligned} \tag{4.90}$$

The Helmholtz problem (4.11)–(4.12), is straightforwardly obtained by replacing previous equations into (4.37) and (4.39), with the usual assumption that $a^e = a^c = 0$ and $\boldsymbol{b}^e = 0$.

Comments on stress tensor and energy dissipation. Although the BVP corresponding to the ENLG model can be derived from (4.84), one can detect some inconsistencies in the previous formulations by investigating the expressions of $\boldsymbol{\sigma}$ and Y for the isotropic case. In particular:

(*i*) *Stress tensor.* Let us compare expressions (4.85) and (4.45). Contrarily to (4.45) (and contrarily to the GNL model), the term $(1-D)$ figures in the denominator of the non-local contributions. It results from the "arbitrary" modification of the free-energy potential by (Peerlings et al., 2004) to account for damage-dependent interactions. Now, the term $\boldsymbol{\sigma}_0 = (1-D)\mathbb{E} : \boldsymbol{\epsilon}$ vanishes when $D \to 1$. However, if an arbitrary small constant value is chosen for h, the second contribution to $\boldsymbol{\sigma}$ in equation (4.85) may eventually tend to infinity when $D \to 1$. This is physically inconsistent since a zero-stress condition should be described.

(*ii*) *Energy dissipation.* Let us now consider the expression (4.90) of the non-local thermodynamic force Z. According to (4.90), Z is always negative. Consequently, the dissipation inequality $\mathcal{D} = (Y_0 + Z)\dot{D} \geqslant 0$ may not be verified when $D \to 1$. Conversely, the Clausius-Duhem inequality is always fulfilled when the expression of Z is derived with the differential geometry-based derivation.

The inconsistencies mentioned above are intrinsically related to how the modified free-energy potential (4.84) was written in a purely Euclidean setting. To obtain the

expression of $\boldsymbol{b}$ allowing for obtaining the Helmholtz problem (4.11)–(4.12) corresponding to the ENLG model, the factor $\sqrt{\det \mathbf{g}}$ was added to the terms related to the non-local strain and its gradient. However, this led to a wrong description of the stress tensor and intrinsic dissipation. In other words, such a way of defining the free-energy potential does not allow for correctly deriving the ENLG model.

3.8 Comparison with other formulations from the literature

3.8.1 Micromorphic model of Poh and Sun (2017)

The free energy reads:

$$\rho\psi = \rho\psi(\boldsymbol{\varepsilon}, D, \bar{e}) = \frac{1}{2}(1-D)\boldsymbol{\varepsilon} : \mathbb{E} : \boldsymbol{\varepsilon} + \frac{1}{2}h\left(e-\bar{e}\right)^2 + \frac{1}{2}hcg(D)\|\nabla\bar{e}\|^2 \tag{4.91}$$

where $g(D)$ is defined in Equation (2.25). Following usual arguments, one can derive the modified Helmholtz problem and obtain Equation (2.24).

According to this formulation, the intrinsic dissipation reads:

$$\mathcal{D} = \frac{1}{2}\left(\boldsymbol{\varepsilon} : \mathbb{E} : \boldsymbol{\varepsilon} - \frac{\partial g}{\partial D}hc\nabla\bar{e}\cdot\nabla\bar{e}\right)\dot{D} \geqslant 0 \tag{4.92}$$

which is always positive for $\dot{D} \geqslant 0$, provided that $\partial g/\partial D < 0$.

Similarities and differences. This model closely resembles the isotropic ENLG damage model, with the only difference being the decreasing function g which is naturally introduced by the metric $\mathbf{g}$ in the ENLG model. However, this latter presents some interesting features:

(i) residual non-local interactions do not exist since the gradient term in (5.1) vanishes when damage approaches the unity (i.e., $\bar{e} \to e$ when $D \to 1$);

(*ii*) vanishing non-local interactions (or vanishing internal length) naturally represent damage-to-fracture transition. This means that a "pseudo-crack" can be described, and interactions between material points crossed by it are no longer allowed;

(*iii*) finally, the ENLG model does not require the introduction of additional parameters for describing the evolving interactions, as this approach relies entirely on a geometric problem description.

3.8.2 Stress-based GNL model of Vandoren and Simone (2018)

As already introduced in Chapter 2, the stress-based gradient-enhanced anisotropic model was proposed by Vandoren and Simone (2018).

Similarities and differences. From a mathematical viewpoint, the stress-based GNL model is very similar to the ENLG one. Choosing, for instance, $\mathbf{c} = \mathbf{g}^{-1}$ (Equation (2.22)), the only missing term in their model is related to $\sqrt{\det \mathbf{g}} = \sqrt{\det \mathbf{c}^{-1}}$, which naturally appears in the ENLG formulation.

However, conceptually, the differences between the two formulations are more pronounced. Stress-based formulations (Giry et al., 2011; Vandoren & Simone, 2018) are suitable for modeling evolving interactions due to damage evolution and vanishing interactions close to stress-free boundaries. In contrast, the ENLG model is suitable for dealing with newly created boundaries (i.e., damaged bands) inside the considered domain only.

The influence of existing boundaries on non-local interactions is not considered in ENL formulations. However, they can be easily introduced by applying a modified metric depending on damage and stress states. For instance, one could imagine writing $\mathbf{g} = [\mathbf{c} \cdot (\mathbf{I} - \mathbf{D})]^{-1}$. A similar formulation that couples the effects of damage and stress on non-local interactions was introduced by (Negi et al., 2020). The free-energy potential proposed by the last cited paper has strong relations with the one proposed for the ENLG model based on a geometric damage description (equation (4.44)).

4 Comments on bifurcation in a gradient-enhanced Eikonal continuum

To better understand the regularization properties of the ENLG model within a general context,this section proposes to investigate the bifurcation in a gradient-enhanced continuum. This analysis is primarily inspired by the work of Pijaudier-Cabot and Benallal (1993). It is proposed here to extend the discussion to the gradient-enhanced models GNL and ENLG in the case of isotropic damage.

Similar to the wave dispersion analysis in Chapter 3, we extend Equation (3.1) to the 3D setting:

$$\nabla \cdot \dot{\boldsymbol{\sigma}} = \rho \frac{\partial \dot{\boldsymbol{u}}^2}{\partial t^2} \tag{4.93}$$

where $\dot{\boldsymbol{u}}$ denotes the velocity field and $\dot{\boldsymbol{\sigma}}$ is given by the linearized material behavior, expressed as:

$$\dot{\boldsymbol{\sigma}} = (1 - D_0)\mathbb{E} : \dot{\boldsymbol{\varepsilon}} - \dot{D}\mathbb{E} : \boldsymbol{\varepsilon}_0 \tag{4.94}$$

with D_0 and $\boldsymbol{\varepsilon}_0$ defining an initial homogeneous equilibrium state. Here, we considered that $h \ll \|\mathbb{E}\|$. To compare the subsequent resulting expressions with those developed in (Pijaudier-Cabot & Benallal, 1993), it is considered that damage evolves based on the non-local counterpart of the thermodynamic force Y, leading to:

$$D = g(\kappa) \qquad f = \bar{Y} - \kappa \qquad \dot{D} = \frac{\partial g}{\partial \kappa}\dot{\kappa} = g'\dot{\kappa} \tag{4.95}$$

with the criterion function f to be considered under the consistency condition $\dot{f} = 0$, implying $\dot{\bar{Y}} = \dot{\kappa}$ as damage evolves. As we will see further on, this choice leads to expressions of $\bar{Y}$ and its derivatives which are more simple to handle and depend also on

$\mathbb{E}$. Consequently, Equation (4.93) can be rewritten as:

$$\nabla \cdot \left[(1 - D_0)\mathbb{E} : \dot{\boldsymbol{\varepsilon}} - g'\dot{\bar{Y}}\mathbb{E} : \boldsymbol{\varepsilon}_0\right] = \rho \frac{\partial \dot{\boldsymbol{u}}^2}{\partial t^2} \tag{4.96}$$

where the classic assumption of damage evolution occurring in all the points of the solid is adopted.

4.1 Linearized gradient-enhanced models

ENLG model. Let us consider the general ENLG Equation (4.61) applied to the thermodynamic force Y::

$$\bar{Y} - \frac{c}{\sqrt{\det \mathbf{g}}} \nabla \cdot (\sqrt{\det \mathbf{g}}\ \mathbf{g}^{-1} \cdot \nabla \bar{Y}) = Y \tag{4.97}$$

Expanding this equation yields:

$$\bar{Y} - \frac{c}{\sqrt{\det \mathbf{g}}} \left[\left(\nabla \cdot (\sqrt{\det \mathbf{g}}\ \mathbf{g}^{-1})\right) \cdot \nabla \bar{Y} + \sqrt{\det \mathbf{g}}\ \mathbf{g}^{-1} : \nabla^{(2)} \bar{Y}\right] = Y \tag{4.98}$$

By following the development in Section 1.3, assuming a small perturbation around the initial state, $\mathbf{g} = \mathbf{g}_0 + \mathbf{g}_a$ and $\bar{Y} = \bar{Y}_0 + \bar{Y}_a$ and differentiating with respect to time while considering the initial homogeneous state, we obtain:

$$\dot{\bar{Y}} - c\mathbf{g}_0^{-1} : \nabla^{(2)} \dot{\bar{Y}} = \dot{Y} \tag{4.99}$$

with $\mathbf{g}_0^{-1} = \mathbf{I} - \mathbf{D}_0$. This equation represents the linearized version of the ENLG model Helmholtz-type equation expressed in a rate form considering anisotropic (damage) interactions. This is equivalent to considering an anisotropic weighting function depending on the normal $\boldsymbol{n}_d$ (as discussed in (Pijaudier-Cabot & Benallal, 1993)).

One can easily retrieve the case of isotropic damage by considering $\mathbf{g}_0^{-1} = (1 - D_0)\mathbf{I}$, which gives:

$$\dot{\bar{Y}} - c(1 - D_0)\nabla^2 \dot{\bar{Y}} = \dot{Y} \tag{4.100}$$

which is essentially equal to the 1D setting described by Equation (3.22) replacing $\bar{e}$ by $\bar{Y}$. Thus, Equation (4.99) generalizes the linearized ENLG model for any dimension, considering isotropic and anisotropic cases.

GNL model. The linearized version of the GNL model equation can be obtained from the ENLG one, considering $\mathbf{g}_0^{-1} = \mathbf{I}$, resulting in:

$$\dot{\bar{Y}} - c\nabla^2 \dot{\bar{Y}} = \dot{Y} \tag{4.101}$$

which is exactly the one derived for the 1D setting in Equation (3.8).

> **Remark 4.8.** *Notice that $\dot{Y}$ is given by:*
>
> $$\dot{Y} = \frac{1}{2}\left(\dot{\boldsymbol{\varepsilon}} : \mathbb{E} : \boldsymbol{\varepsilon}_0 + \boldsymbol{\varepsilon}_0 : \mathbb{E} : \dot{\boldsymbol{\varepsilon}}\right) = \boldsymbol{\varepsilon}_0 : \mathbb{E} : \dot{\boldsymbol{\varepsilon}} \tag{4.102}$$

due to the major symmetries of $\mathbb{E}$.

4.2 Linearized coupled problem for the ENLG model

Following Pijaudier-Cabot and Benallal (1993), let us consider the velocity field written in the form of a harmonic wave propagating in the direction $\boldsymbol{n}_d$:

$$\dot{\boldsymbol{u}} = \boldsymbol{A} \exp\left[-ik(\boldsymbol{n}_d \cdot \boldsymbol{x} - c_p t)\right] \tag{4.103}$$

with $\boldsymbol{A}$ denoting its amplitude and k the wave number. The rate of deformation $\dot{\boldsymbol{\varepsilon}}$ can be computed as:

$$\dot{\boldsymbol{\varepsilon}} = \nabla^s \dot{\boldsymbol{u}} = -\frac{1}{2} ik \left[\boldsymbol{A} \otimes \boldsymbol{n}_d + \boldsymbol{n}_d \otimes \boldsymbol{A}\right] \exp\left[-ik(\boldsymbol{n}_d \cdot \boldsymbol{x} - c_p t)\right] = \hat{\boldsymbol{\varepsilon}} \exp\left[-ik(\boldsymbol{n}_d \cdot \boldsymbol{x} - c_p t)\right] \tag{4.104}$$

where $\hat{\boldsymbol{\varepsilon}}$ denotes the tensorial amplitude.

A particular solution of the non-local field can be written in the form of a harmonic wave:

$$\dot{\bar{Y}} = \hat{Y} \exp\left[-ik(\boldsymbol{n}_d \cdot \boldsymbol{x} - c_p t)\right] \tag{4.105}$$

$$\nabla \dot{\bar{Y}} = -ik\hat{Y}\boldsymbol{n}_d \exp\left[-ik(\boldsymbol{n}_d \cdot \boldsymbol{x} - c_p t)\right] \tag{4.106}$$

$$\nabla^{(2)} \dot{\bar{Y}} = -k^2 \hat{Y} \boldsymbol{n}_d \otimes \boldsymbol{n}_d \exp\left[-ik(\boldsymbol{n}_d \cdot \boldsymbol{x} - c_p t)\right] \tag{4.107}$$

Substituting these expressions into Equation (4.99), we obtain:

$$\hat{Y} = \frac{\boldsymbol{\varepsilon}_0 : \mathbb{E} : \dot{\boldsymbol{\varepsilon}}}{1 + ck^2 \mathbf{g}_0^{-1} : (\boldsymbol{n}_d \otimes \boldsymbol{n}_d)} \tag{4.108}$$

which can be again simplified in the case of isotropic damage as:

$$\hat{Y} = \frac{\boldsymbol{\varepsilon}_0 : \mathbb{E} : \dot{\boldsymbol{\varepsilon}}}{1 + ck^2(1 - D_0)(\boldsymbol{n}_d \cdot \boldsymbol{n}_d)} = \frac{\boldsymbol{\varepsilon}_0 : \mathbb{E} : \dot{\boldsymbol{\varepsilon}}}{1 + ck^2(1 - D_0)} \tag{4.109}$$

Substitution of Equation (4.108) combined with Equation (4.105), Equation (4.104) and Equation (4.103) into Equation (4.96), leads to:

$$\left[(1 - D_0)\left(\boldsymbol{n}_d \cdot \mathbb{E} \cdot \boldsymbol{n}_d\right) - \frac{g'}{1 + ck^2(1 - D_0)} \left(\boldsymbol{n}_d \cdot \mathbb{E} : \boldsymbol{\varepsilon}_0 \otimes \boldsymbol{\varepsilon}_0 : \mathbb{E} \cdot \boldsymbol{n}_d\right)\right] \cdot \boldsymbol{A} = \rho c_p^2 \boldsymbol{A} \tag{4.110}$$

which can be recast in the form:

$$\left[\boldsymbol{n}_d \cdot \overline{\mathbb{L}}(k) \cdot \boldsymbol{n}_d - \rho c_p^2 \mathbf{I}\right] \cdot \boldsymbol{A} = 0 \tag{4.111}$$

Here, $\overline{\mathbb{L}}(k)$ denotes the non-local (dependent on the wave number) tangent operator, defined as:

$$\overline{\mathbb{L}}(k) = (1 - D_0)\mathbb{E} - \frac{g'}{1 + ck^2(1 - D_0)} \mathbb{E} : \boldsymbol{\varepsilon}_0 \otimes \boldsymbol{\varepsilon}_0 : \mathbb{E} \tag{4.112}$$

Remark 4.9. *Considering the minor and major symmetries of* $\mathbb{E}$*, notice that the following equalities were used to derive Equation* (4.110)*:*

$$\begin{aligned}\mathbb{E} : (\boldsymbol{A} \otimes \boldsymbol{n}_d + \boldsymbol{n}_d \otimes \boldsymbol{A}) \cdot \boldsymbol{n}_d &= E_{ijkl}(A_k n_l + n_k A_l) n_j \\ &= n_j E_{jikl} n_l A_k + n_j E_{jilk} n_k A_l \\ &= 2\,(\boldsymbol{n}_d \cdot \mathbb{E} \cdot \boldsymbol{n}_d) \cdot \boldsymbol{A} \qquad (4.113)\\ (\mathbb{E} : \boldsymbol{\varepsilon}_0) \cdot \boldsymbol{n}_d\,(\boldsymbol{\varepsilon}_0 : (\mathbb{E} : (\boldsymbol{n}_d \otimes \boldsymbol{A}))) &= (E_{ijkl}\varepsilon_{kl} n_j)(\varepsilon_{mn} E_{mnqp} n_p) A_q \\ &= (\boldsymbol{n}_d \cdot \mathbb{E} : \boldsymbol{\varepsilon}_0 \otimes \boldsymbol{\varepsilon}_0 : \mathbb{E} \cdot \boldsymbol{n}_d) \cdot \boldsymbol{A} \qquad (4.114)\end{aligned}$$

The expression in Equation (4.110) closely resembles the one obtained by Pijaudier-Cabot and Benallal (1993) for the classic integral approach. In their case, the dependence on the wave number is considered through the Fourier transform of the weighting function, whereas here it is related to the term $ck^2(1 - D_0)$.

If $c = 0$, the continuum has no non-local effects, and we retrieve the tangent operator of a local continuum (see for instance Jirásek (2007)). This is equivalent to a have a Dirac distribution as the weighting function for the integral approach (Pijaudier-Cabot & Benallal, 1993). This condition can be achieved independently of the value of c for the ENLG model. Indeed, for high initial damage levels, the regularizing term $ck^2(1-D_0)$ tends to vanish, which represents the damage-dependent vanishing interactions characteristic of the model.

GNL model. A similar derivation for the GNL model leads to:

$$\overline{\mathbb{L}}(k) = (1 - D_0)\mathbb{E} - \frac{g'}{1 + ck^2}\mathbb{E} : \boldsymbol{\varepsilon}_0 \otimes \boldsymbol{\varepsilon}_0 : \mathbb{E} \qquad (4.115)$$

This formulation behaves similarly to the INL classic approach.

Remark 4.10. *The expression of the tangent operator highlights an essential aspect of a non-local continuum. It depends on the material behavior through* g' *and the regularization technique employed through* c*. Therefore, the behavior influences the regularization properties and vice versa, highlighting that experimental fittings must be carried out at the structural level and not only at the RVE scale.*

4.3 Bifurcation analysis

ENLG model. Let us consider the static case (*i.e.,* $c_p = 0$), so the non-trivial solution of Equation (4.111) is obtained by:

$$\det\left[\boldsymbol{n}_d \cdot \overline{\mathbb{L}}(k) \cdot \boldsymbol{n}_d\right] = 0 \qquad (4.116)$$

which is exactly the same bifurcation condition derived for a local continuum, as described in Chapter 2. Here, the main difference lies in the term $\boldsymbol{n}_d \cdot \overline{\mathbb{L}}(k) \cdot \boldsymbol{n}_d$, which represents a sort of pseudo-acoustic tensor (Pijaudier-Cabot & Benallal, 1993) dependent on the wave number of the bifurcation mode.

From Equation (4.111), we can derive the following bifurcation conditions:

$$\frac{(1-D_0)(1+ck^2(1-D_0))}{g'}\mathbf{I} = (\boldsymbol{n}_d \cdot \mathbb{E} \cdot \boldsymbol{n}_d)^{-1} \cdot (\boldsymbol{n}_d \cdot \mathbb{E} : \boldsymbol{\varepsilon}_0 \otimes \boldsymbol{\varepsilon}_0 : \mathbb{E} \cdot \boldsymbol{n}_d) \tag{4.117}$$

which can be further simplified as:

$$\frac{(1-D_0)(1+ck^2(1-D_0))}{g'} = (\boldsymbol{n}_d \cdot \mathbb{E} : \boldsymbol{\varepsilon}_0) \cdot (\boldsymbol{n}_d \cdot \mathbb{E} \cdot \boldsymbol{n}_d)^{-1} \cdot (\boldsymbol{\varepsilon}_0 : \mathbb{E} \cdot \boldsymbol{n}_d) \tag{4.118}$$

Remark 4.11. *It's worth noting that:*

$$\frac{(1-D_0)(1+ck^2(1-D_0))}{g'}\delta_{rp} = (\boldsymbol{n}_d \cdot \mathbb{E} \cdot \boldsymbol{n}_d)^{-1}_{rj}\, n_i E_{ijkl}\varepsilon_{kl}\varepsilon_{mn}E_{mnpq}n_q \tag{4.119}$$

which leads to ($r = p$):

$$\begin{aligned}\frac{(1-D_0)(1+ck^2(1-D_0))}{g'} &= (\boldsymbol{n}_d \cdot \mathbb{E} \cdot \boldsymbol{n}_d)^{-1}_{pj}\, n_i E_{ijkl}\varepsilon_{kl}\varepsilon_{mn}E_{mnpq}n_q \\ &= (\boldsymbol{n}_d \cdot \mathbb{E} : \boldsymbol{\varepsilon}_0)_j\, (\boldsymbol{n}_d \cdot \mathbb{E} \cdot \boldsymbol{n}_d)^{-1}_{jp}\, (\boldsymbol{\varepsilon}_0 : \mathbb{E} \cdot \boldsymbol{n}_d)_p \\ &= (\boldsymbol{n}_d \cdot \mathbb{E} : \boldsymbol{\varepsilon}_0) \cdot (\boldsymbol{n}_d \cdot \mathbb{E} \cdot \boldsymbol{n}_d)^{-1} \cdot (\boldsymbol{\varepsilon}_0 : \mathbb{E} \cdot \boldsymbol{n}_d)\end{aligned} \tag{4.120}$$

where the symmetry of $(\boldsymbol{n}_d \cdot \mathbb{E} \cdot \boldsymbol{n}_d)^{-1}$ was used.

As pointed out by Pijaudier-Cabot and Benallal (1993) and Leblond et al. (1994), the localization condition in a non-local continuum is satisfied for an admissible direction $\boldsymbol{n}_d$ and its corresponding wave number of the bifurcation mode. This holds true for the ENLG model. Equation (4.118) clarifies that the ENLG model exhibits the same behavior for $D_0 < 1$. Each solution direction $\boldsymbol{n}_d$ has an unique admissible wave number associated with it, which differs from the classic local continuum. In this last case, since $c = 0$, the influence of k vanishes from the left-hand side of Equation (4.118), allowing all wave numbers for a given direction $\boldsymbol{n}_d$.

The limit case where $D_0 \to 1$ demonstrates the re-localizing nature of the ENLG model, retrieving a local bifurcation condition for high damage levels. This behavior is in agreement with the theoretical assumptions of the Eikonal formulation. Indeed, if $D_0 \to 1$ in Equation (4.100), one has $\bar{Y} \to Y$. Consequently, the Green function associated to the Helmholtz-type differential equation tends to the Dirac distribution (see Chapter 2). Thus, the equivalent ENLI formulation also exhibits the same re-localizing behavior. While desired for vanishing interactions in non-local models, this behavior may lead to spurious behavior in numerical simulations upon failure.

It is important to highlight that $D_0 = 1$ corresponds to an initial fully damaged material (equivalent to the appearance of a macro-crack) rendering the entire bifurcation analysis meaningless for any non-local or local continuum model.

GNL model. Similarly, the bifurcation equation for the GNL model is:

$$\frac{(1-D_0)(1+ck^2)}{g'} = (\boldsymbol{n}_d \cdot \mathbb{E} : \boldsymbol{\varepsilon}_0) \cdot (\boldsymbol{n}_d \cdot \mathbb{E} \cdot \boldsymbol{n}_d)^{-1} \cdot (\boldsymbol{\varepsilon}_0 : \mathbb{E} \cdot \boldsymbol{n}_d) \tag{4.121}$$

The only difference compared to the ENLG model is related to the term $1+ck^2$. Notice that the non-local term contributing to the equation does not vanish for high damage levels.

Geometric representation. One searches for the admissible directions $\boldsymbol{n}_d$ and the corresponding wave numbers. The geometric method proposed by Benallal and Lemaitre (1991) and further applied to the non-local integral theory in (Pijaudier-Cabot & Benallal, 1993; Baxevanis et al., 2008) is used here.

Let us consider the ENLG model and an initial isotropic medium. Now, $\mathbb{E}$ reads as in Equation (1.65) and one has:

$$(\boldsymbol{n}_d \cdot \mathbb{E} \cdot \boldsymbol{n}_d)^{-1} = \frac{\mathbf{I}}{G} - \frac{\lambda + G}{G(\lambda + 2G)} \boldsymbol{n}_d \otimes \boldsymbol{n}_d \tag{4.122}$$

$$\mathbb{E} : \boldsymbol{\varepsilon}_0 \cdot \boldsymbol{n}_d = \lambda \mathrm{tr}\, \boldsymbol{\varepsilon}_0 \boldsymbol{n}_d + 2G \boldsymbol{\varepsilon}_0 \cdot \boldsymbol{n}_d \tag{4.123}$$

$$\boldsymbol{n}_d \cdot \mathbb{E} : \boldsymbol{\varepsilon}_0 \cdot \boldsymbol{n}_d = \lambda \mathrm{tr}\, \boldsymbol{\varepsilon}_0 + 2G \boldsymbol{n}_d \cdot \boldsymbol{\varepsilon}_0 \cdot \boldsymbol{n}_d \tag{4.124}$$

and the right-hand side of Equation (4.118) can be re-expressed as:

$$\frac{(\boldsymbol{n}_d \cdot \mathbb{E} : \boldsymbol{\varepsilon}_0) \cdot \mathbf{I} \cdot (\boldsymbol{\varepsilon}_0 : \mathbb{E} \cdot \boldsymbol{n}_d)}{G} - \frac{\lambda + G}{G(\lambda + 2G)} (\boldsymbol{n}_d \cdot \mathbb{E} : \boldsymbol{\varepsilon}_0 \cdot \boldsymbol{n}_d) (\boldsymbol{n}_d \cdot \boldsymbol{\varepsilon}_0 : \mathbb{E} \cdot \boldsymbol{n}_d) \tag{4.125}$$

Substituting Equations (4.123) and (4.124) into the previous equation combined with Equation (4.118), we obtain:

$$4G\varepsilon_T^2 + \frac{4G^2}{\lambda + 2G} \left(\varepsilon_N + \frac{\lambda \mathrm{tr}\, \boldsymbol{\varepsilon}_0}{2G} \right)^2 = \frac{(1 - D_0)(1 + ck^2(1 - D_0))}{g'} \tag{4.126}$$

where ε_T and ε_N denote the tangential and normal components of the strain vector $\boldsymbol{\varepsilon}_0 \cdot \boldsymbol{n}_d$, respectively. They are defined as:

$$\varepsilon_N = \boldsymbol{n}_d \cdot \boldsymbol{\varepsilon}_0 \cdot \boldsymbol{n}_d \tag{4.127}$$

$$\varepsilon_T^2 = (\boldsymbol{\varepsilon}_0 \cdot \boldsymbol{n}_d) \cdot (\boldsymbol{\varepsilon}_0 \cdot \boldsymbol{n}_d) - \varepsilon_N^2 \tag{4.128}$$

In the $(\varepsilon_N, \varepsilon_T)$ plane, the initial strain state $\boldsymbol{\varepsilon}_0$ can be geometrically represented by Mohr circles describing the state for all directions $\boldsymbol{n}_d$. Moreover, Equation (4.126) represents an ellipse in the same plane, whose size is controlled by the term $1+ck^2(1-D_0)$. Thus, different ellipses exist for different wave numbers k. The bifurcation criterion in a gradient-enhanced continuum can be, therefore, interpreted as the condition where the corresponding ellipse, for a given wave number, is tangent to the biggest Mohr circle, defining a unique couple $(k, \boldsymbol{n}_d)$ (see Figures 4.5 and 4.6).

GNL model. The geometric bifurcation expression for the GNL model is similar to that of the ENLG model, with the following equation:

$$4G\varepsilon_T^2 + \frac{4G^2}{\lambda + 2G} \left(\varepsilon_N + \frac{\lambda \mathrm{tr}\, \boldsymbol{\varepsilon}_0}{2G} \right)^2 = \frac{(1 - D_0)(1 + ck^2)}{g'} \tag{4.129}$$

The only difference compared to the ENLG model is the absence of the term $(1 - D_0)$ in vanishing the wave number influence for high damage levels.

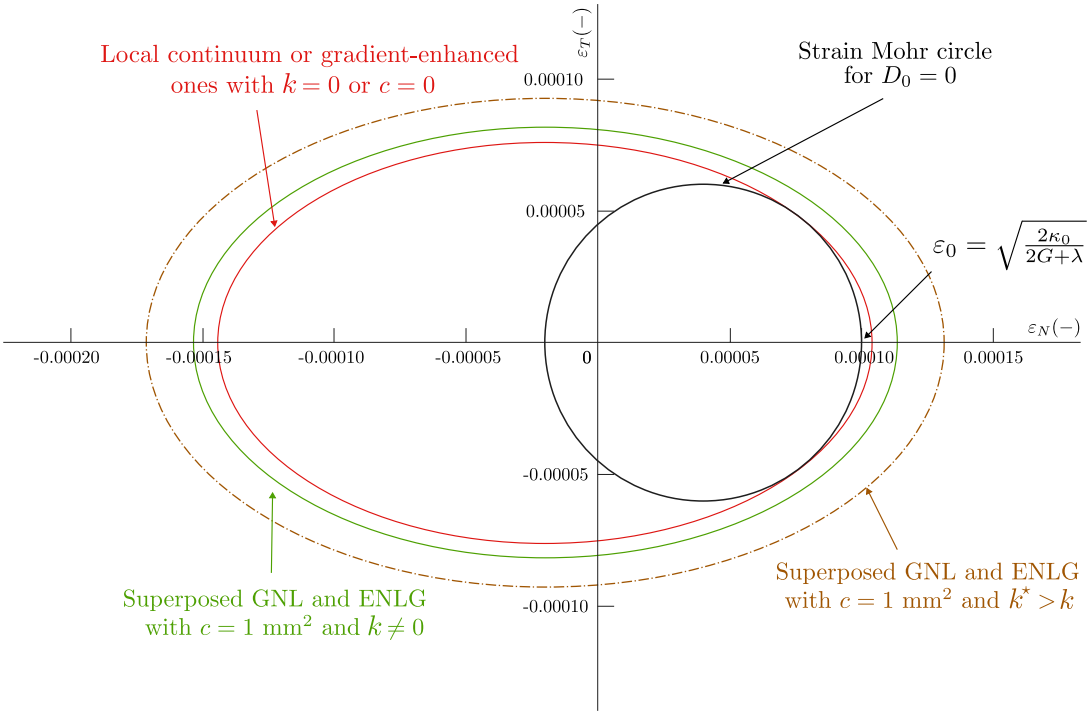

Figure 4.5 • Geometric representation of bifurcation for an initial strain state corresponding to $D_0 = 0.0$.

Illustrative example. Let us consider the following initial state of strains for illustration:

$$\boldsymbol{\varepsilon}_0 = \begin{bmatrix} \varepsilon_{01} & & \\ & -\nu\varepsilon_{01} & \\ & & -\nu\varepsilon_{01} \end{bmatrix} \tag{4.130}$$

along with the damage evolution law:

$$D = \begin{cases} \frac{\sqrt{\kappa_c}}{\sqrt{\kappa}} \frac{\sqrt{\kappa}-\sqrt{\kappa_0}}{\sqrt{\kappa_c}-\sqrt{\kappa_0}} & \text{if } \kappa < \kappa_c \\ 1 & \text{if } \kappa \geqslant \kappa_c \end{cases} \tag{4.131}$$

THis lax is essentially the same as the one proposed in Equation (3.29), modified to account for the fact that here the criterion function is written in terms of the energy release rate. Parameters used in the examples depicted in Figures 4.5 and 4.6 are $E = 20000\,\text{MPa}$, $\nu = 0.2$, $\kappa_0 = 1.11 \times 10^{-4}\text{MPa}$, $\kappa_c = 6.00 \times 10^{-3}\text{MPa}$ and $c = 1\,\text{mm}^2$. The initial state is $\varepsilon_{01} = 0.0001$ with $g' = 5208.33\,\text{MPa}^{-1}$.

The first bifurcation occurs for a local model (*i.e.*, $c = 0$) or for a non-local one with wave number $k = 0$ (*i.e.*, infinite wavelength $2\pi/k$). This is represented in Figure 4.5 by the intersection of the Mohr circle of the strains and the red ellipse at $(\varepsilon_N, \varepsilon_T) = (7.6 \times 10^{-5}, 4.8 \times 10^{-5})$. Considering $\boldsymbol{n}_d = (\cos\theta, \sin\theta, 0)^\top$, the corresponding bifurcation angle between the loading direction and the normal to the discontinuity is $\theta = 26.57°$. Similar results were obtained by Jirásek (2007) and Masseron et al. (2022) with different damage models.

It follows that the bifurcation condition in a local continuum serves as a lower bound for the ENLG and GNL models. For any $c > 0$ and $k > 0$, the corresponding ellipse is

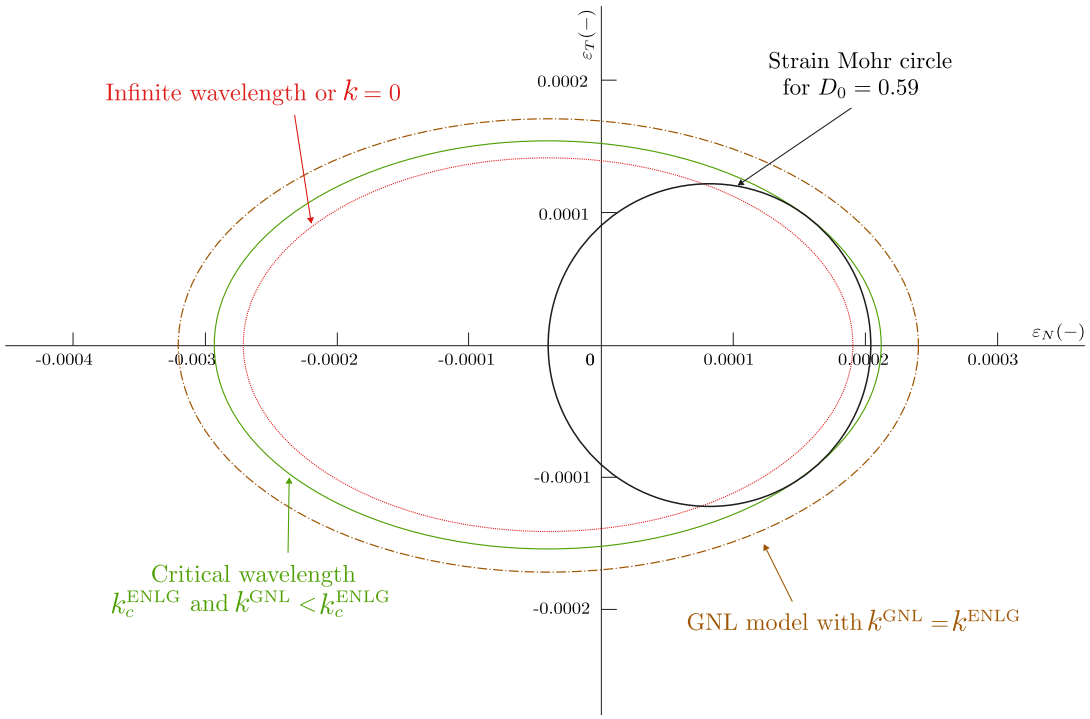

Figure 4.6 • Geometric representation of bifurcation for an initial strain state corresponding to $D_0 = 0.59$.

bigger than that of the local model. For a fixed c, its size increases with the wave number.

For the initial state where $D_0 = 0.0$, there are essentially no differences between the ENLG and GNL models. The gradient-enhanced continuum is exactly the same for both cases, resulting in superposed ellipses in Figure 4.5.

Let us consider a different initial state with $D_0 = 0.59$ and $\varepsilon_{01} = 2.04 \times 10^{-4}$, leading to $g' = 618.30\,\mathrm{MPa}^{-1}$. The corresponding geometric representation is depicted in Figure 4.6. In this case, differences between ENLG and GNL models become apparent through the analysis of the critical wave number (or similarly the critical wavelength). For each model, there exists an unique k_c for which the corresponding ellipse is tangent to the Mohr circle. This is geometrically represented by the green ellipse in Figure 4.6, achievable for both models but with different wave numbers. For this example, from Equations (4.132) and (4.133), one has $k_c^{\mathrm{ENLG}} = 0.68\,\mathrm{mm}^{-1}$ and $k_c^{\mathrm{GNL}} = 0.44\,\mathrm{mm}^{-1}$. For $k^{\mathrm{GNL}} = k_c^{\mathrm{ENLG}}$, one has a bigger ellipse for the GNL model, represented in brown in Figure 4.6, which does not intersect the strain Mohr circle. Thus, for increasing levels of D_0, the critical wave number increases faster for the ENLG model when compared to the GNL model. The associated critical wavelength $2\pi/k_c$ therefore decreases with D_0, reflecting the behavior derived in Chapter 3. It is proportional to $\sqrt{c}$ (see Equations (4.132) and (4.133)), and thus proportional to the internal length, which can be related to the size of the localized zone.

This is an essential feature of ENLG and GNL models. The gradient parameter c, and therefore the internal length, define a finite value of the critical wavelength associated to a bifurcation direction. In contrast, arbitrary wavelengths are possible in a local continuum.

Critical wave number. The critical wave number for each model can be obtained from Equations (4.126) and (4.129) and reads:

$$k_c^{\mathrm{ENLG}} = \sqrt{\frac{1}{c(1-D_0)}\left[\frac{g'}{1-D_0}\left(4G\varepsilon_T^2 + \frac{4G^2}{\lambda+2G}\left(\varepsilon_N + \frac{\lambda \mathrm{tr}\,\boldsymbol{\varepsilon}_0}{2G}\right)^2\right) - 1\right]} \tag{4.132}$$

$$k_c^{\mathrm{GNL}} = \sqrt{\frac{1}{c}\left[\frac{g'}{1-D_0}\left(4G\varepsilon_T^2 + \frac{4G^2}{\lambda+2G}\left(\varepsilon_N + \frac{\lambda \mathrm{tr}\,\boldsymbol{\varepsilon}_0}{2G}\right)^2\right) - 1\right]} \tag{4.133}$$

These expressions resemble the critical wave numbers obtained by Equations (3.15) and (3.25) in Chapter 3 based on the wave dispersion analysis in a one-dimensional bar. A similar expression can be derived from Equations (4.132) and (4.133), by considering $\nu = 0$ and uni-axial strain state on x direction (which implies that $G = E/2$, $\lambda = 0$, $\varepsilon_T = 0$ and $\varepsilon_N = \varepsilon_{01}$), resulting in:

$$k_c^{\mathrm{ENLG}} = \sqrt{\frac{1}{c(1-D_0)}\left(\frac{g'}{1-D_0}2Y_0 - 1\right)} \tag{4.134}$$

$$k_c^{\mathrm{GNL}} = \sqrt{\frac{1}{c}\left(\frac{g'}{1-D_0}2Y_0 - 1\right)} \tag{4.135}$$

Here, $Y_0 = 0.5E\varepsilon_{01}^2$. The above expressions closely resemble the ones obtained in Equations (3.15) and (3.25), with $2Y_0$ instead of ε_0, due to the criterion function written in terms of Y. Thus, the developed geometric representation generalizes the critical wave number obtained by the wave dispersion analysis.

In conclusion, the ENLG regularization preserves the localization limiting character of non-local approaches, such as the one described by Pijaudier-Cabot and Benallal (1993) for the INL model. The minimum wavelength at the onset of localization cannot be zero and has a critical value associated to a specific bifurcation direction. For high initial values of D_0, the ENLG model tends to approach the local condition for bifurcation, reducing the influence of c in the analysis. As explained before, this entirely agrees with the theoretical assumptions of the model and its re-localizing nature. However, it has an impact in numerical simulations, as we will see in the remainder of this thesis.

Yet, the bifurcation condition was developed following the classical assumptions of localization analysis: a homogeneous initial state was considered, and boundary effects were neglected. In reality, the complete regularization properties of non-local models depend on the entire degradation history. Completing the bifurcation analysis could involve considering an initial (possibly anisotropic) damage state that is not homogeneous. For instance, it may be interesting to understand the link between the singularity of the metric tensor and the bifurcation condition.

5 Numerical simulations

The isotropic ENLG and GNL damage models are implemented in a finite element toolbox developed in-house at CEA (Badri et al., 2021; Badri & Rastiello, 2023) (for testing

purposes) using the FreeFEM (Hecht, 2012) platform (https://freefem.org/). Both models are tested in the simulation of two classic problems to highlight differences and underline how the ENLG model behaves in situations where the GNL model shows some well-known drawbacks. Full 2D conditions are considered. Accordingly, the variational equation (4.18) needs to be solved in addition to the equilibrium equation during the solving process.

5.1 Damage model

An isotropic damage model with a single scalar damage variable $D \in [0, 1]$ is considered. Following (Sarkar et al., 2019) and (Negi & Kumar, 2022), parameter h can be taken very small compared to the Young's modulus, and the constitutive stress-strain relation is simplified as:

$$\boldsymbol{\sigma}(\boldsymbol{u}, D) = (1 - D)\mathbb{E} : \boldsymbol{\varepsilon}(\boldsymbol{u}) \tag{4.136}$$

The damage variable evolves according to the exponential evolution model introduced in Equation (1.46), with the damage-driving history variable:

$$\kappa = \max_t(\kappa_0, \bar{e}) \tag{4.137}$$

where $\bar{e} = \bar{e}(\boldsymbol{\varepsilon}(\boldsymbol{u}))$ is the non-local equivalent strain, κ_0 is the damage threshold, B_t the damage brittleness, and α_t is a parameter used to account for residual stresses in the behavior law. The local equivalent strain is computed according to the modified Von Mises definition (De Vree et al., 1995), defined in Equation (1.45).

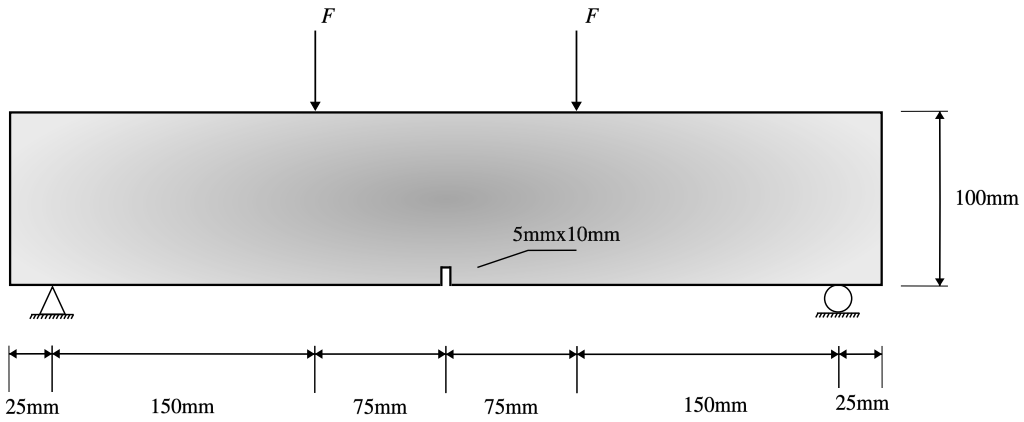

Figure 4.7 • Four-point bending test – Geometry and boundary conditions.

5.2 Finite element implementation

The domain Ω is discretized through a finite element mesh Ω^h containing linear triangular elements (Constant Strain Triangles, CST). The unknown displacement and non-local equivalent strain fields on each finite element are approximated by linear interpolation of their nodal values (denoted by the piece-wise polynomials $\mathbb{P}_1$). This choice is retained here since the damage variable is kept uniform within an element, ensuring compatibility between the linear strain and damage and, therefore, yielding a smooth stress field (Simone et al., 2003a; Peerlings, 1999).

A staggered/partitioned Picard iteration algorithm is employed to handle non-linearity (Badri et al., 2021; Badri & Rastiello, 2023). At iteration $k+1$, one first computes the $[\mathbb{P}_1, \mathbb{P}_1]$ discretized vector-valued displacement field $\boldsymbol{u}^{h,k+1} \in \mathcal{U}^h(\boldsymbol{u}^d)$ such that:

$$\int_{\Omega^h} (1 - D^{h,k}) \boldsymbol{\varepsilon}(\boldsymbol{u}^{h,k+1}) : \mathbb{E} : \boldsymbol{\varepsilon}(\boldsymbol{v}^h)\, dV = \int_{\partial\Omega_F^h} \boldsymbol{t}^d \cdot \boldsymbol{v}^h\, dS \quad \forall\, \boldsymbol{v}^h \in \mathcal{U}^h(\boldsymbol{0}) \tag{4.138}$$

and then computes the $\mathbb{P}_1$ discretized nonlocal equivalent strain field $\bar{e}^{h,k+1}$ solving:

$$\int_{\Omega^h} \frac{1}{1 - D^{h,k}}\, \bar{e}^{h,k+1}\, \eta^h dV + \int_{\Omega^h} c \nabla \bar{e}^{h,k+1} \cdot \nabla \eta^h dV = \int_{\Omega^h} \frac{1}{1 - D^{h,k}}\, e(\boldsymbol{\varepsilon}(\boldsymbol{u}^{h,k+1}))\, \eta^h dV \quad \forall \eta^h \in \mathcal{V}^h \tag{4.139}$$

Here, $(\mathcal{U}^h(\boldsymbol{u}^d), \mathcal{U}^h(\boldsymbol{0}), \mathcal{V}^h)$ are the discretized counterparts of $(\mathcal{U}(\boldsymbol{u}^d), \mathcal{U}(\boldsymbol{0}), \mathcal{V})$, $D^{h,k}$ is the $\mathbb{P}_0$ discretized damage field at iteration k, and $e(\boldsymbol{\varepsilon}(\boldsymbol{u}^{h,k+1}))$ is the $\mathbb{P}_0$ local strain field computed from the symetrized gradient of $\boldsymbol{u}^{h,k+1}$. At each iteration, the field $\bar{e}^{h,k+1}$ is used to update the $\mathbb{P}_0$ history variable field κ^h and compute damage. The computation is repeated till convergence at each pseudo-time step.

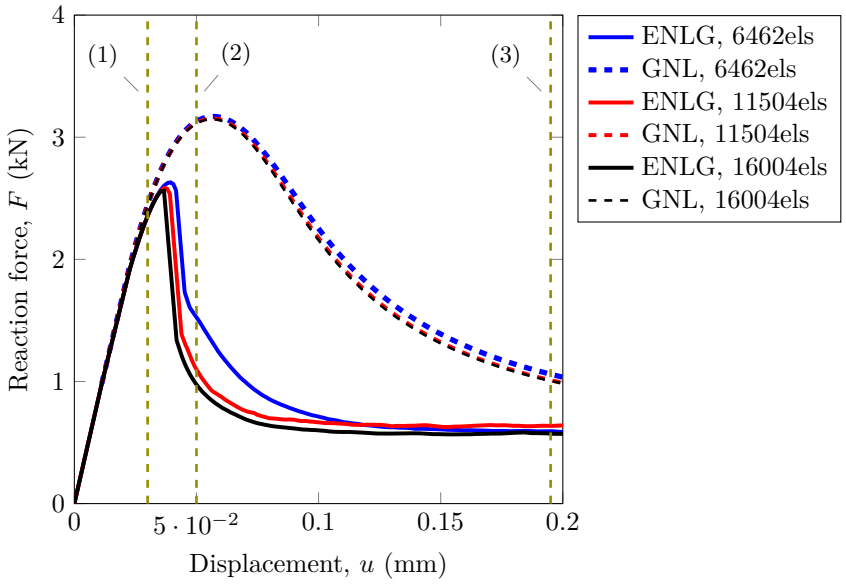

Figure 4.8 • Four-point bending test – Structural force vs. displacement responses computed using the GNL and ENLG models and three different meshes.

5.3 Four-point bending test

A notched beam is submitted to a four-point bending test (Figure 4.7). Numerically, an increasing displacement is imposed at the loading points (denoted by the force F). The structure is discretized using three different meshes with additional refinement in the central zone of the beam. They contain 6262 (coarse mesh), 11504 (medium mesh) and 16004 (fine mesh) elements, respectively. Material parameters used in simulations are given in Table 4.1.

Table 4.1 • Four-point bending test – Material parameters.

E [N/mm^2]	c [mm^2]	κ_0 [-]	B_t [-]	k [-]	α_t [-]	ν [-]
40000	4	0.000075	300	10	0.92	0.2

Global responses. Figure 4.8 shows the structural responses (force vs. displacement) obtained using the ENLG and GNL models for the three considered meshes. Mesh convergence is obtained for the GNL model, whereas slight differences can be observed in the responses upon mesh refinement for the ENLG formulation. Moreover, the ENLG model gives more brittle responses than the GNL model, as is expected for evolving interaction approaches (Giry et al., 2011; Vandoren & Simone, 2018; Rastiello et al., 2018b).

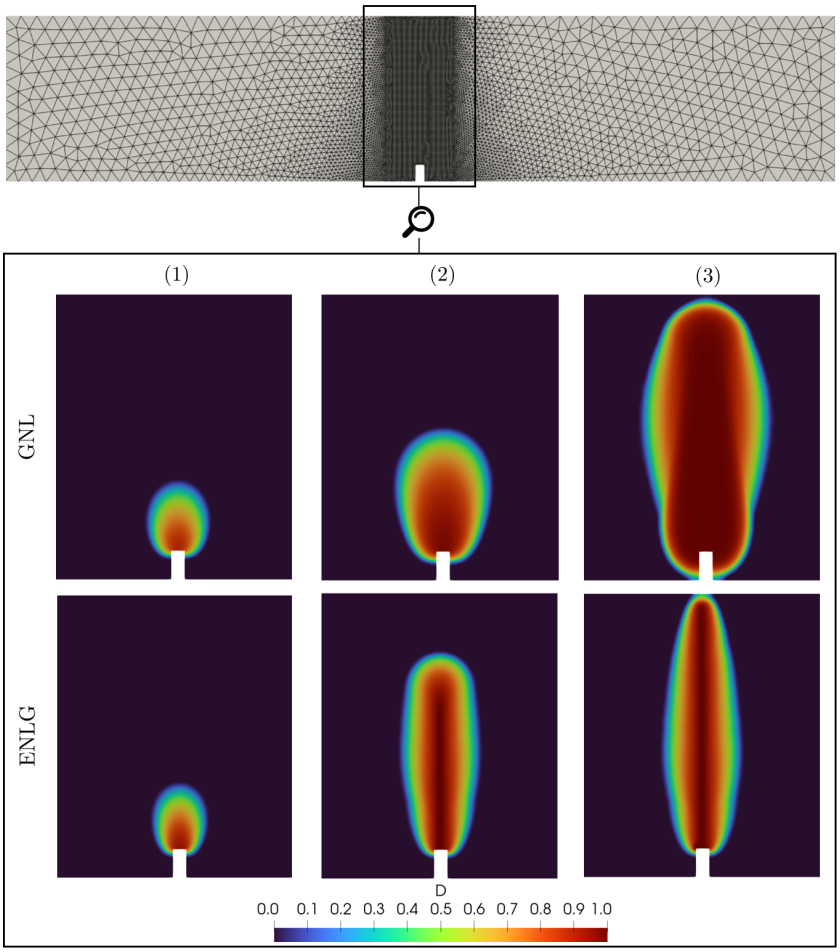

Figure 4.9 • Four-point bending test – Damage evolution computed using the GNL and ENLG models (displacement levels identified by labels (1), (2) and (3) in Figure 4.8).

Damage evolution. The damage maps computed for three different imposed displacement levels using both models are depicted in Figure 4.9. In the early phases of the

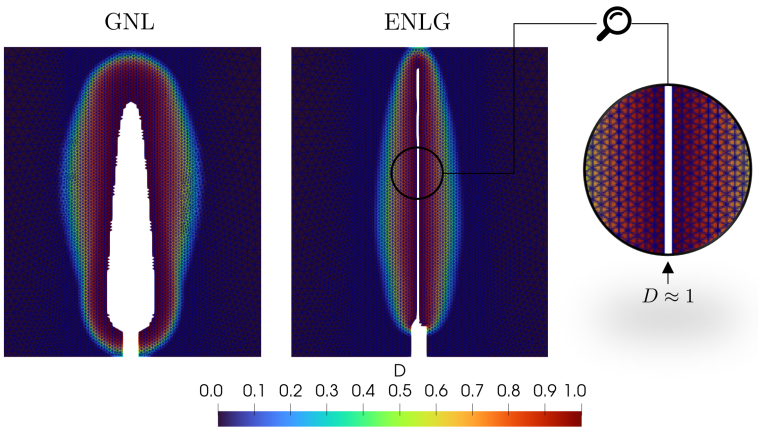

Figure 4.10 • Four-point bending test – Damage maps at the end of the simulation (step (3) in Figure 4.9) for the GNL and ENLG models (post-processing element deletion applied for $D > 0.995$ to identify a "pseudo-crack").

test (step 1), the damage fields provided by the GNL and ENLG models are very similar (damage starts close to the notch). Then, the damaged zone computed by the GNL model becomes wider than the one obtained through the ENLG model. In this latter case, the damage field tends to localize since the early phases of the simulation (i.e., the damage tends to unity on a single line of elements) and propagates towards the upper part of the beam (step 2). At the end of the simulation (step 3), nonphysical damage spreading takes place for the GNL model around the notch. Damage is diffused in a large zone, and the expected "pseudo-crack" path cannot be described. Conversely, the damage is still localized in a smaller damage band (with $D \to 1$ on its center) about $2l_c$ in width for the ENLG model, and the nonphysical damage diffusion does not occur. Very similar behavior was described by (Rastiello et al., 2018b) considering an integral ENL damage model.

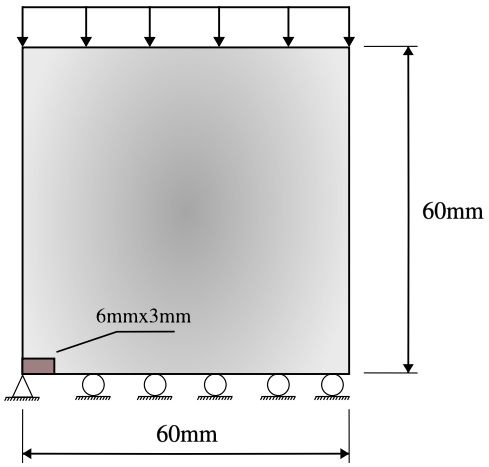

Figure 4.11 • Shear-band test – Geometry and boundary conditions.

This feature can be even better underlined by applying a simple post-treatment of the damage field. Figure 4.10 shows the damage maps at the end of the simulation, considering element deletion when D exceeds the arbitrary threshold value of 0.995 at a

Table 4.2 • Shear-band test – Material parameters.

E [N/mm^2]	c [mm^2]	κ_0 [-]	B_t [-]	k [-]	α_t [-]	ν [-]
20000	2	0.0001	100	1	0.94	0.18

given integration point. In the case of the GNL model, high damage levels are attained over a large region, which cannot be compared to a realistic "pseudo-crack". Conversely, the ENLG model provides a more physical "pseudo-cracking" behavior since $D \to 1$ on a single line of elements. This behavior is directly related to non-local interactions evolution during the computation. In particular, material points separated by the damage band no longer interact due to the damage-dependent Riemannian metric. Consequently, nonphysical damage spreading does not occur. The ENLG not only gives a better description of the "pseudo-crack" path compared to the GNL model but also shows promising features to naturally model damage-to-fracture transition, thus coupling CDM and Fracture Mechanics models.

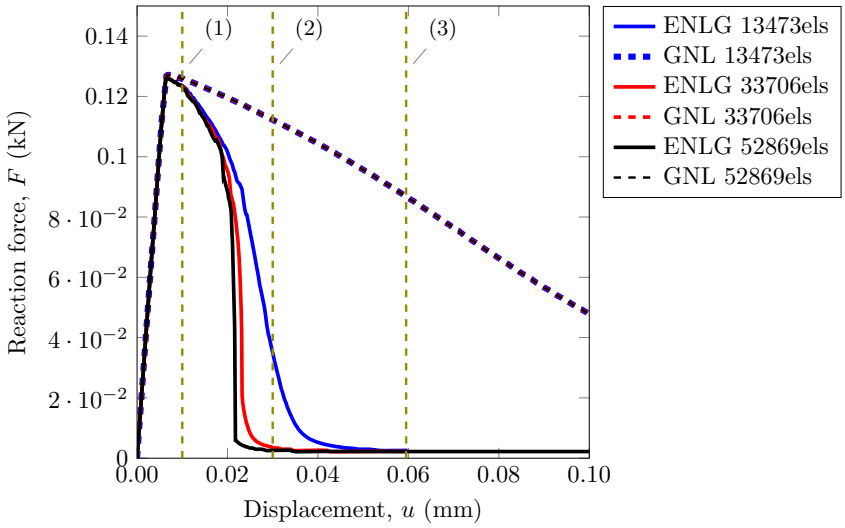

Figure 4.12 • Shear-band test – Structural force vs. displacement responses computed using the GNL and ENLG models and three different meshes.

5.4 Shear-band problem

The second example analyzed is the shear-band test. A square plate is submitted to a compression action on the upper boundary (Figure 4.11). An increasing vertical displacement is applied to the top of the specimen, whereas the bottom of the specimen is constrained. Once again, three different meshes are used for the simulations. They contain 13473 (coarse mesh), 33706 (medium mesh) and 52869 elements (fine mesh), respectively. A rectangular weakened zone (with $\kappa_0^\star = \kappa_0/5$), 6x3 mm^2 in size, is placed on the bottom left of the specimen to initiate damage. Material parameters are given in Table 4.2.

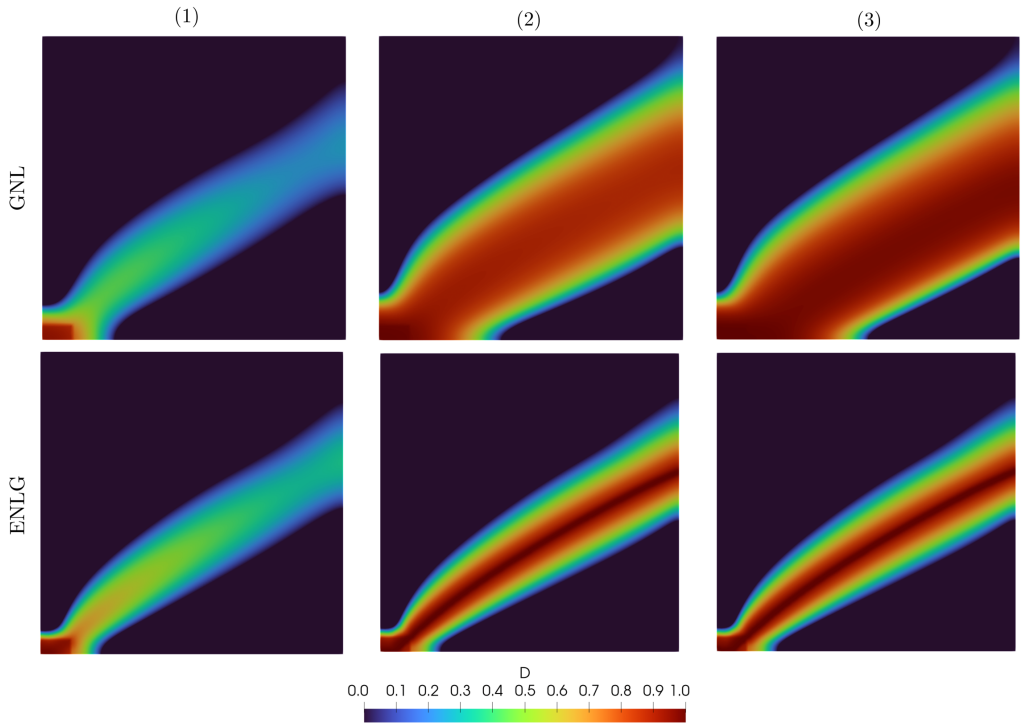

Figure 4.13 • Shear-band test – Damage evolution computed using the GNL and ENLG models (displacement levels identified by labels (1), (2) and (3) in Figure 4.12).

Global responses. The structural responses obtained using the GNL and ENLG models and different meshes is given in Figure 4.12. The maximum reaction force is the same for both models. After the load peak is reached, the responses provided by the two models start to differ. Mesh convergence is obtained for the GNL model, but differences are observed in the responses provided by the ENLG model for the different meshes. A clear tendency toward mesh convergence is, however, observed.

Damage evolution. Figure 4.13 gives the damage maps computed using the GNL and ENLG models for three simulation steps. In the early phases of the simulation (step 1), right after the maximum reaction force, damage initiates in the weakened zone and starts to propagate diagonally in the specimen (step 2). From this point on (step 3), the size of the damage band tends to increase in the transverse direction (the band enlarges). This is a well-known drawback of the classic non-local damage models. Contrarily, the shear band remains stationary for the ENLG model since no non-local interactions occur between material points. High damage levels are concentrated in a thin band a few elements width.

Such behavior becomes clearer when post-processing the results by deleting the elements where damage exceeds the threshold value of 0.999 (see Figure 4.14). For illustration, a very large displacement level is considered in this case ($u = 0.5$ mm). One can see that damage exceeds the threshold value in a larger zone in the case of the GNL model, whereas it tends to concentrate on almost one line of elements in the case of the ENLG model (i.e., a "pseudo-crack" is described). Once again, the ENLG model provides a more physical behavior than the GNL one.

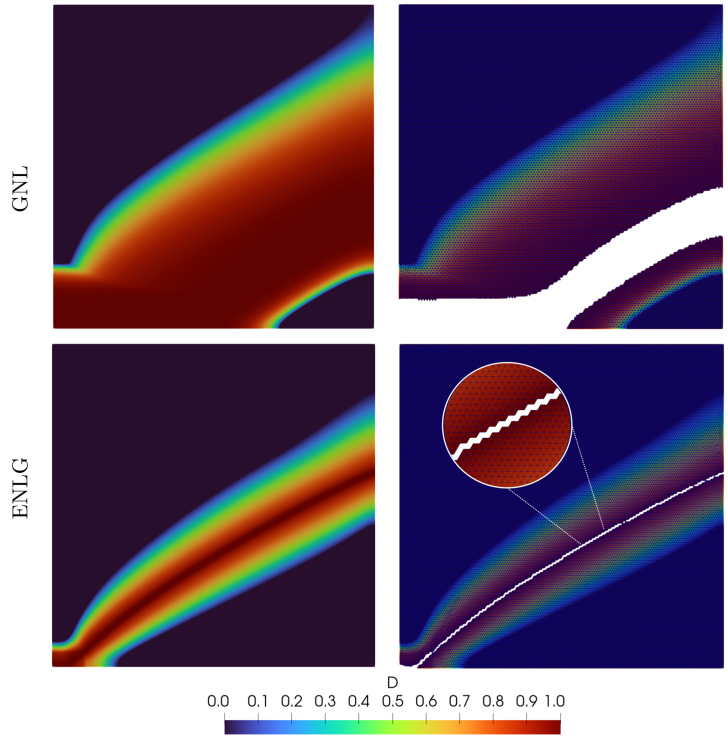

Figure 4.14 • Shear-band test – Damage map computed for a high displacement level ($u = 0.5$ mm) (post-processing element deletion applied for $D > 0.999$ to identify a "pseudo-crack").

Comments on solution oscillations. The small oscillations observed in the force vs. displacement responses illustrated in Figure 4.12 concerning the ENLG model are related to the numerical approximation of the solution. (Vandoren & Simone, 2018) studied this aspect and its consequences on the damage and non-local equivalent strain evolution. They showed that, in a finite element context, the vanishing gradient parameter in (2.22) causes oscillations in the non-local field controlling damage evolution. In this case, mesh convergence could be affected, and minor damage spreading could take place. Such an effect is also present in the ENLG model. It is less pronounced in the 2D formulation used here since the finite element matrix related to the term c in (4.139) does not vanish. However, the contributions where the term $1/(1-D)$ appears can still cause this effect. Simulations in 1D and 3D of the ENLG model will inevitably show this behavior (see (Ribeiro Nogueira et al., 2022a) for the 1D case) since the term related to c vanishes when $D \to 1$.

Vandoren and Simone (2018) proposed to use a minimum value of the gradient parameter to cancel non-local interactions properly and significantly reduce this effect. A similar study should be carried out for the ENLG model. The case of the ENLG model is even more complex, as division by zero appears when $D \to 1$. However, it should be noted that from a physical viewpoint, the displacement field is no longer continuous when this condition occurs. Consequently, instead of correcting the damage formulation, strong discontinuities should be considered in the model to make it more physically and numerically robust.

Summary of Chapter 4

Formulation:

- A thermodynamic framework to derive anisotropic and isotropic ENLG damage models based on a **geometric extension** of the micromorphic approach was proposed.
- Compared to the GNL model, the only modification introduced in the free energy is the consideration of a **Riemannian norm** (*i.e.*, the non-local equivalent strain lives in a space curved by damage).
- The bifurcation analysis shows that the ENLG models **preserves the localization limiting character** of non-local approaches. It differs from the GNL model for $D_0 > 0$ and presents a **re-localizing nature** for high initial damage levels.
- The derived critical wave number **generalizes** the expressions obtained from the wave dispersion analysis in Chapter 3.

Simulations:

- From simplified 2D isotropic damage numerical simulations, it is demonstrated that the ENLG model gives more **realistic crack paths** when compared to the GNL model.
- Damage **re-localizes** in almost one line of elements for the ENLG model, which better describes a sort of "pesudo-crack".
- The numerical examples illustrated in this chapter show that the force-displacement responses provided by the ENLG formulation are **highly brittle**.
- In order to reduce the brittleness of the response, which is intrinsic to the eikonal formulation and more generally to non-local formulations with evolving interactions, one could use a **different constitutive model** or proceed with an *ad-hoc* **calibration** of the model parameters.
- The limit case where $D \to 1$ leads to a division by zero in the ENLG formulation. One has $\mathbf{g}^{-1}$ that becomes **singular**, given that $\det(\mathbf{g}^{-1}) \to 0$, and its inverse (the metric itself) cannot be obtained. In other words, similarly to a black hole in space-time, $D \to 1$ represents the case where a **singularity** appears in the space curved by damage (see Figure 4.1).
- The **transition** from a regularized ENLG damage model to an explicit crack description should be considered (see, for instance, (Mazars & Pijaudier-Cabot, 1996; Simone et al., 2003b; Cazes et al., 2009; Cuvilliez et al., 2012; Negi & Kumar, 2022; Voreux, 2022)). This would be suitable not only to deal with the singularity, but also to provide **direct access** to crack information.

5

Numerical implementations and structural analysis with ENLG anisotropic damage

The main aim of this chapter is to study the performance and capabilities of the ENLG regularization coupled to a tensorial damage behavior. The first sections provide a brief overview of the general equations of Desmorat's anisotropic damage model (Desmorat, 2015) and the ENLG regularization. A visualization technique based on using ellipsoids is then introduced for representing damage and metric tensors, and to illustrate how induced anisotropic behavior naturally results in evolving anisotropic interactions. Subsequently, the numerical solution of the coupled problem is detailed. A staggered scheme is applied to solve the variational formulation at the global level, and an iterative Newton-Raphson procedure is used for constitutive law integration at the quadrature points. Then, the last section offers a discussion concerning the main features of the presented formulation based on the 2D simulation of well-known experimental tests. A purely numerical test case is then developed to show the influence of anisotropic non-local interactions on damage evolution. Finally, first three-dimensional simulations are briefly presented. Except from some modifications in the text and additional comments, this chapter was extracted from Ribeiro Nogueira et al. (2024b) Computer Methods in Applied Mechanics and Engineering, 429, 117100

Contents

1 Introduction

Various anisotropic damage models have been developed to represent quasi-brittle materials such as concrete, masonry, and certain types of rocks. These models use different representations of damage, including vectors (Krajcinovic & Fonseka, 1981), second-order tensors, fourth-order tensors (Krajcinovic & Mastilovic, 1995; Maire & Chaboche, 1997), and even eighth-order tensors (Chaboche, 1982). However, fourth-order and eighth-order tensors prove to be too complex due to the large number of components, making them challenging to fully identify. Consequently, many authors have chosen to work with second-order tensors (Cordebois & Sidoroff, 1982a; Cordebois & Sidoroff, 1982b; Ladevèze, 1983; Murakami, 1988; Halm & Dragon, 1998; Desmorat, 2004; Desmorat, 2015), which restrict the damage description to orthotropic behaviors. This assumption effectively captures observed crack patterns in quasi-brittle materials, where cracks typically propagate either perpendicular or parallel to the loading direction.

An alternative approach to modeling anisotropic damage is presented in (Bažant & Oh, 1983a; Bažant, 1984a; Bažant & Gambarova, 1984; Bažant & Prat, 1988; Bažant et al., 1996). This approach describes material behavior independently on planes of various orientations (micro-planes) within a unitary sphere. Strain or stress vectors on each plane are obtained by projecting their respective macroscopic tensors based on static or kinematic constraints. For quasi-brittle materials, the strain tensor is projected onto each micro-plane, and simple constitutive laws are used to compute stress tensors at micro-planes. The macroscopic stress tensor is then obtained by integrating micro-plane contributions spherically based on the principle of virtual work.

From a numerical perspective, when applied to simulations at the structure scale, all the models cited above yield mesh-dependent results without regularization techniques. Non-local damage models, both integral (Pijaudier-Cabot & Bažant, 1987) and gradient-enhanced (Peerlings et al., 1996a), have been employed to recover objective results. However, these methods fail to reproduce realistic cracking behavior due to issues like parasite damage diffusion, incorrect damage initiation, and attraction to domain boundaries (Geers et al., 1998; Simone et al., 2004; Pijaudier-Cabot et al., 2004;

Krayani et al., 2009; Pijaudier-Cabot & Dufour, 2010; Giry et al., 2011; Desmorat, 2015; Rastiello et al., 2018a; Ribeiro Nogueira et al., 2022a). These drawbacks arise because the interactions are considered constant and isotropic in classic approaches.

To address these limitations, a new class of non-local models with evolving interactions, known as transient internal length models, has been developed. Geers et al. (1998) proposed one of the earliest evolving interaction models, where the gradient parameter varied with strain but remained isotropic. Isotropic damage-dependent evolving interactions were introduced in (Poh & Sun, 2017), utilizing the micromorphic framework to derive a similar gradient-enhanced model. Giry et al. (2011) developed a stress-based evolving interactions integral model, more suitable to handle free boundaries. As stress fields are employed, the interactions become inherently anisotropic. A gradient-enhanced version of this anisotropic interactions approach was presented in (Vandoren & Simone, 2018). Negi et al. (2020) proposed an anisotropic transient-gradient approach based on (Poh & Sun, 2017), coupling the effects of damage and stress fields in the interactions. Several other evolving interaction models have been proposed in the literature (*e.g.*, (Pijaudier-Cabot & Dufour, 2010; Nguyen, 2011; Rojas-Solano et al., 2013; Nguyen et al., 2018; Amani, 2023)).

Inspired by the analogy between non-local interactions and wave propagation time in damaged media, Desmorat and Gatuingt (2007a) and Desmorat et al. (2015a) introduced the Eikonal Non-Local (ENL) regularization. This approach models non-local interactions that depend on the damage field, potentially incorporating anisotropy. In this method, non-local interaction distances are determined as the solution to a stationary eikonal equation with a damage-dependent metric field. Rastiello et al. (2018a) presented a two-dimensional (2D) implementation of the integral ENL regularization for isotropic damage. Additionally, Thierry et al. (2020b) and Ribeiro Nogueira et al. (2022a) conducted studies on the regularization properties of the ENL approach in one-dimensional (1D) settings. Marconi (2022) conducted 2D computations utilizing an ENLG regularized isotropic damage model and investigated the coupling between damage and plasticity within a 1D framework. Recently, Ribeiro Nogueira et al. (2024a) provided a novel theoretical derivation of the gradient-enhanced version of the ENL formulation and applied it to 2D isotropic damage mechanics simulations.

Classic non-local models, characterized by a constant internal length, have been employed in the context of anisotropic damage models in previous works. For example, Desmorat et al. (2007a) utilized the conventional non-local integral approach alongside a second-order damage tensor constitutive relation. Kuhl et al. (2000) incorporated a classic gradient-enhanced model, based on the strain tensor, to regularize the anisotropic microplane formulation for quasi-brittle materials. Zreid and Kaliske (2014) proposed a simplified gradient-enhanced regularization of microplane models, where a scalar quantity is used in the regularization instead of the strain tensor. Additionally, Fassin et al. (2019) introduced a gradient-extended second-order anisotropic damage tensor model while maintaining the internal length isotropic and constant. Initial anisotropic non-local regularization, pertaining to materials with intrinsic anisotropy, has also been applied for modeling composites (Wu et al., 2015; Jin & Arson, 2018; Forghani et al., 2019; Yin et al., 2020; Lu & Guo, 2022). Similar concepts have been explored in the phase-field

community (Li & Maurini, 2019; Teichtmeister et al., 2017; Nagaraja et al., 2023), where the crack energy density was modified using structural tensors containing information about preferential microstructure directions.

This paper introduces a novel approach by coupling an evolving anisotropic interaction gradient-enhanced regularization (Desmorat et al., 2015a; Ribeiro Nogueira et al., 2024a) with an anisotropic damage constitutive behavior (Desmorat, 2015). The key concept is that anisotropic behavior in quasi-brittle materials, such as concrete, is induced by damage, while the medium is initially considered isotropic. The induced anisotropy is incorporated through the ENLG model, where non-local interactions naturally evolve from isotropic to anisotropic based on a damage-dependent Riemannian metric.

The manuscript is structured as follows. Sections 2 and 3 provide a brief overview of the general equations of Desmorat's anisotropic damage model (Desmorat, 2015) and the ENLG regularization. A visualization technique based on using ellipsoids is then introduced for representing damage and metric tensors, and to illustrate how induced anisotropic behavior naturally results in evolving anisotropic interactions. 4 details the numerical solution of the coupled problem. A staggered scheme is applied to solve the variational formulation at the global level, and an iterative Newton–Raphson procedure is used for constitutive law integration at the quadrature points. Finally, 5 offers a discussion concerning the main features of the presented formulation based on the 2D simulation of well-known experimental tests. A purely numerical test case is then developed to show the influence of anisotropic non-local interactions on damage evolution. Finally, a first three-dimensional (3D) simulation is briefly presented, followed by some conclusions to close the article.

2 Anisotropic eikonal gradient-enhanced damage formulation

The ENL formulation, as proposed by Desmorat et al. (2015a), introduces a novel perspective on evolving non-local interactions. The underlying assumption is that damage induces deformation in the space within which interaction distances are computed. The interaction distances between the material points are obtained by solving a time-independent isotropic eikonal equation (a Hamilton–Jacobi stationary equation) with a damage-dependent Riemannian metric function. In this deformed space, the interaction distance between two points corresponds to the length of the shortest (geodesic) path connecting them (see (Rastiello et al., 2018a), for more details and illustrations).

2.1 Eikonal non-local formulation and anisotropic interactions

According to the general framework of anisotropic damage mechanics involving a second-order (symmetric) tensor damage variable $\mathbf{D}$, the differential problem for calculating the

non-local variable $\bar{e}$ that controls damage evolution is computed as follows:

$$\bar{e} - \frac{c}{\sqrt{\det \mathbf{g}}} \nabla \cdot \left(\sqrt{\det \mathbf{g}}\, \mathbf{g}^{-1} \cdot \nabla \bar{e} \right) = e \qquad \Omega \tag{5.1}$$

$$\mathbf{g}^{-1} \cdot \nabla \bar{e} \cdot \boldsymbol{n} = 0 \qquad \partial\Omega \tag{5.2}$$

where $\mathbf{g}$ is a damage-dependent Riemannian metric tensor (it completely defines the deformation of the space where, according to the eikonal formalism, the non-local variable $\bar{e}$ lives):

$$\mathbf{g} = (\mathbf{I} - \mathbf{D})^{-1} \tag{5.3}$$

In these equations, e is the local counterpart of $\bar{e}$, $\mathbf{I}$ is the second-order identity tensor, Ω is the considered domain, $\boldsymbol{n}$ is the outward normal vector to its boundary $\partial\Omega$, c is a parameter homogeneous to the square of a length (introducing an initial length scale in the formulation), ∇ is the gradient operator, $\nabla\cdot$ is the divergence operator, and the symbol $\cdot$ denotes the simple contraction between tensors.

Equation (5.1) was derived by Desmorat et al. (2015a) from the integral-type version of the ENL model by following the same procedure employed by Peerlings et al. (1996a) to derive the classic Gradient-enhanced Non-Local (GNL) formulation. Recently, Ribeiro Nogueira et al. (2024a) proposed a robust thermodynamics framework based on the Micromorphic Media Theory (Forest, 2009) to derive the ENL formulation. Using concepts from differential geometry, the authors independently derived Equation (5.1), obtained the boundary condition Equation (5.2) (a detail not covered in (Desmorat et al., 2015a)), characterized energy dissipation, and verified the Clausius–Duhem inequality.

Considerations of the free-energy potential and material symmetry. To derive the ENLG model based on a micromorphic media framework, Ribeiro Nogueira et al. (2024a) introduced the following free-energy potential:

$$\rho\psi = \rho\psi(\boldsymbol{\varepsilon}, \mathbf{D}, \bar{e}, \tilde{\nabla}\bar{e}) = \rho\psi_0 + \rho\psi^{nl}(\bar{e}, \tilde{\nabla}\bar{e}; \mathbf{g}^{-1}) \tag{5.4}$$

where $\rho\psi_0$ represents a local contribution associated with a specified damage model, and $\rho\psi^{nl}(\bar{e}, \tilde{\nabla}\bar{e}; \mathbf{g}^{-1})$ is the non-local contribution:

$$\rho\psi^{nl}(\bar{e}, \tilde{\nabla}\bar{e}; \mathbf{g}^{-1}) = \frac{1}{2} h (e - \bar{e})^2 + \frac{1}{2} hc \|\tilde{\nabla}\bar{e}\|^2_{\mathbf{g}} \tag{5.5}$$

$$= \frac{1}{2} h (e - \bar{e})^2 + \frac{1}{2} d\bar{e} \cdot \mathbf{g}^{-1} \cdot d\bar{e} \tag{5.6}$$

Here, h is a parameter homogeneous to a stiffness, $\tilde{\nabla}$ denotes the gradient computed in a curved space, $\|\bullet\|_{\mathbf{g}}$ is the Riemannian norm, and $d\bar{e}$ denotes a 1-form. See the cited work for more details.

It is noteworthy that when employing the Euclidean metric, the expression $\rho\psi^{nl}(\bar{e}, \tilde{\nabla}\bar{e}; \mathbf{g}^{-1})$ simplifies to that of the conventional GNL model (Peerlings et al., 1996a; Peerlings et al., 2004). Specifically, $\rho\psi^{nl}_{\mathrm{GNL}}(\bar{e}, \nabla\bar{e}) = \frac{1}{2}h(e-\bar{e})^2 + \frac{1}{2}hc\|\nabla\bar{e}\|^2 = \frac{1}{2}h(e-\bar{e})^2 + \frac{1}{2}\nabla\bar{e}\cdot\nabla\bar{e}$ (which is similar to the phase-field crack density functions). For an isotropic medium, it can be readily verified that the latter potential maintains invariance under rotations and reflections, satisfying the isotropy condition $\rho\psi^{nl}_{\mathrm{GNL}}(\bar{e}, \mathbf{Q} \star \nabla\bar{e}) = \rho\psi^{nl}_{\mathrm{GNL}}(\bar{e}, \nabla\bar{e}), \forall, \mathbf{Q} \in \mathcal{O}(3)$,

where $\mathcal{O}(3)$ denotes the orthogonal group, defined as $\mathcal{O}(3) = \{\mathbf{Q} \,|\, \mathbf{Q}^\top \cdot \mathbf{Q} = \mathbf{I}\}$, and $\star$ denotes a general action of a group.[1] In the case of an anisotropic medium, it is expected that $\rho\psi^{nl}_{\text{GNL}}(\bar{e}, \mathbf{Q}\star\nabla\bar{e}) = \rho\psi^{nl}_{\text{GNL}}(\bar{e}, \nabla\bar{e})$ for all $\mathbf{Q} \in \mathcal{H} \subset \mathcal{O}(3)$, where $\mathcal{H}$ denotes a specified symmetry group of the anisotropic material. This ensures that the anisotropic free energy remains invariant under actions respecting the material symmetry.

Now, the representation theorem (Boehler, 1987) enables the representation of the free energy as an isotropic function by introducing a structural tensor, denoted as $\mathbf{M}$. This is achieved by ensuring that $\mathbf{Q}\star\mathbf{M} = \mathbf{M}$ holds for $\mathbf{Q} \in \mathcal{H} \subset \mathcal{O}(3)$. In the context of the ENLG model, this requirement holds true with considering the structural tensor equal to the inverse of the damage-dependent Riemannian metric ($\mathbf{M} = \mathbf{g}^{-1}$). Consequently, one has:

$$\rho\psi^{nl}(\bar{e}, \mathbf{Q}\star\tilde{\nabla}\bar{e}; \mathbf{Q}\star\mathbf{g}^{-1}) = \rho\psi^{nl}(\bar{e}, \tilde{\nabla}\bar{e}; \mathbf{g}^{-1}) \quad \forall\, \mathbf{Q} \in \mathcal{O}(3) \tag{5.7}$$

This formulation exhibits notable similarities with those developed by Teichtmeister et al. (2017). In a similar way, Reese et al. (2021) explored the use of an anisotropic damage variable as a structural tensor in the definition of free energy.

2.2 Comparison with other gradient formulations with evolving non-local interactions

The general formalism for gradient-damage models can be expressed as follows:

$$\bar{e} - \phi\nabla\cdot(\boldsymbol{\Phi}_1\cdot\nabla\bar{e}) = e \qquad \Omega \tag{5.8}$$

$$\boldsymbol{\Phi}_2\cdot\nabla\bar{e}\cdot\boldsymbol{n} = 0 \qquad \partial\Omega \tag{5.9}$$

Now, different choices for functions $(\phi, \boldsymbol{\Phi}_1, \boldsymbol{\Phi}_2)$ lead to specific models:

(i) GNL model by Peerlings et al. (1996a):

$$\phi = c \qquad \boldsymbol{\Phi}_1 = \mathbf{I} \qquad \boldsymbol{\Phi}_2 = \mathbf{I} \tag{5.10}$$

(ii) Micromophic model by Poh and Sun (2017):

$$\phi = c \qquad \boldsymbol{\Phi}_1 = g(D)\mathbf{I} \qquad \boldsymbol{\Phi}_2 = \mathbf{I} \tag{5.11}$$

where $g(D)$ is an exponentially decreasing function of an isotropic damage variable D. It is chosen such that $g(0) = 0$ and $g(D \to 1) \to R$, with $R > 0$ a small parameter accounting for residual non-local interactions. According to this formulation non-local interactions are isotropic.

(iii) Stress-based gradient-damage model by Vandoren and Simone (2018):

$$\phi = c \qquad \boldsymbol{\Phi}_1 = \mathbf{R}\cdot\mathbf{c}(\boldsymbol{\sigma})\cdot\mathbf{R}^\top = \mathbf{R}\cdot\left(\frac{\sigma_i}{f_t}\boldsymbol{s}_i\otimes\boldsymbol{s}_i\right)\cdot\mathbf{R}^\top \qquad \boldsymbol{\Phi}_2 = \boldsymbol{\Phi}_1 \tag{5.12}$$

where σ_i is the ith principal stress component, $\boldsymbol{s}_i$ is the corresponding eigenvector, f_t is the material strength, and $\mathbf{R}$ is the rotation tensor from the basis of principal

[1] Here, given a second order tensor $\mathbf{A}$, one has: $\mathbf{Q}\star\mathbf{A} = \mathbf{Q}\cdot\mathbf{A}\cdot\mathbf{Q}^\top$.

stress directions to the external basis in which $\nabla\bar{e}$ is written. This approach allows modeling introduced anisotropic non-local interactions (see (Vandoren & Simone, 2018) for modified expressions of tensor $\mathbf{c}(\boldsymbol{\sigma})$).

(*iv*) ENLG model by Desmorat et al. (2015a) and Ribeiro Nogueira et al. (2024a):

$$\phi = \frac{c}{\sqrt{\det \mathbf{g}}} \qquad \boldsymbol{\Phi}_1 = \sqrt{\det \mathbf{g}}\, \mathbf{g}^{-1} \qquad \boldsymbol{\Phi}_2 = \mathbf{g}^{-1} \tag{5.13}$$

Some theoretical similarities and differences between these formulations were analyzed in (Ribeiro Nogueira et al., 2024a). Additionally, the stress-based micromorphic model by Negi et al. (2020) retains the localizing damage character from (Poh & Sun, 2017), and couples it with anisotropic interactions based on (Vandoren & Simone, 2018). It is worth noting that, despite the differences mentioned above, both Negi et al. (2020) and Vandoren and Simone (2018) employed a scalar damage variable, with no applications to anisotropic damage behavior (*e.g.,* tensorial damage or microplane) being developed.

A few comments on anisotropic damage and anisotropic non-local interactions. Here, we distinguish between damage-induced anisotropy at the Representative Elementary Volume (REV) scale and its effects on induced anisotropic non-local interactions at the structural level:

- At the REV level, quasi-brittle materials can be considered as initially isotropic in the sense that the measured elastic properties are the same in all directions. However, during the softening phase, these properties degrade due to the emergence of micro-cracks, which typically form along preferential directions (Berthaud, 1991; Passelègue et al., 2018). Modeling techniques should account for this behavior (see, *e.g.*, (Ramtani et al., 1992; Papa & Taliercio, 1996; Lemaitre et al., 2000)). Recently, Loiseau et al. (2023) demonstrated based on discrete element simulations that isotropic damage models are inadequate for describing the macroscopic stress state of materials experiencing non-proportional loading. This limitation also becomes apparent in the comparison between isotropic and anisotropic damage models in the simulation of a simple non-proportional loading–unloading REV test case (see B).

- Anisotropic damage behavior in the Fracture Process Zone (FPZ) plays also a significant role at the structural scale. Recent observations from the so-called "gap-test" (Nguyen et al., 2020) demonstrated the dependency of the fracture energy and the effective FPZ size on the crack-parallel stress, *i.e.,* the normal stress in the propagation direction, or "T-stress" (Bažant et al., 2022a, 2022b). This behavior entails an increase in fracture energy at moderate crack-parallel compression, attributed to greater friction in inclined micro-cracks. At high compression levels, it is characterized by a widening of the FPZ and a decrease in fracture energy. According to (Bažant et al., 2022a, 2022b; Bažant & Nguyen, 2023), to capture these effects, modeling techniques should incorporate two main ingredients: a tensorial softening (anisotropic) damage law at the REV level, capable of representing oriented

micro-cracks, and two (evolving) independent characteristic lengths for the direction of the damage band and the transverse direction (anisotropic non-local interactions).

The ENLG anisotropic damage model introduced in this contribution, eventually coupled to other suitable tensorial damage laws, may contain the necessary ingredients to capture the T-stress effect. It is worth noting that other approaches, such as crack-band with microplane or lattice approaches, achieve similar outcomes (Bažant et al., 2022b; Lyu et al., 2023). Additionally, various non-local models with anisotropic interactions (*e.g.,* (Giry et al., 2011; Vandoren & Simone, 2018; Negi et al., 2020)) account for two evolving internal lengths.

In this paper, we focus on presenting the model, its characteristics, and numerical implementation. Evaluating its capability to verify experimental size-effect and gap-tests is beyond the scope of this work and is left for future contributions.

2.3 Anisotropic non-local interactions

In contrast to gradient formulations with isotropic damage-dependent non-local interactions, the ENL formulation provide anisotropic interactions by utilizing the inverse of the metric in (5.13). This section conducts a qualitative analysis of damage dependent non-local interactions.

Tensor representation via ellipses (2D) and ellipsoids (3D). Given a vector $\boldsymbol{x}$ in the orthonormal basis $\{\boldsymbol{e}_i\}$ and a symmetric second order tensor $\mathbf{T}$ written in the basis $\{\boldsymbol{e}_i \otimes \boldsymbol{e}_j\}$, a homogeneous polynomial $p(\boldsymbol{x}) = \mathbf{T}(\boldsymbol{x}, \boldsymbol{x}) = \boldsymbol{x} \cdot \mathbf{T} \cdot \boldsymbol{x}$ can be associated with $\mathbf{T}$ by exploiting the fact that this latter is a bi-linear form.

Now, considering the principal basis $\{\boldsymbol{v}_i \otimes \boldsymbol{v}_i\}$ of tensor $\mathbf{T}$, such that $\mathbf{T} = T_i \boldsymbol{v}_i \otimes \boldsymbol{v}_i$ (with T_i denoting the eigenvalues of $\mathbf{T}$), and writing $\boldsymbol{x}$ in the basis $\{\boldsymbol{v}_i\}$, the homogeneous polynomial $p(\boldsymbol{x})$ reads:

$$p(\boldsymbol{x}) = \boldsymbol{x} \cdot \mathbf{T} \cdot \boldsymbol{x} = T_i x_i^2 = \begin{cases} T_1 x_1^2 + T_2 x_2^2 & (\mathbf{T} \in \mathbb{R}^2 \times \mathbb{R}^2) \\ T_1 x_1^2 + T_2 x_2^2 + T_3 x_3^2 & (\mathbf{T} \in \mathbb{R}^3 \times \mathbb{R}^3) \end{cases} \tag{5.14}$$

where Einstein summation was used. It is straightforward to observe that equation:

$$p(\boldsymbol{x}) = 1 \tag{5.15}$$

corresponds to the equation of a parametric ellipsoid in $\mathbb{R}^3$ and an ellipse in $\mathbb{R}^2$. Therefore, one can directly visualize $\mathbf{T}$ once its principal basis is known by simply plotting function (5.15).

> **Remark 5.1.** *This visualization technique is often employed for representing the stress tensor (via the Lamé's stress ellipsoids), Reynolds stress anisotropy (Hamilton & Cal, 2015) or in diffusion-tensor imaging (Westin et al., 2002).*

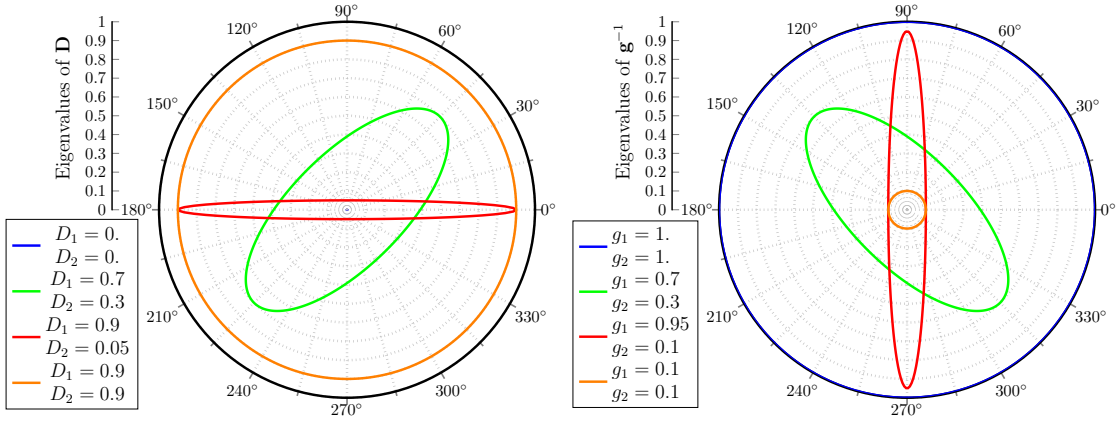

Figure 5.1 • Non-local interactions in 2D – Representation according to (5.16) of tensors $\mathbf{D}$ and $\mathbf{g}^{-1}$.

To obtain a better visualization of $\mathbf{T}$, one can also plot:

$$p(\boldsymbol{x}) = \boldsymbol{x} \cdot \mathbf{T}^{-2} \cdot \boldsymbol{x} = T_i^{-2} x_i^2 = \begin{cases} \dfrac{x_1^2}{T_1^2} + \dfrac{x_2^2}{T_2^2} & (\mathbf{T} \in \mathbb{R}^2 \times \mathbb{R}^2) \\ \dfrac{x_1^2}{T_1^2} + \dfrac{x_2^2}{T_2^2} + \dfrac{x_3^2}{T_3^2} & (\mathbf{T} \in \mathbb{R}^3 \times \mathbb{R}^3) \end{cases} = 1 \tag{5.16}$$

As the inverse and the square of a symmetric tensor are both isomorphisms (structure-preserving bijections), the above polynomial preserves all the properties of (5.15).

Damage and metric tensors representations in 2D. Consider the general form of the 2D damage tensor $\mathbf{D}$ and the corresponding metric inverse $\mathbf{g}^{-1}$ (written in their principal basis):

$$\mathbf{D} = D_1 \boldsymbol{v}_1 \otimes \boldsymbol{v}_1 + D_2 \boldsymbol{v}_2 \otimes \boldsymbol{v}_2 \qquad \mathbf{g}^{-1} = (1 - D_1) \boldsymbol{v}_1 \otimes \boldsymbol{v}_1 + (1 - D_2) \boldsymbol{v}_2 \otimes \boldsymbol{v}_2 \tag{5.17}$$

Figure 5.1 shows their polar visualizations using ellipses in $\mathbb{R}^2$ (oriented according to the principal basis). Four different cases are considered to illustrate the influence of the anisotropic damage (Figure 5.1 (left)) on $\mathbf{g}^{-1}$ (Figure 5.1 (right)) (which can be seen as a non-local interactions tensor):

- In the undamaged state, the damage tensor $\mathbf{D} = \mathbf{0}$ is represented by a single point located at the origin of the axis, whereas $\mathbf{g}^{-1} = \mathbf{I}$ is represented by a circle. This corresponds to considering isotropic non-local interactions, reducing the ENLG model to the GNL model (Peerlings et al., 1996a).
- If isotropic damage takes place ($D_1 = D_2 = D = 0.9$), the interaction tensor is equally reduced in all directions (orange circle in Figure 5.1 (right)).
- Anisotropic interactions are modeled when damage-induced anisotropy appears. The green curve corresponds to $D_1 = 0.7$ and $D_2 = 0.3$ with $\boldsymbol{v}_1 = \sqrt{2}/2(\boldsymbol{e}_x + \boldsymbol{e}_y)$ and $\boldsymbol{v}_2 = \sqrt{2}/2(-\boldsymbol{e}_x + \boldsymbol{e}_y)$. Since the largest damage value occurs at 45°, non-local interactions are strongly reduced in this direction.

- The red curve corresponds to the almost uni-axial damage case in the direction of the axis x, *i.e.*, $D_1 = 0.9$ and $D_2 = 0.05$ with $\boldsymbol{v}_1 = \boldsymbol{e}_x$ and $\boldsymbol{v}_2 = \boldsymbol{e}_y$. Therefore, the ellipse representing non-local interactions is stretched further in the vertical direction, meaning that almost no non-local interactions occur in the horizontal direction.

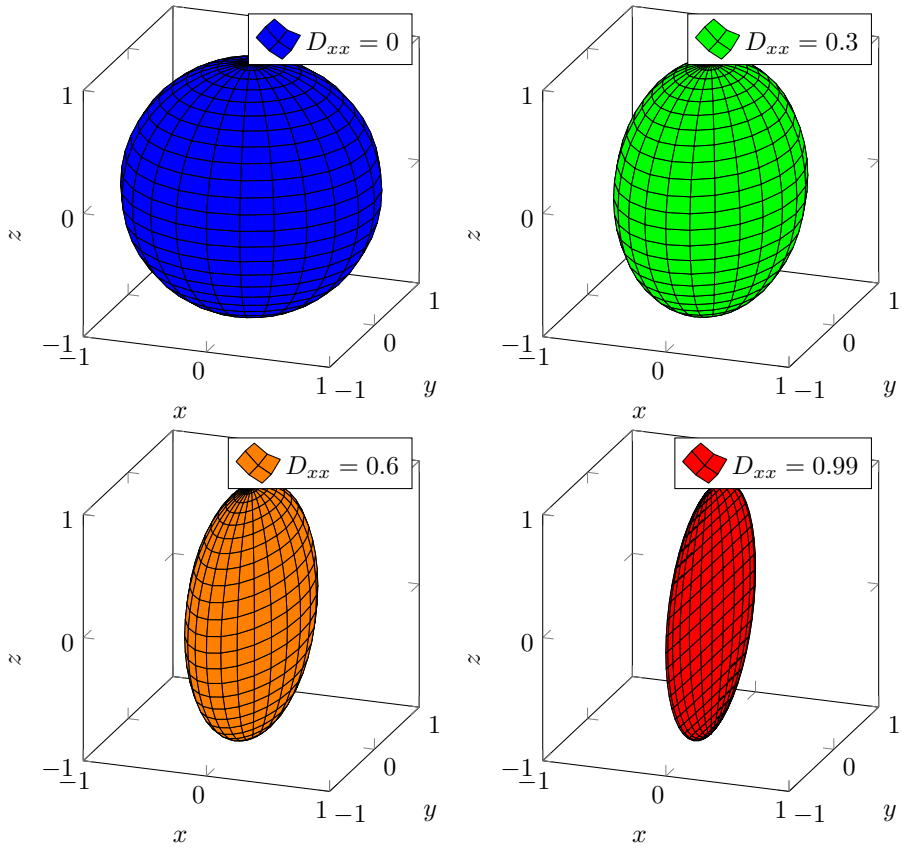

Figure 5.2 • Non-local interactions in 3D – Representation according to (5.16) of tensor $\mathbf{g}^{-1}$ for various damaged states.

Damage and metric tensors representations in 3D. The same considerations hold for the 3D case. Figure 5.2 shows the ellipsoid visualization of tensor $\mathbf{g}^{-1}$ for various uni-axial damaged states. Here, damage is considered to occur only in x direction:

$$\mathbf{D} = D_1 \boldsymbol{v}_1 \otimes \boldsymbol{v}_1 = D_{xx} \boldsymbol{e}_x \otimes \boldsymbol{e}_x \qquad \mathbf{g}^{-1} = (1 - D_{xx}) \boldsymbol{e}_x \otimes \boldsymbol{e}_x \tag{5.18}$$

As expected, in the undamaged case, interactions are represented by a sphere. When damage occurs in the x direction, non-local interactions are progressively reduced in this direction. The higher the damage level, the more important the shrinkage of the ellipsoid in the corresponding direction.

2.4 Quasi-static ENLG damage mechanics boundary value problem

Let us consider a split of $\partial\Omega$ into two sub-domains $\partial\Omega_t$ and $\partial\Omega_u$ such that $\overline{\partial\Omega_u \cup \partial\Omega_t} = \partial\Omega$ and that $\partial\Omega_u \cap \partial\Omega_t = \varnothing$. Dirichlet boundary conditions ($\boldsymbol{u} = \boldsymbol{u}^d$) are imposed on $\partial\Omega_u$ whereas stress tractions ($\boldsymbol{\sigma} \cdot \boldsymbol{n} = \boldsymbol{t}^d$) are imposed on $\partial\Omega_t$. Moreover, let us introduce the following admissibility spaces:

$$\mathcal{U} = \{\boldsymbol{w} \;\mid\; \boldsymbol{w} \in H^1(\Omega) \;\;,\;\; \boldsymbol{w} = \boldsymbol{u}^d \;\; \text{on}\, \partial\Omega_u\} \tag{5.19}$$

$$\mathcal{U}(\mathbf{0}) = \{\boldsymbol{w} \;\mid\; \boldsymbol{w} \in H^1(\Omega) \;\;,\;\; \boldsymbol{w} = \mathbf{0} \;\; \text{on}\, \partial\Omega_u\} \tag{5.20}$$

$$\mathcal{V} = \{w \;\mid\; w \in H^1(\Omega^h)\} \tag{5.21}$$

where H^1 denotes a square integrable Sobolev space.

It is straightforward to demonstrate (Ribeiro Nogueira et al., 2024a) that, under quasi-static conditions, the variational augmented equilibrium problem to be solved at any time t for finding a solution of the ENLG damage mechanics problem involves seeking an admissible displacement field $\boldsymbol{u} \in \mathcal{U}$ and an admissible non-local equivalent strain field $\bar{e} \in \mathcal{V}$ satisfying:

$$\int_\Omega \boldsymbol{\sigma}(\boldsymbol{u}) : \boldsymbol{\varepsilon}(\boldsymbol{v})\, dV = \int_{\partial\Omega_F} \boldsymbol{t}^d \cdot \boldsymbol{v}\, dS \quad \forall\, \boldsymbol{v} \in \mathcal{U}(\mathbf{0}) \tag{5.22}$$

$$\int_\Omega \sqrt{\det\mathbf{g}}\, \bar{e}\eta\, dV + \int_\Omega c\sqrt{\det\mathbf{g}}\, (\mathbf{g}^{-1} \cdot \nabla\bar{e}) \cdot \nabla\eta\, dV = \int_\Omega \sqrt{\det\mathbf{g}}\, e\eta\, dV \quad \forall\, \eta \in \mathcal{V} \tag{5.23}$$

where $\boldsymbol{\sigma}$ is the Cauchy stress tensor, $\boldsymbol{\varepsilon}$ is the small-strain tensor, $\boldsymbol{v}$ is the virtual displacement field, and η is the virtual non-local strain field.

The coupling between the two equations arises from the dependence of $\boldsymbol{\sigma}$ and $\mathbf{g}$ on the non-local strain via the damage tensor ($\bar{e}$ governs its evolution), and the dependency of e on the displacement via the selected equivalent strain definition:

$$\boldsymbol{\sigma} = \boldsymbol{\sigma}(\boldsymbol{u}, \mathbf{D}(\bar{e})) \qquad \mathbf{g} = \mathbf{g}(\mathbf{D}(\bar{e})) \qquad e = e(\boldsymbol{\varepsilon}(\boldsymbol{u})) \tag{5.24}$$

3 Anisotropic damage model

For illustrative purposes, this work adopts the constitutive model proposed by Desmorat (2015) for quasi-brittle materials. Different second-order damage models can be employed with the ENLG regularization, without necessitating modifications to its theoretical or numerical framework.

According to the chosen model, damage is represented using the second-order Ladevèze tensor $\mathbf{H} = (\mathbf{I} - \mathbf{D})^{-\frac{1}{2}}$. Denoting once again with $\boldsymbol{v}_i$ the eigenvectors of $\mathbf{D}$ and with D_i the corresponding eigenvalues, the Ladevèze tensor reads $\mathbf{H} = H_i \boldsymbol{v}_i \otimes \boldsymbol{v}_i = (1 - D_i)^{-\frac{1}{2}} \boldsymbol{v}_i \otimes \boldsymbol{v}_i$. As a consequence, $H_i = 1$ when $D_i = 0$ (undamaged state), and $H_i \to \infty$ when $D_i \to 1$ (fully damaged state). The unbounded nature of H_i enhances the formulation's ability to model the extreme scenario of fully damaged material at infinite strain (Desmorat, 2015). Moreover, from a numerical perspective, such unboundedness simplifies the handling of upper bounds (see, *e.g.*, (Desmorat et al., 2007a)) for damage tensors when implementing the constitutive law at the integration point level.

3.1 Three-dimensional constitutive model

Gibbs free enthalpy. The Gibbs free enthalpy reads:

$$\rho\psi_0^* = \rho\psi_0^*(\boldsymbol{\sigma}, \mathbf{H}) = \frac{\operatorname{tr}(\mathbf{H}\cdot\boldsymbol{\sigma}'\cdot\mathbf{H}\cdot\boldsymbol{\sigma}')}{4G} + \frac{1}{18K}\left[\frac{1}{3}\operatorname{tr}\mathbf{H}^2\langle\operatorname{tr}\boldsymbol{\sigma}\rangle^2 + \langle-\operatorname{tr}\boldsymbol{\sigma}\rangle^2\right] \tag{5.25}$$

where $\langle\cdot\rangle$ denotes the Macaulay operator, $\bullet' = \bullet - \frac{1}{3}\operatorname{tr}(\bullet)\mathbf{I}$ denotes the deviatoric part of tensor $\bullet$ and, G and K are the shear and bulk modulus, respectively.

Constitutive relations. The strain tensor is obtained as:

$$\boldsymbol{\varepsilon} = \rho\frac{\partial\psi_0^*}{\partial\boldsymbol{\sigma}} = \frac{1}{2G}(\mathbf{H}\cdot\boldsymbol{\sigma}'\cdot\mathbf{H})' + \frac{1}{9K}\left[\frac{1}{3}\operatorname{tr}\mathbf{H}^2\langle\operatorname{tr}\boldsymbol{\sigma}\rangle + \langle-\operatorname{tr}\boldsymbol{\sigma}\rangle\right]\mathbf{I} \tag{5.26}$$

The stress–strain constitutive relation is given by:

$$\boldsymbol{\sigma} = \tilde{\mathbb{E}} : \boldsymbol{\varepsilon} \tag{5.27}$$

with:

$$\tilde{\mathbb{E}} = 2G\left[\mathbf{H}^{-1}\underline{\otimes}\mathbf{H}^{-1} - \frac{\mathbf{H}^{-2}\otimes\mathbf{H}^{-2}}{\operatorname{tr}\mathbf{H}^{-2}}\right] + m(\mathbf{H})\mathbf{I}\otimes\mathbf{I} \qquad m(\mathbf{H}) = \begin{cases} \frac{3K}{\operatorname{tr}\mathbf{H}^2} & \text{if } \operatorname{tr}\boldsymbol{\varepsilon} > 0 \\ K & \text{otherwise} \end{cases} \tag{5.28}$$

Damage criterion function. The local damage criterion function reads:

$$f = e - \kappa \tag{5.29}$$

where e is an equivalent measure of the strain (computed using, *e.g.*, the Mazars (Mazars, 1984a) or Von Mises definitions (De Vree et al., 1995)), and κ is the consolidation function:

$$\kappa = \kappa_0 + SR_v^s(\operatorname{tr}\mathbf{H} - 3) \tag{5.30}$$

In non-local computations, the damage criterion function (5.29) is simply modified by substituting e with $\bar{e}$.

Here, S, s and κ_0 are material parameters, and R_v is the triaxiality function (Lemaitre, 1996). According to (Desmorat, 2015), this latter function is computed as:

$$R_v = \min\left[1 + \frac{9}{2}\frac{1-2\nu}{1+\nu}\langle-T_X\rangle^2, B\right] \qquad T_X = \sigma_H/\sigma_{eq} \tag{5.31}$$

where $\sigma_{eq} = \sqrt{3/2\,(\boldsymbol{\sigma}':\boldsymbol{\sigma}')}$ is the Von Mises equivalent stress and $\sigma_H = \operatorname{tr}\boldsymbol{\sigma}/3$ is the hydrostatic stress. Moreover, ν stands for Poisson's ratio and B is a new material parameter bounding the triaxiality function in bi-compression.

Damage evolution. In the original model by Desmorat (2015), the direction of damage evolution is controlled by the effective strain tensor $\langle\tilde{\boldsymbol{\varepsilon}}\rangle = \langle\mathbb{E}^{-1} : \boldsymbol{\sigma}\rangle$. This choice was initially introduced by Chambart (2009) to avoid numerical instabilities at high strain

levels. In the present work, the positive part of the total strain tensor is employed. Using the normalized form proposed in (Loiseau, 2023; Masseron et al., 2023), one can write:

$$\dot{\mathbf{H}} = \dot{\lambda}\,\mathbf{P} \qquad \mathbf{P} = \frac{\langle \boldsymbol{\varepsilon} \rangle}{\|\langle \boldsymbol{\varepsilon} \rangle\|} \tag{5.32}$$

where $\mathbf{P}$ is the normalized damage direction tensor and $\dot{\lambda}$ is the damage multiplier respecting the usual Karush–Kuhn–Tucker (KKT) loading–unloading conditions.

According to Leroux (2012), such a choice allows better representing experimental crack paths. As a counterpart of this, a bifurcation can be obtained in the behavior when this choice is made. It should be noticed that is not a strong limit of the present implementation since instabilities were never experienced in numerical simulations.

3.2 Plane-stress conditions

In addition to the 3D conditions, the simulations in Section 5 will assume plane-stress conditions. The plane-stress formulation is derived using the same approach as applied by Jirásek and Suárez (2016) to the anisotropic damage model proposed by Desmorat et al. (2007a).

Constitutive relations. The in-plane (x, y) stress tensor is written as:

$$\boldsymbol{\sigma}_{\mathbf{2}} = \tilde{\mathbb{E}}_{\mathbf{2}} : \boldsymbol{\varepsilon}_{\mathbf{2}} + \mathbf{e}_{\mathbf{2}} \varepsilon_z \tag{5.33}$$

where:

$$\tilde{\mathbb{E}}_{\mathbf{2}} = 2G \left[\mathbf{H}_{\mathbf{2}}^{-1} \underline{\otimes} \mathbf{H}_{\mathbf{2}}^{-1} - \frac{\mathbf{H}_{\mathbf{2}}^{-2} \otimes \mathbf{H}_{\mathbf{2}}^{-2}}{\operatorname{tr} \mathbf{H}_{\mathbf{2}}^{-2} + H_z^{-2}} \right] + \tilde{K} \mathbf{I}_{\mathbf{2}} \otimes \mathbf{I}_{\mathbf{2}} \qquad \tilde{K} = \begin{cases} \frac{3K}{\operatorname{tr} \mathbf{H}^2 + H_z^2} & \text{if } \operatorname{tr} \boldsymbol{\varepsilon} > 0 \\ K & \text{otherwise} \end{cases} \tag{5.34}$$

$$\mathbf{e}_{\mathbf{2}} = \tilde{K} \mathbf{I}_{\mathbf{2}} - \frac{2G \mathbf{H}_{\mathbf{2}}^{-2} H_z^{-2}}{\operatorname{tr} \mathbf{H}_{\mathbf{2}}^{-2} + H_z^{-2}} \tag{5.35}$$

with $(\bullet)_{\mathbf{2}}$ denoting the two-dimensional counterpart of tensor $(\bullet)$. Accordingly $\mathbf{H}_{\mathbf{2}}$ and $\boldsymbol{\varepsilon}_{\mathbf{2}}$ contains only the in-plane components of $\mathbf{H}$ and $\boldsymbol{\varepsilon}$, respectively. From the three-dimensional constitutive relation, the component σ_z of the stress tensor is expressed as:

$$\sigma_z = \tilde{E} \varepsilon_z + \mathbf{e}_{\mathbf{2}} : \boldsymbol{\varepsilon}_{\mathbf{2}} \tag{5.36}$$

with:

$$\tilde{E} = \frac{2G H_z^{-2} \operatorname{tr} \mathbf{H}_{\mathbf{2}}^{-2}}{\operatorname{tr} \mathbf{H}_{\mathbf{2}}^{-2} + H_z^{-2}} + \tilde{K} \tag{5.37}$$

Enforcing the plane strain condition $\sigma_z = 0$, the out-of-plane strain component reads:

$$\varepsilon_z = -\frac{\mathbf{e}_{\mathbf{2}} : \boldsymbol{\varepsilon}_{\mathbf{2}}}{\tilde{E}} \tag{5.38}$$

Substitution into (5.33) yields:

$$\boldsymbol{\sigma}_{\mathbf{2}} = \tilde{\mathbb{E}}_{\mathbf{2}}^{\star} : \boldsymbol{\varepsilon}_{\mathbf{2}} \qquad \tilde{\mathbb{E}}_{\mathbf{2}}^{\star} = \tilde{\mathbb{E}}_{\mathbf{2}} - \frac{\mathbf{e}_{\mathbf{2}} \otimes \mathbf{e}_{\mathbf{2}}}{\tilde{E}} \tag{5.39}$$

Damage criterion function. The criterion function remains the same as in the 3D case, with the only difference that tr$\mathbf{H}$ in (5.30) is replaced by tr$\mathbf{H_2} + H_z$, and that the triaxility T_X in (5.31) is computed with $\sigma_H = \operatorname{tr} \boldsymbol{\sigma_2}/2$ and $\sigma_{eq} = \sqrt{2\,\boldsymbol{\sigma'_2} : \boldsymbol{\sigma'_2}}$.

Damage evolution. Damage evolution occurs as follows:

$$\dot{\mathbf{H}}_\mathbf{2} = \dot{\lambda}\,\mathbf{P_2} \qquad \dot{H}_z = \dot{\lambda}\,P_z \tag{5.40}$$

with:

$$\mathbf{P_2} = \frac{\langle \boldsymbol{\varepsilon_2} \rangle}{\|\langle \boldsymbol{\varepsilon} \rangle\|} \qquad P_z = \frac{\langle \varepsilon_z \rangle}{\|\langle \boldsymbol{\varepsilon} \rangle\|} \tag{5.41}$$

4 Numerical formulation

The variational formulation for the gradient problem requires solving the weak form of the equilibrium, taking into account anisotropic damage. Given that the effective Hooke's tensor $\tilde{\mathbb{E}}$ is expressed in terms of $\mathbf{H}$ for the employed damage model, anisotropic vanishing non-local interactions are introduced in the variational formulation through the damage-dependent Riemannian metric $\mathbf{g} = (\mathbf{I} - \mathbf{D})^{-1} = \mathbf{H}^2 = \mathbf{H} \cdot \mathbf{H}$.

4.1 Space/time discretized variational formulation

A spatial finite element method is used, with the meshed domain denoted by Ω^h. For quasi-static analysis, a pseudo-time discretization is introduced to represent the applied load, with n denoting the step of the corresponding time t_n. An iterative staggered solution approach is adopted, and Picard iteration is used to solve the augmented equilibrium problem. Linear shape functions are employed for both the displacement and the non-local equivalent strain fields ($\mathbb{P}_1$ fields), while the damage, strain, and stress fields are represented by piece-wise constant functions ($\mathbb{P}_0$ fields). This choice guarantees consistency between fields during the computation of constitutive behavior and helps avoid stress oscillations (Peerlings, 1999; Simone et al., 2003a). In the following, the superscript h is used to denote finite element discretized quantities.

The solving process between iterations k and $k+1$ can be summarized as follows (all quantities without a subscript refer to the present pseudo-time step, t_{n+1}):

(i) Given the damage tensor at the previous iteration $\mathbf{H}^{h,k}$, one finds $\boldsymbol{u}^{h,k+1} \in \mathcal{U}^h$ at iteration $k+1$ such that:

$$\int_{\Omega^h} \boldsymbol{\varepsilon}(\boldsymbol{u}^{h,k+1}) : \tilde{\mathbb{E}}\left(\mathbf{H}^{h,k}\right) : \boldsymbol{\varepsilon}(\boldsymbol{v}^h)\, dV = \int_{\partial\Omega_F^h} \boldsymbol{t}^{d,h} \cdot \boldsymbol{v}^h\, dS \quad \forall\, \boldsymbol{v}^h \in \mathcal{U}^h(\mathbf{0}) \tag{5.42}$$

> **Remark 5.2.** *At the first iteration ($k = 0$), the non-local strain and damage fields are initiated based on the last converged solution, i.e., $\bar{e}^0 = \bar{e}_n$ and $\mathbf{H}^0 = \mathbf{H}_n$.*

(*ii*) The local equivalent strain field is computed based on the updated displacement field, *i.e.*:

$$e^{h,k+1} = e(\boldsymbol{\varepsilon}(\boldsymbol{u}^{h,k+1})) \tag{5.43}$$

In computations, the Mazars and the Von Mises strain measures are employed.

(*iii*) Given e^{k+1}, one searches for $\bar{e}^{h,k+1} \in \mathcal{V}^h$ satisfying:

$$\int_{\Omega^h} \det \mathbf{H}_n^h \, \bar{e}^{h,k+1} \eta^h \, dV + \int_{\Omega^h} c \det \mathbf{H}_n^h \, \boldsymbol{h}(\bar{e}^{h,k+1}; \mathbf{H}_n^h) \cdot \nabla \eta^h \, dV = \int_{\Omega^h} \det \mathbf{H}_n^h \, e^{k+1} \eta^h \, dV \quad \forall \, \eta^h \in \mathcal{V}^h \tag{5.44}$$

where:

$$\boldsymbol{h}(\bar{e}^{h,k+1}; \mathbf{H}_n^h) = (\mathbf{H}_n^h)^{-2} \cdot \nabla \bar{e}^{h,k+1} \tag{5.45}$$

It is noteworthy that a key assumption made here is related to $\mathbf{H}_n^h$, which represents the Ladevèze damage variable from the previous converged step. The hypothesis posits that the damage field responsible for modifying interactions remains unchanged throughout the iterations within a time step computation. This is in agreement with the integral-type ENL model implementation by Rastiello et al. (2018a), where the geodesic distances are computed with the last converged damage scalar field and are then utilized to compute the non-local equivalent strain field in the subsequent step. Additionally, it has been observed that convergence problems and oscillations in the solution fields arise when considering $\mathbf{H}^{h,k}$ inEquation (5.44).

The term $(\mathbf{H}_n^h)^{-2} \cdot \nabla \bar{e}^{h,k+1}$ primarily contributes to reducing interactions (the gradient effect). As observed by (Vandoren & Simone, 2018), vanishing non-local interactions can lead to numerical oscillations in the response and affect convergence rate. Following a similar idea as proposed by (Poh & Sun, 2017), residual non-local interactions can be eventually considered by modifying Equation (5.45) as:

$$\boldsymbol{h}(\bar{e}^{h,k+1}; \mathbf{H}_n^h) = \left[(\mathbf{H}_n^h)^{-2} + \xi \mathbf{I}\right] \cdot \nabla \bar{e}^{h,k+1} \qquad \xi \ll 1 \tag{5.46}$$

This allows for the consideration of the gradient term with minimal contribution upon damage re-localization.

(*iv*) Once $\bar{e}^{k+1}$ is computed, one updates $\mathbf{H}^{h,k+1} = \mathbf{H}(\bar{e}^{h,k+1})$ and substitutes it inEquation (5.42) to continue the iteration process. The numerical algorithm is detailed in A.

(*v*) This process is repeated until convergence with respect to an L^2-norm for both fields, given by:

$$\|\bar{e}^{h,k+1} - \bar{e}^{h,k}\|^2 = \int_{\Omega^h} (\bar{e}^{h,k+1} - \bar{e}^{h,k})^2 dV \leqslant \mathrm{TOL}_u \tag{5.47}$$

$$\|\boldsymbol{u}^{h,k+1} - \boldsymbol{u}^{h,k}\|^2 = \int_{\Omega^h} (\boldsymbol{u}^{h,k+1} - \boldsymbol{u}^{h,k})^2 dV \leqslant \mathrm{TOL}_e \tag{5.48}$$

where TOL_u and TOL_e are user-defined tolerances.

The numerical implementation of the presented formulation is developed in a in-house finite element code at CEA (Badri et al., 2021; Badri & Rastiello, 2023), which is based on the `FreeFEM++` finite element solver (Hecht, 2012).

Modifications to account for plane-stress conditions. As previously detailed, the decomposition of variables into out-of-plane and in-plane components is crucial. Given that $\sigma_z = 0$, the argument of the bi-linear form inEquation (5.42) becomes:

$$\boldsymbol{\varepsilon}(\boldsymbol{u}^{h,k+1}) : \tilde{\mathbb{E}}\left(\mathbf{H}^{h,k}\right) : \boldsymbol{\varepsilon}(\boldsymbol{v}^h) = \boldsymbol{\varepsilon}_{\mathbf{2}}(\boldsymbol{u}^{h,k+1}) : \tilde{\mathbb{E}}^{\star}_{\mathbf{2}}(\mathbf{H}^{h,k}_{\mathbf{2}}, H^{h,k}_z) : \boldsymbol{\varepsilon}_{\mathbf{2}}(\boldsymbol{v}^h) \tag{5.49}$$

Thus, by substituting this expression into Equation (5.42), the weak form of equilibrium still holds. It is further assumed that $\nabla \bar{e} \cdot \mathbf{e}_z = 0$, leading to:

$$(\mathbf{H}^h_n)^{-2} \cdot \nabla \bar{e}^{h,k+1} = (\mathbf{H}^h_{\mathbf{2},n})^{-2} \cdot \nabla \bar{e}^{h,k+1} \tag{5.50}$$

Consequently, the variational equation (5.44) remains valid. The main distinction from the previous case is that:

$$\det \mathbf{H}^h_n = H^h_{n,xx} H^h_{n,yy} H^h_{n,z} - (H^h_{n,xy})^2 H^h_{n,z} = H^h_{n,1} H^h_{n,2} H^h_{n,z} \tag{5.51}$$

4.2 Material law at integration point level

A fully implicit integration algorithm is employed for implementing the anisotropic damage model. This choice, while differing from the explicit approach utilized in (Desmorat, 2015), offers enhanced robustness by ensuring convergence even for larger strain increments. The implementation is carried out using the `mfront` constitutive laws generator (Helfer et al., 2015). The interface between the finite element solver and the constitutive model integrator is handled through a custom interface developed with `mgis` (Mfront Generic Interface Support). Details concerning the material law integration are discussed in A, whereas representative local responses at integration point level are addressed in B.

5 Results and discussion

Numerical 2D simulations are presented to elucidate the principal features of the proposed formulation. Initially, the simulation of the L-shape test, as conducted by Winkler et al. (2001, 2004), is carried out under plane-stress conditions. Subsequently, the focus shifts to the simulation of the three-point bending test developed by Gálvez et al. (1998). Both tests serve as a common benchmark for validating cracking models, especially in scenarios involving mixed-mode conditions. A novel test case simulating non-proportional loading on a hexagonal specimen is then proposed to illustrate the differences between isotropic and anisotropic damage models. Finally, a few 3D results are provided for illustrative purposes and to initiate discussion on perspectives for future developments.

5.1 Mixed-mode 2D L-shape test

Figure 5.3 illustrates the geometry, boundary conditions, and an example of a finite element mesh utilized. In all meshes, the characteristic element size l_e is reduced in the central part of the specimen, where, based on experimental evidence, damage is expected to occur.

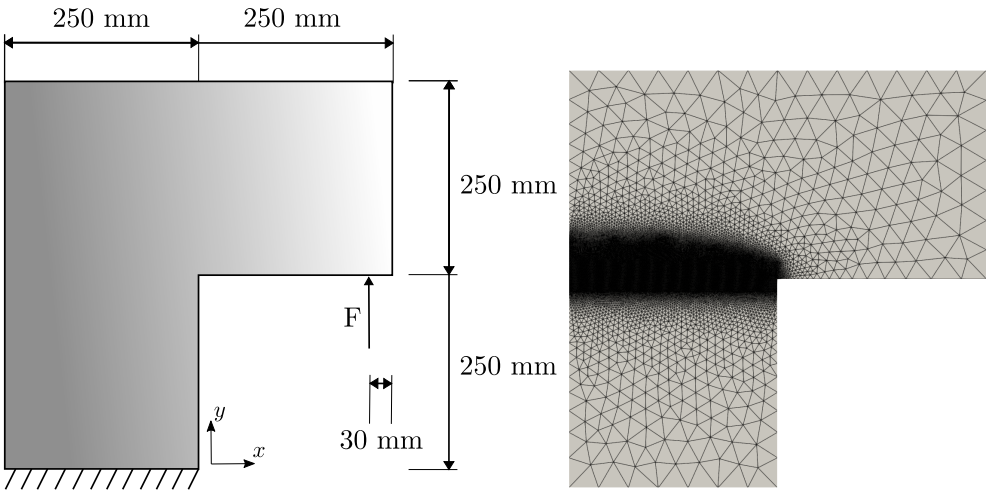

Figure 5.3 • L-shape test – Geometry (thickness = 100 mm) and boundary conditions (Winkler et al., 2001, 2004) (left) and an example of a finite element mesh containing 205 972 CST elements (right).

> **Remark 5.3.** *Finite element meshes are generated using the* `GMSH` *mesh generator (Geuzaine & Remacle, 2009). Accordingly, the characteristic element size corresponds to the length of mesh edges.*

To study mesh convergence, three different meshes are employed in the numerical simulations, containing 58 710 ($l_e = 0.8$ mm), 205 972 ($l_e = 0.4$ mm) and 753 143 ($l_e = 0.2$ mm) Constant Strain Triangles (CST), respectively. The displacement is constrained in the x and y directions at the bottom of the specimen. A displacement-controlled point load is applied vertically to represent the force denoted as F in the figure. The material is assumed to follow the anisotropic damage model described earlier, with the equivalent strain calculated using the Mazars definition (**??**). This decision was made to accurately predict both the peak load and the overall softening regime, following the recommendations of Nguyen et al. (2018) and as also used by Sarkar et al. (2019) for the same reasons.

Several authors (Oliver et al., 2004; Nguyen et al., 2018) have noted that the elastic material parameters provided in (Winkler et al., 2001, 2004) cannot be directly applied in numerical simulations as they lead to an overestimation of the initial structural stiffness.

> **Remark 5.4.** *For example, (Nguyen et al., 2018) considered $E = 21\,000$ MPa and applied the point load at the right of the specimen (not at 30 mm from it). (Wang et al., 2023) made the same assumption concerning the point load position but retained the original material parameters. (Zreid & Kaliske, 2014) applied the point load at a certain distance from the extremity and considered $E = 18\,000$ MPa in computations.*

In the following, to achieve an elastic response consistent with experimental data, Young's modulus is set to $E = 17\,000$ MPa (instead of $E = 25\,850$ MPa, as in (Winkler

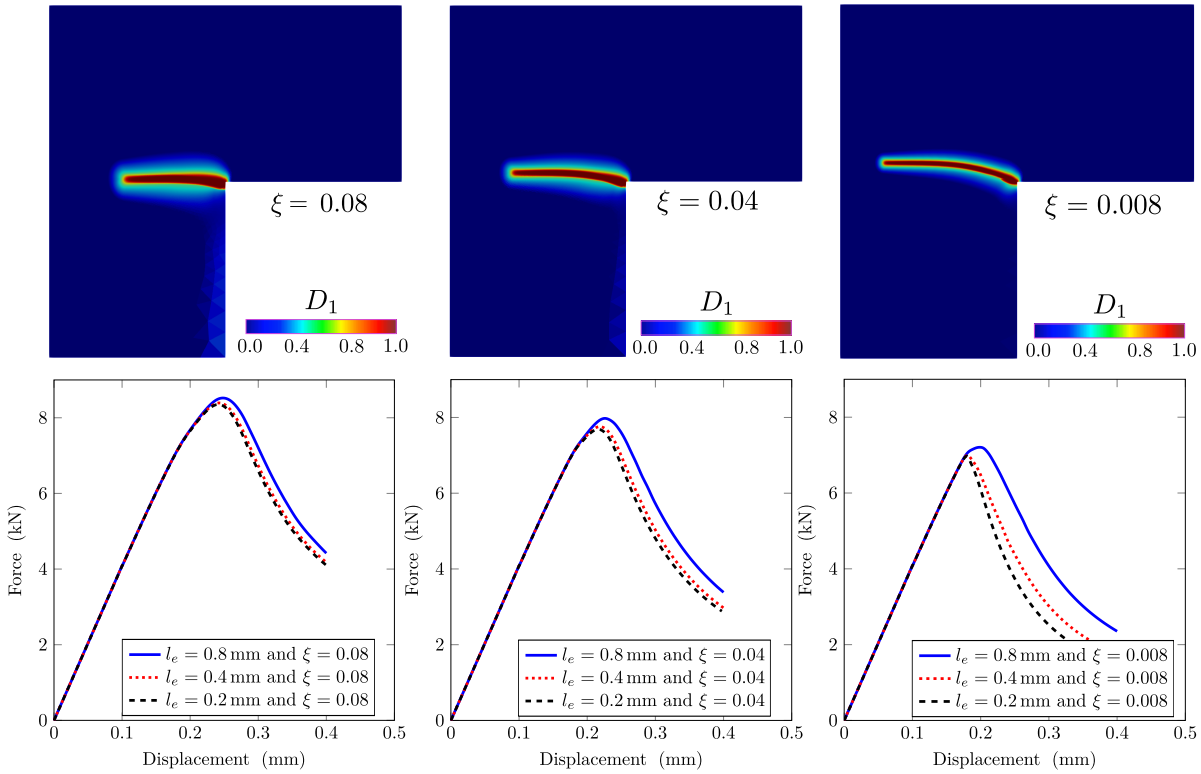

Figure 5.4 • L-shape test – Study on the impact of ξ on the structural responses and damage maps (maximum principal damage component D_1).

et al., 2001, 2004)), while the Poisson's ratio is kept equal to the experimental value ($\nu = 0.18$). Five additional material parameters must be defined for using the anisotropic damage model detailed in 2. In this section, these parameters are set to $\{c, \kappa_0, S, s, B\} = \{7.32\,\text{mm}^2, 1.4 \times 10^{-4}, 3.91 \times 10^{-4}, 4.9, 5/3\}$. Moreover, the analysis is carried out for three different values of ξ to examine the influence of residual non-local interactions on structural responses and damage evolution.

5.1.1 Role of residual non-local interactions on mesh-convergence and damage re-localization

Structural response and mesh convergence. Figure 5.4 presents the structural responses and corresponding damage maps (principal value D_1) for various residual non-local interactions parameter ξ values. Convergence in the overall response with mesh refinement is attained for $\xi = 0.08$ and $\xi = 0.04$, employing a mesh containing 753 143 elements with $l_e = 0.2\,\text{mm}$ in the refined region. Similarly, a trend toward mesh convergence is observed around the peak load in simulations with $\xi = 0.008$ using the same mesh. However, differences emerge in the post-peak phase between meshes with $l_e = 0.4\,\text{mm}$ and $l_e = 0.2\,\text{mm}$. Furthermore, the response showcases decreased brittleness with increasing ξ values, for a given set of material parameters.

Damage evolution. The reduction in brittleness observed in the structural response for larger values of ξ can be attributed to damage diffusion (Figure 5.4 (top)). In the original

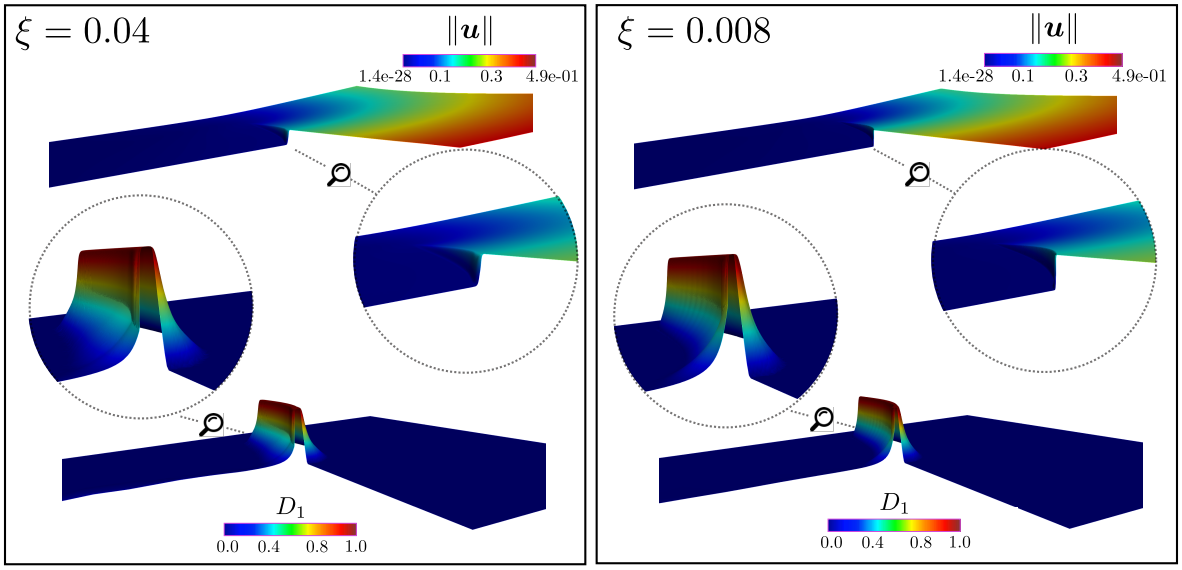

Figure 5.5 • L-shape test – Warp by scalar plots of the maximum principal damage component (D_1) and the norm of the displacement field ($\|\boldsymbol{u}\|$).

ENLG model ($\xi = 0$), non-local interactions vanish upon damage re-localization ($D_i \to 1$). However, with appropriately chosen $\xi > 0$, moderate residual non-local interactions persist, leading to minor damage spreading around the re-localized zone. This behavior also influences the propagation direction associated with the damage band. For instance, the damage band is almost horizontal for $\xi = 0.08$, whereas it progressively becomes more curved as ξ decreases.

These aspects are further illustrated in Figure 5.5, which compares the ability of the ENLG approach to simulate the tendency toward damage-to-fracture transition for $\xi = 0.04$ and $\xi = 0.008$. The first damage eigenvalue D_1 is depicted in Figure 5.5 (bottom left and right), indicating damage re-localization in a narrow zone for both cases. However, the damage spreads over a larger zone for $\xi = 0.04$ compared to $\xi = 0.008$ (as shown in the zoomed-in damage maps). An approximation of a jump in the displacement field (Figure 5.5 (top)) is observed for both values of ξ, which corresponds, in the limit case, to the kinematics of a crack description (discontinuity). Nonetheless, the simulation better describes this approximation with $\xi = 0.008$ (as seen in the zoomed-in displacement field). It is important to note that this is merely a post-processing analysis of the results because the adopted continuous finite element formulation cannot capture displacement jumps.

Comments on the choice of ξ. According to this analysis, the smaller the value of ξ, the better the capability of the ENLG numerical model in representing damage re-localization, thus indirectly depicting a progressive damage-to-fracture transition. As a counterpart to this, finer and finer meshes are needed to achieve mesh convergence of the structural response. The value of ξ in simulations should therefore be carefully chosen depending on the available computer resources (finer the mesh, larger are CPU times) and the intended application of the model.

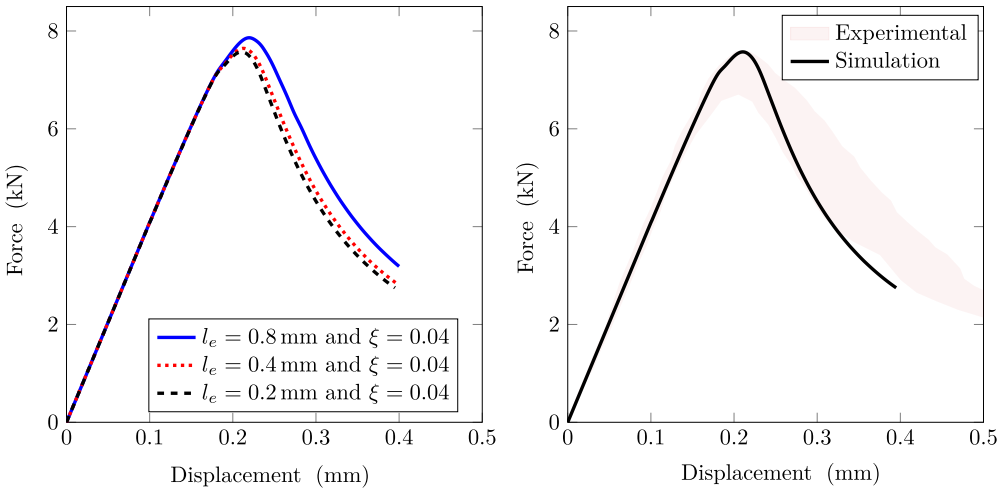

Figure 5.6 • L-shape test – Convergence upon mesh refinement (left) and comparison between numerical (mesh with $l_e = 0.2\,\text{mm}$) and experimental (Winkler et al., 2001, 2004) structural responses (right).

5.1.2 Additional analyses and comparison with experimental results

To compare the results from the numerical simulations with experimental data from the literature, we retain the value of $\xi = 0.04$ for the following analyses. This choice allows for converged results with a relatively high number of elements, yet remaining numerically feasible within a sequential solving framework without excessive spreading of damage.

> **Remark 5.5.** *Parallel solving techniques were not yet studied and are left for future work.*

Representative structural response and mesh convergence. Figure 5.6 (right) shows the optimal (compared to experimental results) structural response obtained with $\{\kappa_0, S\} = \{1.7 \times 10^{-4}, 3.81 \times 10^{-4}\}$, while all the other parameters remain unchanged from the previous section. The overall response aligns with the experimental results, demonstrating that achieving reasonable quasi-brittle responses with the ENLG model, coupled with the presented anisotropic damage behavior law, is feasible. Improved fitting might also be attained by modifying the damage evolution law, since the parameter S controls locally the peak and the post-peak behavior (see, *e.g.*, (Loiseau, 2023)).

Damage evolution. In addition to the structural responses, one can analyze the damage profiles obtained to evaluate the capability of the present approach to represent "cracking" behaviors. Figure 5.7 (top) shows the in-plane components (D_{xx}, D_{yy}, D_{xy}) of the damage tensor at the end of the simulation. As expected, the highest damage level is obtained in the y direction $(D_{yy} > D_{xx} > D_{xy})$, which is mainly perpendicular to the "pseudo-crack" direction. The off-diagonal component D_{xy} is more pronounced close to the corner, where damage starts. There, the principal damage directions are slightly rotated with respect to the main axes (x, y). As shown in Figure 5.7 (bottom), similar considerations hold when considering the principal damage components (D_1, D_2).

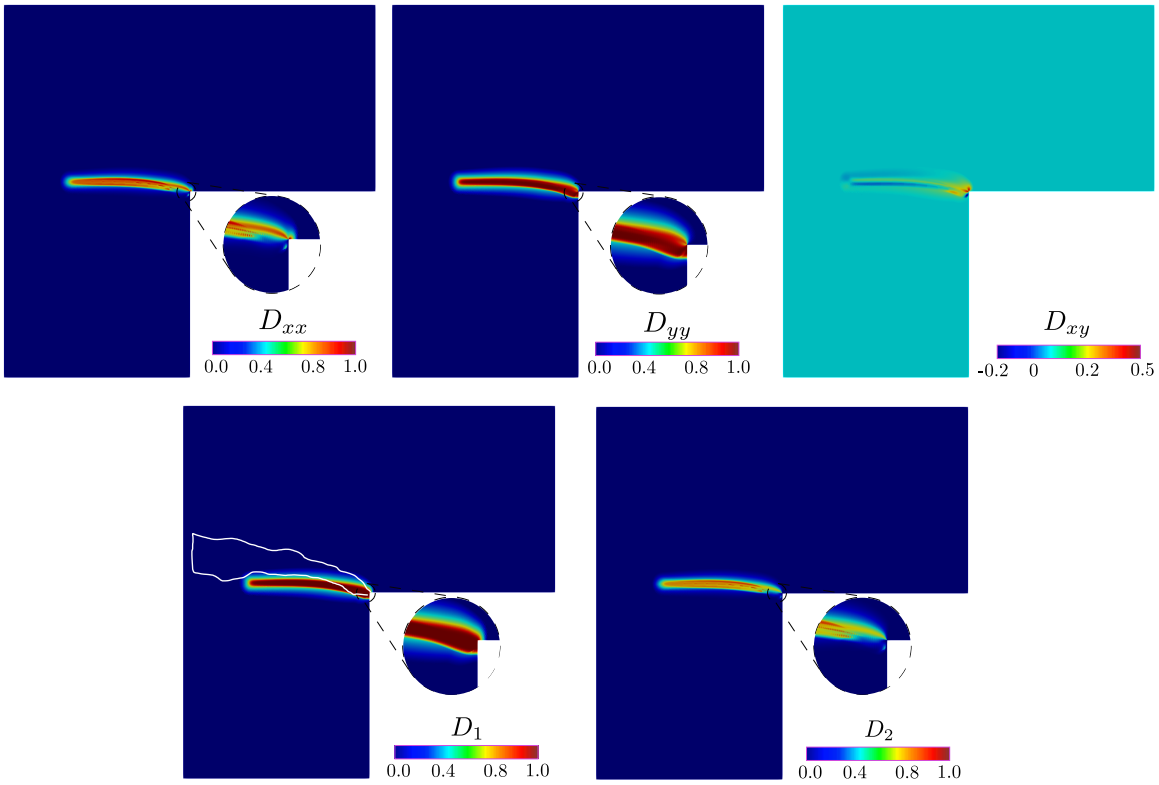

Figure 5.7 • L-shape test – Components of the damage tensor (D_{xx}, D_{yy}, D_{xy}) and associated eigenvalues (D_1, D_2) at the end of the simulation. Solid white lines represent the envelope of experimental crack paths from (Winkler et al., 2001, 2004).

The envelope of crack paths obtained by Winkler et al. (2001, 2004) are represented in Figure 5.7 by solid white lines. A comparison between the damage band obtained by the ENLG model and the experimental crack paths reveals good agreement. However, the curved cracking behavior is less present in numerical results due to the choice of $\xi = 0.04$, which could be better represented for simulations with $\xi = 0.008$, as shown in Figure 5.4. A fitting procedure for $\xi = 0.008$ becomes prohibitive in the sequential solver framework of this contribution due to CPU time, as more elements are required to obtain a converged response.

To highlight the capabilities of the ENLG model to represent a tendency toward a transition from damage to fracture, Figure 5.8 displays profiles of the major principal component of the damage tensor and the resulting displacement field along a line oriented approximately in the major damage principal direction. As shown in the figure, the damage field progressively increases in the region preceding the "pseudo-crack". Subsequently, the damage tends to reach a unitary value in the central zone of a band, whose maximum size remains stationary. As seen before, this is better represented for simulations where $\xi = 0.008$, but it can be still observed here ($\xi = 0.04$) at the propagation front of the damage band. At the same time, the displacement field clearly indicates a tendency toward a discontinuity centered in the middle of the damage band. It is worth noting, however, that this discontinuity cannot be represented in the formulation presented here,

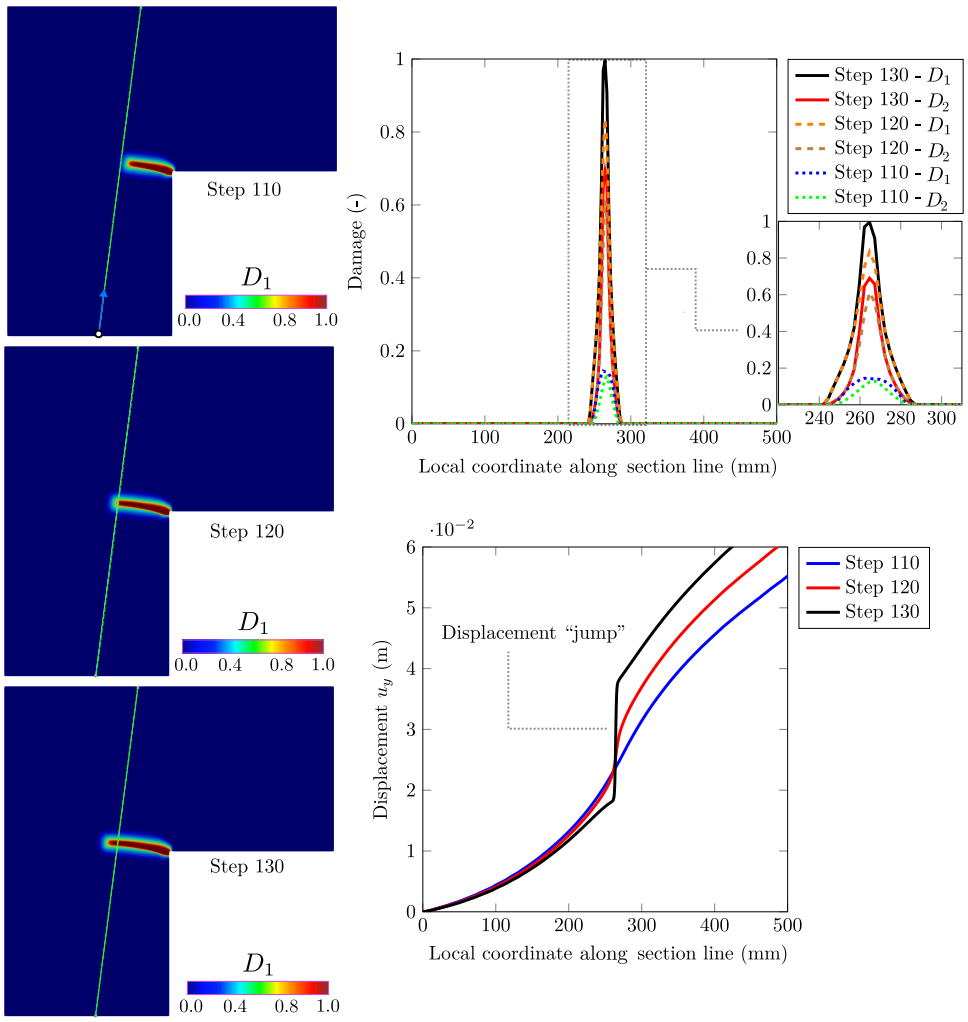

Figure 5.8 • L-shape test – Principal components (D_1, D_2) of the damage tensor and vertical displacement (u_y) along a line approximately aligned with the major principal damage direction in the center of the damaged band for three phases of the damage evolution.

as the displacement field is assumed to be continuous by construction.

5.2 Mixed-mode 2D three-point bending test

The geometric details and boundary conditions for this case are illustrated in Figure 5.9 (top). This configuration corresponds to the small specimens examined in the referenced study (Gálvez et al., 1998), featuring a notch with a width of 2 mm. Four finite element meshes were utilized in the numerical simulations, comprising 4 333, 13 422, 47 564, and 178 476 CST elements, respectively (Figure 5.9 (bottom)). All meshes are locally refined around the notch tip where the onset of damage is expected to occur. The displacement is applied at the upper part of the beam under CMOD (Crack Mouth Opening Displacement) control (calculated as the relative displacement of points A and B in Figure 5.9). The material parameters for this test are chosen as $\{E, \nu, c, \kappa_0, S, s, B\} = \{38\,000 \text{ MPa}, 0.2, 1.0\,\text{mm}^2, 6 \times 10^{-4}, 2 \times 10^{-4}, 4.9, 5/3\}$. Moreover, $\xi = 0.04$. Similar to

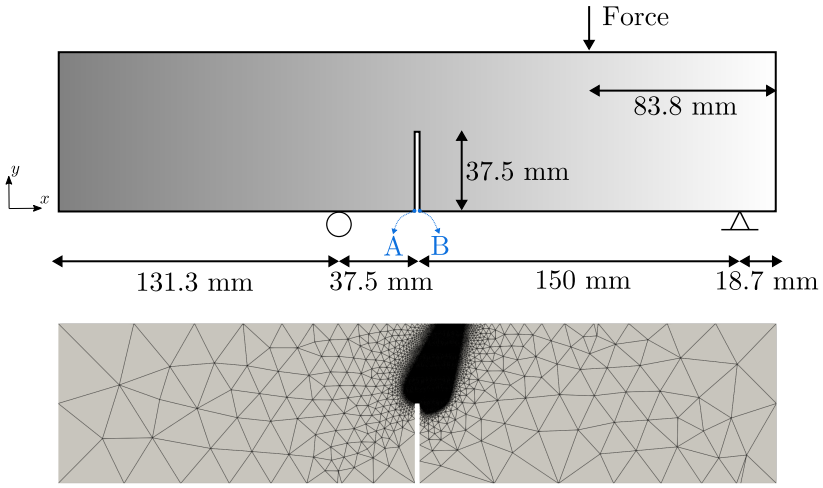

Figure 5.9 • Three-point bending test – Geometry (thickness = 50 mm) and boundary conditions (top) and example of a mesh containing 178 476 elements (bottom).

the L-shape test, Mazars' equivalent strain is utilized in the computations.

> **Remark 5.6.** *A simple path-following algorithm is employed for this purpose, treating the magnitude of the external load as a novel unknown and enhancing the damage mechanics equilibrium problem through an additional constraint equation. A detailed description of the final algorithm is omitted here for conciseness, but further information can be found in (de Borst, 1987; Rastiello et al., 2019; Rastiello et al., 2022), among others.*

5.2.1 Mesh-convergence in terms of damage maps and structural response

Figure 5.10 shows the damage maps (depicting the first principal damage value D_1) obtained for the different meshes alongside the corresponding structural responses. One can observe convergence of the damage pattern upon mesh refinement, as well as in terms of the structural response. Regarding the overall response, convergence is achieved with a mesh containing 178 476 elements with $l_e = 0.1$ mm in the refined region. Thus, the characteristic size of elements required to obtain convergence in this example is two times smaller than the one for the L-shape test. This can be attributed to the utilization of a smaller gradient parameter c in the three-point bending test.

5.2.2 Representative results

Representative structural response and comparison to experimental results. Similar to the L-shape test, the elastic parameters provided in (Gálvez et al., 1998) lead to an overestimation of the initial structural stiffness. To achieve an elastic response consistent with experimental data in this test case, the Young's modulus is set to $E = 33\,000$ MPa in the following simulations. Additionally, to ensure good agreement between simulations and experimental results, the following parameters are also modified: $\{\kappa_0, S\} = \{7 \times$

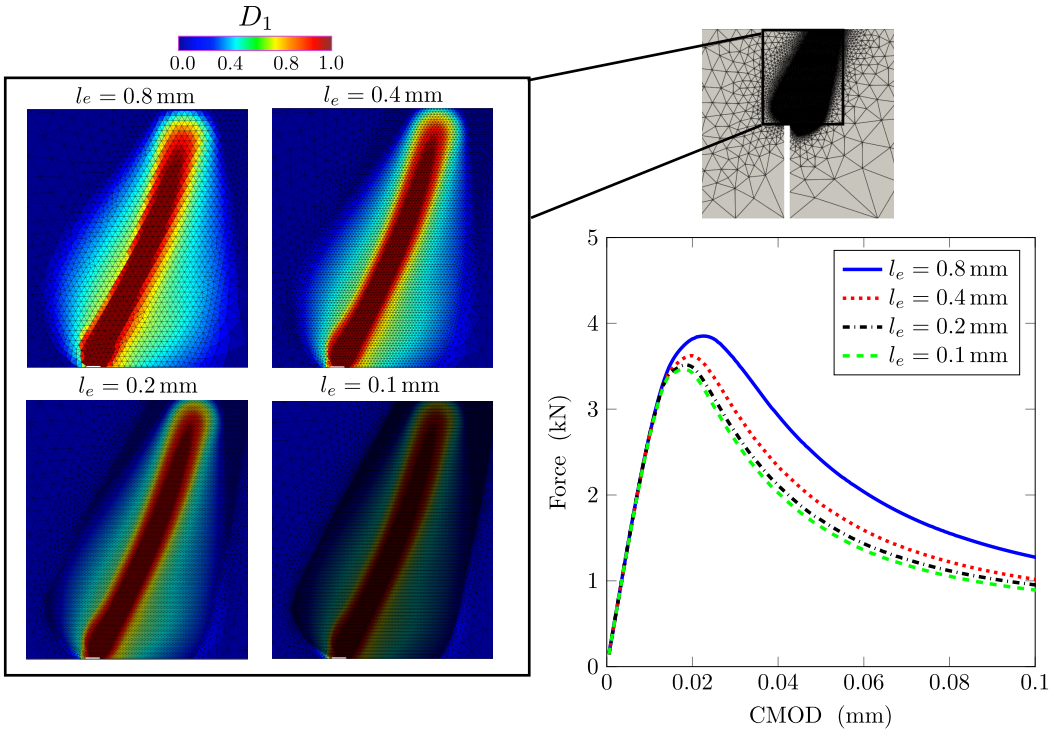

Figure 5.10 • Three-point bending test – Mesh convergence in terms of maps of the maximum principal damage component (D_1) and structural response.

$10^{-4}, 2.4 \times 10^{-4}\}$. All other parameters remain the same as those used to obtain the results depicted in Figure 5.10.

The structural responses obtained for the different meshes are depicted in Figure 5.11 (left). With the new set of parameters, mesh convergence is again achieved with the mesh containing 178 476 elements (with $l_e = 0.1\,\text{mm}$ in the refined region). In Figure 5.11 (center), a comparison is presented between the experimental and numerical (converged) structural Force vs. CMOD responses. It is shown that the numerical simulation provides a good estimation of the ultimate force and effectively captures significant quasi-brittle behavior. Figure 5.11 (right) compares the experimental crack paths (depicted in white) with the damage pattern (D_1 in this case) obtained using the ENLG model at the simulation's conclusion. A good agreement with experimental results is evident, particularly concerning the direction of damage propagation. This underscores the ENLG regularization's ability to replicate realistic crack paths while providing reasonable quasi-brittle responses at the structural scale. However, far from the notch and near the upper part of the beam, the damage pattern tends to the left of the envelop crack paths.

Damage evolution. The evolution of the damage maps obtained using the mesh with $l_e = 0.1\,\text{mm}$ for three different loading stages (CMOD = 0.02 mm, 0.06 mm and 0.1 mm) is presented in Figure 5.12.

Consistent with experimental observations, the damage band exhibit an orientation to the right of the notch and a slight curvature toward the top of the beam. The D_{xx} field indicates considerable damage along the x direction, although it does not consistently

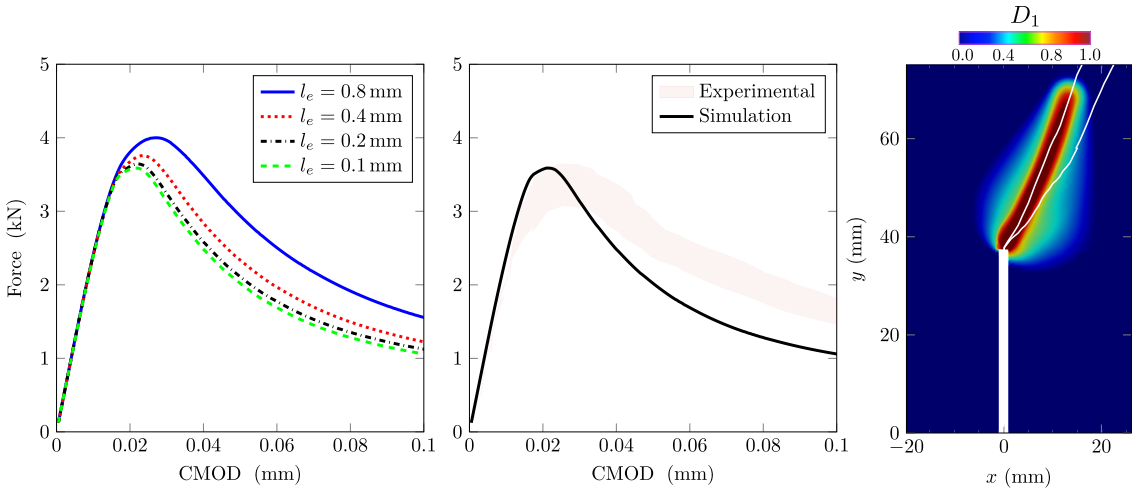

Figure 5.11 • Three-point bending test – Convergence upon mesh refinement in terms of the overall response (left). Comparison between numerical (mesh with $l_e = 0.1\,\text{mm}$) and experimental structural responses (center). Comparison between experimental crack paths (white solid lines) and the maximum principal damage (D_1) pattern obtained at the end of the simulation (right).

align with the principal directions in all elements. Similarly, the D_{yy} map, along with the map for the off-diagonal term D_{xy} (central column in Figure 5.12), reveal that principal directions deviate from the Cartesian axes.

Similar considerations on the damage mechanisms emerge when analyzing the eigenvalues of the damage tensor. The last two columns in Figure 5.12 present color maps for D_1 and D_2, obtained at the Gauss points (D_1 represents the largest damage eigenvalue). The D_1 damage map clearly reveals the emergence of an equivalent "macro-crack" in a specific preferential direction. As expected, neither D_1 nor D_2 correspond precisely to the D_{xx} and D_{yy} damage maps; instead, they represent a combination of the two. This is crucial for accurately modeling the direction of crack paths and the associated principal damage perpendicular to them. The evolution of D_1 also highlights some minor damage spread upon re-localization. It exhibits a sharp profile at the propagation front of the damage band and spreads damage behind it due to the residual non-local interactions.

Non-local interactions evolution. Given the preceding results, it is expected that non-local interactions are significantly diminished in the direction of the major principal damage component. If ellipses are used to represent such interactions, their radius is expected to contract in the same direction. Figure 5.13 illustrates the evolution of interaction ellipses (*i.e.*, tensor $\mathbf{g}^{-1} = \mathbf{H}^{-2}$) for loading steps where CMOD $= 0.02\,\text{mm}$, $0.06\,\text{mm}$ and $0.1\,\text{mm}$ in Figure 5.11. For visualization purposes, the coarse mesh containing 4 333 elements was used.

Blue disks denote the initial isotropic nature of non-local interactions at the beginning of the simulation when the material is still undamaged, and $\mathbf{g}^{-1} = \mathbf{I}$. At CMOD $= 0.02\,\text{mm}$, damage initiates from the notch and reached high levels in certain elements.

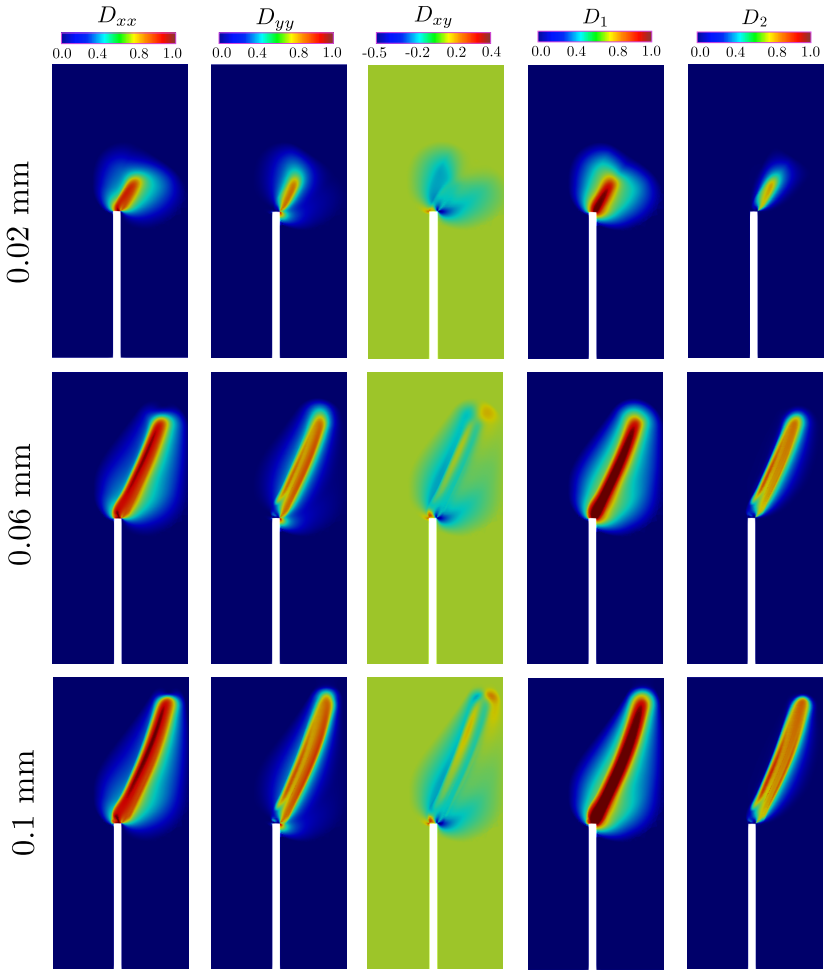

Figure 5.12 • Three-point bending test – Evolution of damage patterns ($D_{xx}, D_{yy}, D_{xy} = D_{yx}, D_1, D_2$) for three different CMOD levels.

As depicted in Figure 5.13, ellipses are oriented in the direction of damage propagation and compressed perpendicular to it. Elements traversed by collapsed ellipses lose the ability to communicate with their neighbors as interactions are reduced. However, elements to the right of the highly damaged zone can still communicate with neighbors from the right and top, which are parallel to the collapsed zone. Ahead of the zone where ellipsoids are formed, blue disks indicate that elements have not yet undergone damage. Finally, as damage propagates toward the top of the beam, a similar collapsed ellipses' behavior is observed at CMOD $= 0.06, \text{mm}$ and CMOD $= 0.1, \text{mm}$.

The evolution of the interaction ellipses, as demonstrated here, reveals the interesting characteristics of the ENLG formulation when coupled with an anisotropic damage model. The ENLG model inherently accounts for two independent material characteristic lengths for the direction of the damage band and one transverse to it. In other words, the anisotropic nature of the non-local interactions allows for a natural distinction between the transverse and parallel directions to the damage band.

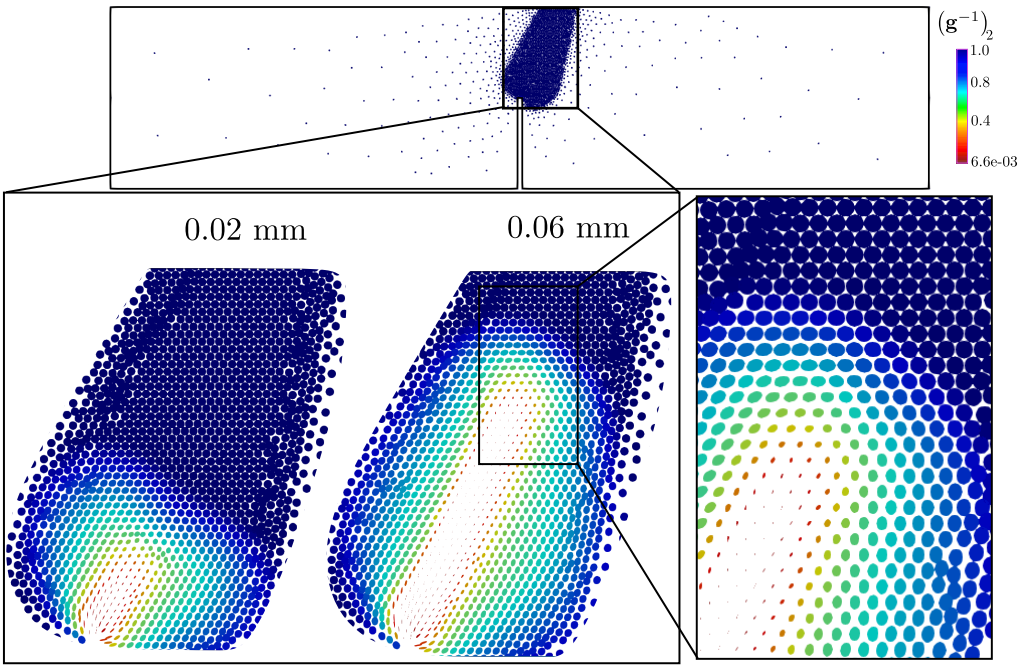

Figure 5.13 • Three-point bending test – Representation according to (5.16) of tensor $\mathbf{g}^{-1} = \mathbf{H}^{-2}$ for two different CMOD levels (0.02 mm, 0.06 mm). The color scale is based on the second (smaller) eigenvalue $(\mathbf{g}^{-1})_2$ (the associated eigenvector gives the direction along which non-local interactions are mostly reduced).

> **Remark 5.7.** *According to Bažant et al. (2022a), the non-local material characteristic length should vary as a function of the normal stress in the principal direction of the damage tensor in the developing damage localization band terminating in fracture. The ENLG model, coupled with an anisotropic damage model, exhibits this desired behavior.*

5.3 Hexagonal specimen under non-proportional loading

To illustrate a scenario where isotropic and anisotropic damage models may yield different results, we suggest examining the response of an hexagonal specimen submitted to non proportional loading. The aim of this purely numerical test-case is solely to highlight how the ENLG formulation with anisotropic non-local interactions and anisotropic damage behavior can result in distinct damage paths compared to an isotropic ENLG model, particularly concerning the influence of preexisting directional damage on damage propagation in a different direction. It is important to note that our intention is not to assert the superiority, if any, of anisotropic damage models over isotropic ones.

Fassin et al. (2019) showed that anisotropic and isotropic damage models may yield significantly different results regarding damage patterns under non-proportional loading conditions. However, their analysis was limited to the impact of anisotropic damage behavior in structural simulations, while the non-local interactions remained isotropic and constant. In the example presented below, we focus on how the induced anisotropic

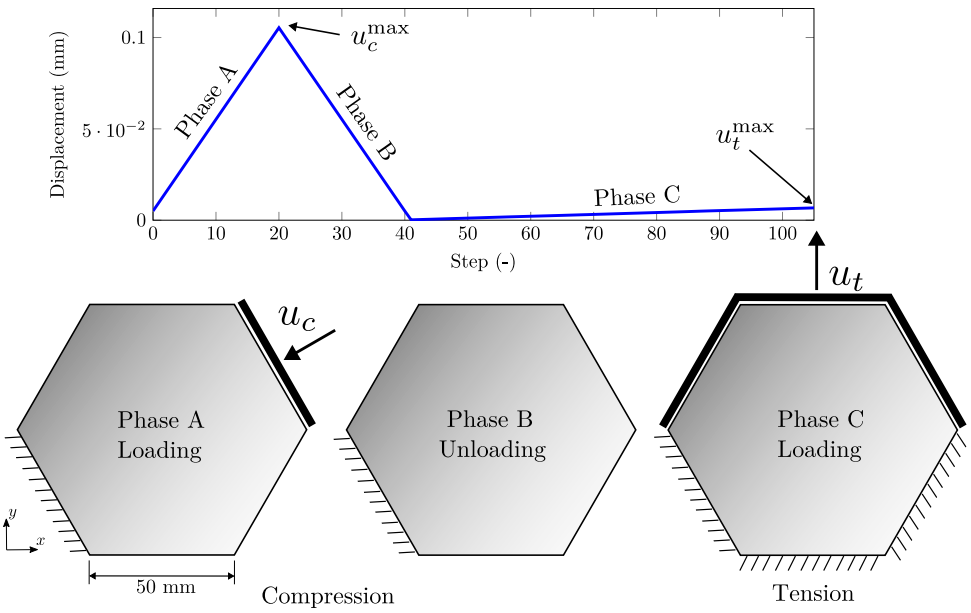

Figure 5.14 • Hexagonal specimen under non-proportional loading – Geometry (thickness = 100 mm) and boundary conditions.

damage behavior leads to evolving anisotropic non-local interactions through the ENLG model and how this can affect the damage patterns.

The geometry and boundary conditions are given in Figure 5.14 (bottom), along with the magnitude of the applied displacement for each loading phase (Figure 5.14 (top)). The specimen is a regular hexagon with 50 mm side length, submitted to a non-proportional loading applied according to three major phases: (*i*) Compression loading until $u_c = u_c^{\max}$ to introduce a diffuse damage in the specimen (Phase A); (*ii*) Unloading phase until $u_c = 0$ to release the compression load (Phase B); (*iii*) Tension loading until $u_t = u_t^{\max}$ to localize damage from the corners (Phase C).

5.3.1 Damage models and material parameters

Three different models are employed for this example: the ENLG (evolving isotropic interactions) model coupled with a simple isotropic damage constitutive law (Ribeiro Nogueira et al., 2024a), the ENLG (evolving anisotropic interactions) model coupled with the tensorial anisotropic damage law by Desmorat (2015), and the GNL (isotropic and constant interactions) model (Peerlings et al., 1996a) coupled with the same anisotropic damage law.

In the isotropic case, damage is modeled through a scalar variable $D \in [0, 1]$ and the constitutive law reads $\boldsymbol{\sigma} = \tilde{\mathbb{E}}^{\text{iso}} : \boldsymbol{\varepsilon}$ with $\tilde{\mathbb{E}}^{\text{iso}} = (1 - D)\mathbb{E}$. The damage criterion function is $f = \bar{e} - \kappa$, with κ the historical maximum of the non-local equivalent strain during loading (this variable is initialized at κ_0). Isotropic damage evolution is considered as $D = 1 - \frac{\kappa_0}{\kappa} \exp\left(-B_t(\kappa - \kappa_0)\right)$, where B_t is a material parameter (see B for a comparison between isotropic and anisotropic damage models at the material point level).

For all the models, the non-local Von Mises equivalent strain with $k = 10$ is used to ensure a larger damage threshold in the compression phase compared to the Mazars'

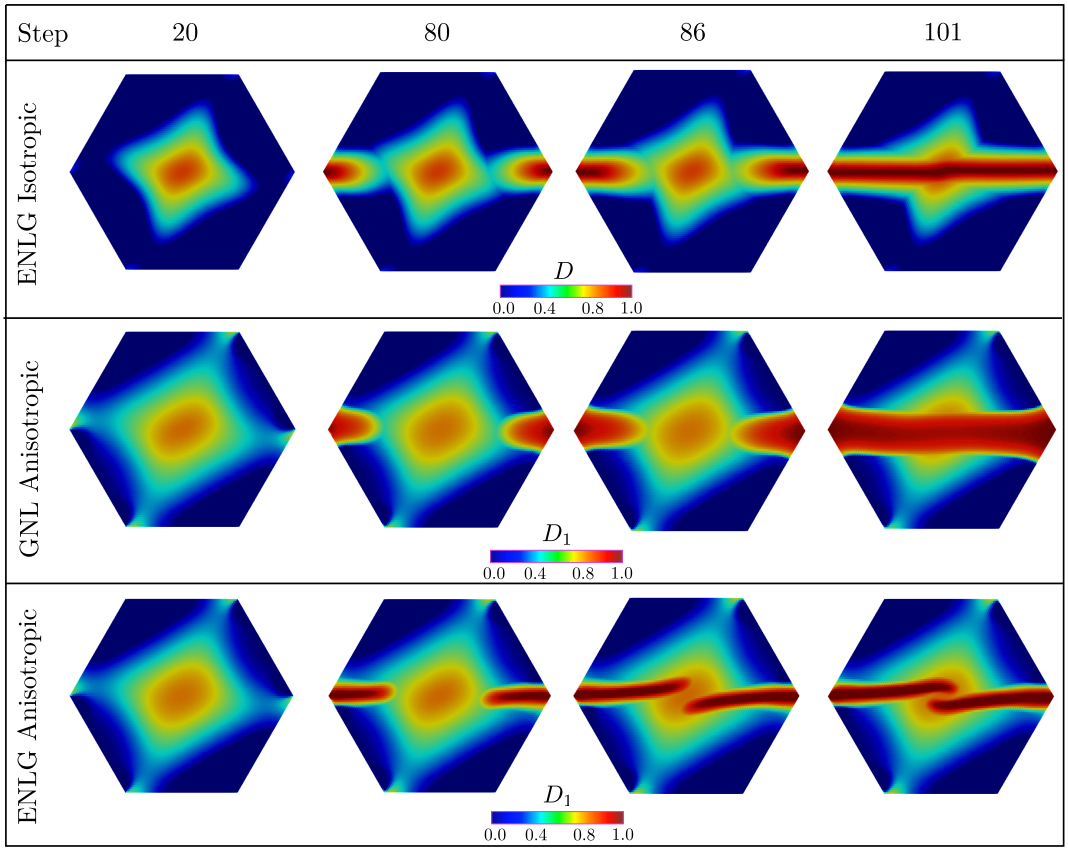

Figure 5.15 • Hexagonal specimen under non-proportional loading – Damage patterns obtained for the different models during the test.

strain. To compare, at least qualitatively, the numerical results obtained with the different models, the remaining material parameters used for simulating this test case were calibrated to provide a similar initial damage state right after Phase A. In particular, the elastic properties are set to $\{E, \nu\} = \{17\,000\,\mathrm{N/mm^2}, 0.18\}$ for all the models. Similarly, the initial length scale parameter is $c = 12\,\mathrm{mm^2}$ for all the models. The remaining parameters are chosen as $\{\kappa_0, B_t\} = \{9.5 \times 10^{-5}, 700\}$ for the isotropic ENLG model, $\{\kappa_0, S, s, B\} = \{7.0 \times 10^{-5}, 9.25 \times 10^{-5}, 4.9, 1.2\}$ for the anisotropic ENLG model, and $\{\kappa_0, S, s, B\} = \{8.0 \times 10^{-5}, 5.8 \times 10^{-5}, 4.9, 1.3\}$ for the GNL anisotropic model. The residual interactions parameter is set to $\xi = 0$ for all the models.

5.3.2 Representative results

Damage evolution. The damage patterns obtained for each model are depicted in Figure 5.15 for four loading steps. For the anisotropic damage behavior, only the first principal damage component is represented, whereas the scalar damage variable is used for the isotropic model.

At Step 20 ($u_c = u_c^{\max}$), it is observed that, for all models, diffuse damage occurs in the central part of the specimen due to extensions perpendicular to the loading direction. At Step 80, a horizontal damage band starts to grow from the corners due to the applied tension loading in the vertical direction. Until this point, the three models give very

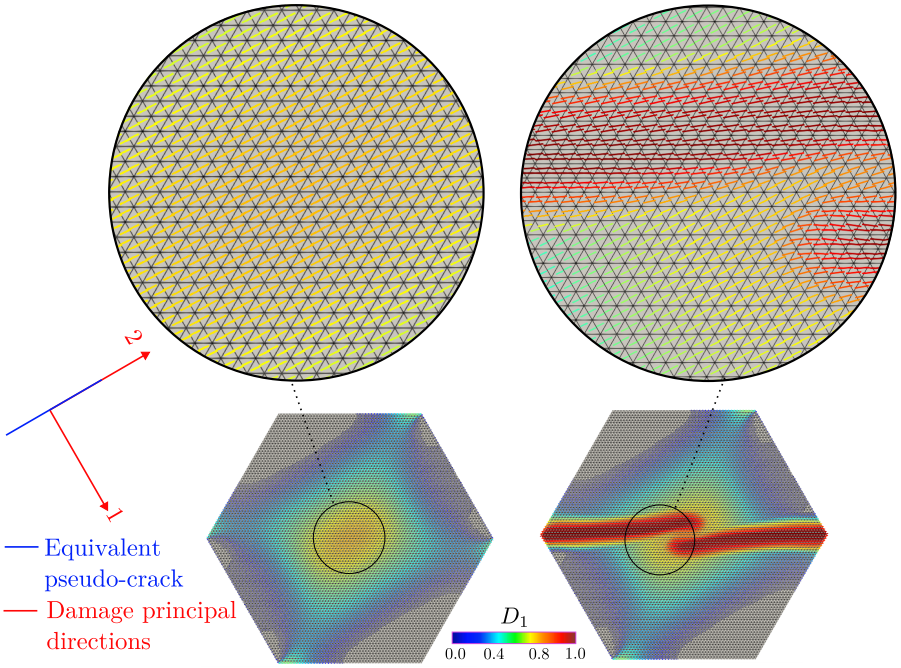

Figure 5.16 • Hexagonal specimen under non-proportional loading – Straight lines (colored based on D_1 values) representing equivalent pseudo-cracks perpendicular to the first principal damage direction.

similar results. However, pronounced differences emerge from Step 86 to Step 101. In the case of the anisotropic ENLG model, the horizontal damage bands become curved when crossing the central zone previously damaged during compression loading. Conversely, the damage bands are not affected by the preexisting damage in the central region for the ENLG isotropic and GNL anisotropic models, resulting in a almost fully horizontal damage pattern. In this second case, this behavior mainly arises from constant isotropic non-local interactions, leading to the diffusion of damage.

Anisotropic interactions and damage-dependent Riemannian metric acting as a structural tensor. To gain further insight into why the damage patterns become curved for the ENLG anisotropic model, it is useful to study how the induced anisotropic behavior affects the evolution of the non-local interactions during the loading steps.

Figure 5.16 shows, for each element, the plane defined by the first damage eigenvector (*i.e.*, the eigenvector associated with the damage eigenvalue D_1) for the ENLG anisotropic damage model, which can be considered representative of elementary "pseudo-cracks" developing within each element. One can observe that in the diffuse damage phase (Phase A), the equivalent "pseudo-cracks" are parallel to the loading (compression) direction. This observation also applies to the GNL anisotropic model; however, it does not hold for the ENLG isotropic case, as the concept of damage principal directions is meaningless with a scalar variable. Then, during the tensile loading phase in the vertical direction, equivalent "pseudo-cracks" are horizontal and start to rotate during damage propagation in the central regions of the specimen (Figure 5.16 right) for the ENLG anisotropic model as an effect of the preexisting damage generated in the compression phase.

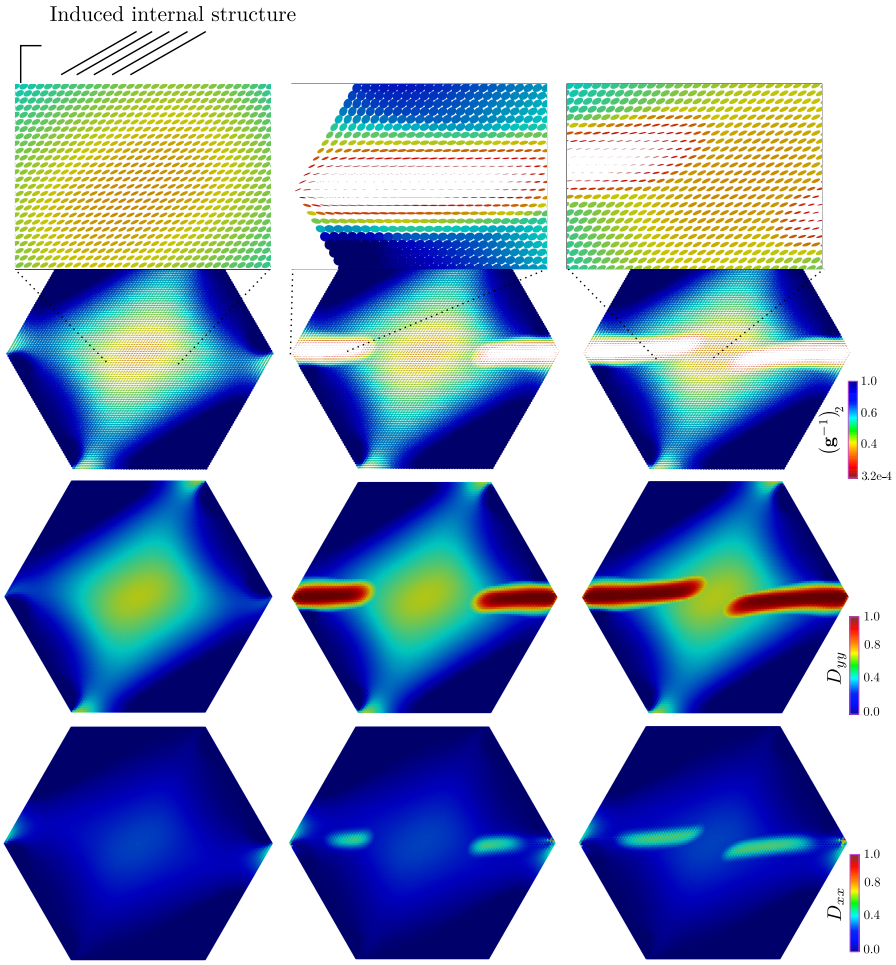

Figure 5.17 • Hexagonal specimen under non-proportional loading – Representation according to (5.16)) of the tensor $\mathbf{g}^{-1} = \mathbf{H}^{-2}$ for three loading steps (20, 80 and 86) (first row). The color scale is based on the second (smaller) eigenvalue $(\mathbf{g}^{-1})_2$ (the associated eigenvector gives the direction along which non-local interactions are mostly reduced). Damage patterns for the components D_{yy} (second row) and D_{xx} (third row) of the damage tensor.

The key point here is that the anisotropic damage behavior induces anisotropic non-local interactions through the inverse of the metric $\mathbf{g}^{-1}$ for the ENLG anisotropic model (Equation (5.13)). Acting as a structural tensor (see Eqs. (5.6),(5.7)), it defines the impact of the damage–induced orthotropic material symmetry on the non-local contribution of the free-energy.

This is further supported by the analysis of interaction ellipses and the corresponding damage patterns for different loading steps (Figure 5.17). One observes that, at Step 20, the interaction ellipses are, again, oriented in the direction of crack propagation and compressed perpendicular to it. The initial damage thus creates an induced internal structure and establishes a preferential direction for damage propagation, influencing the damage pattern during subsequent tensile loading. Such behavior is typically observed in materials with intrinsic (initial) anisotropy (Teichtmeister et al., 2017; Gültekin et al.,

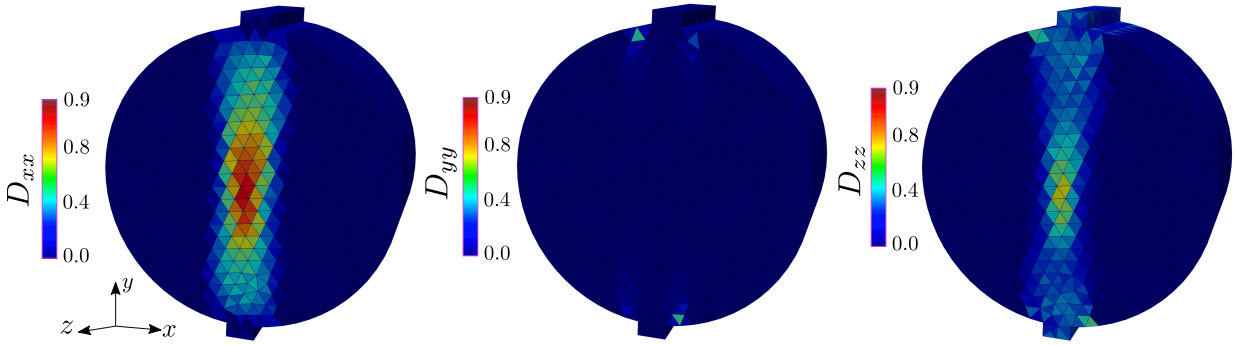

Figure 5.18 • Brazilian test – Damage maps of components D_{xx}, D_{yy} and D_{zz} of the damage tensor.

2018; Li & Maurini, 2019; Gerasimov & De Lorenzis, 2022; Pranavi et al., 2023; Wu et al., 2015; Jin & Arson, 2018; Forghani et al., 2019; Yin et al., 2020; Lu & Guo, 2022). The main difference with the previously cited works is that, here, the material undergoes a transition from isotropic to anisotropic behavior, and the influence of such a damage nature on non-local interactions is naturally taken into account by the evolving damage-dependent metric $\mathbf{g}$.

5.4 Toward 3D simulations

The developments regarding the ENLG anisotropic model presented in this contribution can be readily extended to 3D simulations. For illustrative purposes, let us consider the 3D simulation of the Brazilian test and the mixed-mode three-point bending test.

5.4.1 Brazilian test

This example is used here as a purely numerical test for further studying some anisotropic aspects. For a clear visualization of anisotropic interactions, the domain was discretized with 14 178 linear tetrahedral elements. The displacements are blocked on the bottom part of the cylinder and an increasing negative displacement is applied on the top part, so the specimen is under a compression state. The material parameters for this test are chosen as $\{E, \nu, c, \kappa_0, S, s, B, \xi, k\} = \{25\,850\,\text{MPa},\ 0.18,\ 4.0\,\text{mm}^2,\ 1.25 \times 10^{-4},\ 1.45 \times 10^{-4},\ 4.9,\ 5/3,\ 0, 10\}$.

The damage maps obtained are shown in Figure 5.18 for D_{xx}, D_{yy} and D_{zz}. One can observe that major damage takes place on the x direction, whereas it is less present on z. As expected, D_{yy} remains at zero almost everywhere. Under compression on y, extensions controlling the damage evolution develop on the perpendicular directions. On the contrary, models considering a scalar damage variable do not have the notion of direction. In this last case, damage still develops in the medium (see for instance the simulation of the Brazilian test in (Wang et al., 2023)), but all the directions are damaged in the same way.

As said before, the damage induced anisotropic behavior at the Gauss points is responsible for modifying the non-local interactions at the structure scale. In order to visualize the impact of this influence on the structural response, the tensor representation

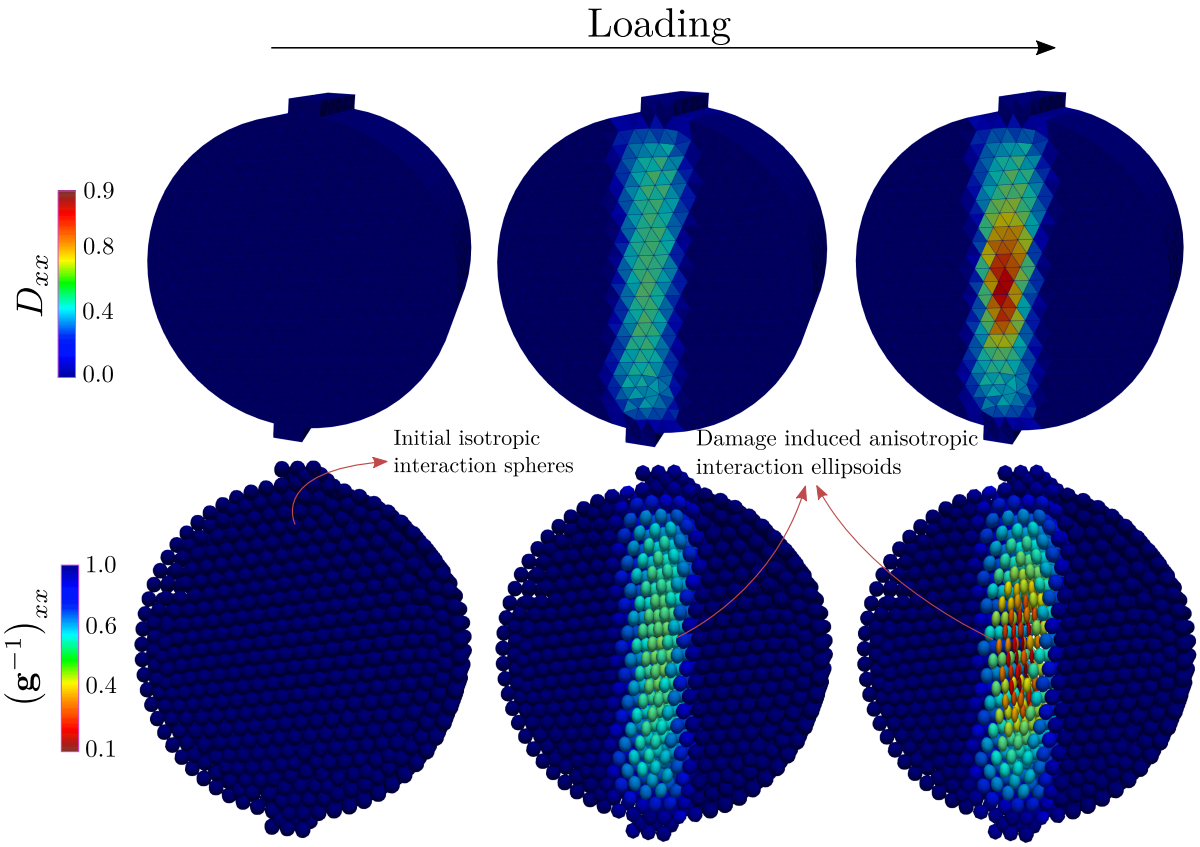

Figure 5.19 • Brazilian test – Ellipsoids representing tensor $\mathbf{g}^{-1} = \mathbf{H}^{-2}$.

by ellipsoids, which was introduced before for the 2D case, is used here. For instance, the second-order identity tensor, which is isotropic, is represented by a sphere in $\mathbb{R}^3$.

Figure 5.19 shows the evolution of the ellipsoids associated to $\mathbf{g}^{-1}$ throughout the damage growth. The first row shows the damage maps for D_{xx} during the load, while the second row depicts the corresponding $\mathbf{g}^{-1}$ ellipsoids colored by the $(\mathbf{g}^{-1})_{xx}$ component. At the beginning of the simulation on the left, no damage takes place and the material is considered as isotropic. As a consequence, ellipsoids interactions are in fact spheres as $\mathbf{g}^{-1} = \mathbf{I}$, representing their isotropic nature. Gauss points are equally influencing their neighbors in all the directions, which corresponds to the case of the classic gradient-enhanced approach (Peerlings et al., 1996a). In Figure 5.19 (middle), one can see a state where damage takes place at small levels, with D_{xx} going up to 0.5. Interactions start to be reduced, and the spheres in the middle of the specimen become ellipsoids. The anisotropic character of the interactions can be easily observed and is predominant on the x direction. On Figure 5.19 (right), high levels of damage (in red) are attained for the D_{xx} component. Ellipsoids minor axes are therefore more affected following the principal damage direction, which represent the anisotropic vanishing interactions upon damage localization. Interactions between these points and the rest of the domain are considerably reduced on x, but not necessarily the same on y and z.

Furthermore, the ellipsoids major axes are mainly orientated following the y direction. Near the highly damaged elements, some of the ellipsoids are slightly rotated, which highlights the multi-axial character of damage (and the intrinsically related non-locality)

in these zones.

5.4.2 Mixed-mode 3D three-point bending test

A relatively coarse mesh ($l_e = 1.0\,\text{mm}$ in the refined region, with 121 021 elements and 66 000 degrees of freedom) was generated. The material parameters for this test are chosen as $\{E, \nu, c, \kappa_0, S, s, B\} = \{38\,000\,\text{MPa},\ 0.2,\ 4\,\text{mm}^2,\ 6\times10^{-4},\ 2.71\times10^{-4},\ 4.9,\ 5/3\}$. Moreover, the residual interactions parameter is set to $\xi = 0.0005$.

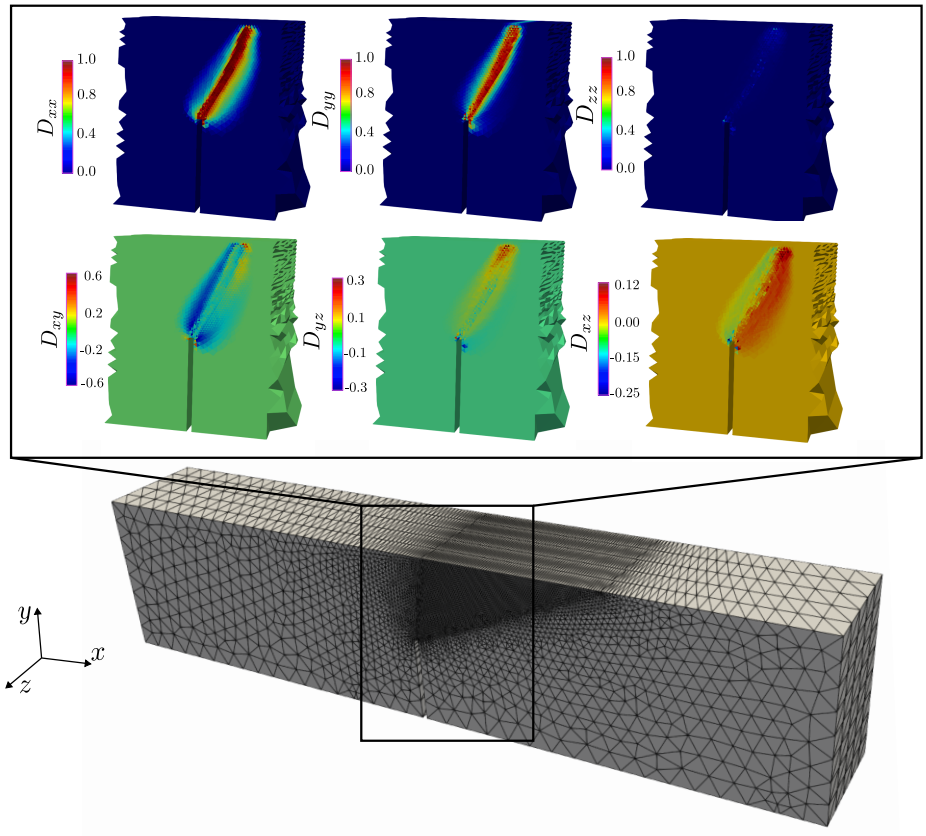

Figure 5.20 • 3D Mixed-mode three-point bending test – Maps of the six components (D_{xx}, D_{yy}, D_{zz}, $D_{xy} = D_{yx}$, $D_{xz} = D_{zx}$, $D_{yz} = D_{zy}$) of the damage tensor $\mathbf{D}$.

Damage evolution. Figure 5.20 displays the maps of the six components of the damage tensor $\mathbf{D}$ in the central region of the beam. Consistent with observations from the 2D simulation of the same test, the damage band exhibits an orientation to the right of the notch. It can be clearly observed that the component D_{zz} remains considerably smaller than D_{xx} and D_{yy} across most regions. This confirms that major damage mechanisms take place in the plane $x - y$. Additionally, Figure 5.21 shows the maps of the damage eigenvalues. Similar to the 2D simulation, the first eigenvalue D_1 indicates that an equivalent "pseudo-crack" appears, which is associated with the damage principal direction.

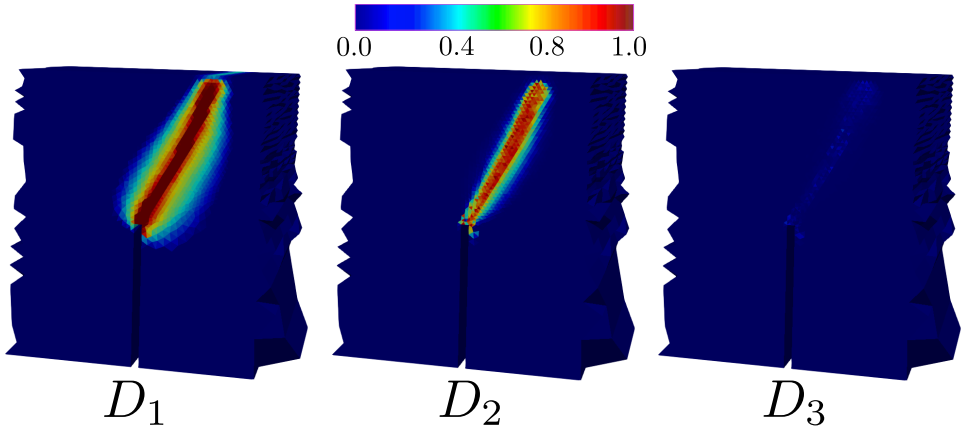

Figure 5.21 • 3D Mixed-mode three-point bending test — Maps of the three eigenvalues (D_1,D_2,D_3) of the damage tensor $\mathbf{D}$.

On the scalability of the model. This 3D simulation highlights a disadvantage of the model. As explained earlier, achieving converged results requires very fine meshes in the simulations. For instance, in the 2D simulation of the three-point bending test, a refinement level of $l_e = 0.1\,\text{mm}$ was necessary to achieve a converged structural response consistent with the reference experimental results. In 2D, this resulted in a mesh containing 178 476 elements (approximately 260 000 degrees of freedom) and a "reasonable" computational time. However, for a 3D simulation of the same experimental test, using a mesh with $l_e = 0.1\,\text{mm}$ in the refined region leads to a number of degrees of freedom exceeding 10 million. Consequently, the analysis becomes computationally prohibitive with the sequential solver employed in this work. The use of parallel solving techniques should be considered in this case. Moreover, while local refinement has been employed in this contribution, in practical scenarios, the crack path is not known *a priori*. Mesh adaptation techniques could thus become useful for the simulation of larger-scale structures.

Summary of Chapter 5

- The ENLG model has been successfully employed to regularize a tensorial anisotropic damage law based on Ladevèze's damage variable **H**. Different second-order damage models (eventually using the damage variable **D** instead of **H**) can be also used **without modifying the general framework**.
- The variational formulation of the coupled problem was established by linking **H** and the damage-dependent Riemannian metric **g** from the ENLG model. It inherently accounts for **two independent material characteristic lengths** for the direction of the damage band and one transverse to it. The framework is applicable to both 2D and 3D analyses.
- A procedure for considering **residual non-local interactions** was proposed through an additional parameter ξ. The smaller the value of ξ, the better the capability of the ENLG model in representing a progressive damage-to-fracture transition. As a counterpart to this, **finer and finer meshes** are needed to achieve mesh convergence of the structural response.
- The numerically obtained structural responses exhibited quasi-brittle behavior **consistent with experimental** observations, as well as damage patterns which closely matched the experimental ones.
- Tensor visualization using **ellipses** highlighted the role of the inverse of the metric (*i.e.,* of damage) in reducing non-local interactions when damage occurs. Additionally, the eigenvectors of the damage tensor provided crucial information about equivalent "pseudo-crack" growth **direction and propagation**.
- The response of a hexagonal specimen under non-proportional loading was studied. In the case of the ENLG model coupled with anisotropic damage, the damage patterns become **curved** when crossing a previously damaged region in a specific preferential direction thanks to the **anisotropic interaction kernel** induced by the damage-dependent Riemannian metric.
- The application of the formulation to 3D simulations is **already possible**. However, parallel solving techniques become necessary to perform damage mechanics simulations with meshes that are fine enough to achieve mesh-converged results **(millions of degrees of freedom)**.

Conclusion and perspectives

Conclusion. This thesis aimed to provide new theoretical and numerical developments concerning modeling quasi-brittle materials. We focused on non-local approaches, specifically those of gradient-enhanced type and the so-called ENLG anisotropic damage model.

In Chapter 1 a comprehensive literature review on experimental observations related to quasi-brittle materials was presented. Essential aspects were described, such as the growth of micro-cracks and their impact on the induced anisotropic behavior of materials. A brief review of existing explicit and implicit crack modeling strategies followed the discussion. Special attention was given to contiuum damage mechaics, which describes the degradation of elastic properties in a homogenized way by a damage state variable. The main principles of this theory were introduced and discussed, highlighting the role of anisotropic damage in describing oriented micro-cracks.

Due to the inherent pathological mesh dependency induced by local damage models in finite element analysis, the numerical solution needs to be regularized. This was briefly explained in the first part of Chapter 2, which provided a few results of a classic localization analysis in softening media. Then, the focus shifted to presenting the so-called non-local approaches, acting as localization limiters and regularizing the response. The concept of neighborhood interactions was introduced, highlighting that the models considering isotropic and constant interactions lead to an incorrect description of material degradation. Common issues of these approaches are damage, excessive diffusion, and spreading and boundary effects. Therefore, various evolving (and eventually anisotropic) non-local interactions approaches were proposed in the literature (Geers et al., 1998; Desmorat & Gatuingt, 2007b; Giry et al., 2011; Poh & Sun, 2017; Vandoren & Simone, 2018) and briefly described in the chapter. The discussion was also extended to other regularization techniques, mainly developed for the setting of isotropic damage (Francfort & Marigo, 1998; Bourdin et al., 2000; Moës et al., 2011).

Chapter 3 provided further insights on non-local approaches by providing theoretical and numerical developments in a 1D setting. Firstly, we conducted a classic wave dispersion analysis (Sluys et al., 1993; Sluys & de Borst, 1994; Peerlings et al., 2001; Di Luzio & Bažant, 2005) to compare the regularization characteristics of ENLG and GNL models. Contrarily to local damage models, propagation is dispersive, and the wave velocity remains real for the gradient-enhanced models. Loading waves can be transformed into a unique stationary harmonic localization wave, and a critical wavelength can be derived. This last is associated with the internal length and the size of the localized zone. Particularly, the impact of the initial strain and damage states was shown in the differences observed between GNL and ENLG models. In both cases, the size of the localization

zone is well-defined. Subsequently, the analysis was complemented by numerical results in a one-dimensional dynamics spalling problem. Damage diffusion and boundary effects were studied, and the capability of the different models in regularizing the response was discussed. The formulations with evolving interactions (Giry, 2011; Desmorat et al., 2015b) proved more efficient in dealing with boundary effects and damage diffusion while retaining their regularization properties.

Further developments concerning the ENLG approach were detailed in Chapter 4. In this chapter, an alternative derivation of this approach was proposed. A thermodynamic framework was detailed to derive anisotropic and isotropic ENLG damage models based on a geometric extension of the micromorphic approach (Forest, 2009). Compared to the GNL model, the only modification introduced in the free energy considers a Riemannian norm (*i.e.,* the non-local equivalent strain lives in a space curved by damage). Qualitative illustrations showed how the interactions between points can be affected by the existing isotropic or anisotropic network of micro-cracks. Based on the work of Pijaudier-Cabot and Benallal (1993), a bifurcation analysis in a gradient-enhanced continuum was then introduced. It was shown that the ENLG model preserves the localization-limiting character of non-local approaches. It differs from the GNL model and presents a re-localizing nature for high initial damage levels. The derived critical wave number generalizes the expressions obtained from the wave dispersion analysis in Chapter 3. The numerical formulation of the coupled problem was derived, and a few results concerning 2D isotropic damage simulations were provided. It was demonstrated that the ENLG model gives more realistic crack paths than the GNL model. Damage re-localizes in almost one line of elements for the ENLG model, which better describes a sort of "pseudo-crack". The limit case where damage tends to the unity leads to a division by zero in the ENLG formulation. One has the inverse of the metric that becomes singular, and its inverse (the metric itself) cannot be obtained. In other words, similarly to a black hole in space-time, this represents the case where a singularity appears in the space curved by damage.

Chapter 5 addressed the coupling between an evolving anisotropic interactions gradient-enhanced regularization (ENLG model) and an anisotropic damage constitutive behavior. A tensorial anisotropic damage law was used based on the second-order Ladevèze's damage variable $\mathbf{H}$ (Desmorat, 2015). The plane-stress version of the model was therefore derived to simulate 2D specimens. The variational formulation of the coupled problem was established by linking $\mathbf{H}$ and the damage-dependent Riemannian metric $\mathbf{g}$ from the ENLG model. It inherently accounts for two independent material characteristic lengths for the direction of the damage band and one transverse to it.

The developed framework was applied to both 2D and 3D analyses. Inspired by the works of Poh and Sun (2017) and Negi et al. (2020), a procedure for considering residual non-local interactions was proposed through an additional parameter. It was shown that this aspect is necessary to provide mesh-converged simulations with a relatively high, but still numerically attainable, number of elements in the refined region. The numerically obtained structural responses exhibited quasi-brittle behavior consistent with experimental observations and damage patterns that closely matched the experimental ones. Moreover, the anisotropic nature of damage enriches the behavior at the Gauss points, providing

crucial information about equivalent "pseudo-crack" growth direction and propagation.

A novel hexagonal test was also proposed to show how induced anisotropic interactions can affect the response. It was shown that the metric acts as a structural tensor, describing the impact of the induced material orthotropy in the evolution of the damage patterns.

Finally, it was shown that the developments regarding the ENLG anisotropic model presented in this dissertation can be readily extended to 3D. However, due to the high level of refinement required in the zone where damage initiates and propagates, the analysis becomes computationally prohibitive with the sequential solver employed in this work. Moreover, while local refinement has been used in this contribution, in practical scenarios, the crack path is not known *a priori*.

In conclusion, this thesis aimed to study the advantages and inconveniences of using evolving non-local interactions approaches for degradation modeling in quasi-brittle materials. Particularly, the capabilities of the ENLG model were studied. It was shown that this model has interesting characteristics, such as its re-localizing nature and anisotropic interactions aspects. It progressively describes the damage-to-fracture transition while retaining its regularization nature.

Perspectives to further research may concentrate on a variety of different topics. We can divide future works into two central axes: one concerning specific theoretical and numerical aspects of the modeling techniques and the second mainly related to the application of the developed models. In the following, a few suggestions are given, which are by no means exhaustive but may provide helpful ideas.

Perspectives in terms of theoretical and numerical developments of the modeling techniques. From a theoretical point of view, extending the bifurcation analysis of the ENLG model to incorporate anisotropic (potentially non-homogeneous) damage settings would yield valuable insights into how the singularity of the metric relates to its re-localizing behavior. This analysis could provide useful information on possible transition criteria to introduce a discontinuity in the formulation. Additionally, it is important to investigate the potential impacts of the non-local contribution in the energy dissipation (see Chapter 4). At first view, since high non-local strain gradients take place during damage re-localization, the non-local term in Equation (4.76) might significantly contribute to the energy.

Another important point to consider is the differential-geometry nature of the ENLG model. While the developments in this thesis enabled a thermodynamic derivation of the ENLG from the micromorphic approach, a rigorous mathematical framework is still required. In this context, the Riemannian metric is seen as the Euclidean one scaled by damage and is solely used only to compute the non-local equivalent strain, while all the other quantities remain in the Euclidean space. Further studies would require defining different manifolds, establishing (damage-dependent) transformation between them and the associated push-back and push-forward operations (see, for instance, Das et al. (2021)). Additionally, a more general geometric framework of damage models may be also constructed based on the gauge theory (*e.g.,* Pathrikar et al. (2021))

From a numerical point of view, short-term developments could extend the ENLG approach to initial anisotropic media (*e.g.,* masonry (Tisserand et al., 2022), composites

(Yin et al., 2020), etc.). This extension may involve utilizing the metric as a structural tensor that differs from the identity tensor at the undamaged state (see Teichtmeister et al. (2017) for examples of initial structural tensor for different class of symmetries).

Developments concerning the transition from damage to fracture (implemented in strong discontinuity framework) (*e.g.,* Mazars and Pijaudier-Cabot (1996), Simone et al. (2003b), Cazes et al. (2009), Cuvilliez et al. (2012), and Negi and Kumar (2022)) should be also considered. In the case of the E-FEM method, for instance, stress-locking effects may arise due to the loss of continuity of the crack-path, and tracking algorithms may become necessary (*e.g.,* Oliver et al. (2002b), Riccardi et al. (2017), and Alsahly et al. (2018)). However, the anisotropic character and the re-localizing behavior of the ENLG model may avoid the need for tracking algorithms (see, for instance, first results in a 1D setting (Thierry, 2019).

This transition approach could also be also extended to multi-physics coupling scenarios, where the ENLG anisotropic model, possibly coupled to strong discontinuity approaches, could describe the evolution of the material's anisotropic permeability/diffusion properties (Armero & Callari, 1999; Bary et al., 2000; Callari & Armero, 2002; Callari et al., 2010; Rastiello et al., 2015, 2016).

Finally, it is essential to highlight that the applicability of the ENLG approach to different loading and physical scenarios needs to be addressed. While quasi-static simulations were the focus of this manuscript, extending the analysis to dynamic loading is a logical next step. In fast dynamics, for instance, one could study the coupling between the ENLG model and delay-damage approaches (Allix & Deü, 1997a; Allix et al., 2003; Desmorat et al., 2010).

Perspectives in terms of applications. As highlighted in Chapter 5, real-scale 3D simulations become prohibitive within a sequential solver. Additional numerical developments, particularly concerning parallel computation (*e.g.,* Badri et al. (2021) and Badri and Rastiello (2023)), may be considered to perform damage mechanics simulations with meshes that are fine enough to achieve mesh-converged results (millions of degrees of freedom). It would be interesting to see which level of resolution would be required to provide converged results for minimal residual interactions. Additionally, mesh adaptation techniques (*e.g.,* Patzák and Jirásek (2004)) could become useful, especially when crack paths are unknown. Another option is to consider the coupling with more advanced meshing techniques which avoid re-meshing, such as the X-MESH approach (Moës et al., 2023; Quiriny et al., 2024).

Regarding the application of ENLG formulations to the simulation of civil engineering structures, a first aspect to address is the introduction of re-bars inside the concrete (see, for instance, Ranjbaran (1991) and Sellier and Millard (2019)). It would be necessary to evaluate whether an explicit or implicit description of the bars would be adequate. In the explicit case, the main scientific question concerns the boundary condition used on the steel-concrete interface.

In the same context, the predictive capabilities of the ENLG model need evaluation. It is crucial to verify the capabilities of the proposed formulation to address size effects (Grégoire et al., 2013; Hoover et al., 2013) in notched and unnotched three-point bending

tests, as well as the effects of crack-parallel stresses. This would require the simulation of gap-tests (Nguyen et al., 2020) and other "distinctive experiments" (see Bažant and Nguyen (2023)).

Lastly, is the curved damage pattern obtained for the hexagonal specimen something that can be experimentally confirmed? Experimental campaigns on quasi-brittle materials for such a test may be challenging due to the applied tension loading. However, alternative configurations could be explored to reproduce similar loading conditions. Additionally, better control during tensile loading could potentially be achieved with fiber-reinforced concretes, for instance.

Appendices

A

Implicit damage model integration at Gauss point level

Constitutive model integration is performed once one has computed the displacement and non-local equivalent strain fields at global iteration $(k+1)$. These fields being known, the goal is to determine $\mathbf{H}$ and $\tilde{\mathbb{E}}$. For brevity, the global iteration index $(k+1)$ and the subscript h are omitted. Additionally, for ease of variable initialization, the model is reformulated using the tensor $\mathbf{A} = \mathbf{H} - \mathbf{I}$. Consequently, in the undamaged state, $\mathrm{tr}\,(\mathbf{A}) = 0$. The evolution of damage is thus calculated as follows:

(i) Compute the total strain $\boldsymbol{\varepsilon}$ based on the last computed displacement.

(ii) Compute a trial of the criterion function:

$$f_{\text{try}} = \bar{e} - \kappa^k \qquad \kappa^k = \kappa_0 + SR_v^s \mathrm{tr}\,(\mathbf{A}^k) \tag{0.1}$$

where $\bar{e}$ is the last computed non-local strain, and the triaxiality function R_v is evaluated based on the solution at previous global iteration with $T_X^k = \frac{\mathrm{tr}\,\boldsymbol{\sigma}^k}{3\sigma_{eq}^k}$.

- If $f_{\text{try}} < 0$, there is no damage evolution, *i.e.*, $\mathbf{A} = \mathbf{A}^k$.
- Otherwise, an iterative procedure is employed to find a solution satisfying $f(\mathbf{A}) = 0$. In this case (we denote with letter i the local sub-iterations):
  - One then looks for $\delta\mathbf{A}^{i+1}$ such that:

$$f^{i+1} \approx f^i + \left.\frac{df}{d\mathbf{A}}\right|_i : \delta\mathbf{A}^{i+1} = f^i - SR_v^s \mathrm{tr}\,(\delta\mathbf{A}^{i+1}) = 0 \tag{0.2}$$

with:

$$f^i = \bar{e} - \kappa_0 - SR_v^s \mathrm{tr}\,(\mathbf{A}^i) \qquad \mathrm{tr}\,(\delta\mathbf{A}^{i+1}) = \delta\lambda^{i+1}\,\mathrm{tr}\,(\mathbf{P}^k) \tag{0.3}$$

Here, the damage rate direction tensor $\mathbf{P}^k$ is defined after having computed the total (or effective) strain tensor at previous global iteration. Finally, one has:

$$\delta\lambda^{i+1} = \frac{\bar{e} - \kappa_0}{SR_v^s \mathrm{tr}\,(\mathbf{P}^k)} - \frac{\mathrm{tr}\,(\mathbf{A}^i)}{\mathrm{tr}\,(\mathbf{P}^k)} \tag{0.4}$$

and then:

$$\mathbf{A}^{i+1} = \mathbf{A}^i + \delta\lambda^{i+1}\mathbf{P}^k \tag{0.5}$$

∗ Once local convergence is achieved, one sets:

$$\mathbf{A} = \mathbf{A}^{i+1} \tag{0.6}$$

(*iii*) Update the Ladevèze damage variable at convergence:

$$\mathbf{H} = \mathbf{A} + \mathbf{I} \tag{0.7}$$

compute the effective Hooke's tensor $\tilde{\mathbb{E}} = \tilde{\mathbb{E}}(\mathbf{H})$ from (5.28), and compute the stress tensor $\boldsymbol{\sigma} = \tilde{\mathbb{E}} : \boldsymbol{\varepsilon}$. Finally, compute the tensorial damage variable $\mathbf{D}$.

Plane stress modifications in constitutive behavior integration. While the general process for integrating constitutive behavior remains largely unchanged, there are specific modifications introduced for plane stress conditions. These adjustments include:

(*i*) The same procedure as described earlier is applicable to $\boldsymbol{\varepsilon}_{\mathbf{2}}$.

(*ii*) The variation in the damage multiplier is determined by:

$$\delta\lambda^{i+1} = \frac{\bar{e} - \kappa_0}{SR_v^s \left(\mathrm{tr}\left(\mathbf{P}_{\mathbf{2}}^k\right) + \langle\varepsilon_z^k\rangle / \|\langle\boldsymbol{\varepsilon}\rangle\|\right)} - \frac{\mathrm{tr}\left(\mathbf{A}_{\mathbf{2}}^i\right) + A_z^i}{\mathrm{tr}\left(\mathbf{P}_{\mathbf{2}}^k\right) + \langle\varepsilon_z^k\rangle / \|\langle\boldsymbol{\varepsilon}\rangle\|} \tag{0.8}$$

where $\mathbf{A}_{\mathbf{2}} = \mathbf{H}_{\mathbf{2}} - \mathbf{I}_{\mathbf{2}}$, the triaxiality function R_v is computed after evaluating T_X^k based on $\boldsymbol{\sigma}_{\mathbf{2}}^k$ (see 3), and we assume the damage direction tensor depending on the total strain (similar formulas hold when considering the effective strain). Thus, one has:

$$\delta\mathbf{A}_{\mathbf{2}}^{i+1} = \delta\lambda^{i+1}\mathbf{P}_{\mathbf{2}}^k \qquad \delta A_z^{i+1} = \delta\lambda^{i+1}\langle\varepsilon_z^k\rangle / \|\langle\boldsymbol{\varepsilon}\rangle\| \tag{0.9}$$

(*iii*) At convergence, update the Ladevèze damage variable $\mathbf{H}_{\mathbf{2}} = \mathbf{A}_{\mathbf{2}} + \mathbf{I}_{\mathbf{2}}$, compute the two-dimensional effective Hooke's tensor $\tilde{\mathbb{E}}_{\mathbf{2}}^{\star} = \tilde{\mathbb{E}}_{\mathbf{2}}^{\star}(\mathbf{H}_{\mathbf{2}}, H_z)$ from (5.39), and calculate the stress tensor $\boldsymbol{\sigma}_{\mathbf{2}} = \tilde{\mathbb{E}}_{\mathbf{2}}^{\star} : \boldsymbol{\varepsilon}_{\mathbf{2}}$. Finally, compute the tensorial damage variable $\mathbf{D}_{\mathbf{2}} = \mathbf{I}_{\mathbf{2}} - \mathbf{H}_{\mathbf{2}}^{-2}$ and $D_z = 1 - H_z^{-2}$.

Representative local responses obtained using the chosen anisotropic damage model at the integration point level are presented in B.

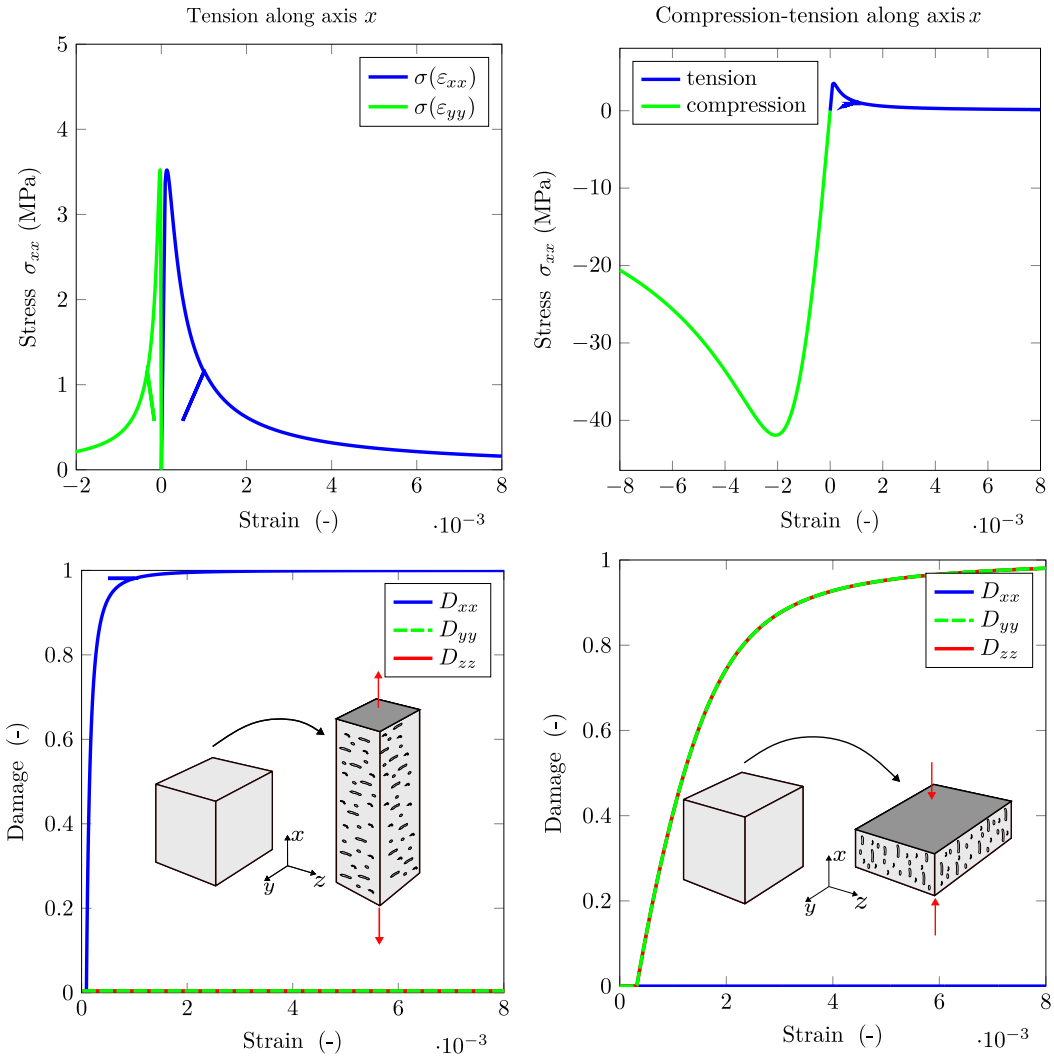

Figure A.1 • Local models – Desmorat's model responses in tension (top-left) and compression (top-right). Evolution of damage tensor components under tension (bottom-left) and compression (bottom-right). Micro-cracks are illustrated to highlight the preferential directions of damage.

Appendix A. Implicit damage model integration at Gauss point level

B

Representative local responses of the anisotropic damage model

Representative responses simulated using the anisotropic damage model discussed in 2 are provided. These numerical results are obtained through `mtest`, an open-source Python tool distributed alongside `Mfront`. This tool enables the simulation of complex loading conditions at the integration point level, facilitating the testing and validation of constitutive law implementations without the need for a finite element solver.

1 Pure tension/compression

Figure A.1 (top) displays a typical response obtained with the anisotropic damage model under tension and compression. The parameters used for this test are the ones proposed in (Desmorat, 2015), *i.e.*, $\{E, \nu, \kappa_0, S, s, B\} = \{37\,000\,\text{MPa},\ 0.2,\ 9e{-}5,\ 1.45e{-}4,\ 4.9,\ 5/3\}$. The tension–compression dissymmetry behavior is illustrated in Figure A.1 (top-right). This dissymmetry arises due to micro-cracks developing as a consequence of extensions perpendicular to the applied load, induced by the Poisson's effect. As a result, damage variable components evolve more slowly under compression conditions.

Figure A.1 (bottom) depicts the corresponding evolution of the damage variable under tension and compression. In uniaxial tension along x, micro-cracks develop perpendicular to the applied load, as qualitatively represented in Figure A.1 (bottom-left). Consequently, the damage component D_{xx} rapidly evolves to unity, reflecting the direct tension applied in this direction. Meanwhile, due to Poisson's effect, shrinkage occurs on y and z (resulting in negative strains), causing the damage components D_{yy} and D_{zz} to remain unchanged. In contrast, uniaxial compression along x leads to micro-cracks developing parallel to the applied load, as illustrated in Figure A.1 (bottom-right). Extensions (resulting in positive strains) appear on y and z, causing the damage component D_{xx} to remain constant. The damage principal directions align with y and z but are associated with indirect extensions. Consequently, D_{yy} and D_{zz} are equal and evolve much more slowly than in the direct tension case.

2 Non-proportional loading

Non-proportional loading is simulated here to illustrate one of the advantages of employing the anisotropic damage model over an isotropic one. The total loading time is discretized into 2000 pseudo-time steps. A non-proportional load is applied, initially imposing an increasing strain component ε_{xx} until step 500 (see Figure B.1). Subsequently, an unloading phase occurs until step 1000, where $\varepsilon_{xx} = 0$ and $\sigma_{xx} = 0$ (see Figure B.1). From step 1000 until 2000 (end of the simulation), an increasing strain component ε_{yy} is applied (depicted by the red curve in Figure B.1), with no conditions imposed on the other components.

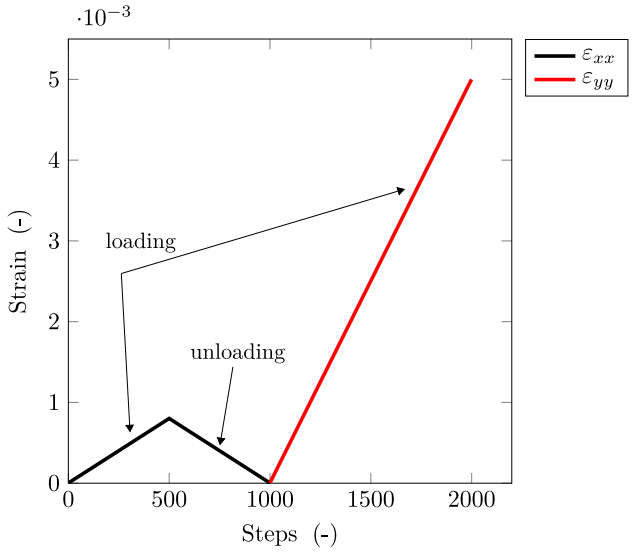

Figure B.1 • Local models – Non-proportional strains applied at the quadrature point.

Isotropic vs anisotropic models. The stress–strain response obtained with the isotropic model is shown in Figure B.2 (top-left). Elastic parameters are consistent with the ones previously used, $\{E, \nu\} = \{37\,000 \text{ MPa}, 0.2\}$. Moreover, $\{\kappa_0, B_t\} = \{1 \times 10^{-4}, 1000\}$, which are typically used for the isotropic damage evolution considered here. Figure B.2 (top-right) illustrates that the response follows the same effective modulus during unloading on x and loading on y. This is expected since, once damaged, all components of the effective Hooke's tensor $\tilde{\mathbb{E}}^{\text{iso}}$ are affected by the same factor $(1 - D)$. Consequently, $\tilde{\mathbb{E}}^{\text{iso}}$ remains isotropic.

On the contrary, the Hooke's tensor evolves from isotropic to orthotropic in the case of the tensorial damage model used here. The stress–strain response for the loading case presented is depicted in Figure B.2 (bottom-left). For comparison purposes, elastic material parameters are kept consistent with those used for the isotropic model. The other parameters are taken as in 4.2. The response does not follow the same effective modulus during reloading on the y direction, reflecting the induced anisotropy due to damage. The effective Hooke's tensor components evolve differently as damage takes place. For instance, from the expression of the effective Hooke's tensor (Eq. (5.28)), one

observes that the components:

$$\tilde{E}_{1111} = 2G\left[H_{11}^{-1}H_{11}^{-1} - \frac{H_{11}^{-2}H_{11}^{-2}}{\operatorname{tr}\mathbf{H}^{-2}}\right] + \frac{3K}{\operatorname{tr}\mathbf{H}^{2}} \qquad \tilde{E}_{2222} = 2G\left[H_{22}^{-1}H_{22}^{-1} - \frac{H_{22}^{-2}H_{22}^{-2}}{\operatorname{tr}\mathbf{H}^{-2}}\right] + \frac{3K}{\operatorname{tr}\mathbf{H}^{2}} \tag{2.1}$$

are naturally different once damage occurs. As illustrated in Figure B.2 (bottom-right), the components $\tilde{E}_{1111}$ and $\tilde{E}_{2222}$ are initially the same in the elastic phase (*i.e.*, when the material is isotropic). However, they evolve differently as a function of the damage state. This induced anisotropic behavior is essential for accurately capturing the anisotropic nature of non-local interactions, which is represented in this work by a damage-dependent Riemannian metric.

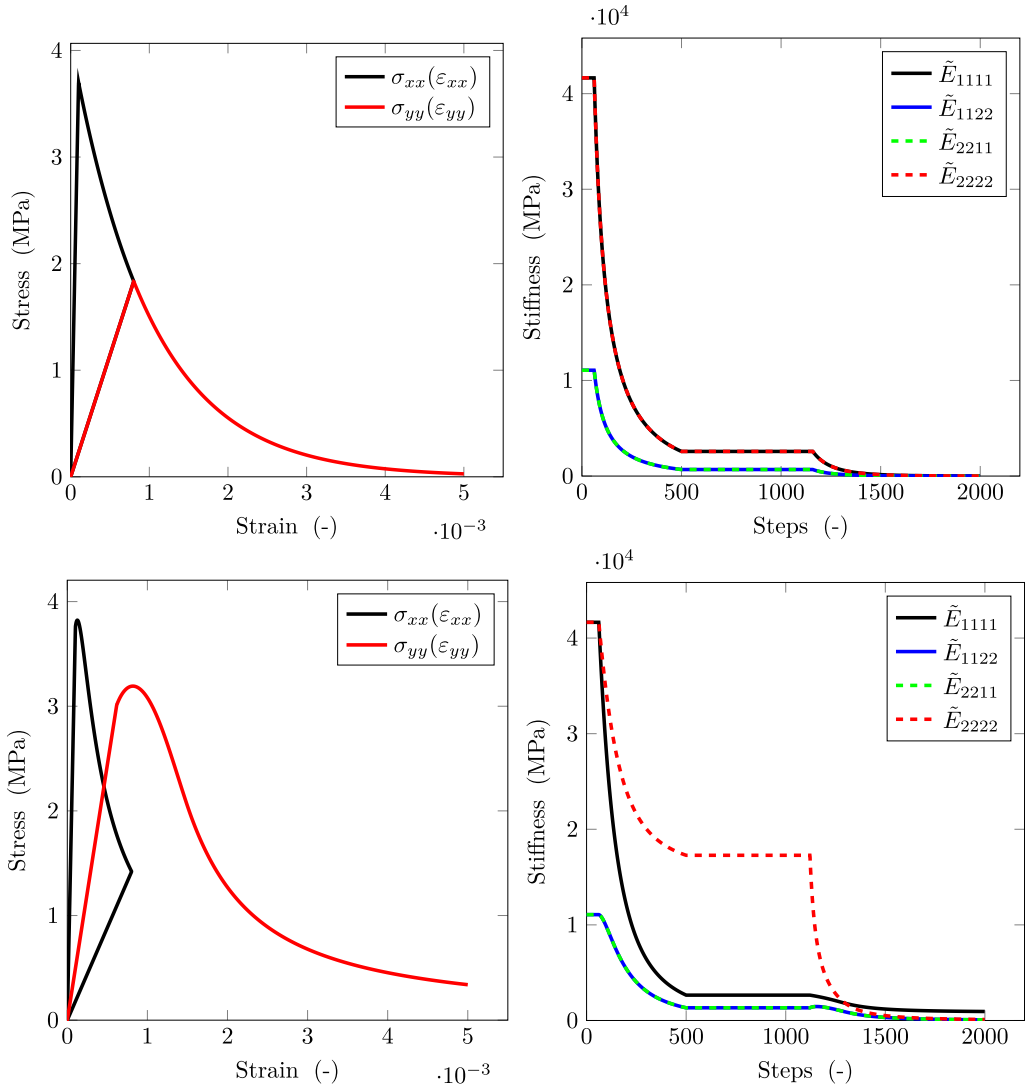

Figure B.2 • Local models – Isotropic model: stress–strain response during non-proportional loading (top-left) and evolution of $\tilde{\mathbb{E}}^{\text{iso}}$ components (top-right). Desmorat's model: stress–strain response during non-proportional loading (bottom-left) and evolution of $\tilde{\mathbb{E}}$ components (bottom-right).

C

Partitioned path-following algorithm for CMOD control

After assembly, the finite element problem can be written in matrix format such as the equilibrium reads:

$$\mathbf{K}_{uu}\mathbf{d} = \mathbf{F} \tag{0.1}$$

where $\mathbf{K}_{uu}$ and $\mathbf{F}$ are respectively the assembled stiffness matrix from the bi-linear and linear forms of equation 5.42. The unknown displacements vector is denoted $\mathbf{d}$. Similarly, the weak form of the gradient problem reads:

$$\mathbf{K}_{ee}\mathbf{e} = \mathbf{F}_e \tag{0.2}$$

where $\mathbf{e}$ is the vector of the nodal non-local equivalent strain unknowns. The bi-linear and linear forms from equation 5.44 lead to the construction of $\mathbf{K}_{ee}$ and $\mathbf{F}_e$, respectively. Dirichlet boundary conditions are considered within the penalization method, such as one has:

$$\left(\mathbf{K}_{uu} + \beta \mathbf{1}_L \mathbf{1}_L^T\right)\mathbf{d} = \mathbf{F} + \beta u_L^d \mathbf{1}_L \tag{0.3}$$

where β is a terrible giant value, as named in `FreeFem` solver. The column vector $\mathbf{1}_L$ contains a 1 for the L-nth degree of freedom and zeros elsewhere. The corresponding imposed displacement value is u_L^d.

For indirect control, an additional variable γ is introduced to control the amplitude of the applied displacements, such as $u_L^d = 1 \times \gamma$, with γ a new unknown of the problem. Therefore, a new equation must be added, which is related to the control condition to be satisfied, such as:

$$P(\gamma, \mathbf{d}) = 0 \tag{0.4}$$

A partitioned method is used, such as $\mathbf{d} = \mathbf{d}_{\mathrm{I}} + \gamma \mathbf{d}_{\mathrm{II}}$. Given the known solution $(\mathbf{d}_n, \gamma_n, \mathbf{e}_n)$ at pseudo-time step n, one searchs for $(\mathbf{d}_{n+1}, \gamma_{n+1}, \mathbf{e}_{n+1})$. The control conditions is written in terms of CMOD $= u^x(B) - u^x(A)$, where u^x denotes the x component of the displacement field.

For a given iteration and under the CMOD control for the three-point bending problem studied here, the condition rewrites:

$$\begin{aligned} P(\gamma, \mathbf{d}) &= \mathrm{CMOD}_{n+1} - \mathrm{CMOD}_n - \Delta\tau \\ &= \left[\mathbf{d}^x_{n+1}(B) - \mathbf{d}^x_{n+1}(A)\right] - \left[\mathbf{d}^x_n(B) - \mathbf{d}^x_n(A)\right] - \Delta\tau \\ &= \left[\mathbf{d}^x_{\mathrm{I},n+1}(B) + \gamma_{n+1}\mathbf{d}^x_{\mathrm{II},n+1}(B) - \mathbf{d}^x_{\mathrm{I},n+1}(A) - \gamma_{n+1}\mathbf{d}^x_{\mathrm{II},n+1}(A)\right] - \left[\mathbf{d}^x_n(B) - \mathbf{d}^x_n(A)\right] - \Delta\tau \\ &= \gamma_{n+1}\left[\mathbf{d}^x_{\mathrm{II},n+1}(B) - \mathbf{d}^x_{\mathrm{II},n+1}(A)\right] + \left[\mathbf{d}^x_{\mathrm{I},n+1}(B) - \mathbf{d}^x_{\mathrm{I},n+1}(A)\right] - \left[\mathbf{d}^x_n(B) - \mathbf{d}^x_n(A)\right] - \Delta\tau \end{aligned} \tag{0.5}$$

and finally, the loading multiplier reads:

$$\gamma_{n+1} = \frac{\Delta\tau - \left[\mathbf{d}^x_{\mathrm{I},n+1}(B) - \mathbf{d}^x_{\mathrm{I},n+1}(A)\right] + \left[\mathbf{d}^x_n(B) - \mathbf{d}^x_n(A)\right]}{\left[\mathbf{d}^x_{\mathrm{II},n+1}(B) - \mathbf{d}^x_{\mathrm{II},n+1}(A)\right]} \tag{0.6}$$

Here $\mathbf{d}^x(\bullet)$ denotes the degree of freedom associated to $u_x(\bullet)$ and $\Delta\tau$ is the step length parametrizing the equilibrium path. For each iteration $k+1$, the partitioned staggered global problem is then solved in five steps:

(i) Obtain $\mathbf{d}^{k+1}_{\mathrm{I},n+1}$ by solving $\mathbf{K}^k_{uu,n+1}\mathbf{d}^{k+1}_{\mathrm{I},n+1} = \mathbf{F}$

(ii) Obtain $\mathbf{d}^{k+1}_{\mathrm{II},n+1}$ by solving $\left(\mathbf{K}^k_{uu,n+1} + \beta\mathbf{1}_L\mathbf{1}_L^T\right)\mathbf{d}^{k+1}_{\mathrm{II},n+1} = 1 \times \beta\mathbf{1}_L$

(iii) Obtain γ^{k+1}_{n+1} from equation 0.6 and compute $\mathbf{d}^{k+1}_{n+1} = \mathbf{d}^{k+1}_{\mathrm{I},n+1} + \gamma^{k+1}_{n+1}\mathbf{d}^{k+1}_{\mathrm{II},n+1}$.

(iv) With $\mathbf{d}^{k+1}_{n+1}$, calculate the vector related to the local equivalent field $\mathbf{F}^{k+1}_{e,n+1}$. Then, solve for $\mathbf{e}^{k+1}_{n+1}$ from $\mathbf{K}_{ee,n}\mathbf{e}^{k+1}_{n+1} = \mathbf{F}^{k+1}_{e,n+1}$.

(v) Check for convergence.

D

Extended abstract in french

1 Contexte général et motivations

Prédire avec précision la réponse des structures soumises à des scénarios de chargement complexes est une tâche difficile en ingénierie. En pratique, les codes de conception se concentrent sur la capacité portante et l'analyse limite, ce qui implique l'utilisation de facteurs de sécurité. Par conséquent, la description fine des mécanismes de défaillance et de la dissipation d'énergie est souvent simplifiée ou complètement négligée. Cette approche est généralement acceptée principalement pour des raisons pragmatiques : les systèmes conçus peuvent généralement résister aux sollicitations pendant leur durée de vie. Cependant, étant donné que les capacités réelles sont, en fait, inconnues, un surdimensionnement devient inévitable.

Dans le contexte du changement climatique, le surdimensionnement est directement liée à la consommation de ressources et, donc, aux émissions de gaz à effet de serre (GES). IEA (2019) a estimé qu'en 2018, 11% de l'énergie utilisée et des émissions de CO2 liées aux processus provenaient de la fabrication de matériaux et de produits de construction (par exemple, ciment, acier et verre). Nous devons donc réduire l'excès de matériau utilisé sur les chantiers de construction et dans l'industrie. Par conséquent, une meilleure compréhension de la dégradation des matériaux (c'est-à-dire l'apparition de micro et macro-fissures et leur influence sur les propriétés des matériaux) et de la durabilité devient indispensable. En particulier, étudier la nucléation et la propagation des fissures est essentiel pour évaluer les performances structurelles de manière réaliste. C'est déjà le cas pour l'analyse des structures sensibles, où il y a peu de marge d'erreur. Par exemple, l'ouverture des fissures est une donnée essentielle pour l'estimation du taux de fuite à travers les parois de confinement des centrales nucléaires. Dans ce contexte, les prévisions doivent être plus précises et fournir des informations utiles sur la durée de vie des ouvrages. Par conséquent, l'étude de la dégradation des matériaux joue un rôle important dans ces estimations.

La recherche sur les mécanismes de fissuration a également attiré l'attention dans d'autres problèmes d'ingénierie liés à la transition énergétique. On peut citer la fragilisation par l'hydrogène dans les métaux (transition d'un comportement ductile à quasi-fragile ou fragile), impliquant des risques de sécurité sévères dans son transport et son stockage,

ou l'étude des réseaux de fractures dans les systèmes géothermiques. Enfin, mais non des moindres, l'étude des mécanismes de fracture joue également un rôle majeur dans la compréhension de la mécanique des glaces. En particulier, des modèles précis décrivant la dégradation deviennent essentiels dans l'estimation de la perte de masse des calottes glaciaires, ce qui contribue considérablement à l'élévation du niveau de la mer.

Les matériaux quasi-fragiles sont présents presque partout, et certains exemples sont le béton et le mortier, certaines roches, les céramiques résistantes, la maçonnerie, la glace de mer, le bois et bien d'autres. La dégradation des propriétés mécaniques les caractérise principalement en raison de la fissuration lorsqu'ils sont soumis à une charge. Il est donc indéniable qu'il est nécessaire de décrire leur comportement.

2 Approche scientifique et objectifs

L'objectif principal de cette thèse est de fournir des développements théoriques et numériques concernant la modélisation des mécanismes de dégradation dans les milieux quasi-fragiles. L'objectif est de fournir, *in fine*, un cadre numérique fiable et robuste pour prédire la fissuration dans les simulations des structures. À cette fin, nous nous limitons à étudier uniquement la dégradation des matériaux induite par le chargement mécanique.

La mécanique des milieux continus est utilisée, de sorte que le milieu est décrit sur la base d'un volume élémentaire représentatif, dont la taille est suffisamment plus grande que l'hétérogénéité du matériau et plus petite que la structure considérée. Ainsi, le comportement du matériau est défini de manière homogénéisée suivant un cadre thermodynamique cohérent. La dissipation d'énergie et les processus irréversibles associés sont étudiés suivant les principes de la thermodynamique, ce qui peut garantir qu'une relation de comportement est physiquement admissible. Par conséquent, la dégradation des propriétés mécaniques est modélisée par une variable interne supplémentaire appelée endommagement (Kachanov, 1958; Rabotnov, 1969; Lemaitre, 1971; Mazars, 1984b). En conséquence, les micro-fissures sont décrites implicitement dans le volume élémentaire représentatif, et la rupture est considérée comme une conséquence d'un niveau de dégradation très important. Les modèles d'endommagement isotrope et anisotrope sont considérés dans cette thèse.

Les simulations sont considérées dans le cadre de l'analyse par éléments finis. En raison de la dépendance au maillage bien connue et inévitable, des techniques de régularisation doivent être envisagées, étant donné que la localisation des déformations ne peut pas être décrite avec des modèles d'edommagement locaux (Bažant & Oh, 1983b; Bazant et al., 1984). Cette dissertation travaille avec des modèles d'endommagement non local de types intégral et gradient, qui agissent comme limiteurs de localisation (Pijaudier-Cabot & Bažant, 1987; Peerlings et al., 1996a). L'étude de ces techniques est au cœur des développements décrits dans ce travail. Le concept d'un milieux continu non-local introduit l'idée que la relation de comportement en un point donné est une fonction de ce qui se passe dans tout le domaine. Les interactions de voisinage sont donc utilisées pour enrichir la description du milieux en ajoutant des gradients ou une moyenne spatiale

basée sur une longueur caractéristique du matériau (Bažant & Jirásek, 2002). L'hypothèse principale est que la variable d'endommagement est supposée croître en fonction d'une déformation équivalente non locale (Jirásek, 1998).

Bien que la régularisation de la réponse permette de retrouver l'objectivité vis-à-vis du maillage, les modèles d'endommagement non-local classiques présentent certaines incohérences physiques et ne peuvent pas décrire avec précision tous les phénomènes physiques liés à la fissuration (Geers et al., 1998; Simone et al., 2004; Krayani et al., 2009; Giry et al., 2011). Certains de ces aspects sont étudiés en détail dans ce travail, soulignant la nécessité de considérer des approches non locales avec interactions évolutives. Nous nous concentrons principalement sur l'approche Eikonal à gradient implicite (Desmorat et al., 2015b). Avec l'équilibre, elle considère une équation différentielle supplémentaire de type Helmholtz à résoudre pour la déformation équivalente non locale. À partir d'une théorie des milieux micromorphes basée sur la géométrie différentielle, une nouvelle dérivation de ce modèle est proposée, qui vérifie l'inégalité de Clausius-Duhem. L'idée principale est que l'endommagement est supposé courber l'espace où se produisent les interactions non locales. Une telle déformation de l'espace est représentée par l'introduction d'une métrique riemannienne dépendante de l'endommagement. Nous proposons de voir cette métrique basée sur une analyse qualitative de la manière dont le développement des micro-fissures modifie les interactions du milieu.

La formulation variationnelle (forme faible) du problème couplé est dérivée pour le cas générique d'un tenseur de dommage anisotrope d'ordre deux. Un schéma point fixe est appliqué à la formulation variationnelle au niveau global pour résoudre le problème non linéaire couplé, tandis qu'une procédure itérative de Newton-Raphson est utilisée pour l'intégration du comportement aux points de quadrature. Les simulations numériques fournies considèrent à la fois l'endommagement isotrope et anisotrope. Sur la base des concepts de la théorie de la représentation tensorielle (Boehler, 1987), nous proposons de considérer la métrique comme un tenseur de structure modifiant les interactions non locales. Les polynômes homogènes correspondants des tenseurs sont utilisés pour introduire un outil de visualisation utilisant des ellipses. Il met en évidence comment l'endommagement anisotrope induit naturellement des interactions non locales évolutives anisotropes. Les résultats numériques sont fournis et comparés aux données expérimentales existantes de la littérature. La discussion se concentre sur les capacités du modèle à représenter des mécanismes de fissuration réalistes et sur son application possible aux structures à grande échelle.

3 Organisation du manuscrit

Cette thèse est organisée en deux parties principales et cinq chapitres. La première partie est consacrée à la présentation d'une introduction générale aux principaux concepts étudiés dans ce travail. La deuxième partie rassemble les principales contributions de cette dissertation au sujet en termes de dérivations théoriques, de formulations, de développements numériques et de résultats.

Les deux premiers chapitres sont présentés dans la première partie. Chapter 1 fournit

d'abord un aperçu des observations expérimentales tirées de la littérature concernant les matériaux quasi-fragiles. Les observations décrites soulignent la nécessité de mieux comprendre les mécanismes de dégradation de ces matériaux. Deuxièmement, les stratégies de modélisation des fissures les plus courantes sont passées en revue. Une attention particulière est accordée à la mécanique de l'endommagement, qui est la base de tous les développements de cette dissertation. Les concepts essentiels de cette théorie sont décrits, et quelques modèles d'endommagement sont finalement présentés.

Chapter 2 fournit une revue de la littérature sur la théorie non locale de l'endommagement. Il est souligné que, du point de vue de la structure, les simulations par éléments finis avec des modèles d'endommagement locaux ne peuvent pas fournir des résultats significatifs. Les éléments critiques de la localisation des déformations et de la bifurcation sont introduits pour souligner la nécessité de régulariser la solution. On fournit une discussion sur la non-localité dans un sens large et sur la manière dont le terme « non local » est compris par différentes communautés. Ensuite, les approches classiques intégrales et à gradient sont décrites dans le cadre de la mécanique de l'endommagement. Le concept d'interactions non locales entre les points d'un milieu est introduit. Il est expliqué pourquoi des interactions évolutives et éventuellement anisotropes doivent être envisagées. Une attention particulière est accordée à la formulation Eikonale. Enfin, d'autres approches de régularisation bien connues sont brièvement décrites.

Les trois derniers chapitres sont présentés dans la deuxième partie. Chapters 3 and 4 sont composés d'articles de revues publiés, avec quelques développements, illustrations et modifications supplémentaires pour s'adapter au style et au suivi global de cette thèse. Il en va de même pour Chapter 5, sauf qu'au moment de la soumission de ce manuscrit, l'article correspondant est en cours de révision.

Chapter 3 se concentre sur les développements théoriques et numériques unidimensionnels concernant les modèles d'endommagement non locaux (Ribeiro Nogueira et al., 2022a). Il commence par une analyse de la dispersion des ondes sur les modèles d'endommagement locaux et à gradient. Par la suite, les effets de bord et la diffusion de l'endommagement sont étudiés en analysant un test numérique d'écaillage. Un code éléments finis en dynamique explicite est développé à cet effet. Enfin, les approches classiques et évolutives des interactions non locales sont comparées.

Chapter 4 fournit une dérivation alternative du modèle d'endommagement Eikonal à gradient (Ribeiro Nogueira et al., 2024a). Comme point de départ, il est proposé de considérer l'approche micromorphe basée sur une description géométrique du problème. Certains concepts de géométrie différentielle sont brièvement introduits, et la forme forte du modèle Eikonal, avec sa condition aux limites, est dérivée. Quelques commentaires supplémentaires sur l'analyse de la bifurcation des modèles à gradient sont fournis, établissant une relation avec les résultats présentés dans l'analyse de la dispersion des ondes du Chapter 3. Enfin, la mise en œuvre numérique de l'approche Eikonale à gradient est décrite, et ses propriétés de régularisation sont évaluées à travers des simulations numériques 2D avec endommagement isotrope.

Enfin, Chapter 5 traite de l'extension du modèle Eikonal à gradient au cas de l'endommagement anisotrope. Le modèle est couplé à un comportement prenant en compte un tenseur d'endommagement d'ordre deux. Un comportement spécifique en contraintes

planes est dérivé pour les simulations 2D. La visualisation des ellipsoïdes représentant l'endommagement et la métrique illustre comment le comportement anisotrope induit naturellement des interactions anisotropes évolutives. La solution numérique du problème couplé est détaillée, tant au niveau de la structure qu'au niveau des points de quadrature. Une discussion complète sur les avantages de tels modèles est fournie, présentant des résultats structurels bien connus dans des contextes bidimensionnels et tridimensionnels.

Bibliography

Aifantis, E. C. (1984). On the Microstructural Origin of Certain Inelastic Models. *Journal of Engineering Materials and Technology*, *106*(4), 326–330. https://doi.org/10.1115/1.3225725 (cit. on pp. 51, 56)

Aifantis, E. C. (1987). The physics of plastic deformation. *International Journal of Plasticity*, *3*(3), 211–247. https://doi.org/10.1016/0749-6419(87)90021-0 (cit. on p. 56)

Alam, S. Y., Saliba, J., & Loukili, A. (2014). Fracture examination in concrete through combined digital image correlation and acoustic emission techniques. *Construction and Building Materials*, *69*, 232–242. https://doi.org/10.1016/j.conbuildmat.2014.07.044 (cit. on p. 15)

Alfaiate, J., Wells, G., & Sluys, L. (2002). On the use of embedded discontinuity elements with crack path continuity for mode-I and mixed-mode fracture. *Engineering Fracture Mechanics*, *69*(6), 661–686. https://doi.org/10.1016/S0013-7944(01)00108-4 (cit. on p. 20)

Allix, O. (2001). A composite damage meso-model for impact problems. *Composites Science and Technology*, *61*(15), 2193–2205. https://doi.org/10.1016/S0266-3538(01)00113-0 (cit. on p. 34)

Allix, O., & Deü, J. (1997a). Delay-damage modelling for fracture prediction of laminated composites under dynamic loading. *Engineering Transactions*, *45(1)*, 29–46 (cit. on p. 180).

Allix, O., & Deü, J.-F. (1997b). Delayed-Damage Modelling for Fracture Prediction of Laminated Composites under Dynamic Loading. *Engineering Transactions*, *45*(1), 29. https://doi.org/10.24423/engtrans.680.1997 (cit. on p. 34)

Allix, O., Feissel, P., & Thévenet, P. (2003). A delay damage mesomodel of laminates under dynamic loading: Basic aspects and identification issues. *Computers & Structures*, *81*(12), 1177–1191 (cit. on p. 180).

Alsahly, A., Callari, C., & Meschke, G. (2018). An algorithm based on incompatible modes for the global tracking of strong discontinuities in shear localization analyses. *Computer Methods in Applied Mechanics and Engineering*, *330*, 33–63. https://doi.org/10.1016/j.cma.2017.10.014 (cit. on p. 180)

Alshibli, K. A., & Sture, S. (2000). Shear Band Formation in Plane Strain Experiments of Sand. *Journal of Geotechnical and Geoenvironmental Engineering*, *126*(6), 495–503. https://doi.org/10.1061/(ASCE)1090-0241(2000)126:6(495) (cit. on p. 44)

Amani, J. (2023). *A transient-anisotropic gradient-enhanced damage model with displacement smoothing for failure analysis in quasi-brittle materials* (Doctoral dissertation). Technische Universiteit Delft. (Cit. on p. 143).

Andrieux, S., Bamberger, Y., & Marigo, J.-J. (1986). A model of micro-cracked material for concretes and rocks. *Journal of Theoretical and Applied Mechanics*, *5*(3), 471–513 (cit. on p. 9).

Anthoine, A., Magonette, G., & Magenes, G. (1995). Shear-compression testing and analysis of brick masonry walls. *Tenth European Conference on Earthquake Engineering*, *3*, 1657–1662 (cit. on p. 8).

Armero, F., & Callari, C. (1999). AN ANALYSIS OF STRONG DISCONTINUITIES IN A SATURATED PORO-PLASTIC SOLID, 27 (cit. on p. 180).

Arslan, A., Ince, R., & Karihaloo, B. L. (2002). Improved Lattice Model for Concrete Fracture. *Journal of Engineering Mechanics*, *128*(1), 57–65. https://doi.org/10.1061/(ASCE)0733-9399(2002)128:1(57) (cit. on p. 18)

Askes, H., & Sluys, L. (2002). Explicit and implicit gradient series in damage mechanics. *European Journal of Mechanics - A/Solids*, *21*(3), 379–390. https://doi.org/10.1016/S0997-7538(02)01214-7 (cit. on p. 58)

Azinpour, E., Ferreira, J. P. S., Parente, M. P. L., & de Sa, J. C. (2018). A simple and unified implementation of phase field and gradient damage models. *Advanced Modeling and Simulation in Engineering Sciences*, *5*(1), 15. https://doi.org/10.1186/s40323-018-0106-7 (cit. on p. 87)

Babuška, I., & Melenk, J. M. (1997). THE PARTITION OF UNITY METHOD. *International Journal for Numerical Methods in Engineering*, *40*(4), 727–758. https://doi.org/10.1002/(SICI)1097-0207(19970228)40:4<727::AID-NME86>3.0.CO;2-N (cit. on p. 21)

Badri, M. A., & Rastiello, G. (2023). Hpc finite element solvers for phase-field models for fracture in solids In *Numerical modeling strategies for sustainable concrete structures* (P. Rossi & J.-L. Tailhan, Eds.). Cham, Springer International Publishing. 22–32. (Cit. on pp. 132, 134, 155, 180).

Badri, M. A., Rastiello, G., & Foerster, E. (2021). Preconditioning strategies for vectorial finite element linear systems arising from phase-field models for fracture mechanics. *Computer Methods in Applied Mechanics and Engineering*, *373*, 113472 (cit. on pp. 132, 134, 155, 180).

Barenblatt, G. (1962). The Mathematical Theory of Equilibrium Cracks in Brittle Fracture. In *Advances in Applied Mechanics* (pp. 55–129). Elsevier. https://doi.org/10.1016/S0065-2156(08)70121-2. (Cit. on pp. 21, 22)

Bary, B., Bournazel, J.-P., & Bourdarot, E. (2000). Poro-Damage Approach Applied to Hydro-Fracture Analysis of Concrete. *Journal of Engineering Mechanics*, *126*(9), 937–943. https://doi.org/10.1061/(ASCE)0733-9399(2000)126:9(937) (cit. on p. 180)

Batdorf, S., & Budianski, B. (1949). A mathematical theory of plasticity based on the concept of slip. *Technical Note No.1871. National Advisory Committee for Aeronautics, Washington, DC.* (cit. on p. 39).

Baxevanis, T., Pijaudier-Cabot, G., & Dufour, F. (2008). Bifurcation and creep effects in a viscoelastic non-local damageable continuum. *European Journal of Mechanics - A/Solids*, *27*(4), 548–563. https://doi.org/10.1016/j.euromechsol.2007.11.009 (cit. on p. 129)

Bazant, Z., Belytschko, T. B., & Chang, T.-P. (1984). Continuum theory for strain-softening. *Journal of Engineering Mechanics*, *110*, 1666–1692 (cit. on pp. 2, 48, 51, 56, 196).

Bažant, Z., & Oh, B. (1983a). Microplane model for fracture analysis of concrete structures. *Proc. Symposium on the Interaction of Non-nuclear Munitions with Structures, held at US Air Force Academy, Colorado Springs. (publ. by McGregor and Werner, Washington DC)* (cit. on pp. 39, 142).

Bažant, Z., & Prat, P. C. (1988). Microplane model for brittle-plastic material: I. theory. *ASCE J. Eng. Mech*, *114*, 1672–1688 (cit. on pp. 39, 142).

Bažant, Z. P., & Pfeiffer, P. A. (1986). Shear fracture tests of concrete. *Materials and Structures*, *19*(2), 111–121. https://doi.org/10.1007/BF02481755 (cit. on p. 16)

Bažant, Z. P., & Pfeiffer, P. A. (1987). Determination of Fracture Energy from Size Effect and Brittleness Number. *ACI Materials Journal*, *84*(6). https://doi.org/10.14359/2526 (cit. on p. 16)

Bažant, Z. P. (1976). Instability, Ductility, and Size Effect in Strain-Softening Concrete. *Journal of the Engineering Mechanics Division*, *102*(2), 331–344. https://doi.org/10.1061/JMCEA3.0002111 (cit. on p. 48)

Bažant, Z. P. (1984a). Microplane Model for Strain-controlled Inelastic Behaviour. In *Mechanics of Engineering Materials* (C. S. Desai and R. H. Gallagher, pp. 46–56). John Wiley & Sons Ltd. (Cit. on pp. 39, 142).

Bažant, Z. P. (1984b). Size Effect in Blunt Fracture: Concrete, Rock, Metal. *Journal of Engineering Mechanics*, *110*(4), 518–535. https://doi.org/10.1061/(ASCE)0733-9399(1984)110:4(518) (cit. on pp. 15, 16)

Bažant, Z. P. (1991). Why Continuum Damage is Nonlocal: Micromechanics Arguments. *Journal of Engineering Mechanics*, *117*(5), 1070–1087. https://doi.org/10.1061/(ASCE)0733-9399(1991)117:5(1070) (cit. on p. 59)

Bažant, Z. P. (1993). Scaling laws in mechanics of failure. *Journal of Engineering Mechanics*, *119*(9), 1828–1844. https://doi.org/10.1061/(ASCE)0733-9399(1993)119:9(1828) (cit. on p. 16)

Bažant, Z. P. (1994). Nonlocal damage theory based on micromechanics of crack interactions. *Journal of Engineering Mechanics*, *120*, 593–617 (cit. on p. 59).

Bažant, Z. (2002). *Scaling of structural strength*. Hermes Penton Science. (Cit. on pp. 15, 16).

Bažant, Z. P. (2019). Design of quasibrittle materials and structures to optimize strength and scaling at probability tail: An apercu. *Proceedings of the Royal Society A: Mathematical, Physical and Engineering Sciences*, *475*(2224), 20180617. https://doi.org/10.1098/rspa.2018.0617 (cit. on pp. 8, 16)

Bažant, Z. P., & Belytschko, T. B. (1985). Wave Propagation in a Strain-Softening Bar:Exact Solution. *Journal of Engineering Mechanics*, *111*(3), 381–389. https://doi.org/10.1061/(ASCE)0733-9399(1985)111:3(381) (cit. on p. 48)

Bažant, Z. P., Dönmez, A. A., & Nguyen, H. T. (2022a). Précis of gap test results requiring reappraisal of line crack and phase-field models of fracture mechanics. *Engineering Structures*, *250*, 113285 (cit. on pp. 107, 147, 167).

Bažant, Z. P., & Gambarova, P. G. (1984). Crack Shear in Concrete: Crack Band Microplane Model. *Journal of Structural Engineering*, *110*(9), 2015–2035. https://doi.org/10.1061/(ASCE)0733-9445(1984)110:9(2015) (cit. on pp. 9, 39, 142)

Bažant, Z. P., & Jirásek, M. (2002). Nonlocal Integral Formulations of Plasticity and Damage: Survey of Progress. *Journal of Engineering Mechanics*, *128*(11), 1119–1149. https://doi.org/10.1061/(ASCE)0733-9399(2002)128:11(1119) (cit. on pp. 2, 48, 51, 52, 58, 197)

Bažant, Z. P., Luo, W., Chau, V. T., & Bessa, M. A. (2016). Wave Dispersion and Basic Concepts of Peridynamics Compared to Classical Nonlocal Damage Models. *Journal of Applied Mechanics*, *83*(11), 111004. https://doi.org/10.1115/1.4034319 (cit. on p. 68)

Bažant, Z. P., Nguyen, H. T., & Abdullah Dönmez, A. (2022b). Critical Comparison of Phase-Field, Peridynamics, and Crack Band Model M7 in Light of Gap Test and Classical Fracture Tests. *Journal of Applied Mechanics*, *89*(6), 061008. https://doi.org/10.1115/1.4054221 (cit. on pp. 66, 68, 147, 148)

Bažant, Z. P., & Nguyen, H. T. (2023). Proposal of m-Index for Rating Fracture and Damage Models by Their Ability to Represent a Set of Distinctive Experiments.

Journal of Engineering Mechanics, *149*(8), 04023047. https://doi.org/10.1061/JENMDT.EMENG-6887 (cit. on pp. 68, 147, 181)

Bažant, Z. P., & Oh, B. H. (1983b). Crack band theory for fracture of concrete. *Matériaux et Constructions*, *16*(3), 155–177. https://doi.org/10.1007/BF02486267 (cit. on pp. 2, 23, 24, 47, 51, 196)

Bažant, Z. P., & Pijaudier-Cabot, G. (1988). Nonlocal Continuum Damage, Localization Instability and Convergence. *Journal of Applied Mechanics*, *55*(2), 287–293. https://doi.org/10.1115/1.3173674 (cit. on pp. 51, 54)

Bažant, Z. P., & Planas, J. (2019). *Fracture and Size Effect in Concrete and Other Quasibrittle Materials* (1st ed.). Routledge. https://doi.org/10.1201/9780203756799. (Cit. on pp. 15, 16)

Bažant, Z. P., Tabbara, M. R., Kazemi, M. T., & Pijaudier-Cabot, G. (1990). Random Particle Model for Fracture of Aggregate or Fiber Composites. *Journal of Engineering Mechanics*, *116*(8), 1686–1705. https://doi.org/10.1061/(ASCE)0733-9399(1990)116:8(1686) (cit. on p. 18)

Bažant, Z. P., Xiang, Y., & Prat, P. C. (1996). Microplane Model for Concrete. I: Stress-Strain Boundaries and Finite Strain. *Journal of Engineering Mechanics*, *122*(3), 245–254. https://doi.org/10.1061/(ASCE)0733-9399(1996)122:3(245) (cit. on pp. 39, 142)

Bazilevs, Y., Behzadinasab, M., & Foster, J. T. (2022). Simulating concrete failure using the Microplane (M7) constitutive model in correspondence-based peridynamics: Validation for classical fracture tests and extension to discrete fracture. *Journal of the Mechanics and Physics of Solids*, *166*, 104947. https://doi.org/10.1016/j.jmps.2022.104947 (cit. on p. 68)

Belytschko, T., Gracie, R., & Ventura, G. (2009). A review of extended/generalized finite element methods for material modeling. *Modelling and Simulation in Materials Science and Engineering*, *17*(4), 043001. https://doi.org/10.1088/0965-0393/17/4/043001 (cit. on p. 21)

Benallal, A., Billardon, R., & Geymonat, G. (1993). Bifurcation and Localization in Rate-Independent Materials. Some General Considerations. In Q. S. Nguyen (Ed.), *Bifurcation and Stability of Dissipative Systems* (pp. 1–44). Springer. https://doi.org/10.1007/978-3-7091-2712-4_1. (Cit. on pp. 45, 75)

Benallal, A., & Lemaitre, J. (1991). Localization Phenomena in Thermo-Elastoplasticity. In M. Życzkowski (Ed.), *Creep in Structures* (pp. 223–235). Springer Berlin Heidelberg. https://doi.org/10.1007/978-3-642-84455-3_28. (Cit. on p. 129)

Benallal, A., & Billardon, R. (1991). Hierarchy of Localization Phenomena Inside, at the Boundaries and Interfaces of Solids. In J.-P. Boehler & A. S. Khan (Eds.), *Anisotropy and Localization of Plastic Deformation* (pp. 39–42). Springer Netherlands. https://doi.org/10.1007/978-94-011-3644-0_9. (Cit. on pp. 45, 47)

Bernard, P. E., Moës, N., & Chevaugeon, N. (2012). Damage growth modeling using the Thick Level Set (TLS) approach: Efficient discretization for quasi-static loadings. *Computer Methods in Applied Mechanics and Engineering*, *233-236*, 11–27. https://doi.org/10.1016/j.cma.2012.02.020 (cit. on pp. 66, 67)

Berthaud, Y. (1991). Damage measurements in concrete via an ultrasonic technique. Part I Experiment. *Cement and Concrete Research*, *21*, 73–82. https://doi.org/https://doi.org/10.1016/0008-8846(91)90033-E (cit. on pp. 12, 147)

Bischoff, P. H., & Perry, S. H. (1991). Compressive behaviour of concrete at high strain rates. *Materials and Structures*, *24*(6), 425–450. https://doi.org/10.1007/BF02472016 (cit. on p. 8)

Bittencourt, T., Ingraffea, A., & L1orca, J. (1992). Simulation of arbitrary, cohesive crack propagation. In *Fracture mechanics of concrete structures*. Elsevier Science Publishing Co., Inc., New York, N.Y. (Cit. on p. 22).

Boehler, J. P. (1987). *Applications of Tensor Functions in Solid Mechanics* (J. P. Boehler, Ed.). Springer Vienna. https://doi.org/10.1007/978-3-7091-2810-7. (Cit. on pp. 3, 29, 146, 197)

Bogucka, J., Dębiński, J., Litewka, A., & Mesquita, A. (1998). Experimental verification of mathematical model for oriented damage of concrete. *Mecânica Experimental*, *3*, 11–18 (cit. on p. 12).

Borino, G., Fuschi, P., & Polizzotto, C. (1999). A Thermodynamic Approach to Nonlocal Plasticity and Related Variational Principles. *Journal of Applied Mechanics*, *66*(4), 952–963. https://doi.org/10.1115/1.2791804 (cit. on p. 106)

Bouchard, P., Bay, F., Chastel, Y., & Tovena, I. (2000). Crack propagation modelling using an advanced remeshing technique. *Computer Methods in Applied Mechanics and Engineering*, *189*(3), 723–742. https://doi.org/10.1016/S0045-7825(99)00324-2 (cit. on p. 19)

Bourdin, B., Francfort, G., & Marigo, J.-J. (2000). Numerical experiments in revisited brittle fracture. *Journal of the Mechanics and Physics of Solids*, *48*(4), 797–826. https://doi.org/10.1016/S0022-5096(99)00028-9 (cit. on pp. 52, 65, 177)

Bourdin, B. (2001). Filters in topology optimization. *International Journal for Numerical Methods in Engineering*, *50*(9), 2143–2158. https://doi.org/10.1002/nme.116 (cit. on p. 50)

Buades, A., Coll, B., & Morel, J. M. (2005a). A Review of Image Denoising Algorithms, with a New One. *Multiscale Modeling & Simulation*, *4*(2), 490–530. https://doi.org/10.1137/040616024 (cit. on p. 49)

Buades, A., Coll, B., & Morel, J.-M. (2005b). A non-local algorithm for image denoising In *2005 IEEE Computer Society Conference on Computer Vision and*

Pattern Recognition (CVPR'05). 60–65 vol. 2. https://doi.org/10.1109/CVPR.2005.38. (Cit. on p. 50)

Buades, A., Coll, B., & Morel, J.-M. (2008). Nonlocal Image and Movie Denoising. *International Journal of Computer Vision*, *76*(2), 123–139. https://doi.org/10.1007/s11263-007-0052-1 (cit. on p. 49)

Callari, C., & Armero, F. (2002). Finite element methods for the analysis of strong discontinuities in coupled poro-plastic media. *Computer Methods in Applied Mechanics and Engineering*, *191*(39-40), 4371–4400. https://doi.org/10.1016/S0045-7825(02)00374-2 (cit. on p. 180)

Callari, C., Armero, F., & Abati, A. (2010). Strong discontinuities in partially saturated poroplastic solids. *Computer Methods in Applied Mechanics and Engineering*, *199*(23-24), 1513–1535. https://doi.org/10.1016/j.cma.2010.01.002 (cit. on p. 180)

Camacho, G., & Ortiz, M. (1996). Computational modelling of impact damage in brittle materials. *International Journal of Solids and Structures*, *33*(20-22), 2899–2938. https://doi.org/10.1016/0020-7683(95)00255-3 (cit. on pp. 22, 98)

Capecchi, D., Ruta, G., & Trovalusci, P. (2010). From classical to Voigt's molecular models in elasticity. *Archive for History of Exact Sciences*, *64*(5), 525–559. https://doi.org/10.1007/s00407-010-0065-y (cit. on p. 53)

Carneiro, F. (1943). A new method for determining the tension stress in the concrete. In *Proceeedings 5th meet of association brazilian for standardization - abnt.* (Cit. on p. 9).

Carol, I., Jirásek, M., & Bažant, Z. (2001). A thermodynamically consistent approach to microplane theory. Part I. Free energy and consistent microplane stresses. *International Journal of Solids and Structures*, *38*(17), 2921–2931. https://doi.org/10.1016/S0020-7683(00)00212-2 (cit. on pp. 39, 40)

Cazes, F., Coret, M., Combescure, A., & Gravouil, A. (2009). A thermodynamic method for the construction of a cohesive law from a nonlocal damage model. *International Journal of Solids and Structures*, *46*(6), 1476–1490. https://doi.org/10.1016/j.ijsolstr.2008.11.019 (cit. on pp. 140, 180)

Cazes, F., & Moës, N. (2015). Comparison of a phase-field model and of a thick level set model for brittle and quasi-brittle fracture. *International Journal for Numerical Methods in Engineering*, *103*(2), 114–143. https://doi.org/10.1002/nme.4886 (cit. on p. 66)

Chaboche, J. (1982). The concept of effective stress applied to elasticity and to viscoplasticity in the presence of anisotropic damage. In *Mechanical Behavior of Anisotropic Solids / Comportment Méchanique des Solides Anisotropes: Proceedings of the Euromech Colloquium 115 Villard-de-Lans, June 19-22, 1979 / Colloque Euromech 115 Villard-de-Lans, 19-22 juin 1979* (pp. 737–760). Springer Netherlands. (Cit. on pp. 35, 142).

Chambart, M. (2009). *Endommagement anisotrope et comportement dynamique des structures en béton armé jusqu'à la ruine.* (Doctoral dissertation). École normale supérieure de Cachan - ENS Cachan. (Cit. on p. 152).

Chevaugeon, N., & Moës, N. (2022). Lipschitz regularization for fracture: The lip-field approach. *Computer Methods in Applied Mechanics and Engineering*, *402*, 115644. https://doi.org/10.1016/j.cma.2022.115644Getrightsandcontent (cit. on pp. 52, 67)

Chow, C. L., & Wang, J. (1987a). An anisotropic theory of continuum damage mechanics for ductile fracture. *Engineering Fracture Mechanics*, *27*(5), 547–558. https://doi.org/10.1016/0013-7944(87)90108-1 (cit. on p. 36)

Chow, C. L., & Wang, J. (1987b). An anisotropic theory of elasticity for continuum damage mechanics. *International Journal of Fracture*, *33*(1), 3–16. https://doi.org/10.1007/BF00034895 (cit. on p. 36)

Coleman, B. D., & Noll, W. (1963). The thermodynamics of elastic materials with heat conduction and viscosity. *Archive for Rational Mechanics and Analysis*, *13*(1), 167–178. https://doi.org/10.1007/BF01262690 (cit. on p. 28)

Comi, C., Mariani, S., & Perego, U. (2007). An extended FE strategy for transition from continuum damage to mode I cohesive crack propagation. *International Journal for Numerical and Analytical Methods in Geomechanics*, *31*(2), 213–238. https://doi.org/10.1002/nag.537 (cit. on pp. 59, 74, 76, 79)

Cordebois, J., & Sidoroff, F. (1982a). Anisotropic damage in elasticity and plasticity. *Journal de Mécanique Théorique et Appliquée, numéro spécial*, 45–60 (cit. on pp. 35, 36, 38, 142).

Cordebois, J. P., & Sidoroff, F. (1982b). Damage Induced Elastic Anisotropy. In J.-P. Boehler (Ed.), *Mechanical Behavior of Anisotropic Solids / Comportment Méchanique des Solides Anisotropes* (pp. 761–774). Springer Netherlands. https://doi.org/10.1007/978-94-009-6827-1_44. (Cit. on p. 142)

Cormery, F., & Welemane, H. (2002). A critical review of some damage models with unilateral effect. *Mechanics Research Communications*, *29(5)*, 391–395. https://doi.org/10.1016/S0093-6413(02)00262-8 (cit. on p. 37)

Cosserat, E., & Cosserat, F. (1909). *Théorie des corps déformables*. Editions Hermann, Paris. (Cit. on p. 51).

Cundall, P. A., & Strack, O. D. L. (1979). A discrete numerical model for granular assemblies. *Géotechnique*, *29*(1), 47–65. https://doi.org/10.1680/geot.1979.29.1.47 (cit. on p. 18)

Cusatis, G., Mencarelli, A., Pelessone, D., & Baylot, J. (2011a). Lattice Discrete Particle Model (LDPM) for failure behavior of concrete. II: Calibration

and validation. *Cement and Concrete Composites*, *33*(9), 891–905. https://doi.org/10.1016/j.cemconcomp.2011.02.010 (cit. on p. 18)

Cusatis, G., Pelessone, D., & Mencarelli, A. (2011b). Lattice Discrete Particle Model (LDPM) for failure behavior of concrete. I: Theory. *Cement and Concrete Composites*, *33*(9), 881–890. https://doi.org/10.1016/j.cemconcomp.2011.02.011 (cit. on p. 18)

Cuvilliez, S., Feyel, F., Lorentz, E., & Michel-Ponnelle, S. (2012). A finite element approach coupling a continuous gradient damage model and a cohesive zone model within the framework of quasi-brittle failure. *Computer Methods in Applied Mechanics and Engineering*, *237-240*, 244–259. https://doi.org/10.1016/j.cma.2012.04.019 (cit. on pp. 140, 180)

D'Addetta, G. A., Kun, F., & Ramm, E. (2002). On the application of a discrete model to the fracture process of cohesive granular materials. *Granular Matter*, *4*(2), 77–90. https://doi.org/10.1007/s10035-002-0103-9 (cit. on p. 18)

Dandekar, D. (2001). Shock response of boron carbide. *Technical Report ARL-TR-2456, Army Research Laboratory, Aberdeen Proving Ground* (cit. on p. 98).

Dandekar, D., & Bartkowski, P. (2001). Tensile strengths of silicon carbide (sic) under shock loading. *Technical Report ARL-TR-2430, Army Research Laboratory, Aberdeen Proving Ground* (cit. on p. 98).

Das, S., Sharma, S., Ramaswamy, A., Roy, D., & Reddy, J. N. (2021). A Geometrically Inspired Model for Brittle Damage in Compressible Elastomers. *Journal of Applied Mechanics*, *88*(8), 081002. https://doi.org/10.1115/1.4050620 (cit. on pp. 111, 179)

de Borst, R., Benallal, A., & Heeres, O. (1996). A gradient-enhanced damage approach to fracture. *Journal de Physique IV Proceedings, EDP Sciences*, *06 (C6)*, C6-491-C6–502. https://doi.org/10.1051/jp4:1996649 (cit. on p. 87)

de Borst, R., Pamin, J., Peerlings, R. H. J., & Sluys, L. J. (1995). On gradient-enhanced damage and plasticity models for failure in quasi-brittle and frictional materials. *Computational Mechanics*, 130–141. https://doi.org/10.1007/BF00356485 (cit. on p. 57)

de Borst, R., & Verhoosel, C. V. (2016). Gradient damage vs phase-field approaches for fracture: Similarities and differences. *Computer Methods in Applied Mechanics and Engineering*, *312*, 78–94. https://doi.org/10.1016/j.cma.2016.05.015 (cit. on p. 66)

de Borst, R. (1987). Computation of post-bifurcation and post-failure behavior of strain-softening solids. *Computers & Structures*, *25*(2), 211–224. https://doi.org/https://doi.org/10.1016/0045-7949(87)90144-1 (cit. on p. 163)

De Vree, J., Brekelmans, W., & van Gils, M. (1995). Comparison of nonlocal approaches in continuum damage mechanics. *Computers & Structures*, *55*(4), 581–588. https://doi.org/10.1016/0045-7949(94)00501-S (cit. on pp. 33, 133, 152)

Denoual, C., & Hild, F. (2002). Dynamic fragmentation of brittle solids: A multi-scale model. *European Journal of Mechanics - A/Solids*, *21*(1), 105–120. https://doi.org/10.1016/S0997-7538(01)01187-1 (cit. on p. 9)

Desmorat, R. (2004). Modèle d' endommagement anisotrope avec forte dissymétrie traction/compression. *In : 5è journées du Regroupement Francophone pour la Recherche et la Formation sur le Béton (RF2B), 5-6 July, Liège, Belgium* (cit. on pp. 35, 142).

Desmorat, R., Chambart, M., Gatuingt, F., & Guilbaud, D. (2010). Delay-active damage versus non-local enhancement for anisotropic damage dynamics computations with alternated loading. *Engineering Fracture Mechanics*, *77*(12), 2294–2315. https://doi.org/10.1016/j.engfracmech.2010.04.006 (cit. on pp. 9, 99, 180)

Desmorat, R., & Gatuingt, F. (2007a). Introduction of an internal time in nonlocal integral theories. *Internal report LMT* (cit. on p. 143).

Desmorat, R., Gatuingt, F., & Jirasek, M. (2015a). Nonlocal models with damage-dependent interactions motivated by internal time. *Engineering Fracture Mechanics*, *142*, 255–275 (cit. on pp. 143–145, 147).

Desmorat, R., Gatuingt, F., & Jirásek, M. (2015b). Nonlocal models with damage-dependent interactions motivated by internal time. *Engineering Fracture Mechanics*, *142*, 255–275. https://doi.org/10.1016/j.engfracmech.2015.06.015 (cit. on pp. 2, 59, 60, 62–65, 83, 84, 101, 107, 111, 118, 120, 178, 197)

Desmorat, R., Gatuingt, F., & Ragueneau, F. (2007a). Nonlocal anisotropic damage model and related computational aspects for quasi-brittle materials. *Engineering Fracture Mechanics*, *74(10)*, 1539–1560. https://doi.org/10.1016/j.engfracmech.2006.09.012 (cit. on pp. 38, 116, 143, 151, 153)

Desmorat, R., Ragueneau, F., & Pham, H. (2007b). *Continuum damage mechanics* for hysteresis and fatigue of quasi-brittle materials and structures. *International Journal for Numerical and Analytical Methods in Geomechanics*, *31*(2), 307–329. https://doi.org/10.1002/nag.532 (cit. on pp. 9, 34)

Desmorat, R. (2015). Anisotropic damage modeling of concrete materials. *International Journal of Damage Mechanics*, *25*(6), 818–852. https://doi.org/10.1177/1056789515606509 (cit. on pp. 35, 38, 47, 116, 120, 141–144, 151, 152, 156, 168, 178, 189)

Desmorat, R., & Gatuingt, F. (2007b). Introduction of an internal time in nonlocal integral theories. *Internal report LMT-Cachan. ENS Cachan/CNRS/Université Paris 6/PRES Unive*, *268* (cit. on pp. 59, 61–63, 177).

Di Luzio, G., & Bažant, Z. P. (2005). Spectral analysis of localization in nonlocal and over-nonlocal materials with softening plasticity or damage. *International Journal of Solids and Structures*, *42*(23), 6071–6100. https://doi.org/10.1016/j.ijsolstr.2005.03.038 (cit. on pp. 59, 74, 79, 177)

Dias-da-Costa, D., Alfaiate, J., Sluys, L., & Júlio, E. (2009). A discrete strong discontinuity approach. *Engineering Fracture Mechanics*, *76*(9), 1176–1201. https://doi.org/10.1016/j.engfracmech.2009.01.011 (cit. on p. 20)

Dubé, J.-F., Pijaudier-Cabot, G., & Borderie, C. L. (1996). Rate Dependent Damage Model for Concrete in Dynamics. *Journal of Engineering Mechanics*, *122*(10), 939–947. https://doi.org/10.1061/(ASCE)0733-9399(1996)122:10(939) (cit. on p. 34)

Dugdale, D. (1960). Yielding of steel sheets containing slits. *Journal of the Mechanics and Physics of Solids*, *8*(2), 100–104. https://doi.org/10.1016/0022-5096(60)90013-2 (cit. on pp. 21, 22)

Einstein, A., Podolsky, B., & Rosen, N. (1935). Can Quantum-Mechanical Description of Physical Reality Be Considered Complete? *Physical Review*, *47*(10), 777–780. https://doi.org/10.1103/PhysRev.47.777 (cit. on p. 49)

Elices, M., Guinea, G., Gómez, J., & Planas, J. (2002). The cohesive zone model: Advantages, limitations and challenges. *Engineering Fracture Mechanics*, *69*(2), 137–163. https://doi.org/10.1016/S0013-7944(01)00083-2 (cit. on p. 22)

Eringen, A. C. (1976). Nonlocal Polar Field Theories. In *Continuum Physics* (pp. 205–267). Elsevier. https://doi.org/10.1016/B978-0-12-240804-5.50009-9. (Cit. on p. 51)

Eringen, A. C. (1978). Nonlocal continuum mechanics and some applications. In *Nonlinear equations in physics and mathematics* (pp. 271–318). D.Reidel Publishing Company. (Cit. on p. 51).

Eringen, A. C. (1999). *Microcontinuum Field Theories*. Springer New York. https://doi.org/10.1007/978-1-4612-0555-5. (Cit. on p. 51)

Eringen, A. C. (2002). *Nonlocal continuum field theories*. Springer. (Cit. on pp. 50, 52, 53).

Eringen, A. C., & Suhubi, E. S. (1964). Nonlinear theory of simple micro-elastic solids—I. *International Journal of Engineering Science*, *2*(2), 189–203 (cit. on p. 51).

Eringen, A. C., & Kafadar, C. B. (1976). Polar Field Theories. In *Continuum Physics* (pp. 1–73). Elsevier. https://doi.org/10.1016/B978-0-12-240804-5.50007-5. (Cit. on pp. 50, 51)

Erzar, B., & Forquin, P. (2010). An Experimental Method to Determine the Tensile Strength of Concrete at High Rates of Strain. *Experimental Mechanics*, *50*(7), 941–955 (cit. on pp. 81, 85).

Evans, R. H., & Marathe, M. S. (1968). Microcracking and stress-strain curves for concrete in tension. *Matériaux et Constructions*, *1*(1), 61–64. https://doi.org/10.1007/BF02479001 (cit. on p. 9)

Falk, M. L., Needleman, A., & Rice, J. R. (2001). A critical evaluation of cohesive zone models of dynamic fractur. *Le Journal de Physique IV*, *11*(PR5), Pr5–43–Pr5–50. https://doi.org/10.1051/jp4:2001506 (cit. on p. 22)

Fassin, M., Eggersmann, R., Wulfinghoff, S., & Reese, S. (2019). Gradient-extended anisotropic brittle damage modeling using a second order damage tensor – Theory, implementation and numerical examples. *International Journal of Solids and Structures*, *167*, 93–126 (cit. on pp. 143, 167).

Feenstra, P. (1993). *Computational aspects of biaxial stress in plain reinforced concrete* (Doctoral dissertation). TU Delft. (Cit. on p. 82).

Feng, D.-C., & Wu, J.-Y. (2018). Phase-field regularized cohesive zone model (CZM) and size effect of concrete. *Engineering Fracture Mechanics*, *197*, 66–79. https://doi.org/10.1016/j.engfracmech.2018.04.038 (cit. on p. 66)

Fichant, S., La Borderie, C., & Pijaudier-Cabot, G. (1999). Isotropic and anisotropic descriptions of damage in concrete structures. *Mechanics of Cohesive-frictional Materials, Wiley*, *4*, 339–359 (cit. on p. 35).

Forest, S. (2009). Micromorphic Approach for Gradient Elasticity, Viscoplasticity, and Damage. *Journal of Engineering Mechanics*, *135*(3), 117–131 (cit. on pp. 61, 65, 99, 106, 111, 112, 115, 118, 145, 178).

Forghani, A., Poursartip, A., & Vaziri, R. (2019). An orthotropic non-local approach to modeling intra-laminar damage progression in laminated composites. *International Journal of Solids and Structures*, *180-181*, 160–175 (cit. on pp. 143, 172).

Francfort, G., & Marigo, J.-J. (1998). Revisiting brittle fracture as an energy minimization problem. *Journal of the Mechanics and Physics of Solids*, *46*(8), 1319–1342 (cit. on pp. 52, 65, 177).

Frémond, M., & Nedjar, B. (1996). Damage, gradient of damage and principle of virtual power. *International Journal of Solids and Structures*, *33*(8), 1083–1103 (cit. on p. 51).

Gálvez, J. C., Elices, M., Guinea, G. V., & Planas, J. (1998). Mixed Mode Fracture of Concrete under Proportional and Nonproportional Loading. *International Journal of Fracture*, *94*, 267–284 (cit. on pp. 156, 162, 163).

Ganghoffer, J. (2003). New concepts in nonlocal continuum mechanics and new materials obeying a generalised continuum behaviour. *International Journal of Engineering Science*, *41*(3-5), 291–304 (cit. on pp. 111, 120).

Ganghoffer, J., & de Borst, R. (2000). A new framework in nonlocal mechanics. *International Journal of Engineering Science*, *38*(4), 453–486 (cit. on p. 111).

Gatuingt, F., & Pijaudier-Cabot, G. (2002). Coupled damage and plasticity modelling in transient dynamic analysis of concrete. *International Journal for Numerical and Analytical Methods in Geomechanics*, *26*(1), 1–24. https://doi.org/10.1002/nag.188 (cit. on p. 34)

Geers, M., de Borst, R., Brekelmans, W., & Peerlings, R. (1998). Strain-based transient-gradient damage model for failure analyses. *Computer Methods in Applied Mechanics and Engineering*, *160*(1-2), 133–153 (cit. on pp. 2, 58–60, 83, 90, 101, 102, 142, 143, 177, 197).

Gerasimov, T., & De Lorenzis, L. (2022). Second-order phase-field formulations for anisotropic brittle fracture. *Computer Methods in Applied Mechanics and Engineering*, *389*, 114403. https://doi.org/10.1016/j.cma.2021.114403 (cit. on p. 172)

Germain, P., Nguyen, Q. S., & Suquet, P. (1983). Continuum Thermodynamics. *Journal of Applied Mechanics*, *50*(4), 1010–1020 (cit. on p. 30).

Geuzaine, C., & Remacle, J.-F. (2009). Gmsh: A 3-d finite element mesh generator with built-in pre- and post-processing facilities. *International Journal for Numerical Methods in Engineering*, *79*(11), 1309–1331. https://doi.org/https://doi.org/10.1002/nme.2579 (cit. on p. 157)

Giry, C. (2011). *Modélisation objective de la localisation des déformations et de la fissuration des structures en béton soumises à des chargements statiques ou dynamiques* (Doctoral dissertation). Université de Grenoble. (Cit. on pp. 54, 178).

Giry, C., Dufour, F., & Mazars, J. (2011). Stress-based nonlocal damage model. *International Journal of Solids and Structures*, *48*(25-26), 3431–3443. https://doi.org/10.1016/j.ijsolstr.2011.08.012 (cit. on pp. 2, 59–61, 83, 84, 86, 88, 89, 102, 124, 135, 143, 148, 177, 197)

Grégoire, D., Rojas-Solano, L., & Pijaudier-Cabot, G. (2013). Failure and size effect for notched and unnotched concrete beams. *International Journal for Numerical and Analytical Methods in Geomechanics*, *37*(10), 1434–1452. https://doi.org/10.1002/nag.2180 (cit. on pp. 15, 180)

Grégoire, D., Verdon, L., Lefort, V., Grassl, P., Saliba, J., Regoin, J.-P., Loukili, A., & Pijaudier-Cabot, G. (2015). Mesoscale analysis of failure in quasi-brittle materials: Comparison between lattice model and acoustic emission data. *International Journal for Numerical and Analytical Methods in Geomechanics*, *39*(15), 1639–1664. https://doi.org/10.1002/nag.2363 (cit. on pp. 14, 15)

Griffith, A. A. (1921). The phenomena of rupture and flow in solids. *Philosophical Transactions of the Royal Society of London*, *221*, 582–593 (cit. on p. 19).

Gültekin, O., Dal, H., & Holzapfel, G. A. (2018). Numerical aspects of anisotropic failure in soft biological tissues favor energy-based criteria: A rate-dependent anisotropic crack phase-field model. *Computer Methods in Applied Mechanics and Engineering*, *331*, 23–52. https://doi.org/10.1016/j.cma.2017.11.008 (cit. on p. 171)

Gupta, A. K., & Akbar, H. (1984). Cracking in Reinforced Concrete Analysis. *Journal of Structural Engineering*, *110*(8), 1735–1746. https://doi.org/10.1061/(ASCE)0733-9445(1984)110:8(1735) (cit. on p. 23)

Haag, R. (1992). *Local Quantum Physics*. Springer Berlin Heidelberg. https://doi.org/10.1007/978-3-642-97306-2. (Cit. on p. 49)

Hadamard, J. (1903). *Lecons sur la propagation des ondes et les équations de l'hydrodynamique*. Hermann, Paris (reedition J. Math. Phys., 11:941, 1970). (Cit. on p. 45).

Halm, D., & Dragon, A. (1998). An anisotropic model of damage and frictional sliding for brittle materials. *European Journal of Mechanics A/Solids*, *17(3)*, 439–460 (cit. on pp. 35, 37, 142).

Halphen, B., & Nguyen, Q. S. (1975). Sur les matériaux standard généralisés. *Journal de Mécanique*, *14*(1), 39–63 (cit. on p. 30).

Hamilton, N., & Cal, R. B. (2015). Anisotropy of the Reynolds stress tensor in the wakes of wind turbine arrays in Cartesian arrangements with counter-rotating rotors. *Physics of Fluids*, *27*(1), 015102 (cit. on p. 148).

Hecht, F. (2012). New development in freefem++. *J. Numer. Math.*, *20*(3-4), 251–265 (cit. on pp. 133, 155).

Helfer, T., Michel, B., Proix, J. M., Salvo, M., Sercombe, J., & Casella, M. (2015). Introducing the open- source mfront code generator: Application to mechanical behaviours and material knowledge management within the pleiades fuel element modelling platform. *Computers and Mathematics with Applications*, *70(5)*, 994–1023 (cit. on p. 156).

Herrmann, H. J., Hansen, A., & Roux, S. (1989). Fracture of disordered, elastic lattices in two dimensions. *Physical Review B*, *39*(1), 637–648. https://doi.org/10.1103/PhysRevB.39.637 (cit. on p. 18)

Hill, R. (1948). A VARIATIONAL PRINCIPLE OF MAXIMUM PLASTIC WORK IN CLASSICAL PLASTICITY. *The Quarterly Journal of Mechanics and Applied Mathematics*, *1*(1), 18–28. https://doi.org/10.1093/qjmam/1.1.18 (cit. on p. 30)

Hill, R. (1958). A general theory of uniqueness and stability in elastic-plastic solids. *Journal of the Mechanics and Physics of Solids*, *6*(3), 236–249. https://doi.org/10.1016/0022-5096(58)90029-2 (cit. on pp. 45, 59)

Hill, R. (1962). Acceleration waves in solids. *Journal of the Mechanics and Physics of Solids*, *10*(1), 1–16 (cit. on p. 45).

Hill, R. (1967). The essential structure of constitutive laws for metal composites and polycrystals. *Journal of the Mechanics and Physics of Solids*, *15*(2), 79–95. https://doi.org/10.1016/0022-5096(67)90018-X (cit. on p. 30)

Hillerborg, A., Modéer, M., & Petersson, P.-E. (1976). Analysis of crack formation and crack growth in concrete by means of fracture mechanics and finite elements. *Cement and Concrete Research*, *6*(6), 773–781. https://doi.org/10.1016/0008-8846(76)90007-7 (cit. on pp. 22–24, 47)

Hobbs, M., Dodwell, T., Hattori, G., & Orr, J. (2022). An examination of the size effect in quasi-brittle materials using a bond-based peridynamic model. *Engineering Structures*, *262*, 114207. https://doi.org/10.1016/j.engstruct.2022.114207 (cit. on p. 68)

Hoover, C. G., P. Bažant, Z., Vorel, J., Wendner, R., & Hubler, M. H. (2013). Comprehensive concrete fracture tests: Description and results. *Engineering Fracture Mechanics*, *114*, 92–103. https://doi.org/10.1016/j.engfracmech.2013.08.007 (cit. on pp. 15, 180)

Hordjik, D. (1991). *Local approach to fatigue of concrete* (Doctoral dissertation). Delft University of Technology. (Cit. on p. 9).

Hrennikoff, A. (1941). Solution of Problems of Elasticity by the Framework Method. *Journal of Applied Mechanics*, *8*(4), A169–A175. https://doi.org/10.1115/1.4009129 (cit. on p. 18)

Hudson, J., Brown, E., & Fairhurst, C. (1971). Shape of the complete stress-strain curve for rock In *Proc. 13th symposium rock mechanics, university of illinois, urbana, illinois.* (Cit. on p. 8).

IEA. (2019). *Global status report for buildings and construction 2019* (tech. rep.). International Energy Agency. (Cit. on pp. 1, 195).

Irwin, G. (1957). Analysis of stresses and strains near the end of a crack traversing a plate. *Journal of Applied Mechanics*, *24*, 361–364 (cit. on p. 19).

Jin, W., & Arson, C. (2018). Anisotropic nonlocal damage model for materials with intrinsic transverse isotropy. *International Journal of Solids and Structures*, *139-140*, 29–42 (cit. on pp. 143, 172).

Jirásek, M. (2004). Nonlocal Theories in Continuum Mechanics. *Acta Polytechnica*, *44*(5-6). https://doi.org/10.14311/610 (cit. on p. 51)

Jirásek, M., & Patzák, B. (2002). Consistent tangent stiffness for nonlocal damage models. *Computers & Structures*, *80*(14-15), 1279–1293. https://doi.org/10.1016/S0045-7949(02)00078-0 (cit. on p. 33)

Jirásek, M., & Suárez, F. (2016). Localization properties of Desmorat's anisotropic damage model. *Computers & Structures*, *174*, 139–153. https://doi.org/10.1016/j.compstruc.2015.08.011 (cit. on pp. 46, 153)

Jirásek, M. (1998). Nonlocal models for damage and fracture: Comparison of approaches. *International Journal of Solids and Structures*, *35*(31-32), 4133–4145. https://doi.org/10.1016/S0020-7683(97)00306-5 (cit. on pp. 2, 55, 197)

Jirásek, M. (2000). Comparative study on ®nite elements with embedded discontinuities. *Comput. Methods Appl. Mech. Engrg.*, 24 (cit. on p. 20).

Jirásek, M. (2007). Mathematical analysis of strain localization. *Revue européenne de génie civil*, *11*(7-8), 977–991. https://doi.org/10.3166/regc.11.977-991 (cit. on pp. 45, 46, 127, 130)

Jirásek, M. (2011). Damage and Smeared Crack Models. In F. Pfeiffer, F. G. Rammerstorfer, J. Salençon, G. Hofstetter, & G. Meschke (Eds.), *Numerical Modeling of Concrete Cracking* (pp. 1–49). Springer Vienna. https://doi.org/10.1007/978-3-7091-0897-0_1. (Cit. on p. 23)

Jirásek, M., & Bauer, M. (2012). Numerical aspects of the crack band approach. *Computers & Structures*, *110-111*, 60–78. https://doi.org/10.1016/j.compstruc.2012.06.006 (cit. on pp. 33, 47)

Jirásek, M., & Belytschko, T. (2002). Computational Resolution of Strong Discontinuities. (Cit. on p. 21).

Jirásek, M., & Desmorat, R. (2019). Localization analysis of nonlocal models with damage-dependent nonlocal interaction. *International Journal of Solids and Structures*, *174-175*, 1–17. https://doi.org/10.1016/j.ijsolstr.2019.06.011 (cit. on pp. 59, 63, 87)

Jirásek, M., & Grassl, P. (2008). Evaluation of directional mesh bias in concrete fracture simulations using continuum damage models. *Engineering Fracture Mechanics*, *75*(8), 1921–1943. https://doi.org/10.1016/j.engfracmech.2007.11.010 (cit. on p. 47)

Jirásek, M., & Zimmermann, T. (1998a). Analysis of Rotating Crack Model. *Journal of Engineering Mechanics*, *124*(8), 842–851. https://doi.org/10.1061/(ASCE)0733-9399(1998)124:8(842) (cit. on p. 23)

Jirásek, M., & Zimmermann, T. (1998b). Rotating Crack Model with Transition to Scalar Damage. *Journal of Engineering Mechanics*, *124*(3), 277–284. https://doi.org/10.1061/(ASCE)0733-9399(1998)124:3(277) (cit. on p. 23)

Kachanov, L. M. (1958). Time of rupture process under creep conditions (in russian). *Izvestia Academia Nauk, USSR*, *8*, 26–31 (cit. on pp. 2, 24, 196).

Kachanov, M., Tsukrov, I., & Shafiro, B. (1994). Effective Moduli of Solids With Cavities of Various Shapes. *Applied Mechanics Reviews*, *47*(1S), S151–S174. https://doi.org/10.1115/1.3122810 (cit. on p. 40)

Kachanov, M. (1992). Effective Elastic Properties of Cracked Solids: Critical Review of Some Basic Concepts. *Applied Mechanics Reviews*, *45*(8), 304–335. https://doi.org/10.1115/1.3119761 (cit. on p. 40)

Kachanov, M. (1993). Elastic Solids with Many Cracks and Related Problems. In *Advances in Applied Mechanics* (pp. 259–445). Elsevier. https://doi.org/10.1016/S0065-2156(08)70176-5. (Cit. on p. 40)

Kakarla, S. (2020). *From anisotropic damage to multiple cracks by coupling a microplane model and a strong discontinuity formulation in the embedded finite element method* (Doctoral dissertation). Université Paris-Saclay. CEA, Service d'études mécaniques et thermiques. ENS Paris-Saclay. (Cit. on p. 20).

Kakarla, S., Rastiello, G., Richard, B., & Giry, C. (2021). Coupled continuous–discrete formulation based on microplane and strong discontinuity models for representing non-orthogonal intersecting cracks. *Engineering Fracture Mechanics*, *245*, 107565. https://doi.org/10.1016/j.engfracmech.2021.107565 (cit. on pp. 20, 47)

Klepaczko, J., & Brara, A. (2001). An experimental method for dynamic tensile testing of concrete by spalling. *International Journal of Impact Engineering*, *25*, 387–409. https://doi.org/10.1016/S0734-743X(00)00050-6 (cit. on pp. 9, 81)

Krajcinovic, D., & Fonseka, G. U. (1981). The continuous damage theory of brittle materials, parts i and ii. *Journal of Applied Mechanics*, *48*, 809–824 (cit. on pp. 35, 142).

Krajcinovic, D., & Mastilovic, S. (1995). Some fundamental issues of damage mechanics. *Mechanics of materials*, *21*, 217–230 (cit. on pp. 35, 142).

Krayani, A., Pijaudier-Cabot, G., & Dufour, F. (2009). Boundary effect on weight function in nonlocal damage model. *Engineering Fracture Mechanics*, *76*(14), 2217–2231. https://doi.org/10.1016/j.engfracmech.2009.07.007 (cit. on pp. 2, 54, 59, 81, 83, 84, 89, 142, 197)

Kuhl, E., Ramm, E., & De Borst, R. (2000). An anisotropic gradient damage model for quasi-brittle materials. *Computer Methods in Applied Mechanics and Engineering*, *183*(1-2), 87–103 (cit. on p. 143).

Kuhl, E., Steinmann, P., & Carol, I. (2001). A thermodynamically consistent approach to microplane theory. Part II. Dissipation and inelastic constitutive modeling. *International Journal of Solids and Structures*, *38*(17), 2933–2952. https://doi.org/10.1016/S0020-7683(00)00213-4 (cit. on p. 40)

Labuz, J., & Biolzi, L. (1998). Characteristic strength of quasi-brittle materials. *International Journal of Solids and Structures*, *35*(31-32), 4191–4203. https://doi.org/10.1016/S0020-7683(97)00309-0 (cit. on pp. 9, 15)

Ladevèze, P. (1983). On an anisotropic damage theory. *In Proc. CNRS Int. Coll 351 Villars-de-Lans, Failure crieria of structured media* (cit. on pp. 35–37, 142).

Landis, E. N. (1999). Micro–macro fracture relationships and acoustic emissions in concrete. *Construction and Building Materials*, *13*(1-2), 65–72. https://doi.org/10.1016/S0950-0618(99)00009-4 (cit. on pp. 9, 15)

Lasry, D., & Belytschko, T. (1988). Localization limiters in transient problems. *International Journal of Solids and Structures*, *24(6)*, 581–597 (cit. on pp. 56, 82).

Lazarov, B. S., & Sigmund, O. (2011). Filters in topology optimization based on Helmholtz-type differential equations. *International Journal for Numerical Methods in Engineering*, *86*(6), 765–781. https://doi.org/10.1002/nme.3072 (cit. on p. 50)

Leblond, J. B., Perrin, G., & Devaux, J. (1994). Bifurcation Effects in Ductile Metals With Nonlocal Damage. *Journal of Applied Mechanics*, *61*(2), 236–242. https://doi.org/10.1115/1.2901435 (cit. on p. 128)

Lemaitre, J. (1971). Evaluation of dissipation and damage in metals. *In Proceedings of ICM Kyoto* (cit. on pp. 2, 31, 196).

Lemaitre, J., Chaboche, J., Benallal, A., & Desmorat, R. (2009). *Mécanique des matériaux solides - 3ème édition*. Dunod. (Cit. on pp. 25, 26, 45, 46).

Lemaitre, J., & Desmorat, R. (2005). *Engineering damage mechanics: Ductile, creep, fatigue and brittle failures.* Springer Nature Switzerland AG. (Cit. on pp. 25, 35, 38).

Lemaitre, J. (1996). *A Course on Damage Mechanics*. Springer Berlin Heidelberg. https://doi.org/10.1007/978-3-642-18255-6. (Cit. on pp. 25, 35, 152)

Lemaitre, J., Desmorat, R., & Sauzay, M. (2000). Anisotropic damage law of evolution. *European Journal of Mechanics - A/Solids*, *19*(2), 187–208. https://doi.org/10.1016/S0997-7538(00)00161-3 (cit. on pp. 37, 147)

Leroux, A. (2012). *Modèle multiaxial d'endommagement anisotrope: Gestion numérique de la rupture et application à la ruine de structures en béton armé sous impacts.* (Doctoral dissertation). École normale supérieure de Cachan - ENS Cachan. (Cit. on p. 153).

Li, B., & Maurini, C. (2019). Crack kinking in a variational phase-field model of brittle fracture with strongly anisotropic surface energy. *Journal of the Mechanics and Physics of Solids*, *125*, 502–522 (cit. on pp. 144, 172).

Li, C., Yang, D., Xie, H., Ren, L., & Wang, J. (2023a). Size effect of fracture characteristics for anisotropic quasi-brittle geomaterials. *International Journal of*

Mining Science and Technology, *33*(2), 201–213. https://doi.org/10.1016/j.ijmst.2022.11.004 (cit. on p. 15)

Li, J.-L., Wei, X.-D., & Zhao, G.-F. (2023b). An integrated experimental and numerical study of size effect on the mode I fracture toughness of rock. *Engineering Fracture Mechanics*, *287*, 109327. https://doi.org/10.1016/j.engfracmech.2023.109327 (cit. on p. 15)

Loiseau, F., Oliver-Leblond, C., Verbeke, T., & Desmorat, R. (2023). Anisotropic damage state modeling based on harmonic decomposition and discrete simulation of fracture. *Engineering Fracture Mechanics*, *293*, 109669 (cit. on p. 147).

Loiseau, F. (2023). *Formulation of anisotropic damage in quasi-brittle materials and structures based on discrete element simulation* (Doctoral dissertation). Université Paris-Saclay, ENS Paris-Saclay. (Cit. on pp. 153, 160).

Lorentz, E., & Andrieux, S. (1999). A variational formulation for nonlocal damage models. *International Journal of Plasticity*, *15*(2), 119–138 (cit. on p. 51).

Lu, X., & Guo, X. (2022). An interactive orthotropic non-local damage model for progressive failure analysis of composite laminates. *Composite Structures*, *295*, 115841 (cit. on pp. 143, 172).

Lyu, Y., Pathirage, M., Nguyen, H. T., Bažant, Z. P., & Cusatis, G. (2023). Dissipation mechanisms of crack-parallel stress effects on fracture process zone in concrete. *Journal of the Mechanics and Physics of Solids*, *181*, 105439. https://doi.org/10.1016/j.jmps.2023.105439 (cit. on p. 148)

Maire, J., & Chaboche, J. (1997). A new formulation of continuum damage mechanics (CDM) for composite materials. *Aerospace Science and Technology*, *1*(4), 247–257. https://doi.org/10.1016/S1270-9638(97)90035-3 (cit. on pp. 35, 37, 142)

Marconi, F. (2022). *Damage-fracture transition by an eikonal-based gradient-type formulation for damage (-plastic) model.* (Doctoral dissertation). Université Paris-Saclay. (Cit. on pp. 62, 64, 87, 143).

Mariani, S., & Gobat, G. (2019). Identification of strength and toughness of quasi-brittle materials from spall tests: A sigma-point kalman filter approach. *Inverse Problems in Science and Engineering*, *27*(9), 1318–1346 (cit. on p. 98).

Mariano, P. M. (2010). Physical significance of the curvature varifold-based description of crack nucleation. *Rendiconti Lincei - Matematica e Applicazioni*, 215–233 (cit. on p. 111).

Mariano, P. M., & Stazi, F. L. (2005). Computational aspects of the mechanics of complex materials. *Archives of Computational Methods in Engineering*, *12*(4), 391–478 (cit. on p. 111).

Marigo, J. (1981). Formulation d'une loi d'endommagement d'un matériau élastique. *CR Acad Sci Paris*, *292*(19), 1309–1312 (cit. on pp. 31, 32).

Masseron, B., Rastiello, G., & Desmorat, R. (2022). Analytical strain localization analysis of isotropic and anisotropic damage models for quasi-brittle materials. *International Journal of Solids and Structures*, 111869 (cit. on pp. 45, 46, 116, 130).

Masseron, B., Rastiello, G., Moës, N., & Desmorat, R. (2023). Lip-field regularization of anisotropic damage In *The seventh international conference on computational modeling of fracture and failure of materials and structures*. Prague, Czech Republic. 234. (Cit. on pp. 65, 67, 153).

Mazars, J. (1984a). *Application de la mécanique de l' endommagement au comportement non linéaire et à la rupture du béton de structure.* (Doctoral dissertation). Université de Paris 6. (Cit. on p. 152).

Mazars, J. (1984b). *Application de la mécanique de l'endommagement au comportement non-linéaire et à la rupture du béton de structure.* (Doctoral dissertation). Université Paris VI (Thèse de doctorat d'état). (Cit. on pp. 2, 10, 32, 35, 196).

Mazars, J., Berthaud, Y., & Ramtani, S. (1990). The unilateral behaviour of damaged concrete. *Engineering Fracture Mechanics*, (4/5), 629–635. https://doi.org/https://doi.org/10.1016/0013-7944(90)90145-7 (cit. on p. 11)

Mazars, J. (1986). A description of micro- and macroscale damage of concrete structures. *Engineering Fracture Mechanics*, *25*(5-6), 729–737. https://doi.org/https://doi.org/10.1016/0013-7944(86)90036-6 (cit. on pp. 32, 33)

Mazars, J., & Pijaudier-Cabot, G. (1996). From damage to fracture mechanics and conversely: A combined approach. *International Journal of Solids and Structures*, *33*(20-22), 3327–3342 (cit. on pp. 140, 180).

Melenk, J., & Babuška, I. (1996). The partition of unity finite element method: Basic theory and applications. *Computer Methods in Applied Mechanics and Engineering*, *139*(1-4), 289–314. https://doi.org/10.1016/S0045-7825(96)01087-0 (cit. on p. 21)

Miehe, C., Welschinger, F., & Hofacker, M. (2010). Thermodynamically consistent phase-field models of fracture: Variational principles and multi-field FE implementations. *International Journal for Numerical Methods in Engineering*, *83*(10), 1273–1311 (cit. on pp. 52, 65).

Mindlin, R. D. (1964). Micro-structure in linear elasticity. *Archive for Rational Mechanics and Analysis*, *16*(1), 51–78. https://doi.org/10.1007/BF00248490 (cit. on p. 51)

Miyauchi, K., & Murata, K. (2007). Strain-softening behavior of wood under tension perpendicular to the grain. *Journal of Wood Science*, *53*(6), 463–469. https://doi.org/10.1007/s10086-007-0899-3 (cit. on p. 8)

Moës, N., Stolz, C., Bernard, P.-E., & Chevaugeon, N. (2011). A level set based model for damage growth: The thick level set approach. *International Journal for Numerical Methods in Engineering*, *86*(3), 358–380 (cit. on pp. 52, 66, 177).

Moës, N., & Belytschko, T. (2002). Extended finite element method for cohesive crack growth. *Engineering Fracture Mechanics*, *69*(7), 813–833. https://doi.org/10.1016/S0013-7944(01)00128-X (cit. on p. 21)

Moës, N., & Chevaugeon, N. (2021). Lipschitz regularization for softening material models: The Lip-field approach. *Comptes Rendus. Mécanique*, *349*(2), 415–434 (cit. on pp. 52, 67).

Moës, N., Dolbow, J., & Belytschko, T. (1999). A finite element method for crack growth without remeshing. *International Journal for Numerical Methods in Engineering*, *46*(1), 131–150. https://doi.org/10.1002/(SICI)1097-0207(19990910)46:1<131::AID-NME726>3.0.CO;2-J (cit. on p. 21)

Moës, N., Remacle, J.-F., Lambrechts, J., Lé, B., & Chevaugeon, N. (2023). The eXtreme Mesh deformation approach (X-MESH) for the Stefan phase change model. *Journal of Computational Physics*, *477*, 111878. https://doi.org/10.1016/j.jcp.2022.111878 (cit. on p. 180)

Moreau, K., Moës, N., Chevaugeon, N., & Salzman, A. (2017). Concurrent development of local and non-local damage with the Thick Level Set approach: Implementation aspects and application to quasi-brittle failure. *Computer Methods in Applied Mechanics and Engineering*, *327*, 306–326. https://doi.org/10.1016/j.cma.2017.08.045 (cit. on p. 66)

Mosler, J., & Meschke, G. (2004). Embedded crack vs. smeared crack models: A comparison of elementwise discontinuous crack path approaches with emphasis on mesh bias. *Computer Methods in Applied Mechanics and Engineering*, *193*(30-32), 3351–3375. https://doi.org/10.1016/j.cma.2003.09.022 (cit. on p. 47)

Mühlhaus, H. B., & Aifantis, E. C. (1991). A variational principle for gradient plasticity. *International Journal of Solids and Structures*, *28*, 845–857 (cit. on pp. 56, 82).

Murakami, S. (1988). Mechanical modeling of material damage. *Journal of Applied Mechanics*, *55(2)*, 280–286 (cit. on pp. 35, 142).

Murakami, S. (2012). *Continuum Damage Mechanics* (Vol. 185). Springer Netherlands. https://doi.org/10.1007/978-94-007-2666-6. (Cit. on p. 35)

Nagaraja, S., Römer, U., Matthies, H. G., & De Lorenzis, L. (2023). Deterministic and stochastic phase-field modeling of anisotropic brittle fracture. *Computer Methods in Applied Mechanics and Engineering*, *408*, 115960 (cit. on p. 144).

Nedjar, B. (1995). *Mécanique de l'endommagement. théorie du premier gradient et application au béton* (Doctoral dissertation). Ecole Nationale des Ponts et Chaussées. (Cit. on p. 56).

Negi, A., & Kumar, S. (2022). A continuous–discontinuous localizing gradient damage framework for failure analysis of quasi-brittle materials. *Computer Methods in Applied Mechanics and Engineering*, *390*, 114434 (cit. on pp. 133, 140, 180).

Negi, A., Kumar, S., & Poh, L. H. (2020). A localizing gradient damage enhancement with micromorphic stress-based anisotropic nonlocal interactions. *International Journal for Numerical Methods in Engineering*, *121*(18), 4003–4027 (cit. on pp. 59, 61, 124, 143, 147, 148, 178).

Nguyen, G. D. (2011). A damage model with evolving nonlocal interactions. *International Journal of Solids and Structures*, *48*(10), 1544–1559 (cit. on pp. 59, 143).

Nguyen, H., Pathirage, M., Rezaei, M., Issa, M., Cusatis, G., & Bažant, Z. P. (2020). New perspective of fracture mechanics inspired by gap test with crack-parallel compression. *Proceedings of the National Academy of Sciences*, *117*(25), 14015–14020. https://doi.org/10.1073/pnas.2005646117 (cit. on pp. 147, 181)

Nguyen, T. H., Bui, T. Q., & Hirose, S. (2018). Smoothing gradient damage model with evolving anisotropic nonlocal interactions tailored to low-order finite elements. *Computer Methods in Applied Mechanics and Engineering*, *328*, 498–541. https://doi.org/10.1016/j.cma.2017.09.019 (cit. on pp. 33, 59, 143, 157)

Nouailletas, O., Borderie, C. L., Perlot, C., Rivard, P., & Ballivy, G. (2015). Experimental Study of Crack Closure on Heterogeneous Quasi-Brittle Material. *Journal of Engineering Mechanics*, *141*(11), 04015041. https://doi.org/10.1061/(ASCE)EM.1943-7889.0000928 (cit. on p. 11)

Oliver, J. (1996). Modelling strong discontinuities in solid mechanics via strain softening constitutive equations. part 1: Fundamentals. *International journal for numerical methods in engineering*, *39*, 3575–3600. https://doi.org/10.1002/(SICI)1097-0207(19961115)39:21<3575::AID-NME65>3.0.CO;2-E (cit. on p. 20)

Oliver, J., Huespe, A., Pulido, M., & Blanco, S. (2004). Computational modeling of cracking of concrete in strong discontinuity settings. *Computers and Concrete*, *1*(1), 61–76. https://doi.org/10.12989/CAC.2004.1.1.061 (cit. on pp. 20, 157)

Oliver, J., Huespe, A. E., Samaniego, E., & Chaves, E. W. V. (2002a). On strategies for tracking strong discontinuities in computational failure mechanics In *Fifth world congress on computational mechanics.* (Cit. on p. 21).

Oliver, J., Huespe, A. E., Samaniego, E., & Chaves, E. W. V. (2002b). On strategies for tracking strong discontinuities in computational failure mechanics In *Fifth world congress on computational mechanics.* (Cit. on p. 180).

Oliver, J., Huespe, A. E., & Sánchez, P. J. (2006). A comparative study on finite elements for capturing strong discontinuities: E-FEM vs X-FEM. *Computer Methods in Applied Mechanics and Engineering*, *195*(37), 4732–4752. https://doi.org/10.1016/j.cma.2005.09.020 (cit. on p. 21)

Oliver-Leblond, C. (2019). Discontinuous crack growth and toughening mechanisms in concrete: A numerical study based on the beam-particle approach. *Engineering Fracture Mechanics*, *207*, 1–22. https://doi.org/10.1016/j.engfracmech.2018.11.050 (cit. on p. 19)

Ortiz, M., Leroy, Y., & Needleman, A. (1987). A finite element method for localized failure analysis. *Computer Methods in Applied Mechanics and Engineering*, *61*(2), 189–214. https://doi.org/10.1016/0045-7825(87)90004-1 (cit. on p. 20)

Papa, E., & Taliercio, A. (1996). Anisotropic damage model for the multiaxial static and fatigue behaviour of plain concrete. *Engineering Fracture Mechanics*, *55*(2), 163–179. https://doi.org/10.1016/0013-7944(96)00004-5 (cit. on p. 147)

Parrilla Gómez, A., Moës, N., & Stolz, C. (2015). Comparison between thick level set (TLS) and cohesive zone models. *Advanced Modeling and Simulation in Engineering Sciences*, *2*(1), 18. https://doi.org/10.1186/s40323-015-0041-9 (cit. on p. 66)

Passelègue, F. X., Pimienta, L., Faulkner, D., Schubnel, A., Fortin, J., & Guéguen, Y. (2018). Development and Recovery of Stress-Induced Elastic Anisotropy During Cyclic Loading Experiment on Westerly Granite. *Geophysical Research Letters*, *45*(16), 8156–8166. https://doi.org/10.1029/2018GL078434 (cit. on pp. 12, 13, 147)

Pathirage, M., Tong, D., Thierry, F., Cusatis, G., Grégoire, D., & Pijaudier-Cabot, G. (2023). Discrete modeling of concrete failure and size-effect. *Theoretical and Applied Fracture Mechanics*, *124*, 103738. https://doi.org/10.1016/j.tafmec.2022.103738 (cit. on p. 18)

Pathrikar, A., Rahaman, M. M., & Roy, D. (2021). A gauge theory for brittle damage in solids and a peridynamics implementation. *Computer Methods in Applied Mechanics and Engineering*, *385*, 114036. https://doi.org/10.1016/j.cma.2021.114036 (cit. on p. 179)

Patzák, B., & Jirásek, M. (2004). Adaptive Resolution of Localized Damage in Quasi-brittle Materials. *Journal of Engineering Mechanics*, *130*(6), 720–732. https://doi.org/10.1061/(ASCE)0733-9399(2004)130:6(720) (cit. on p. 180)

Peerlings, R., de Borst, R., Brekelmans, W., & de Vree, J. (1996a). Gradient-enhanced damage model for quasi-brittle materials. *International Journal for Numerical Methods in Engineering*, *39*, 391–403 (cit. on pp. 2, 52, 56–58, 64, 75, 82, 87, 109, 142, 145, 146, 149, 168, 173, 196).

Peerlings, R. H. J., de Borst, R., Brekelmans, W. a. M., & Geers, M. G. D. (1998). Gradient-enhanced damage modelling of concrete fracture. *Mechanics of Cohesive-frictional Materials*, *3*(4), 323–342. https://doi.org/10.1002/(SICI)1099-1484(1998100)3:4<323::AID-CFM51>3.0.CO;2-Z (cit. on pp. 33, 58)

Peerlings, R. H. J., De Borst, R., Brekelmans, W. a. M., De Vree, J. H. P., & Spee, I. (1996b). Some observations on localisation in non-local and gradient damage models. *European Journal of Mechanics A: Solids 15(6), 937-953. (1996)* (cit. on pp. 58, 74, 79).

Peerlings, R., Geers, M., de Borst, R., & Brekelmans, W. (2001). A critical comparison of nonlocal and gradient-enhanced softening continua. *International Journal of Solids and Structures*, *38*(44-45), 7723–7746. https://doi.org/10.1016/S0020-7683(01)00087-7 (cit. on pp. 57, 58, 74, 76, 78–80, 91, 177)

Peerlings, R., Massart, T., & Geers, M. (2004). A thermodynamically motivated implicit gradient damage framework and its application to brick masonry cracking. *Computer Methods in Applied Mechanics and Engineering*, *193*(30-32), 3403–3417. https://doi.org/10.1016/j.cma.2003.10.021 (cit. on pp. 52, 58, 61, 99, 106, 110, 116, 117, 121, 122, 145)

Peerlings, R. H. J. (1999). *Enhanced damage modelling for fracture and fatigue* (Doctoral dissertation). Technische Universiteit Eindhoven. (Cit. on pp. 51, 56, 57, 133, 154).

Peng, S., Parent, T., Sbartaï, Z. M., & Morel, S. (2022). Experimental characterisation of masonry unit–mortar interface under uniaxial cyclic tension. *Engineering Fracture Mechanics*, *274*, 108790. https://doi.org/10.1016/j.engfracmech.2022.108790 (cit. on pp. 8, 10)

Pensée, V., Kondo, D., & Dormieux, L. (2002). Micromechanical Analysis of Anisotropic Damage in Brittle Materials. *Journal of Engineering Mechanics*, *128*(8), 889–897. https://doi.org/10.1061/(ASCE)0733-9399(2002)128:8(889) (cit. on p. 40)

Pham, K., Amor, H., Marigo, J.-J., & Maurini, C. (2011). Gradient Damage Models and Their Use to Approximate Brittle Fracture. *International Journal of Damage Mechanics*, *20*(4), 618–652 (cit. on p. 52).

Pijaudier-Cabot, G., & Bažant, Z. P. (1987). Nonlocal Damage Theory. *Journal of Engineering Mechanics*, *113*(10), 1512–1533. https://doi.org/10.1061/(ASCE)0733-9399(1987)113:10(1512) (cit. on pp. 2, 52–54, 58, 142, 196)

Pijaudier-Cabot, G., & Benallal, A. (1993). Strain localization and bifurcation in a nonlocal continuum. *International Journal of Solids and Structures*, *30*(13), 1761–1775. https://doi.org/10.1016/0020-7683(93)90232-V (cit. on pp. 58, 79, 124–129, 132, 178)

Pijaudier-Cabot, G., & Dufour, F. (2010). Non local damage model: Boundary and evolving boundary effects. *European Journal of Environmental and Civil Engineering*, *14*(6-7), 729–749 (cit. on pp. 59, 62, 83, 143).

Pijaudier-Cabot, G., & Grégoire, D. (2014). A review of non local continuum damage: Modelling of failure? *Networks & Heterogeneous Media*, *9*(4), 575–597. https://doi.org/10.3934/nhm.2014.9.575 (cit. on pp. 54, 84, 87)

Pijaudier-Cabot, G., Haidar, K., & Dubé, J.-F. (2004). Non-local damage model with evolving internal length. *International Journal for Numerical and Analytical Methods in Geomechanics*, *28*(78), 633–652 (cit. on pp. 59, 142).

Pijaudier-Cabot, G., Hajimohammadi, A., Nouailletas, O., Borderie, C. L., Padin, A., & Mathieu, J.-P. (2022). Determination of the fracture energy of rocks from size effect tests: Application to shales and carbonate rocks. *Engineering Fracture Mechanics*, *271*, 108630. https://doi.org/10.1016/j.engfracmech.2022.108630 (cit. on p. 15)

Poh, L. H., & Sun, G. (2017). Localizing gradient damage model with decreasing interactions. *International Journal for Numerical Methods in Engineering*, *110*(6), 503–522 (cit. on pp. 59, 61, 123, 143, 146, 147, 155, 177, 178).

Polizzotto, C., Borino, G., & Fuschi, P. (1998). A thermodynamically consistent formulation of nonlocal and gradient plasticity. *Mechanics Research Communications*, *25*(1), 75–82 (cit. on p. 106).

Polizzotto, C. (2003). Unified thermodynamic framework for nonlocal/gradient continuum theories. *European Journal of Mechanics - A/Solids*, *22*(5), 651–668 (cit. on p. 106).

Popescu, S. (2014). Nonlocality beyond quantum mechanics. *Nature Physics*, *10*(4), 264–270. https://doi.org/10.1038/nphys2916 (cit. on p. 49)

Pranavi, D., Rajagopal, A., & Reddy, J. N. (2023). Phase field modeling of anisotropic fracture. *Continuum Mechanics and Thermodynamics*. https://doi.org/10.1007/s00161-023-01260-6 (cit. on p. 172)

Quiriny, A., Lambrechts, J., Moës, N., & Remacle, J.-F. (2024). X-Mesh: A new approach for the simulation of two-phase flow with sharp interface. *Journal of Computational Physics*, *501*, 112775. https://doi.org/10.1016/j.jcp.2024.112775 (cit. on p. 180)

Rabotnov, Y. N. (1969). Creep problems in structure members. *North Holland, Amsterdam.* (cit. on pp. 2, 31, 196).

Ragueneau, F., La Borderie, C., & Mazars, J. (2000). Damage model for concrete-like materials coupling cracking and friction, contribution towards structural damping: First uniaxial applications. *Mechanics of Cohesive-frictional Materi-*

als, *5*(8), 607–625. https://doi.org/10.1002/1099-1484(200011)5:8<607::AID-CFM108>3.0.CO;2-K (cit. on p. 9)

Ramtani, S. (1990). *Contribution a la modélisation du comportement multi-axial du béton endommagé avec description du caractère unilatéral.* (Doctoral dissertation). Université Paris VI. (Cit. on p. 10).

Ramtani, S., Berthaud, Y., & Mazars, J. (1992). Orthotropic behavior of concrete with directional aspects: Modelling and experiments. *Nuclear Engineering and Design*, *133*(1), 97–111. https://doi.org/10.1016/0029-5493(92)90094-C (cit. on p. 147)

Ranjbaran, A. (1991). Embedding of reinforcements in reinforced concrete elements implemented in DENA. *Computers & Structures*, *40*(4), 925–930. https://doi.org/10.1016/0045-7949(91)90322-D (cit. on p. 180)

Rashid, Y. (1968). Ultimate strength analysis of prestressed concrete pressure vessels. *Nuclear Engineering and Design*, *7*(4), 334–344. https://doi.org/10.1016/0029-5493(68)90066-6 (cit. on p. 23)

Rastiello, G., Giry, C., Gatuingt, F., & Desmorat, R. (2018a). From diffuse damage to strain localization from an eikonal non-local (enl) continuum damage model with evolving internal length. *Computer Methods in Applied Mechanics and Engineering*, *113*, 1512–1233 (cit. on pp. 143, 144, 155).

Rastiello, G., Riccardi, F., & Richard, B. (2019). Discontinuity-scale path-following methods for the embedded discontinuity finite element modeling of failure in solids. *Computer Methods in Applied Mechanics and Engineering*, *349*, 431–457 (cit. on p. 163).

Rastiello, G., Desmettre, C., Tailhan, J.-L., Rossi, P., Charron, J.-P., & Dal Pont, S. (2016). Modeling of fluid leakage through multi-cracked RC structural elements using a numerical probabilistic cracking approach. *Materials and Structures*, *49*(8), 3095–3108. https://doi.org/10.1617/s11527-015-0706-3 (cit. on p. 180)

Rastiello, G., Giry, C., Gatuingt, F., & Desmorat, R. (2018b). From diffuse damage to strain localization from an Eikonal Non-Local (ENL) Continuum Damage model with evolving internal length. *Computer Methods in Applied Mechanics and Engineering*, *331*, 650–674. https://doi.org/10.1016/j.cma.2017.12.006 (cit. on pp. 63, 64, 83, 88, 101, 107, 135, 136)

Rastiello, G., Oliveira, H. L., & Millard, A. (2022). Path-following methods for unstable structural responses induced by strain softening: A critical review. *Comptes Rendus. Mécanique*, *350*, 205–236. https://doi.org/10.5802/crmeca.112 (cit. on pp. 87, 163)

Rastiello, G., Tailhan, J.-L., Rossi, P., & Dal Pont, S. (2015). Macroscopic probabilistic cracking approach for the numerical modelling of fluid leakage in

concrete. *Annals of Solid and Structural Mechanics*, *7*(1-2), 1–16. https://doi.org/10.1007/s12356-015-0038-6 (cit. on pp. 23, 180)

Reese, S., Brepols, T., Fassin, M., Poggenpohl, L., & Wulfinghoff, S. (2021). Using structural tensors for inelastic material modeling in the finite strain regime – A novel approach to anisotropic damage. *Journal of the Mechanics and Physics of Solids*, *146*, 104174. https://doi.org/10.1016/j.jmps.2020.104174 (cit. on p. 146)

Reinhardt, H., & Cornelissen, H. (1984). Post-peak cyclic behaviour of concrete in uniaxial tensile and alternating tensile and compressive loading. *Cement and Concrete Research*, *14*(2), 263–270. https://doi.org/10.1016/0008-8846(84)90113-3 (cit. on pp. 9, 11)

Ribeiro Nogueira, B., Giry, C., Rastiello, G., & Gatuingt, F. (2022a). One-dimensional study of boundary effects and damage diffusion for regularized damage models. *Comptes Rendus. Mécanique*, *350*(G3), 507–546 (cit. on pp. 4, 63, 64, 73, 89, 96–98, 103, 139, 143, 198).

Ribeiro Nogueira, B., Rastiello, G., Giry, C., Gatuingt, F., & Callari, C. (2024a). Differential geometry-based thermodynamics derivation of isotropic and anisotropic eikonal non-local gradient (ENLG) damage models using a micromorphic media framework. *Engineering Fracture Mechanics*, *295*, 109670. https://doi.org/10.1016/j.engfracmech.2023.109670 (cit. on pp. 4, 65, 105, 119, 143–145, 147, 151, 168, 198)

Ribeiro Nogueira, B., Rastiello, G., Giry, C., Gatuingt, F., & Callari, C. (2024b). Eikonal gradient-enhanced regularization of anisotropic second-order tensorial continuum damage models for quasi-brittle materials. *Computer Methods in Applied Mechanics and Engineering* (cit. on p. 141).

Ribeiro Nogueira, B., Rostagni, H., Rastiello, G., Giry, C., Gatuingt, F., Callari, C., Ragueneau, F., Bitard, I., & Richard, B. (2022b). Damage mechanics implementations using mfront: Orthotropic, anisotropic microplane and embedded strong-discontinuity models for quasi-brittle materials In *8th mfront user day*. Gif-sur-Yvette, France. (Cit. on pp. 20, 47, 49).

Riccardi, F., Kishta, E., & Richard, B. (2017). A step-by-step global crack-tracking approach in E-FEM simulations of quasi-brittle materials. *Engineering Fracture Mechanics*, *170*, 44–58. https://doi.org/10.1016/j.engfracmech.2016.11.032 (cit. on pp. 21, 180)

Rice, J. R. (1968). A path independent integral and the approximate analysis of strain concentration by notches and cracks. *Journal of Applied Mechanics*, *35(2)*, 379–386 (cit. on p. 19).

Richard, B., & Ragueneau, F. (2013). Continuum damage mechanics based model for quasi brittle materials subjected to cyclic loadings: Formulation, numerical

implementation and applications. *Engineering Fracture Mechanics*, *98*, 383–406. https://doi.org/10.1016/j.engfracmech.2012.11.013 (cit. on p. 34)

Richard, B., Ragueneau, F., Cremona, C., & Adelaide, L. (2010). Isotropic continuum damage mechanics for concrete under cyclic loading: Stiffness recovery, inelastic strains and frictional sliding. *Engineering Fracture Mechanics*, *77*(8), 1203–1223. https://doi.org/10.1016/j.engfracmech.2010.02.010 (cit. on pp. 9, 34)

Rizzi, E., Carol, I., & Willam, K. (1995). Localization Analysis of Elastic Degradation with Application to Scalar Damage. *Journal of Engineering Mechanics*, *121*(4), 541–554. https://doi.org/10.1061/(ASCE)0733-9399(1995)121:4(541) (cit. on p. 45)

Rojas-Solano, L. B., Grégoire, D., & Pijaudier-Cabot, G. (2013). Interaction-based non-local damage model for failure in quasi-brittle materials. *Mechanics Research Communications*, *54*, 56–62 (cit. on pp. 59, 84, 143).

Rossi, P. (1991). A physical phenomenon which can explain the mechanical behaviour of concrete under high strain rates. *Materials and Structures*, *24*(6), 422–424. https://doi.org/10.1007/BF02472015 (cit. on p. 9)

Rossi, P., & Wu, X. (1992). Probabilistic model for material behaviour analysis and appraisement of concrete structures. *Magazine of Concrete Research*, *44*(161), 271–280. https://doi.org/10.1680/macr.1992.44.161.271 (cit. on p. 23)

Rossi, P., Wu, X., Le Maou, F., & Belloc, A. (1994a). Scale effect on concrete in tension. *Materials and Structures*, *27*(8), 437–444. https://doi.org/10.1007/BF02473447 (cit. on p. 15)

Rossi, P., Ulm, F.-J., & Hachi, F. (1996). Compressive Behavior of Concrete: Physical Mechanisms and Modeling. *Journal of Engineering Mechanics*, *122*(11), 1038–1043. https://doi.org/10.1061/(ASCE)0733-9399(1996)122:11(1038) (cit. on p. 23)

Rossi, P., Van Mier, J. G. M., Toutlemonde, F., Le Maou, F., & Boulay, C. (1994b). Effect of loading rate on the strength of concrete subjected to uniaxial tension. *Materials and Structures*, *27*(5), 260–264. https://doi.org/10.1007/BF02473042 (cit. on p. 9)

Rots, J. (1988). *Computational modeling of concrete fracture* (Doctoral dissertation). Technische Universiteit Delft. (Cit. on p. 23).

Roux, S., Réthoré, J., & Hild, F. (2009). Digital image correlation and fracture: An advanced technique for estimating stress intensity factors of 2D and 3D cracks. *Journal of Physics D: Applied Physics*, *42*(21), 214004. https://doi.org/10.1088/0022-3727/42/21/214004 (cit. on p. 15)

Rudnicki, J., & Rice, J. (1975). Conditions for the localization of deformation in pressure-sensitive dilatant materials. *Journal of the Mechanics and Physics of Solids*, *23*(6), 371–394 (cit. on p. 45).

Saanouni, K., Forster, C., & Hatira, F. B. (1994). On the Anelastic Flow with Damage. *International Journal of Damage Mechanics*, *3*(2), 140–169. https://doi.org/10.1177/105678959400300203 (cit. on p. 36)

The Sage Developers. (2022). *Sagemath, the Sage Mathematics Software System (Version 9.7)*. (Cit. on p. 107).

Salzman, A., Moës, N., & Chevaugeon, N. (2016). On use of the thick level set method in 3D quasi-static crack simulation of quasi-brittle material. *International Journal of Fracture*, *202*(1), 21–49. https://doi.org/10.1007/s10704-016-0132-8 (cit. on p. 66)

Sarkar, S., Singh, I., Mishra, B., Shedbale, A., & Poh, L. (2019). A comparative study and ABAQUS implementation of conventional and localizing gradient enhanced damage models. *Finite Elements in Analysis and Design*, *160*, 1–31 (cit. on pp. 133, 157).

Saroukhani, S., Vafadari, R., & Simone, A. (2013). A simplified implementation of a gradient-enhanced damage model with transient length scale effects. *Computational Mechanics*, *51*, 899–909 (cit. on p. 60).

Schuler, H., Mayrhofer, C., & Thoma, K. (2006). Spall experiments for the measurement of the tensile strength and fracture energy of concrete at high strain rates. *International Journal of Impact Engineering*, *32*(10), 1635–1650. https://doi.org/10.1016/j.ijimpeng.2005.01.010 (cit. on p. 81)

Sellier, A., Casaux-Ginestet, G., Buffo-Lacarrière, L., & Bourbon, X. (2013a). Orthotropic damage coupled with localized crack reclosure processing: Part II: Applications. *Engineering Fracture Mechanics*, *97*, 168–185. https://doi.org/10.1016/j.engfracmech.2012.10.016 (cit. on p. 34)

Sellier, A., Casaux-Ginestet, G., Buffo-Lacarrière, L., & Bourbon, X. (2013b). Orthotropic damage coupled with localized crack reclosure processing. Part I: Constitutive laws. *Engineering Fracture Mechanics*, *97*, 148–167. https://doi.org/10.1016/j.engfracmech.2012.10.012 (cit. on p. 34)

Sellier, A., & Millard, A. (2019). A homogenized formulation to account for sliding of non-meshed reinforcements during the cracking of brittle matrix composites: Application to reinforced concrete. *Engineering Fracture Mechanics*, *213*, 182–196. https://doi.org/10.1016/j.engfracmech.2019.04.008 (cit. on p. 180)

Sethian, J. A. (1996). A fast marching level set method for monotonically advancing fronts. *Proceedings of the National Academy of Sciences*, *93*(4), 1591–1595. https://doi.org/10.1073/pnas.93.4.1591 (cit. on p. 63)

Shah, S. P. (1990). Experimental methods for determining fracture process zone and fracture parameters. *Engineering Fracture Mechanics*, *35*(1), 3–14. https://doi.org/10.1016/0013-7944(90)90178-J (cit. on p. 14)

Shedbale, A. S., Sun, G., & Poh, L. H. (2021). A localizing gradient enhanced isotropic damage model with Ottosen equivalent strain for the mixed-mode fracture of concrete. *International Journal of Mechanical Sciences*, *199*, 106410. https://doi.org/10.1016/j.ijmecsci.2021.106410 (cit. on p. 33)

Shi, C., van DAM, A., van MIER, J., & Sluys, B. (2000). Crack interaction in concrete. *Materials for buildings and structures*, *6*, 125–131 (cit. on p. 47).

Sidoroff, F. (1981). Description of Anisotropic Damage Application to Elasticity. In J. Hult & J. Lemaitre (Eds.), *Physical Non-Linearities in Structural Analysis* (pp. 237–244). Springer Berlin Heidelberg. https://doi.org/10.1007/978-3-642-81582-9_35. (Cit. on pp. 35, 36)

Silling, S. A. (2000). Reformulation of elasticity theory for discontinuities and long-range forces. *Journal of the Mechanics and Physics of Solids*, *48*(1), 175–209. https://doi.org/10.1016/S0022-5096(99)00029-0 (cit. on p. 67)

Silling, S. A., Epton, M., Weckner, O., Xu, J., & Askari, E. (2007). Peridynamic States and Constitutive Modeling. *Journal of Elasticity*, *88*(2), 151–184. https://doi.org/10.1007/s10659-007-9125-1 (cit. on pp. 67, 68)

Silling, S., & Askari, E. (2005). A meshfree method based on the peridynamic model of solid mechanics. *Computers & Structures*, *83*(17-18), 1526–1535. https://doi.org/10.1016/j.compstruc.2004.11.026 (cit. on p. 67)

Simo, J. C., Oliver, J., & Armero, F. (1993). An analysis of strong discontinuities induced by strain-softening in rate-independent inelastic solids. *Computational Mechanics*, *12*(5), 277–296. https://doi.org/10.1007/BF00372173 (cit. on p. 20)

Simone, A., Askes, H., Peerlings, R. H. J., & Sluys, L. J. (2003a). Interpolation requirements for implicit gradient-enhanced continuum damage models. *Communications in Numerical Methods in Engineering*, *19*(7), 563–572. https://doi.org/10.1002/cnm.597 (cit. on pp. 87, 88, 133, 154)

Simone, A. (2007). Explicit and implicit gradient-enhanced damage models. *Revue Européenne de Génie Civil*, *11*(7-8), 1023–1044. https://doi.org/10.1080/17747120.2007.9692975 (cit. on p. 58)

Simone, A., Askes, H., & Sluys, L. J. (2004). Incorrect initiation and propagation of failure in non-local and gradient-enhanced media. *International Journal of Solids and Structures*, *41*(2), 351–363. https://doi.org/10.1016/j.ijsolstr.2003.09.020 (cit. on pp. 2, 59, 83, 142, 197)

Simone, A., Wells, G. N., & Sluys, L. J. (2003b). From continuous to discontinuous failure in a gradient-enhanced continuum damage model. *Computer Methods in Applied Mechanics and Engineering*, *192*(41), 4581–4607 (cit. on pp. 140, 180).

Sluys, L. (1992). *Wave propagation, localisation and dispersion in softening solids.* (Doctoral dissertation). Delft University of Technology. (Cit. on pp. 47, 74–76).

Sluys, L., & de Borst, R. (1994). Dispersive properties of gradient-dependent and rate-dependent media. *Mechanics of Materials*, *18*(2), 131–149. https://doi.org/10.1016/0167-6636(94)00009-3 (cit. on pp. 53, 58, 74, 76, 177)

Sluys, L., De Borst, R., & Mühlhaus, H.-B. (1993). Wave propagation, localization and dispersion in a gradient-dependent medium. *International Journal of Solids and Structures*, *30*(9), 1153–1171. https://doi.org/10.1016/0020-7683(93)90010-5 (cit. on pp. 74, 76, 177)

Steinmann, P., & Carol, I. (1998). A framework for geometrically nonlinear continuum damage mechanics. *International Journal of Engineering Science*, *36*(15), 1793–1814 (cit. on p. 111).

Suhubl, E. S., & Eringen, A. C. (1964). Nonlinear theory of micro-elastic solids—II. *International Journal of Engineering Science*, *2*(4), 389–404 (cit. on p. 51).

Swain, M. V. (1991). Quasi-brittle behaviour of ceramics and its relevance for thermal shock. *Engineering Fracture Mechanics*, *40*(4-5), 871–877. https://doi.org/10.1016/0013-7944(91)90246-W (cit. on p. 8)

Tailhan, J.-L., Dal Pont, S., & Rossi, P. (2010). From local to global probabilistic modeling of concrete cracking. *Annals of Solid and Structural Mechanics*, *1*(2), 103–115. https://doi.org/10.1007/s12356-010-0008-y (cit. on p. 23)

Tailhan, J., Rossi, P., Phan, T., Rastiello, G., & Foulliaron, J. (2013). Multiscale probabilistic approaches and strategies for the modelling of concrete. In *Framcos-8*. (Cit. on p. 23).

Taylor, G. I. (1938). Plastic strain in metals. *J. Inst. Metals*, *62*, 307–324 (cit. on p. 39).

Teichtmeister, S., Kienle, D., Aldakheel, F., & Keip, M. .-. (2017). Phase field modeling of fracture in anisotropic brittle solids. *International Journal of Non-Linear Mechanics*, *97*, 1–21 (cit. on pp. 144, 146, 171, 180).

Terrien, M. (1980). Emission acoustique et "comportement mécanique post-critique" d'un béton sollicité en traction. *Bulletin de liaison des laboratoires des ponts et chaussees*, *105* (cit. on pp. 8, 10).

Thierry, F. (2019). Damage-to-fracture transition through an Eikonal Non-Local (ENL) continuum damage formulation with embedded strong discontinuities In *Proceedings of the 10th International Conference on Fracture Mechanics of Concrete*

and Concrete Structures. IA-FraMCoS. https://doi.org/10.21012/FC10.233386. (Cit. on p. 180)

Thierry, F., Rastiello, G., Giry, C., & Gatuingt, F. (2020a). One-dimensional Eikonal Non-Local (ENL) damage models: Influence of the integration rule for computing interaction distances and indirect loading control on damage localization. *Mechanics Research Communications*, *110*, 103620. https://doi.org/10.1016/j.mechrescom.2020.103620 (cit. on pp. 63, 84, 87, 101)

Thierry, F., Rastiello, G., Giry, C., & Gatuingt, F. (2020b). One-dimensional eikonal non-local (enl) damage models: Influence of the integration rule for computing interaction distances and indirect loading control on damage localization. *Mechanics Research Communications*, *110*, 103620 (cit. on p. 143).

Thomas, T. (1961). *Plastic flow and fracture in solids by tracy y thomas*. Elsevier Science. (Cit. on p. 45).

Tijssens, M. G., Sluys, B. L., & Van Der Giessen, E. (2000). Numerical simulation of quasi-brittle fracture using damaging cohesive surfaces. *European Journal of Mechanics - A/Solids*, *19*(5), 761–779. https://doi.org/10.1016/S0997-7538(00)00190-X (cit. on pp. 22, 23)

Tisserand, P.-J., Rostagni, H., Giry, C., Nguyen, T. T. H., Desmorat, R., & Ragueneau, F. (2022). An orthotropic damage model with internal sliding and friction for masonry-like material. *Engineering Fracture Mechanics*, *267*, 108397. https://doi.org/10.1016/j.engfracmech.2022.108397 (cit. on p. 179)

Truesdell, C., & Noll, W. (1965). The Non-Linear Field Theories of Mechanics. In C. Truesdell & W. Noll (Eds.), *The Non-Linear Field Theories of Mechanics / Die Nicht-Linearen Feldtheorien der Mechanik* (pp. 1–541). Springer. https://doi.org/10.1007/978-3-642-46015-9_1. (Cit. on pp. 29, 50)

Truesdell, C., & Toupin, R. (1960). The Classical Field Theories. In S. Flügge (Ed.), *Principles of Classical Mechanics and Field Theory / Prinzipien der Klassischen Mechanik und Feldtheorie* (pp. 226–858). Springer. https://doi.org/10.1007/978-3-642-45943-6_2. (Cit. on p. 50)

Tupek, M., Rimoli, J., & Radovitzky, R. (2013). An approach for incorporating classical continuum damage models in state-based peridynamics. *Computer Methods in Applied Mechanics and Engineering*, *263*, 20–26. https://doi.org/10.1016/j.cma.2013.04.012 (cit. on p. 68)

Valoroso, N., & Stolz, C. (2022). Graded damage in quasi-brittle solids. *International Journal for Numerical Methods in Engineering*, nme.6947. https://doi.org/10.1002/nme.6947 (cit. on p. 52)

Vandoren, B., & Simone, A. (2018). Modeling and simulation of quasi-brittle failure with continuous anisotropic stress-based gradient-enhanced damage models. *Computer Methods in Applied Mechanics and Engineering*, *332*, 644–685. https:

//doi.org/10.1016/j.cma.2017.12.027 (cit. on pp. 59, 61, 102, 123, 124, 135, 139, 143, 146–148, 155, 177)

Vassaux, M., Oliver-Leblond, C., Richard, B., & Ragueneau, F. (2016). Beam-particle approach to model cracking and energy dissipation in concrete: Identification strategy and validation. *Cement and Concrete Composites*, *70*, 1–14. https://doi.org/10.1016/j.cemconcomp.2016.03.011 (cit. on p. 18)

Voreux, O. (2022). *High temperature fatigue crack growth modeling in Nickel-based superalloys using a local approach to fracture* (Doctoral dissertation). Université Paris-Saclay. (Cit. on p. 140).

Wang, J., Poh, L. H., & Guo, X. (2023). Localizing gradient damage model based on a decomposition of elastic strain energy density. *Engineering Fracture Mechanics*, *279*, 109032. https://doi.org/10.1016/j.engfracmech.2022.109032 (cit. on pp. 157, 172)

Weibull, W. (1939). *A Statistical Theory of the Strength of Materials*. Generalstabens litografiska anstalts förlag. (Cit. on p. 15).

Wells, G., & Sluys, L. (2001). Three-dimensional embedded discontinuity model for brittle fracture. *International Journal of Solids and Structures*, *38*(5), 897–913. https://doi.org/10.1016/S0020-7683(00)00029-9 (cit. on p. 20)

Westin, C. .-., Maier, S. E., Mamata, H., Nabavi, A., Jolesz, F. A., & Kikinis, R. (2002). Processing and visualization for diffusion tensor MRI. *Medical Image Analysis*, *6*(2), 93–108 (cit. on p. 148).

Winkler, B., Hofstetter, G., & Lehar, H. (2004). Application of a constitutive model for concrete to the analysis of a precast segmental tunnel lining. *International Journal for Numerical and Analytical Methods in Geomechanics*, *28*(7-8), 797–819 (cit. on pp. 47, 156–158, 160, 161).

Winkler, B., Hofstetter, G., & Niederwanger, G. (2001). Experimental verification of a constitutive model for concrete cracking. *Proceedings of the Institution of Mechanical Engineers, Part L: Journal of Materials: Design and Applications*, *215*(2), 75–86 (cit. on pp. 47, 156, 157, 160, 161).

Wu, J.-Y., Nguyen, V. P., Thanh Nguyen, C., Sutula, D., Bordas, S., & Sinaie, S. (2019). Phase field modelling of fracture. *Advances in Applied Mechanics*, *53*, 1–183, https://www.sciencedirect.com/science/article/pii/S0065215619300134 (cit. on p. 66).

Wu, L., Sket, F., Molina-Aldareguia, J., Makradi, A., Adam, L., Doghri, I., & Noels, L. (2015). A study of composite laminates failure using an anisotropic gradient-enhanced damage mean-field homogenization model. *Composite Structures*, *126*, 246–264 (cit. on pp. 143, 172).

Xu, X.-P., & Needleman, A. (1994). Numerical simulations of fast crack growth in brittle solids. *Journal of the Mechanics and Physics of Solids*, *42*(9), 1397–1434. https://doi.org/10.1016/0022-5096(94)90003-5 (cit. on p. 22)

Yin, B., Zreid, I., Lin, G., Bhashyam, G., & Kaliske, M. (2020). An anisotropic damage formulation for composite materials based on a gradient-enhanced approach: Formulation and implementation at small strain. *International Journal of Solids and Structures*, *202*, 631–645. https://doi.org/10.1016/j.ijsolstr.2020.06.035 (cit. on pp. 143, 172, 180)

Zhang, J.-Z., & Zhou, X.-P. (2022). Fracture process zone (FPZ) in quasi-brittle materials: Review and new insights from flawed granite subjected to uniaxial stress. *Engineering Fracture Mechanics*, *274*, 108795. https://doi.org/10.1016/j.engfracmech.2022.108795 (cit. on p. 15)

Zhu, Q., Kondo, D., & Shao, J. (2008). Micromechanical analysis of coupling between anisotropic damage and friction in quasi brittle materials: Role of the homogenization scheme. *International Journal of Solids and Structures*, *45*(5), 1385–1405. https://doi.org/10.1016/j.ijsolstr.2007.09.026 (cit. on p. 40)

Zreid, I., & Kaliske, M. (2014). Regularization of microplane damage models using an implicit gradient enhancement. *International Journal of Solids and Structures*, *51*(19-20), 3480–3489 (cit. on pp. 143, 157).

Zubelewicz, A., & Bažant, Z. P. (1987). Interface element modeling of fracture in aggregate composites. *Journal of Engineering Mechanics*, *113*(11), 1619–1630. https://doi.org/10.1061/(ASCE)0733-9399(1987)113:11(1619) (cit. on p. 18)